Modification and Evaluation of PAN and PP Membranes with Polymer Brushes *via* UV-induced Graft Polymerization

Dissertation

to obtain the academic degree
Dr. rer. nat.

submitted to the Department of Chemistry
Institute of Pharmacy
Faculty of Mathematics, Informatics and Natural Sciences
University of Hamburg

by

Timo Friedrich

Hamburg 2025

The research reported herein was conducted from 2022 to 2025 at the Institute of Pharmacy, Department of Pharmaceutical and Medicinal Chemistry, University of Hamburg, under the supervision of Prof. Dr. Wolfgang Maison.

First reviewer: Prof. Dr. Wolfgang Maison

Second reviewer: Prof. Dr. Ralph Holl

Date of Disputation: 12.12.2025

Committee: Prof. Dr. Wolfgang Maison, Prof. Dr. Volkmar Vill, Prof. Dr. Bianka Siewert

I would rather have questions that can't be answered than answers that can't be questioned.

– Richard P. Feynmann

List of publications

1) Friedrich, T.; Timm, D.; Glass, S.; Schneider, E. S.; Filiz, V.; Maison, W. Postfunctionalization of PAN Membranes *via* UV-Grafting of Charged and Zwitterionic Polymer Brushes. *Langmuir* **2025**. DOI: 10.1021/acs.langmuir.5c05068

2) Friedrich, T.; Kobus, M.; Mesgarha, S.; Moretto, E.; Grosche, L.; Maison, W. Tailoring the properties of functional materials with *N*-oxides. *Adv. Funct. Mater.* **2025**. DOI: 10.1002/adfm.202515786.

3) Kobus, M.; Friedrich, T.; Zorn, E.; Burmeister, N.; Maison, W. Medicinal Chemistry of Drugs with *N*-Oxide Functionalities. *J. Med. Chem.* **2024**, 67 (7), 5168-5184. DOI: 10.1021/acs.jmedchem.4c00254.

4) Burmeister, N.; Vollstedt, C.; Kroger, C.; Friedrich, T.; Scharnagl, N.; Rohnke, M.; Zorn, E.; Wicha, S. G.; Streit, W. R.; Maison, W. Zwitterionic surface modification of polyethylene *via* atmospheric plasma-induced polymerization of (vinylbenzyl-)sulfobetaine and evaluation of antifouling properties. *Colloids Surf. B* **2023**, 224, 113195. DOI: 10.1016/j.colsurfb.2023.113195.

5) Burmeister, N.; Zorn, E.; Farooq, A.; Preuss, L.; Vollstedt, C.; Friedrich, T.; Mantel, T.; Scharnagl, N.; Rohnke, M.; Ernst, M.; *et al.* Surface Grafted N-Oxides have Low-Fouling and Antibacterial Properties. *Adv. Mater. Interfaces* **2023**, 10, 2300505. DOI: 10.1002/admi.202300505.

List of conferences

1) Presentation & Poster: Friedrich, T.; Functionalized PAN Membranes: Tackling Fouling in Water Purification Systems. International PhD Student & Postdoc Meeting 2025, DPhG, Graz, 26-28th February 2025.

Table of contents

List of abbreviations

AFM	Atomic force microscopy
APTES	(3-Aminopropyl)triethoxysilane
BAPO	Phenylbis(2,4,6-trimethylbenzoyl)phosphine oxide
BiBB	2-Bromoisobutyryl bromide
BSA	Bovine serum albumin
BTEAC	Benzyltriethylammonium chloride
CA	Cellulose acetate
CB	Carboxybetaine
CFU	Colony forming units
COSY	Correlation spectroscopy
CTAB	Cetyltrimethylammonium bromide
DAC	[2-(Acryloyloxy)ethyl]trimethylammonium chloride
DDBAC	Dodecyldimethylbenzylammonium chloride
DMAEMA	2-(Dimethylamino)ethyl methacrylate
DMAPMA	*N*-[3-(Dimethylamino)propyl]methacrylamide
DMOTPAC	Dimethyloctadecyl[3-(trimethoxysilyl)propyl]ammonium chloride
DMF	Dimethylformamide
EDC	1-Ethyl-3-(3-dimethylaminopropyl)carbodiimide
EDTA	Ethylenediaminetetraacetic acid
EDX	Energy-dispersive X-ray spectroscopy
EPS	Extracellular polymeric substances
e.g.	*exempli gratia*
eq.	Equivalent
et al.	*et alii*
GHS	Globally harmonized system
GPC	Gel permeation chromatography
HA	Humic acid
HMBC	Heteronuclear multiple bond correlation

HSQC	Heteronuclear single quantum coherence
i.e.	*id est*
IR	Infrared spectroscopy
LAP	Lithium phenyl(2,4,6-trimethylbenzoyl)phosphinate
LBL	Layer-by-layer
LED	Light-emitting diode
MAPTAC	[3-(Methacryloylamino)propyl]trimethylammonium chloride
METAC	2-(Methacryloyloxy)ethyl trimethylammonium chloride
MF	Microfiltration
MPC	2-Methacryloyloxyethyl phosphorylcholine
MS	Mass spectrometry
MWCO	Molecular weight cut-off
NF	Nanofiltration
NHS	*N*-Hydroxysuccinimide
NIPS	Non-solvent induced phase separation
NMR	Nuclear magnetic resonance
NMP	*N*-Methyl-2-pyrrolidon
NOM	Natural organic matter
NOx	*N*-Oxide
NWF	Nonwoven fabric membranes
PA	Polyamide
PAH	Polyallylamine hydrochloride
PAN	Polyacrylonitrile
PB	Phosphobetaine
PBS	Phosphate buffered saline
PE	Polyethylene
PEG	Polyethylene glycol
PES	Polyethersulfone
PET	Polyethylene terephthalate
PFP	Pentafluorophenol

PI	Polyimide
PP	Polypropylene
PS	Polystyrene
PSF	Polysulfone
PSS	Polystyrene sulfonate
PU	Polyurethane
PVDF	Polyvinylidene fluoride
QAC	Quaternary ammonium compound
RO	Reverse osmosis
RT	Room temperature
S. aureus	*Staphylococcus aureus*
SB	Sulfobetaine
SEM	Scanning electron microscope
SI-ATRP	Surface initiated atom transfer radical polymerization
TGA	Thermogravimetric analysis
TLC	Thin-layer chromatography
UF	Ultrafiltration
UV-Vis	Ultraviolet-visible
VBTAC	(Vinylbenzyl)trimethylammonium chloride
VBTOH	1-Hydroxy-*N*,*N*-dimethyl-*N*-(4-vinylbenzyl)methanaminium
WCA	Water contact angle
XPS	X-ray photoelectron spectroscopy

1 Zusammenfassung

Biofouling stellt eine zentrale Herausforderung in der Membranfiltration dar, da es zur Porenverstopfung führt und die Permeabilität erheblich einschränkt. In dieser Arbeit wurde eine schonende und vielseitig einsetzbare Methode zur Oberflächenfunktionalisierung von Polyacrylnitril (PAN)-Ultrafiltrationsmembranen sowie von Polypropylen (PP)-Vliesmembranen für die Wasseraufbereitung entwickelt, mit dem Ziel, Biofouling durch die Einführung von Zwitterionen und quaternären Ammonium Verbindungen (QAVs) effektiv zu reduzieren.

Die Modifikation der PAN-Membranen erfolgte mittels UV-induzierter Pfropfpolymerisation unter Einsatz der Photoinitiatoren Phenylbis(2,4,6-trimethylbenzoyl)-phosphinoxid (BAPO) und Lithium-Phenyl-2,4,6-trimethylbenzoylphosphinat (LAP). Die funktionalisierten Polymerbürsten wurden entweder direkt durch geeignete Monomere (z. B. mit [2-(Methacryloyloxy)ethyl]trimethylammoniumchlorid (METAC) oder Phosphobetain) oder nach der Polymerisation aus tertiären Aminen über Umsetzungen von 2-(Dimethylamino)ethylmethacrylat (DMAEMA) bzw. *N-[3-*(Dimethylamino)propyl]methacrylamid (DMAPMA) zu den korrespondierenden Carboxybetainen, Sulfobetainen, *N*-Oxiden oder Ammoniumalkoholen erhalten.

Die Membranen zeigten eine Permeabilität von 80–120 L m^{-2} h^{-1} bar^{-1}, was ein Hinweis darauf ist, dass die Porenstruktur bei der Pfropfpolymerisation und der Funktionalisierung weitgehend erhalten blieb. Bestätigt wurde dies durch SEM-Analysen, Porengrößenbestimmungen (8.39–11.1 nm), Porositätsmessungen (1.65–5.40%) sowie durch IR-, XPS- und EDX-Daten. Ein zentrales Ergebnis war der Nachweis, dass auch die inneren Porenwände erfolgreich funktionalisiert wurden. Zeta-Potenzial-Messungen zeigten eine signifikante Erhöhung der Oberflächenladung im Vergleich zu nicht modifiziertem PAN. TGA-Analysen belegten eine besonders hohe thermische Stabilität der Phosphobetaine, während *N*-Oxide die geringste Stabilität aufwiesen.

Um die Fähigkeit der modifizierten Membranen zur Entfernung geladener Verunreinigungen aus Trinkwasser zu untersuchen, wurden Adsorptionsstudien sowohl unter statischen als auch unter dynamischen Bedingungen durchgeführt. Als Modellsubstanz für anionische Verunreinigungen wurde Acid Orange 7 ausgewählt, während Methylenblau als Repräsentant kationischer Substanzen diente. Die

Ergebnisse zeigten eine ausgeprägte Affinität der funktionalisierten Membranen zu anionischen Substanzen, wobei unter beiden Versuchsbedingungen Adsorptionskapazitäten von bis zu 10^{17} Molekülen pro cm^2 erreicht wurden. Im Gegensatz dazu wurden kationische Substanzen nur in sehr geringem Maße adsorbiert, da elektrostatische Abstoßungseffekte infolge des Donnan-Effekts ihre Anlagerung an die Membranoberfläche verhinderten.

Die Membranen wiesen ausgeprägte Antifouling-Eigenschaften auf, da insbesondere Bovines Serumalbumin (BSA) und Lysozym nicht adsorbiert wurden. Antimikrobielle Effekte gegenüber *Staphylococcus aureus* wurden nicht beobachtet.

Die etablierte UV-Pfropfpolymerisation konnte erfolgreich auf PP-Vliesmembranen übertragen werden. Hierbei wurden die QAVs 4-(Vinylbenzyl)-trimethylammoniumchlorid (VBTAC) und 2-Hydroxy-*N*,*N*-dimethyl-*N*-(4-vinylbenzyl)-ethan-1-aminiumbromid (VBTOH) sowie neu synthetisierte Styrol-basierte Carboxybetaine mit unterschiedlicher Spacerlänge (C1 und C3) kovalent immobilisiert. Die erfolgreiche Modifikation wurde durch IR-Spektroskopie bestätigt. Kontaktwinkelmessungen zeigten eine deutlich erhöhte Hydrophilie für Carboxybetaine (19–25°) und QAVs (60–80°) im Vergleich zu unbehandelten PP (131°). Auch bei diesen Membranen wurde eine hohe Adsorption anionischer Substanzen, jedoch keine signifikante Wechselwirkung mit kationischen Substanzen beobachtet. Während VBTAC und insbesondere VBTOH antibakterielle Wirkung gegenüber *Staphylococcus aureus* zeigten, überzeugten die Carboxybetaine durch ihre Antifouling-Eigenschaften gegenüber Proteinen wie BSA und Lysozym.

Darüber hinaus wurde das Potenzial der mit Poly(carboxybetain) funktionalisierten Membranen zur kovalenten Immobilisierung bioaktiver Moleküle untersucht. Dafür wurden Meerrettichperoxidase Enzyme entweder über *in situ* aktivierte *N*-Hydroxysuccinimid (NHS)-Ester oder Pentafluorophenol (PFP)-Ester, welche mit UV-Pfropfpolymerisation eingeführt wurden, an die Membranoberfläche gebunden. In beiden Fällen konnte die erfolgreiche Immobilisierung sowie die enzymatische Aktivität mittels Farbreaktion nachgewiesen werden, wobei die PFP-Methode eine deutlich höhere Aktivität aufwies. Diese Arbeit liefert somit ein vielseitiges Konzept zur gezielten Oberflächenfunktionalisierung von Membranen mit antimikrobieller und Antifouling-Wirkung und eröffnet neue Perspektiven für Anwendungen in der Wasser- und Luftfiltration (Figure 1).

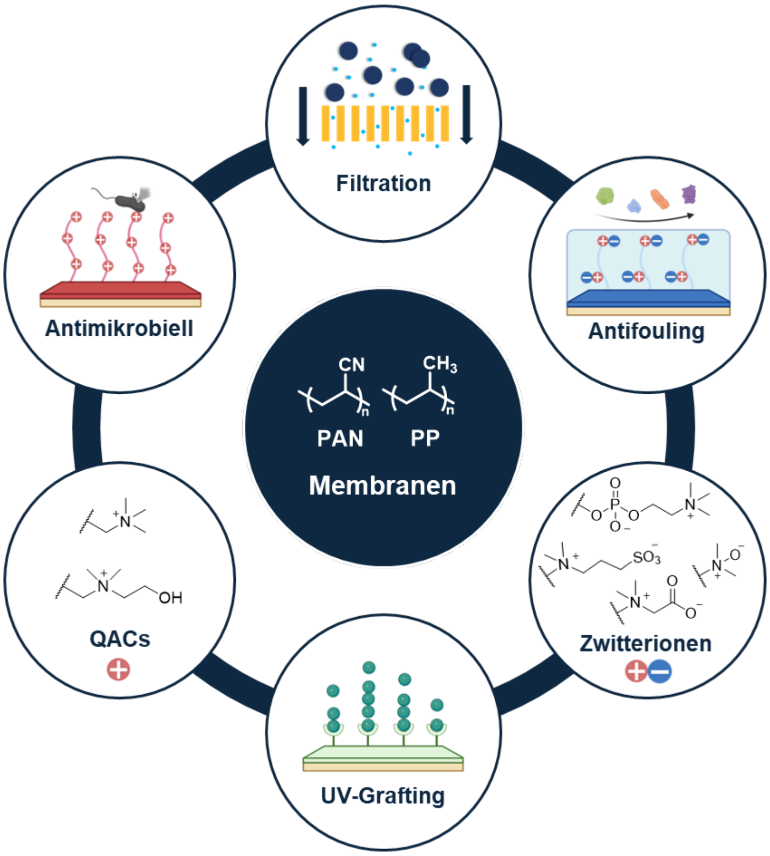

Figure 1: UV-induzierte Oberflächenmodifizierung von PAN- und PP-Membranen durch kovalente Verknüpfung antimikrobieller QACs sowie zwitterionischer Verbindungen zur Reduktion von Biofouling, mit dem Ziel, die Membraneigenschaften für Anwendungen in der Wasseraufbereitung gezielt zu verbessern.

2 Summary

Biofouling is a major problem for membrane filtration because it blocks the pores of the membrane and significantly decreases flux. This work developed a mild and modular method to functionalize the surfaces of polyacrylonitrile (PAN) ultrafiltration membranes for water purification and polypropylene (PP) nonwoven membranes for air filtration. The goal was to reduce biofouling by introducing zwitterions and quaternary ammonium compounds (QACs).

The PAN membranes were modified by UV-induced graft polymerization using the photoinitiators phenylbis(2,4,6-trimethylbenzoyl)phosphine oxide (BAPO) and lithium phenyl-2,4,6-trimethylbenzoylphosphinate (LAP). The functionalized polymer brushes were either synthesized directly using suitable monomers (e.g., with [2-(methacryloyloxy)ethyl]trimethylammonium chloride (METAC) or phosphobetaine) or after polymerization from tertiary amines via reactions of 2-(dimethylamino)ethylmethacrylate (DMAEMA) or *N*-[3-(dimethylamino)propyl]methacrylamide (DMAPMA) to the corresponding carboxybetaine, sulfobetaine, *N*-oxides or ammonium alcohols.

The resulting membranes exhibited a permeability of 80–120 L m^{-2} h^{-1} bar^{-1}, indicating that the polymerization did not significantly affect the pore structure. These results were supported by SEM, pore size analyses (8.39–11.1 nm), porosity measurements (1.65–5.40%), IR, XPS and EDX data. Of particular note is the evidence showing that the inner pore walls were also successfully functionalized. Zeta potential measurements revealed that the functionalized membranes displayed a significantly higher positive surface charge than pristine PAN. TGA analyses revealed that phosphobetaine had particularly high thermal stability, while *N*-oxides had the lowest stability.

In order to investigate the ability of the modified membranes to remove charged contaminants from drinking water, adsorption studies were conducted under both static and dynamic conditions. Acid orange 7 was selected as the model substance for anionic contaminants, while methylene blue served as the representative for cationic substances. The results revealed that the functionalized membranes exhibited a strong preference for anionic substances, achieving adsorption capacities of up to 10^{17} molecules per cm^2 under both test conditions. In contrast, cationic substances were only adsorbed to a very limited extent, as electrostatic repulsion effects due to the Donnan effect prevented their attachment to the membrane surface. The membranes exhibited clear antifouling properties, since BSA and lysozyme were not adsorbed to the membrane surface. The modified membranes showed no antimicrobial effects against *Staphylococcus aureus*.

The UV graft polymerization process was successfully transferred to nonwoven polypropylene (PP) membranes. The QACs 4-(Vinylbenzyl)trimethylammonium chloride (VBTAC) and 2-Hydroxy-*N*,*N*-dimethyl-*N*-(4-vinylbenzyl)-ethan-1-aminium-bromide (VBTOH) and a newly synthesized, styrene-based carboxybetaine with variable spacer length (C1 and C3) were covalently immobilized. IR spectroscopy validated the modifications and contact angle measurements revealed an increase in hydrophilicity for the carboxybetaine (19–25°) and the QACs (60–80°) compared to pristine PP (131°).

Similar to PAN membranes, high adsorption capacities were observed for anionic contaminants, but not cationic ones. VBTAC and VBTOH showed pronounced antibacterial activity against *Staphylococcus aureus*, while the carboxybetaine demonstrated significant antifouling properties against proteins such as bovine serum albumin (BSA) and lysozyme.

Finally, the suitability of the poly(carboxybetaine) functionalized membranes for the covalent immobilization of bioactive molecules was investigated. For this purpose, horseradish peroxidase enzymes were bound to the membrane surface either *via in situ* activated *N*-hydroxysuccinimide (NHS) esters or pentafluorophenol (PFP) esters, which were introduced by UV graft polymerization. Immobilization proved successful in both cases, with the PFP strategy exhibiting higher enzymatic activity. These results demonstrate that the functionalized membranes developed have great potential for applications in biofouling control and the selective binding of biological or ionic species (Figure 2).

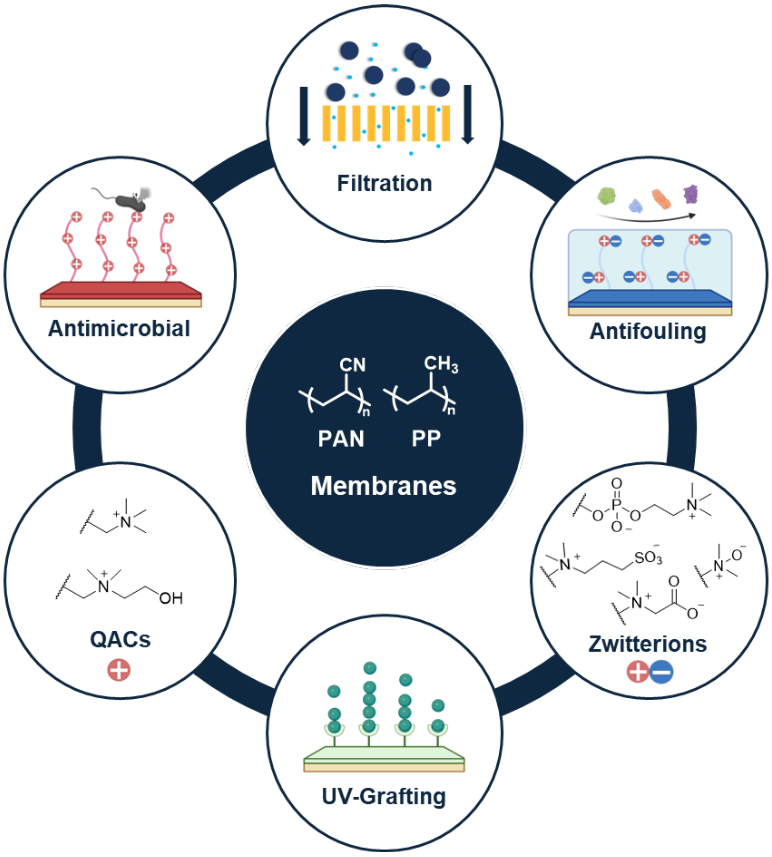

Figure 2: UV-induced surface modification of PAN and PP membranes through covalent bonding of antimicrobial QACs and zwitterionic compounds to reduce biofouling, with the aim of specifically improving membrane properties for applications in water treatment.

3 Introduction

Water is an essential resource for life on earth. Despite its importance, fresh water is often severely limited in availability.[1] Around 96.5% of the world's water reserves are found in oceans and seas, and as saltwater they are not directly drinkable or usable. Another 1% is saline groundwater. Only around 2.5% of the world's water is fresh water, with approximately 69% of this amount being held in ice sheets and glaciers. The remaining 31% is distributed among surface waters, such as lakes and rivers, soil moisture and underground aquifers, with the latter accounting for the largest share.[2]

Increasing water scarcity is one of the biggest obstacles to sustainable development today. Since 2000, over 2.4 billion people have lived in regions experiencing chronic water shortages, and this figure could rise to 4.8 billion by 2025. Currently, around 40% of the world's population is affected by water scarcity, and around 1000 children die every day from diseases caused by poor water quality and sanitation.[3] The projected ratio of human water demand to water availability in 2050 is shown in Figure 3.

The per capita availability of annual water resources (AWR) is a quantitative measure of water availability. A region is considered water-stressed if the available water volume is less than 2000 m^3 per person per year, which can lead to problems during periods of drought or artificial water shortages.[3]

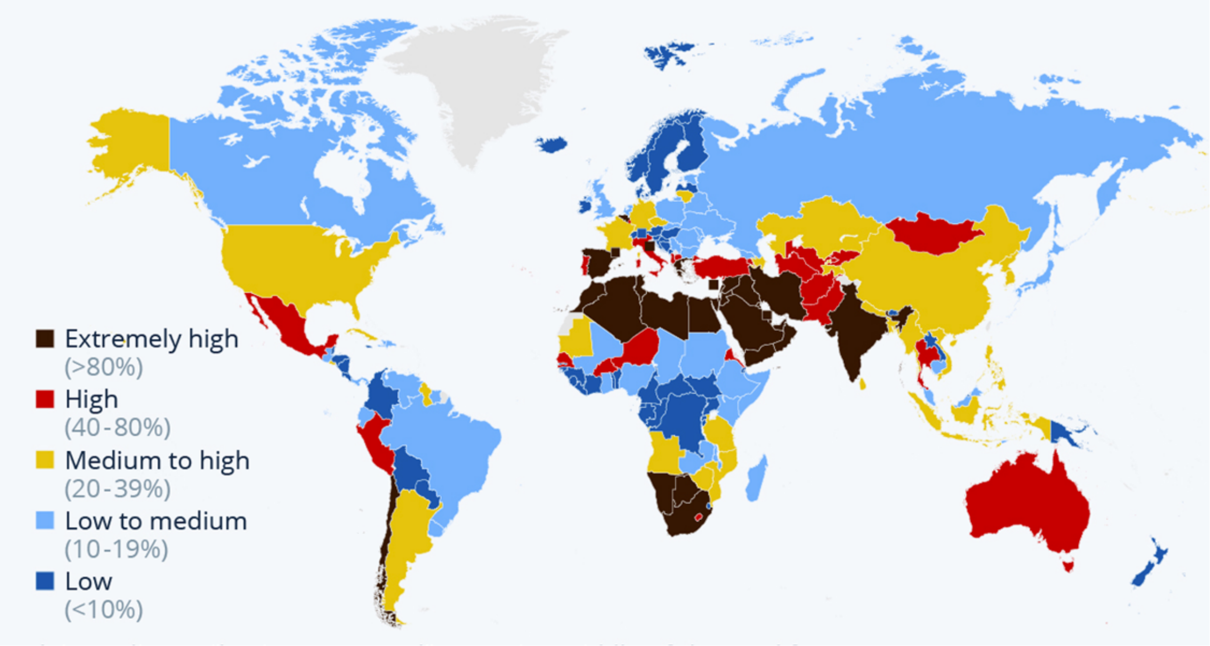

Figure 3: Projected ratio of human water demand to water availability (water stress level) in 2050.[4]

A range of 1000–1700 m^3 of AWR per person is defined as a regular water stress situation, while values below 1000 m^3 are classified as chronic water scarcity and below 500 m^3 as absolute water scarcity.[1, 3]

The causes of water scarcity are numerous and frequently interconnected. Climate change and increasingly long periods of drought are leading to a drastic decline in precipitation, causing soil dehydration and reducing agricultural yields.[5] At the same time, the global population is growing, contributing to a significant increase in water demand.[6] To feed the growing population, food production must increase by around 50% by 2050, which will be accompanied by a projected 40–50% increase in water consumption in agriculture and a 50–70% increase in the municipal and industrial sectors.[3, 7] Added to this is the issue of increasing water pollution from agricultural inputs such as pesticides and fertilizers, inadequately treated wastewater, and industrial emissions.[8] Notably, agriculture currently accounts for around 70% of global fresh water consumption, thus contributing significantly to the global water crisis.[9]

Given the challenges outlined above, the efficient treatment and reuse of water is becoming increasingly important. Membrane-based separation processes are a key technology for overcoming the global water crisis. These processes can reliably remove pollutants, microorganisms, salts and organic contaminants in both drinking water production and wastewater treatment or seawater desalination.[10]

Despite their high potential, membranes are susceptible to biofouling. The uncontrolled accumulation of microorganisms, biomacromolecules, or biofilms on the membrane surface leads to a significant decrease in filtration performance, increased operating costs, and a shorter service life for the modules.[11] Consequently, biofouling is considered one of the main causes of performance loss in membrane systems. Research is increasingly focusing on surface modifications to solve this problem. The aim is to control or prevent specific interactions between the membrane surface and potential foulants, for example by introducing functionalities that are hydrophilic, antimicrobial or fouling-resistant.[12] The focus is not only on functionality, but also on making the manufacturing processes environmentally friendly. Green synthesis strategies, such as UV-induced graft polymerization under mild conditions, offer new possibilities for developing high-performance, environmentally friendly membrane materials sustainably.

4 Theory

4.1 Membranes

Membranes are semi-permeable barriers that separate substances based on their physical properties, such as size or charge. Membranes can be isotropic or anisotropic in structure. Depending on pore size, they are classified as microfiltration, ultrafiltration, nanofiltration, or reverse osmosis. Various operating modes, such as dead-end and cross-flow filtration, are used in applications.

4.1.1 Types

Isotropic membranes, also referred to as symmetrical membranes, have a uniform chemical composition and physical structure across their entire cross-section. The three main types are microporous membranes, nonporous dense membranes, and electrically charged membranes. Anisotropic membranes, also known as asymmetrical membranes, consist of multiple layers with varying pore sizes and permeabilities. They are typically classified into two main types: Loeb-Sourirajan membranes and composite membranes, the latter including thin-film membranes (Figure 4).[13, 14]

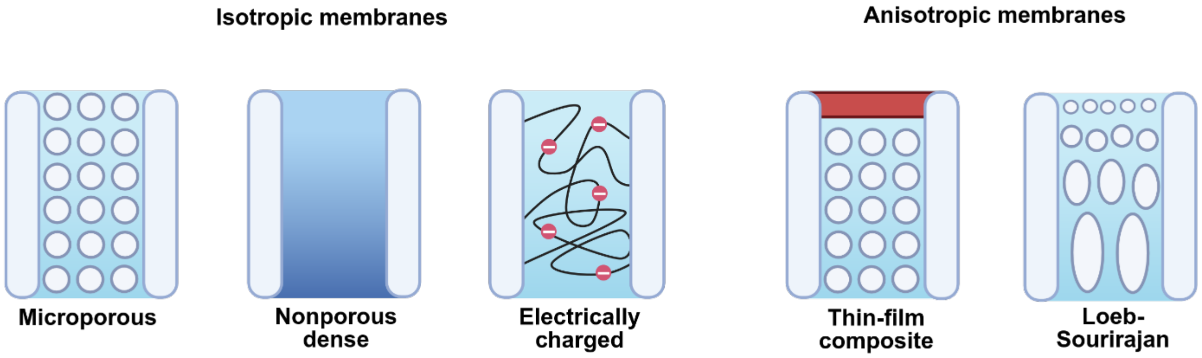

Figure 4: Main types of isotropic (microporous, nonporous dense, electrically charged) and anisotropic membranes (Loeb-Sourirajan and thin-film composite).

Microporous membranes have significantly larger pores than the molecular size of permeating substances passing through them. This enables them to separate submicron size molecules and particles. These membranes are also referred to as micro or ultrafiltration membranes. The separation of dissolved substances mainly depends on the size of the molecules in relation to the pore size of the membrane. Mechanisms such as sieving (size exclusion) and adsorption play a central role in this process. A major disadvantage of porous membranes is their susceptibility to fouling, which often leads to clogged pores. This increases the membrane's resistance and causes a decrease in flux over time.[13, 15]

Nonporous dense membranes are made of compact polymer films that separate substances based on their solubility and diffusivity in the membrane material. These membranes are also referred to as homogeneous and are primarily used to separate small molecules that porous membranes do not retain. Separation occurs *via* the solution-diffusion mechanism. In this process, the transport rate of substances depends on the solubility and diffusivity of the molecules. The component with the highest solubility or diffusivity permeates through the membrane the fastest. One disadvantage of these membranes is their low flow rate. Applications include reverse osmosis, nanofiltration, and gas separation.[13, 15]

Electrically charged membranes are gel-like polymer structures with fixed incorporated charges. These membranes are also called ion exchange membranes because they selectively allow oppositely charged ions to pass through while excluding ions with the same charge through electrostatic repulsion. There are three types of electrically charged membranes: monopolar, bipolar, and mosaic. Monopolar membranes carry either positive or negative charges and act as anion or cation exchangers. Bipolar membranes contain both types of charges in layers, and mosaic membranes contain both types of charges mixed. Separation is achieved through charge and size exclusion, which is particularly used in processes such as electrodialysis.[16-18]

Loeb-Sourirajan membranes are homogenous in terms of their composition but show differences in pore size and porosity across the various membrane layers. The top layer is dense, while the layers below become increasingly porous.[14, 15]

Thin-film membranes consist of two distinct layers made of different materials. The top layer, also known as the skin or active layer, is very thin and consists of a highly cross-linked polymer that performs the selective separation function. The skin lies on top of a significantly thicker and highly porous bottom layer that gives the membrane mechanical stability.[14, 15]

4.1.2 Separation

In pressure-driven membrane processes, such as microfiltration (MF), ultrafiltration (UF), nanofiltration (NF), and reverse osmosis (RO), pressure on the feed side of the membrane separates water into permeate and retentate. Permeate is usually purified water, while retentate is a concentrated residual solution that requires further treatment before disposal. The permeability and selectivity of the membrane determine which substances are retained in each process. Depending on the technology used, various particles and dissolved substances can be removed, including suspended solids, oil emulsions, bacteria, viruses, macromolecules, organic compounds, and monovalent and divalent ions (Figure 5). The required operating pressure varies depending on the process.[19]

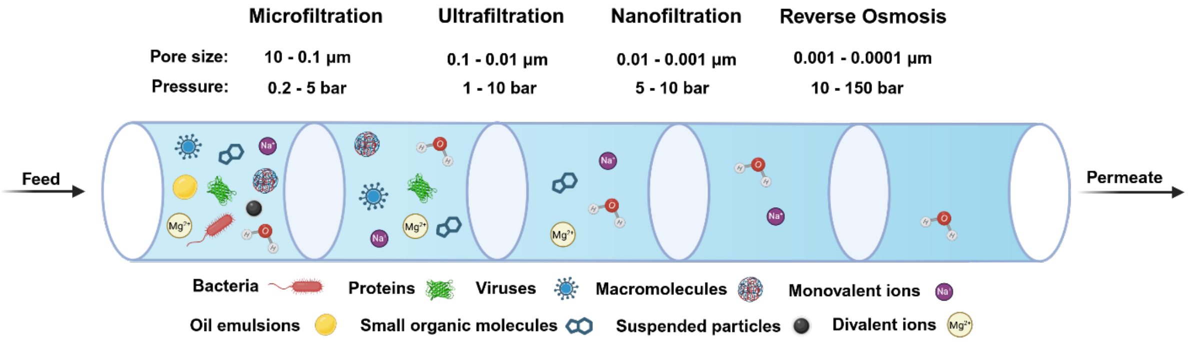

Figure 5: Microfiltration, ultrafiltration, nanofiltration, and reverse osmosis are used for water treatment. Depending on the pore size and operating pressure, they specifically remove particles, germs, organic substances, or dissolved salts.

MF membranes have pores diameters between 10 and 0.1 µm and operate at pressures ranging from 0.2 to 5 bar. They mainly remove larger particles (> 1 µm) by sieving. MF membranes are often used as a preliminary stage for UF processes.[19, 20]

UF is a pressure-driven membrane process with pore sizes between 0.01 and 0.1 µm and typical operating pressures of 1 to 10 bar. In this process, liquid is forced through the membrane by hydrostatic pressure. While water and small dissolved molecules pass through the membrane, larger particles such as bacteria, viruses, and colloids are retained. UF plays a central role in water and wastewater treatment, particularly in drinking water treatment and as a pretreatment for reverse osmosis plants for seawater or brackish water desalination.[19, 21]

NF is a membrane process with pore sizes ranging from 0.01 to 0.001 µm and typically operates at pressures of 5 to 10 bar. It separates dissolved substances with a molecular weight between approximately 100 and 1000 Da (molecular weight cut-off, MWCO). In water treatment, NF is used for softening, disinfection, and removal of color, taste, odor, organic trace substances, and divalent ions, among other things. Separation is achieved through a combination of steric repulsion (sieving effect) and electrostatic interaction (Donnan effect) and is made possible by high transmembrane pressure.[19, 22]

In RO, a membrane with pore sizes between 0.001 and 0.0001 µm is used at a pressure of 10 to 150 bar. This pressure is sufficient to overcome the osmotic pressure of the salt solution. Water then flows from the salt-rich feed solution to the low-salt permeate solution. Since the 1950s, RO has been one of the most important methods for desalinating seawater and producing fresh water. Monovalent salts, such as sodium chloride, can also be retained almost completely.[19, 23]

4.1.3 Operation modes

A key problem with UF and MF is the decrease in permeate flow caused by deposits on the membrane. These deposits act like a filter cake, increasing flow resistance. There are two operating modes: in dead-end filtration, the medium flows vertically through the membrane, and in cross-flow filtration, the flow is parallel to the membrane surface (Figure 6).[24, 25]

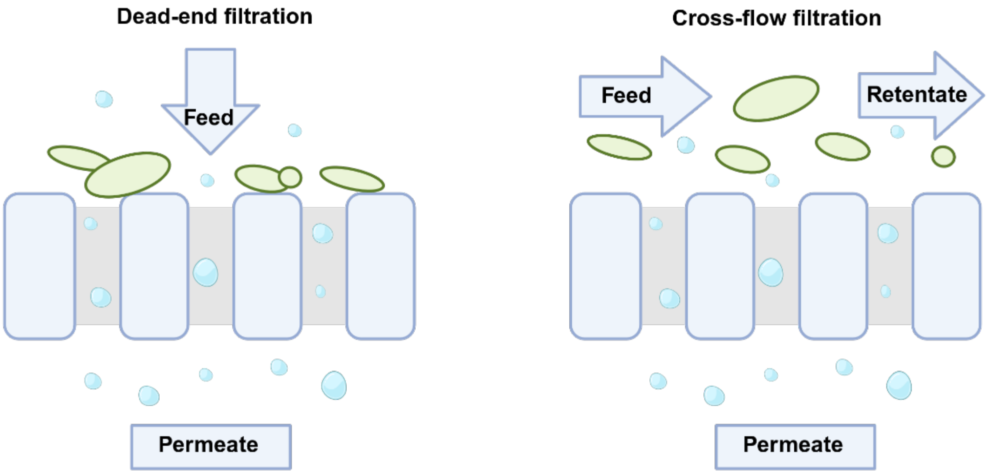

Figure 6: Dead-end and cross-flow filtration with orthogonal and parallel feed orientations relative to the membrane and their impact on cake layer formation.

In dead-end filtration, the membrane is exposed to the feed flow orthogonally, causing all retained particles to accumulate on its surface as a cake layer. This increases flow resistance over time and reduces the permeate flux. To avoid complete clogging, the membrane must be backwashed at regular intervals, making the process inherently discontinuous. Permeate loss is typically compensated by adjusting the feed pressure (0.5–2.5 bar), and flushing occurs once the maximum pressure is reached. Although the energy demand is generally low, increasing solids content shortens filtration intervals and requires more frequent backwashing, leading to higher energy consumption and reduced efficiency. Under such conditions, cross-flow filtration becomes a more effective alternative.[24, 25]

In contrast to dead-end filtration, cross-flow filtration involves feeding the water parallel to the membrane surface. Particles also accumulate on the membrane, but the parallel flow serves to control the formation of this cake layer. The shear forces generated on the membrane surface allow some of the deposited substances to be removed. One disadvantage of cross-flow operation is the high energy requirement resulting from the necessary membrane overflow. The energy consumption results from the pressure loss on the feed side along the membrane caused by the high flow velocity.[24, 25]

4.2 Membrane fabrication techniques

The manufacturing method for polymer membranes is largely determined by the properties of the polymer and the desired membrane structure. Common processes include phase separation, melt blowing, interfacial polymerization, stretching, track-etching, and electrospinning.

4.2.1 Non-solvent induced phase separation (NIPS)

Non-solvent induced phase separation (NIPS) is a method used to produce porous polymer membranes and was first introduced in 1960 by LOEB and SOURIRAJAN (Figure 7).[26] This process uses various polymers, including polysulfone[27] (PSF), polyethersulfone[28] (PES), polyacrylonitrile[29] (PAN), cellulose acetate[30] (CA), polyvinylidene fluoride[31] (PVDF), polyimides[32] (PI), and polyamides[33] (PA).

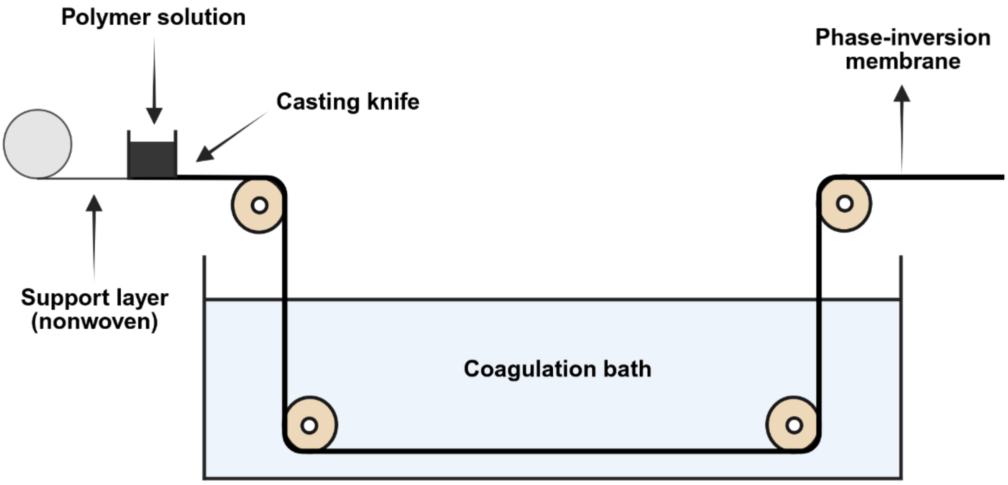

Figure 7: NIPS process. (**1**) A polymer is dissolved to obtain a homogeneous dope solution. (**2**) This is cast on to support material. (**3**) The liquid film is transferred to a coagulation bath containing a non-solvent. (**4**) Phase separation occurs through the exchange of solvent and non-solvent. (**5**) The result is an asymmetric membrane with a selective top layer and a support layer.

Initially, the selected polymer is dissolved in a suitable solvent or mixture of solvents to create a homogeneous polymer solution, also known as a dope solution. The polymer solution contains typically 15 to 25 wt% polymer. The typical solvents include dimethylformamide (DMF), *N*-methyl-2-pyrrolidone (NMP), and dimethylacetamide (DMAc). Additionally, additives can be introduced to influence the pore structure of the resulting membrane.[34]

The polymer solution is cast on to a support material, which is often a nonwoven polymer or glass. The liquid film is then transferred to a coagulation bath containing a non-solvent. Contact with the non-solvent causes a phase reversal, during which the solvent diffuses out of the polymer film and is replaced by the non-solvent. This leads to precipitation and the formation of an asymmetric membrane structure with a porous, selective top layer and a support layer for mechanical stability.[35]

PAN is well known for its chemical stability and hydrophilicity. It is resistant to solvents and cleaning agents, including hydrogen peroxide and sodium hypochlorite.[29] Compared to hydrophobic materials, such as PSF and PES, which are susceptible to fouling, PAN is characterized by a low tendency to foul when filtering aqueous media.[36] It is used as a substrate material for ultrafiltration[37], nanofiltration[38], and reverse osmosis[39] membranes. Additionally, PAN is already established in various commercial applications such as filtration, oil-water separation and hemodialysis.[40]

4.2.2 Melt blowing

The melt blown process is used to manufacture nonwoven fabric membranes (NWFs) and was introduced in 1954 by WENTE.[41] This process uses thermoplastic polymers, such as polypropylene[42] (PP), polystyrene[43] (PS), polyethylene terephthalate[44] (PET), polyethylene[45] (PE) and polyurethane[46] (PU). One major advantage of this technology is that it does not require solvents.

First, the desired polymer, in solid form (*e.g.*, pellets, granules, or powder), is fed into an extruder and melted. The molten polymer is then transferred to the die assembly *via* a gear pump. There, it is pressed through fine openings and immediately encounters converging streams of hot air traveling at high speeds. The airflow pulls on the molten polymer, stretching and converting it into fine fibers with a very small diameter.[47, 48] Typically, the fiber diameter is considerably reduced in the process. For example, isotactic PP can be reduced from 0.4 mm to approximately 1.6 µm (a factor of 250) or from 0.2 mm to approximately 300 nm (a factor of 667).[49, 50] A collector then collects the stretched polymer filaments, forming a tangled fiber network with the typical structure of a nonwoven fabric. Finally, the nonwoven fabric is wound into a cylindrical roll to facilitate further processing and handling (Figure 8).

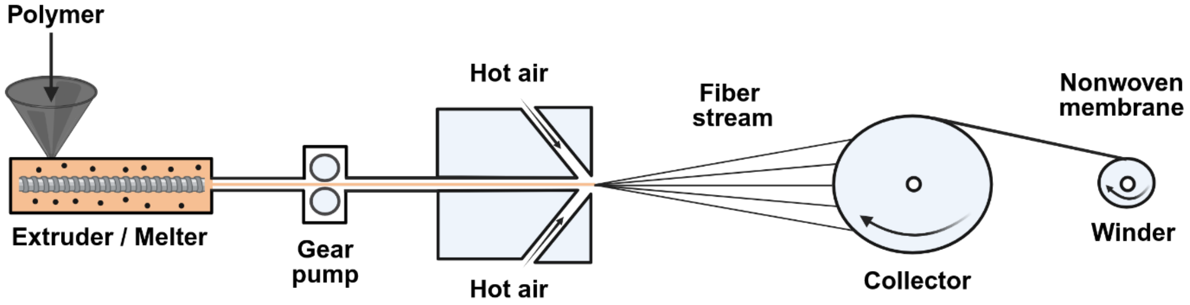

Figure 8: Melt blown process. (**1**) The polymer is fed into the extruder. (**2**) A gear pump conveys the melt to the nozzle. (**3**) When exiting through fine openings, the melt encounters hot air streams at high speed. (4) The air pulls the melt apart into fine microfibers. (**5**) These microfibers are deposited on a collector and form a nonwoven fleece.

Nonwoven melt blown PP has many applications, including use as a filter material for fuel purification, air filtration, and solid-liquid and oil-water separations.[51] It is also used as an oil absorber and for the adsorption of heavy metal ions, such as Cd^{2+} and Pb^{2+}, as well as for the removal of organic pollutants.[52-54] In the medical field, it is used to make surgical and face masks.[55]

4.3 Membrane fouling

A key problem in operating membrane systems is membrane fouling, which significantly reduces the performance and efficiency of membrane-based processes. This complex phenomenon, which is not yet clearly defined, generally describes the undesirable accumulation of particles, colloids, macromolecules, or salts on the membrane surface or in the pores. Different forms of fouling occur depending on the membrane process used and the type of contaminants present, including inorganic deposits, organic fouling, and biofouling.[12]

Membrane fouling can be classified as either reversible or irreversible (Figure 9). Both forms reduce permeate flux and impair membrane performance. Reversible fouling can typically be removed by washing with deionized water, which restores the original flux. Irreversible fouling, on the other hand, requires more complex measures, such as chemical cleaning or replacing the membrane, because the deposits cannot be removed easily.[56-58] Reversible fouling is often caused by a cake or gel layer of foulants that have been deposited on the membrane's surface.[56, 59] In contrast, irreversible fouling typically involves the strong bonding of solutes to the membrane through physisorption and/or chemisorption, which occur both on the surface and in the pores.[56, 58] The rate and extent of irreversible membrane fouling are influenced by multiple variables, including the membrane’s physical and chemical properties (such as surface charge, roughness, and hydrophobicity), the types of ions present in the solution, environmental factors like temperature and pH, as well as operational parameters such as cross-flow velocity and applied pressure.[60]

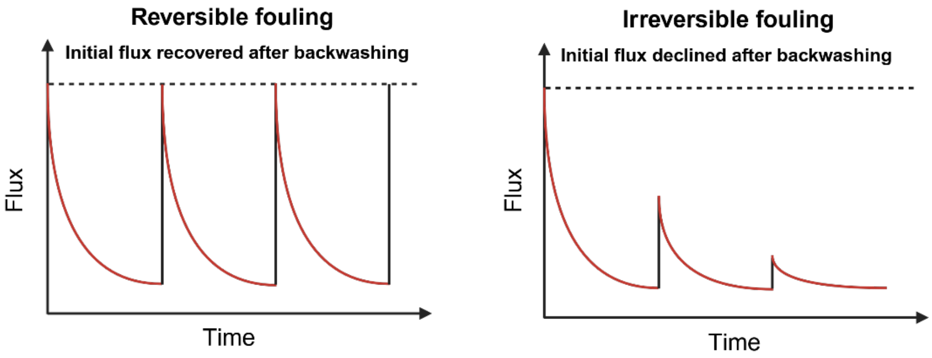

Figure 9: Reversible fouling is characterized by full flux restoration after backwashing. In contrast, irreversible fouling is defined by permanently reduced flux after backwashing.

4.3.1 Membrane fouling mechanisms

Membrane fouling can be divided into two categories: internal and external. Internal fouling occurs when particles penetrate and become lodged in the pores of the membrane. This partially or completely blocks the pores, reducing the effective pore diameter and flow rate. The aforementioned behavior can be described by three models: standard, intermediate, and complete blockage.[61-63]

In standard blockage, particles smaller than the pores penetrate and deposit on the inner surfaces of the pores. This reduces the effective pore diameter. In intermediate blockage, a similar mechanism occurs, but the particles can deposit not only on the pore walls but also on particles that have already settled. This behavior only occurs under certain conditions, allowing particles to overlap within the pore structure. In complete blockage, the pores are completely clogged with particles. Further deposition is no longer possible because the pore space is filled.[61-63]

In contrast, external fouling describes contamination on the membrane surface. It is caused by the accumulation of colloids that settle on the surface. This accumulation can initially block pore entrances and eventually lead to the formation of a cake layer or film on the membrane. This type of contamination can be partially removed by cleaning procedures and is described by the cake filtration model. The four fouling models are shown in Figure 10.[61-63]

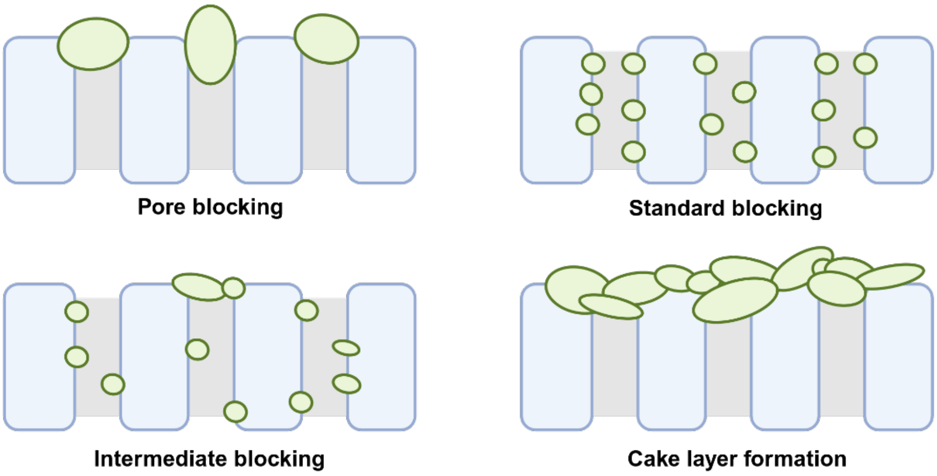

Figure 10: Overview of common fouling models: pore blocking, standard blocking, intermediate blocking, and cake formation on the membrane surface.

4.3.2 Inorganic fouling

Inorganic fouling, also known as scaling, occurs when poorly soluble salts become supersaturated in a solution and then precipitate onto the membrane surface. This leads to crystal formation and a subsequent decrease in permeate flow. Due to concentration polarization, the concentration of dissolved salts in the immediate vicinity of the membrane can be 4 to 10 times higher than in the feed stream.[64, 65] This local supersaturation promotes the precipitation of inorganic salts, such as calcium carbonate ($CaCO_3$), calcium sulfate ($CaSO_4$), calcium phosphate ($Ca_3(PO_4)_2$), and barium sulfate ($BaSO_4$). Inorganic fouling frequently occurs in processes such as nanofiltration and reverse osmosis. [66, 67]

Figure 11 shows that inorganic fouling can occur through chemical and biological precipitation. In chemical precipitation, salts precipitate when their solubility limit is exceeded. In biological precipitation, the anionic groups of biological macromolecules, such as polysaccharides, proteins, and nucleic acids, bind to metal ions in the solution. These biopolymers contain functional groups, such as carboxylate (COO^-), carbonate (CO_3^{2-}), sulfate (SO_4^{2-}), phosphate (PO_4^{3-}), and hydroxide (OH^-), that easily react with cations, such as magnesium (Mg^{2+}), aluminum (Al^{3+}), iron (Fe^{3+}), and calcium (Ca^{2+}).[68, 69] For example, the reaction between carboxyl groups and calcium ions can result in the formation of a stable, dense gel layer.[70]

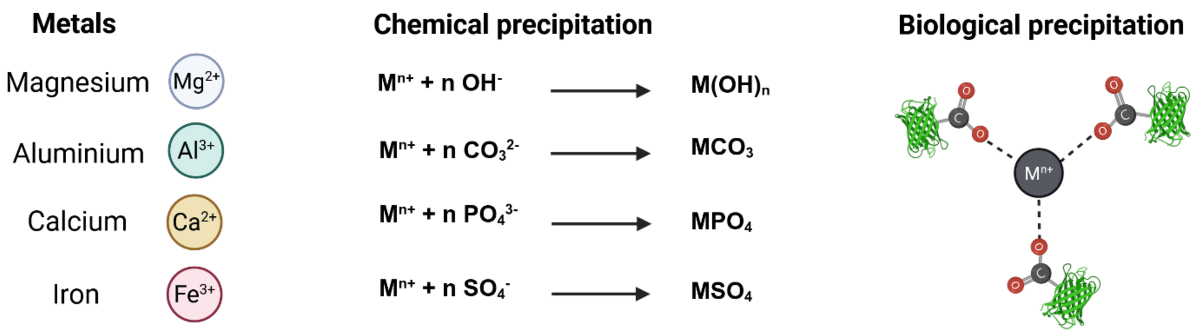

Figure 11: Mechanisms of inorganic fouling. Chemical precipitation through supersaturation of poorly soluble salts and biological precipitation through the precipitation of metal ions with the anionic groups of biopolymers.

The combination of different types of fouling, such as biofouling, organic fouling, and inorganic fouling, can have a synergistic effect and further increase the amount of deposited substances on the membrane surface. Although inorganic fouling contributes only about fifteen percent to total fouling, its behavior is not yet fully understood.[61]

4.3.3 Organic fouling

Organic membrane fouling is often defined as the deposition of natural organic matter (NOM). These compounds are problematic in membrane filtration and occur in high concentrations in wastewater and certain lake and seawater samples. These compounds include proteins, amino sugars, polysaccharides, polyhydroxyaromatic compounds, and humic substances (Figure 12).[71-73]

NOM induced fouling can negatively impact the permeability of the membrane as well as its ability to retain dissolved substances. The degree of organic membrane fouling depends on several factors, including the ionic strength and pH of the solution, the type of dissolved ions, the chemical and structural properties of the membrane surface, the molecular weight and polarity of the NOM compounds, and the permeate flow, hydrodynamic conditions, and operating parameters.[74] Generally, hydrophilic membrane surfaces are considered less susceptible to organic fouling. However, since hydrophobic membranes amongst others are used for filtration, organic fouling poses a particular challenge in this application.[75]

The main cause of organic fouling by NOM is humic acid (HA), which is a collective term for complex mixtures of organic acids containing carboxyl and phenolic functional groups. HA is produced by the decomposition of organic matter and gives many swamps and rivers their yellowish-brown color.[72] Due to their structural diversity, HAs have a wide range of molecular weights, typically between 700 and 200000 Da, with smaller and larger molecules present.[76] HA systems are therefore usually characterized by average values. For example, an average HA molecule can behave like an acid with two or three free protons. It is important to note that HAs can serve as a nutrient source for bacteria, triggering secondary biofouling.[77]

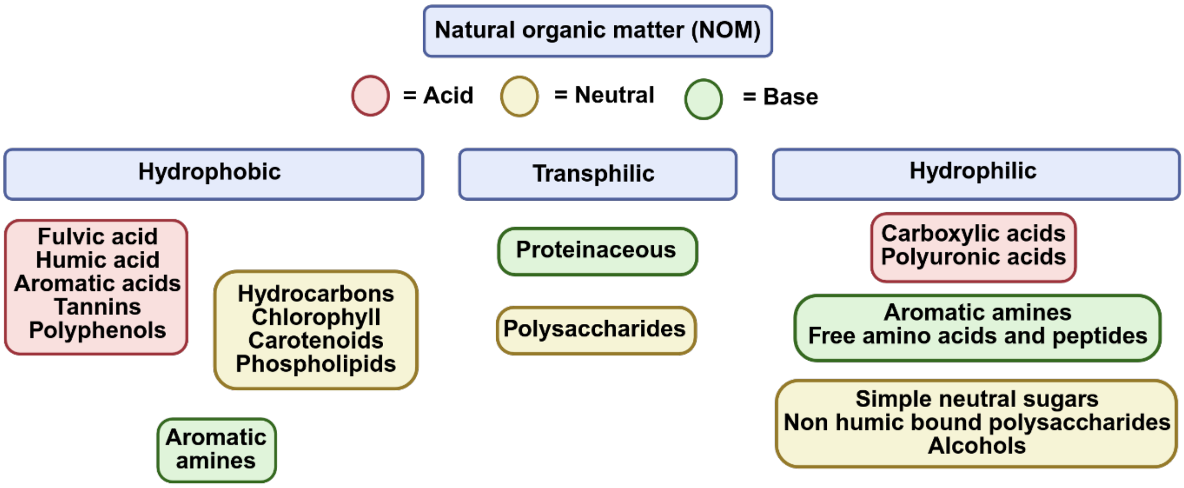

Figure 12: Classification of natural organic matter (NOM) based on polarity (hydrophobic, transphilic, hydrophilic) and acid-base character (acidic, neutral, basic).

4.3.4 Biofouling

Biofouling is the accumulation, retention, growth, and metabolism of microorganisms, such as marine bacteria, diatoms, green algae, and flocs, on membrane surfaces. Biofouling poses a significant problem in many membrane applications, especially in water and wastewater treatment, desalination, reverse osmosis, and membrane bioreactors. Biofouling accounts for over 45% of all fouling phenomena.[61, 78]

The effects of biofouling are manifold. For example, the formation of a biofilm on the membrane surface acts as a gel-like diffusion barrier that significantly reduces water flux. Additionally, biodegradation damage of the membrane polymer can occur. Reduced flow necessitates an increase in operating pressure to maintain the desired production rate, which significantly increases energy consumption. Consequently, the service life of the membrane is considerably shortened.[11, 61]

Biofilm formation typically occurs in five steps, as shown schematically in Figure 13. First, planktonic bacteria, *i.e.,* free-floating bacteria, reversibly bind to the membrane surface. This adhesion occurs through van der Waals forces and hydrophobic or electrostatic interactions. Second, a monolayer begins to form as the bacteria produce an extracellular matrix of proteins, glycoproteins, glycolipids, polysaccharides, and DNA. These substances are referred to within the matrix as extracellular polymeric substances (EPS). After this step, the microorganisms are irreversibly bound to the surface.[79-81]

In the third step, microcolonies form. Communication within the matrix takes place *via* signal molecules as part of a process known as *quorum sensing*, whereby gene expression depends on population density. The fourth step involves the three-dimensional growth and maturation of the colonies. In the final step, dispersion occurs. Individual bacteria or small aggregates detach from the biofilm to colonize new surfaces.[81]

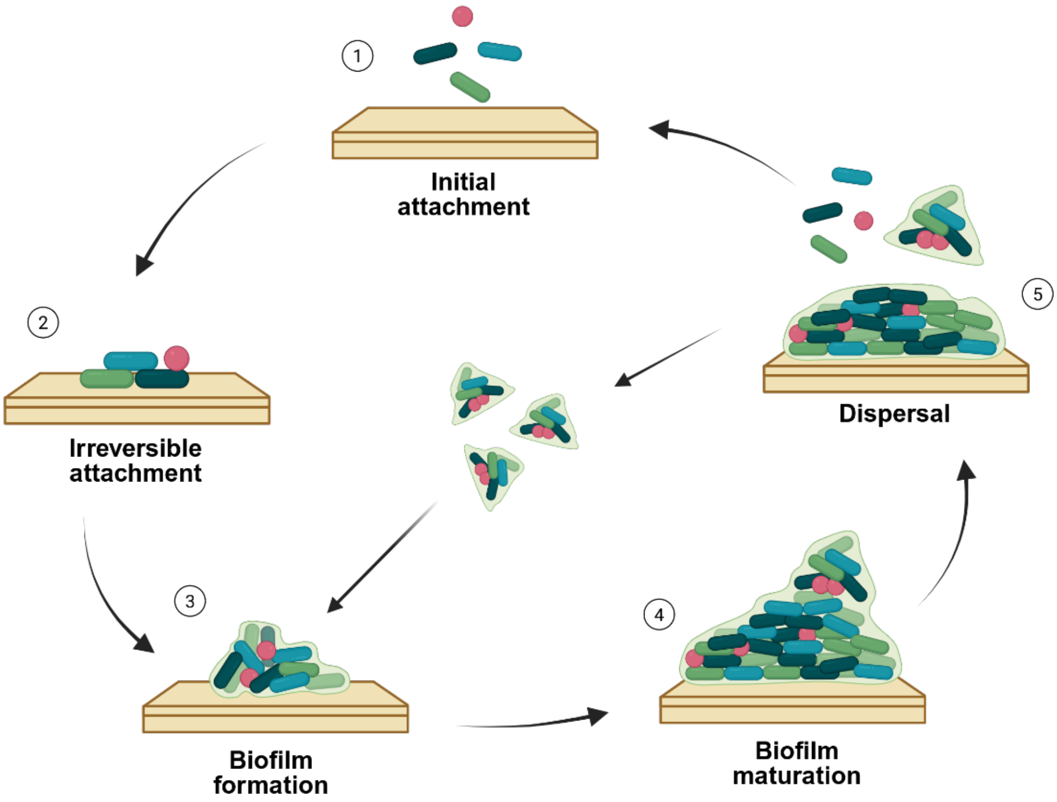

Figure 13: Biofilm formation. (**1**) Reversible attachment of microorganisms to the surface. (**2**) Irreversible adhesion. (**3**) Start of biofilm formation with the production of extracellular polymeric substances. (**4**) Maturation of the biofilm into a structured, multi-layered community. (**5**) Release of individual cells or cell clusters to colonize new surfaces.

There are two ways dispersion can occur. Active dispersion is observed when microorganisms leave the matrix in a targeted manner, such as through chemical gradients or in response to extracellular signaling molecules.[81] In passive dispersion, microorganisms are triggered to leave the matrix by mechanical or physical forces, such as shear stress.[82]

Biofouling is primarily caused by bacterial species, including *Corynebacterium*, *Pseudomonas*, *Bacillus*, *Arthrobacter*, *Flavobacterium*, and *Aeromonas*. To a lesser extent, fungi such as *Trichoderma* and *Penicillium*, as well as other eukaryotic microorganisms, contribute to biofilm formation.[11, 83] Some microorganisms can attach to membrane surfaces quickly. For instance, *Pseudomonas vesicularis*, *Acinetobacter calcoaceticus*, and *Staphylococcus warneri* have been found in tap water and can adhere to surfaces within minutes.[84]

Since microorganisms and their metabolic products replicate, biofouling on membranes is considered an irreversible process. Due to its complex and dynamic nature, biofouling is difficult to control and only responds to a limited extent to conventional cleaning methods.[85, 86]

4.3.5 Antifouling strategies

Biofouling is one of the biggest challenges in membrane technology because it significantly impairs the performance and lifespan of membranes. Various strategies have been developed to reduce biofouling, ranging from physically and chemically cleaning the membrane to functionalizing its surface. Passive approaches include hydrophilic or zwitterionic coatings, while active approaches use antimicrobial agents.

Membrane cleaning

Two common methods for cleaning membranes are physical and chemical cleaning (Figure 14). Physical cleaning is usually carried out by backwashing or relaxation phases. Backwashing, also known as water flushing, reverses the flow direction to remove reversible contamination and substances deposited on the membrane surface. This enables the permeate flow to be effectively restored.[87] Important parameters for backwashing are frequency, duration, and the ratio between the two. The relaxation phase briefly interrupts filtration while air bubbles continue to flow over the membrane. During relaxation deposits can diffuse away from the membrane surface due to existing concentration gradients.[87, 88]

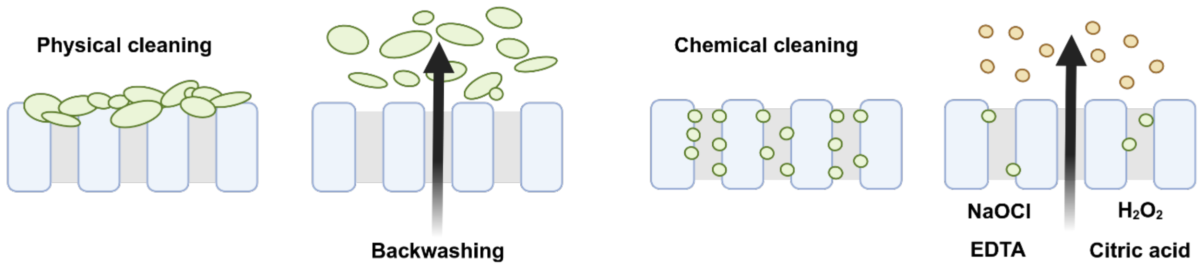

Figure 14: Overview of cleaning methods for membranes. Physical cleaning by backwashing and chemical cleaning with active ingredients such as sodium hypochlorite (NaOCl), hydrogen peroxide (H_2O_2), EDTA or citric acid.

The goal of chemical cleaning is to remove irreversible contamination, such as scaling, organic fouling, and biofouling, that cannot be adequately addressed by physical methods. Sodium hypochlorite (0.1–0.5 wt%) is commonly used for removing organic and biological deposits. Citric acid and EDTA are used to remove inorganic deposits. Oxidizing agents, such as sodium hypochlorite (NaOCl) and hydrogen peroxide (H_2O_2), work through oxidation and disinfection.[89] These agents hydrolyze organic substances, dissolving biofilms and particulate deposits on the membrane.

Passive antifouling strategy

The passive strategy is designed to prevent bacteria, algae, and proteins from adhering to the membrane surface. This approach does not kill microorganisms. To prevent adhesion, the membrane surface can be modified with polymer brushes. These are polymer chains that are covalently bonded to the surface. If the graft density is high enough, the polymer chains repel each other and form brush-like structures.[90] These brushes can then act as a physical barrier. When microorganisms or foulants approach the surface, the polymer brushes are compressed. This is entropically unfavorable because the number of possible conformations decreases. The resulting steric repulsion can counteract adhesion (Figure 15A).[91, 92]

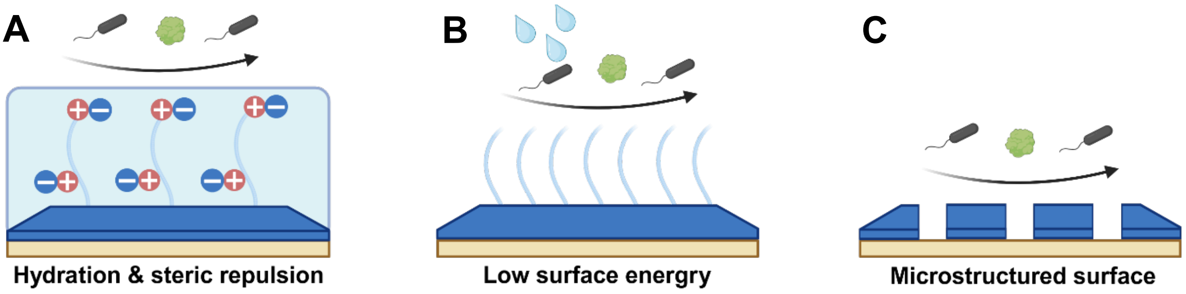

Figure 15: Passive antifouling strategies. (**A**) Hydration and steric repulsion, (**B**) low surface energy, and (**C**) microstructured membrane surfaces to minimize the adhesion of fouling substances.

Polyethylene glycol (PEG) is the most well-known material used to make polymer brushes. It is highly effective at preventing protein adsorption. PEGs antifouling activity is based on its highly hydrated surface and steric repulsion.[93] PEG is water-soluble, highly flexible, non-toxic, biocompatible, and has low immunogenicity.[94] A major disadvantage of PEG is its poor long-term stability. It is oxidatively and enzymatically degraded.[95, 96] Additionally, PEG exhibits reduced antifouling activity against positively charged proteins, such as lysozyme, thereby limiting its universal applicability.[97] At temperatures above 35 °C, hydration of the PEG-modified surface decreases while protein adsorption increases. This can be a disadvantage for biomedical applications.[90]

To overcome the limitations of PEG, researchers are focusing on zwitterionic materials. These materials contain zwitterions, such as carboxybetaines[98], sulfobetaines[99], phosphobetaines[100], *N*-oxides[101], and sulfur ylides[102] (Figure 16). Zwitterionic materials are inspired by phosphatidylcholine head groups found in phospholipid bilayers of cell membranes. These materials have positive and negative charges yet remain electrically neutral overall. Zwitterionic polymers are considered promising next-generation antifouling materials because they can form a dense hydrate shell *via* electrostatic interactions. These interactions are stronger than hydrogen bonds, resulting in a dense and tightly bound layer of water on the surface.[12, 103]

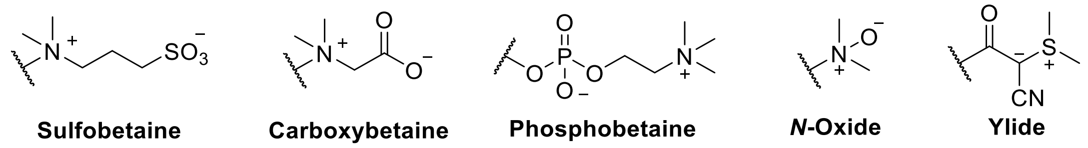

Figure 16: Structural examples of common zwitterionic groups for antifouling coatings, including sulfobetaines, carboxybetaines, phosphobetaines, *N*-oxides and ylides.

Another way to reduce the adhesion of microorganisms is to minimize the surface energy of the material (Figure 15B). This approach involves using, for example, highly hydrophobic polymers.[90] Additionally, the polymers should have a low modulus of elasticity and a smooth surface. Accumulation of microorganisms is inevitable with such materials. However, due to their weak interaction with the surface, microorganisms can easily be removed by hydrodynamic shear forces or mechanical washing.[104] This approach therefore relies on a dynamic environment. Well-known examples of hydrophobic polymer membranes used thus far, as shown in Figure 17, include polytetrafluoroethylene[105] (PTFE), polydimethylsiloxane[106] (PDMS) and polyvinylidene fluoride[107] (PVDF).

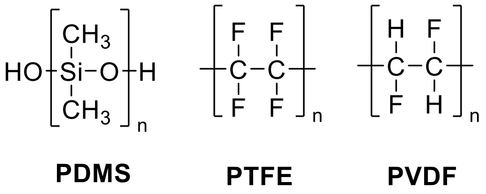

Figure 17: Structural examples of superhydrophobic polymers, including PDMS, PTFE and PVDF.

The microstructure of a surface can significantly impact a membrane's antifouling properties (Figure 15C). One well-known example from nature is the lotus leaf, which has a surface consisting of cylindrical structures that are approximately 10 µm in size. These structures trap air, resulting in poor wettability. Additionally, the structures are covered with nanometer-sized, waxy hairs that create a superhydrophobic surface.[90] Water forms into spherical droplets that roll off, taking dirt particles with them. For example, Chen *et al.* developed a lotus effect-inspired biomimetic PVDF membrane.[108]

Active antifouling strategy

The active strategy prevents adhesion by killing the microorganisms. This involves modifying the surfaces with biocides. These destroy the cell membrane, cell communication, or the extracellular matrix of the biofilm. The active strategy can be divided into two different approaches (Figure 18). In the first approach, the biocide is covalently bound to the surface. The microorganisms are then lysed upon contact with the surface. In the second approach, the biocide is released from the material. The microorganisms are lysed even before contact with the surface.[109]

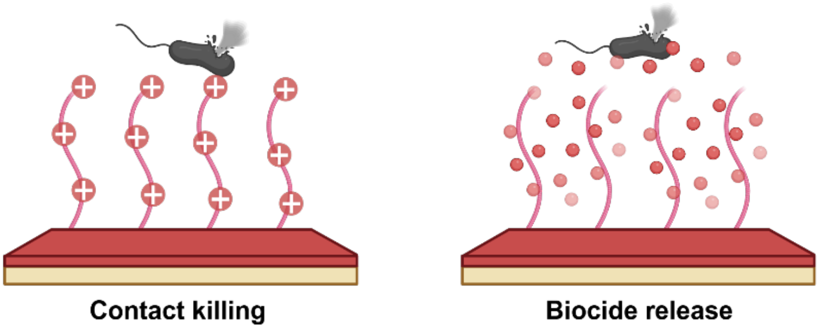
Contact killing
Biocide release

Figure 18: Active antifouling strategies. Contact killing and biocide release membrane surfaces to control biofilms and microbial colonization.

Cationic antimicrobial materials are designed to give membrane surfaces antifouling properties by killing microorganisms physically. Quaternary ammonium compounds (QACs) are among the best-known representatives. These are organic molecules with a positive charge, and four alkyl groups are covalently bonded to a central nitrogen atom (R_4N^+). Contact killing strategies for preventing fouling in water treatment have been developed by integrating QAC-based materials or by undergoing quaternization reactions during membrane production (Figure 19). QAC-based antibiofouling membranes can be constructed using grafting (*e.g.*, with DAC[110]), blending (*e.g.*, with DDBAC[111], BEATC[112], or CTAB[113]) or layer-by-layer techniques (*e.g.*, with DMOTPAC[114]).

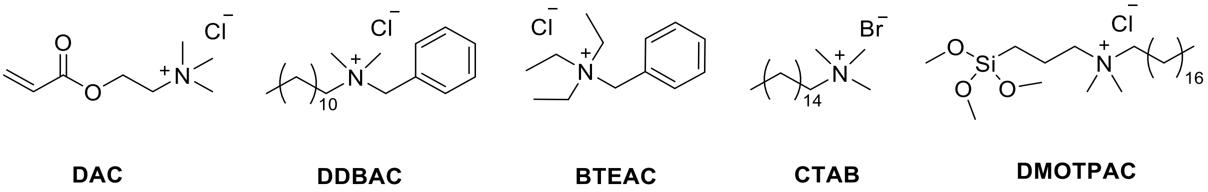

Figure 19: Quaternary ammonium compounds (QACs) used in water treatment membranes prepared *via* blending, grafting, or layer-by-layer techniques.

The release killing strategy involves releasing antimicrobial agents from the membrane surface to prevent biofouling. Metal-based nanomaterials, such as silver and copper compounds, are often used for this purpose. The released ions, such as Ag^+ and Cu^{2+}, generate reactive oxygen species or bind to cellular components, including enzymes and DNA. This leads to disturbances in cell metabolism and ultimately kills the microorganisms.[115, 116] However, uncontrolled release of these substances is challenging because heavy metal ions pose potential environmental and health risks. As a more environmentally friendly alternative, antimicrobial agents of natural origin, such as capsaicin, chitin, and lysozyme, are increasingly used to develop antifouling membranes based on the leaching strategy.[117-119] The exact mechanism by which QACs kill microorganisms is not yet fully understood. Three potential mechanisms are being discussed, namely the polymeric spacer effect, the phospholipid sponge effect, and the ion exchange effect (Figure 20).

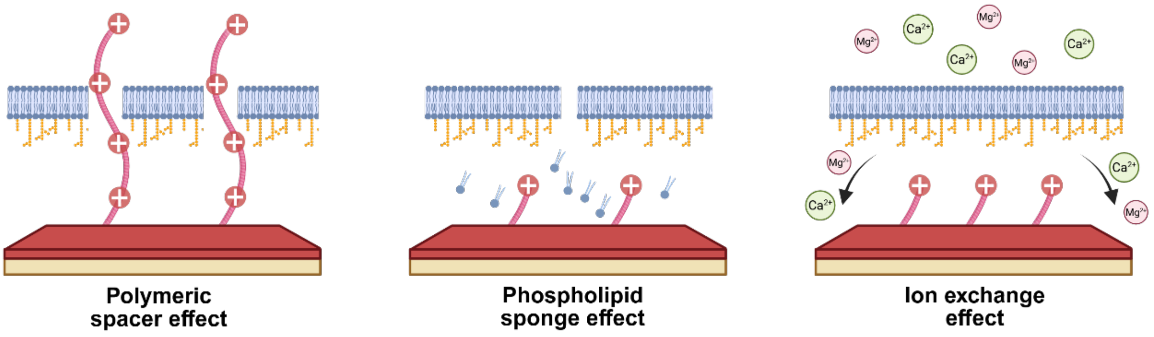

Figure 20: Antimicrobial effect of quaternary ammonium compounds (QACs), including polymeric spacer effect, phospholipid sponge effect, and ion exchange effect.

According to the polymer spacer effect, a QAC polymer can penetrate the cell wall of an adhering bacterium. If the polymer reaches the cytoplasmic membrane, it can kill the cell by damaging the phospholipid bilayer.[120] The phospholipid sponge effect is the ability of a polycationic network on a surface to extract negatively charged phospholipids from a bacterial cell membrane and bind them within the polymer matrix.[121] In the ion exchange mechanism, the positively charged head of the QACs binds to the polar membrane surface, replacing stabilizing Mg^{2+} and Ca^{2+} ions. The lipophilic tail region embeds itself in the phospholipid bilayer, causing the membrane to lose fluidity and break into segments.[122] One disadvantage of biocide-modified surfaces is that they accumulate dead microorganisms. When the surface becomes blocked, the antifouling effect decreases, allowing new microorganisms to settle. Therefore, this approach should combine several antifouling strategies.[123]

4.4 Membrane modification

Surface modification of membranes is an effective method for reducing interactions between the membrane surface and fouling substances. This reduces membrane fouling, extends the service life of the membrane, and improves its performance. Typical techniques for modifying membrane surfaces include surface grafting, blending, and layer-by-layer assembly.

4.4.1 Grafting

A graft copolymer consists of a main chain to which brush-like side chains are anchored. Modification with polymer brushes allows, for example, the wettability, biocompatibility, and mechanical properties to be specifically adjusted. Graft copolymers can be produced using three basic approaches: grafting to, grafting from, and grafting through (Figure 21). The properties of the polymer brushes depend largely on the graft density, chain length, and chemical composition.[124]

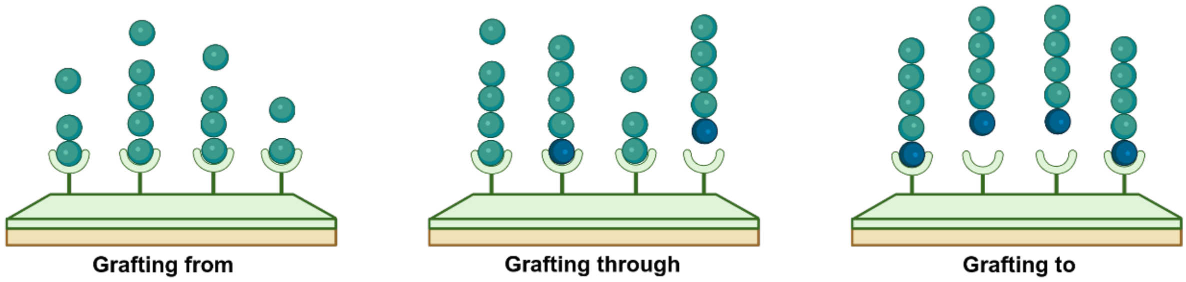

Figure 21: Methods for producing graft polymer brushes: grafting to (bonding of polymers), grafting from (growth from the surface), and grafting through (copolymerization with macromonomers).

In the grafting to approach, a pre-made polymer with a reactive end group is covalently bonded to a previously functionalized surface. Due to steric hindrance caused by the volume of the polymer tangle, the achievable graft densities are usually limited.[125] In the grafting from process, polymerization takes place directly on the surface by reacting monomers with previously generated reactive groups, such as radicals. This process allows for a higher graft density because the polymer chains grow directly from the surface.[126] The grafting through approach, also known as the macromonomer method, combines these two processes. In this process, a functionalized surface copolymerizes with a monomer and a macromonomer. The resulting graft density depends on the ratio of these two components.[127] Polymerization can be carried out *via* various mechanisms, including cationic, anionic, radical, and living polymerization.[128]

In plasma-induced polymerization, the type of process gas used plays a decisive role because it significantly influences the formation of functional groups on the surface of the material being processed. There are two main types of process gases: reactive gases (*e.g.*, O_2, NH_3, CO_2, CO) and inert gases (*e.g.*, He, Ar). During plasma formation, the process gas breaks down into reactive fragments that react with the material surface.[129] ULBRICHT *et al.*, for example, treated PAN ultrafiltration membranes with helium plasma and then exposed them to an air atmosphere. This resulted in the formation of peroxide groups on the membrane surface, which served as initiators for graft polymerization with acrylic acid through thermolysis (Figure 22A).[130]

There are two ways to carry out photo-induced grafting: with or without a photoinitiator. In photo-induced grafting without a photoinitiator, free radicals form directly on the polymer backbone of the membrane through UV irradiation. These radicals then react with monomer radicals to form a grafted copolymer.[131] In contrast, surface modification with a photoinitiator, radical sites necessary for grafting are created by the photoinitiator's reaction with the base polymer's hydrogen atoms under UV irradiation. This creates reactive radical centers on the membrane surface where grafting can occur.[132] For example, ZHAO *et al.* have successfully polymerized HEMA onto the surface of PP using benzophenone as a photoinitiator for water treatment applications (Figure 22B).[133]

Surface-initiated atom transfer radical polymerization (SI-ATRP) is a controlled living polymerization method that is often used to produce functionalized membranes. It enables polymers to be applied to substrates in a targeted manner, allowing parameters such as graft density, chain length, and chemical composition to be precisely controlled.[134] YANG *et al.*, for example, treated the surface of PA reverse osmosis membranes with 3-aminopropyltriethoxysilane (APTES) to introduce amino groups and then immobilized 2-bromoisobutyrate bromide (BiBB) as an initiator. In the next step, the zwitterionic sulfobetaine monomer DMAPS was polymerized on the membrane surface in using a copper(I) catalyst *via* SI-ATRP (Figure 22C).[135]

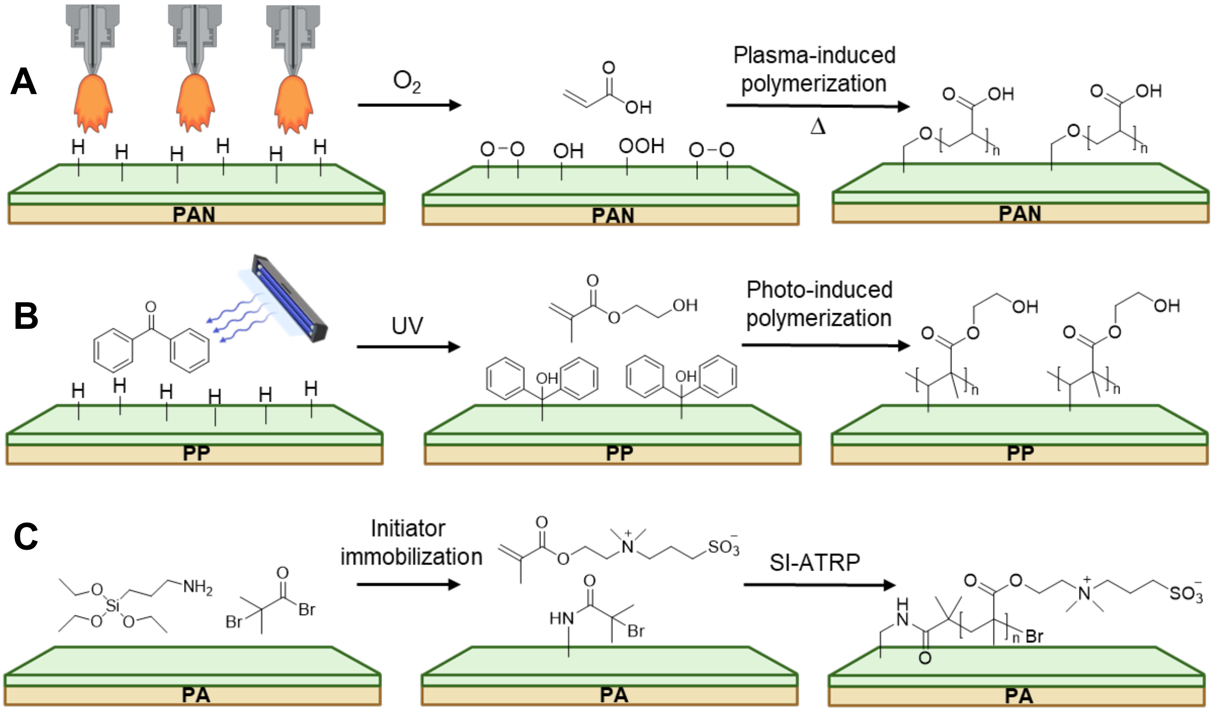

Figure 22: Methods of graft polymerization for surface modification of membranes: (**A**) plasma-induced graft polymerization of acrylic acid onto PAN, (**B**) photoinitiated graft polymerization of HEMA onto PP using benzophenone as a photoinitiator and (**C**) surface-initiated atom transfer radical polymerization (SI-ATRP) of DMAPS on PA.

4.4.2 Blending

Polymer blends are considered one of the most practical methods because they combine the properties of different materials to create a new composite with adjustable properties that compensate for the weaknesses of the individual components. Additionally, polymer blends offer advantages such as good reproducibility, easy processing, and cost efficiency. However, a major challenge is the limited miscibility of the components at the molecular level. The thermodynamics of polymer blends play a decisive role here because they significantly influence the molecular dispersion state, the morphology of two-phase systems, phase boundary adhesion, and ultimately, the properties of the product.[136]

For example, a blend membrane composed of polyethersulfone (PES) and polyphenylsulfone (PPSU) was produced by YAHYA *et al.* for the nanofiltration of wastewater (Figure 23). In this process, PPSU and a defined portion of PES were dissolved in dimethyl sulfoxide (DMSO) and stirred continuously overnight until a homogeneous casting solution was obtained. The solution was then applied to a glass plate, and the phase inversion was completed by immersing the membrane in a bath of deionized water.[137]

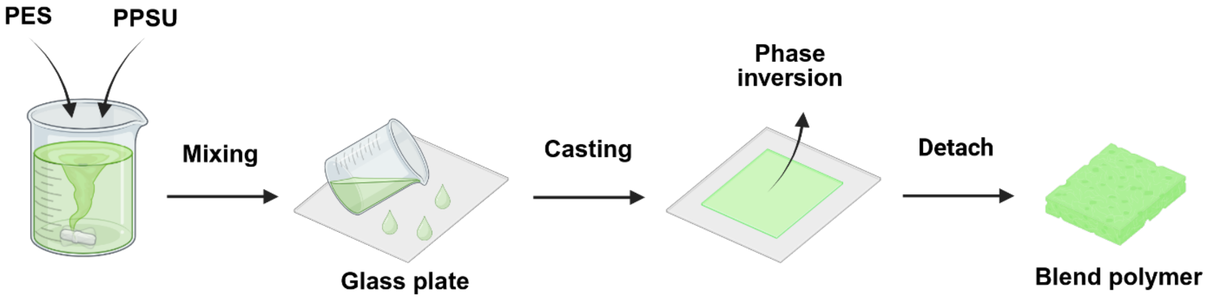

Figure 23: Blend membrane made of polyethersulfone (PES) and polyphenylsulfone (PPSU) by mixing in DMSO, applying to a glass plate, and then reversing the phases using a water bath.

4.4.3 Layer-by-layer

The layer-by-layer (LBL) method involves the sequential adsorption of polycations and polyanions onto a charged surface. After each adsorption step, the surface is rinsed to remove weakly bound polymer chains. The LBL method's main advantage lies in its ability to precisely control layer thickness in the nanometer range during deposition, which can be adjusted by the number of adsorption cycles.[136] For example, TEKINALP *et al.* used the layer-by-layer method to apply the polyanion polystyrene sulfonate (PSS) and the polycation polyallylamine hydrochloride (PAH) alternately to a membrane (Figure 24). The resulting anion exchange membrane is used in electrodialysis to separate monovalent and multivalent anions.[138]

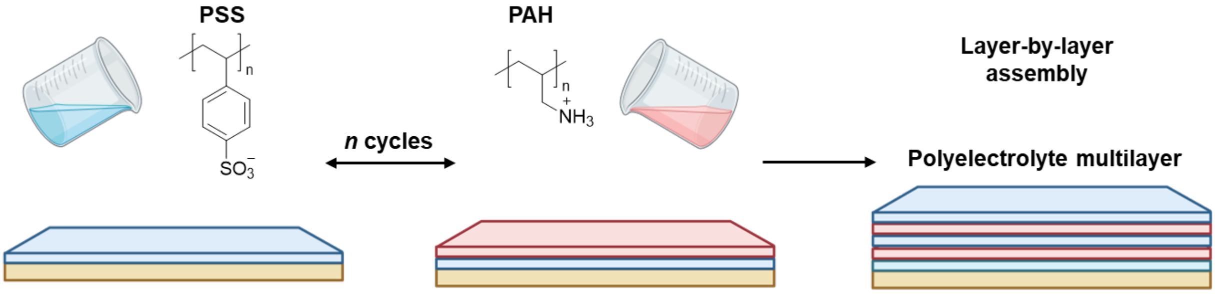

Figure 24: Layer-by-layer (LBL) method for membrane surface modification *via* alternating adsorption of polycations and polyanions, enabling nanometer-scale thickness control.

5 Aim of the thesis

The aim of this work is to develop a method for the efficient and mild modification of polymer membranes by UV-induced grafting using acylphosphine oxides as photoinitiators. This fast, versatile and economical grafting technique will be used to produce novel membrane surfaces with improved antifouling properties. The focus is on functionalization with cationic and zwitterionic polymer brushes to make the membrane surfaces less sensitive to biofouling, to extend their lifetime and thus to contribute to the reduction of plastic waste in membrane separation processes. A key feature of the chosen strategy is the modular structure of the monomers used, which allows the synthesis of various charged and zwitterionic brush polymers while minimizing the number of synthetic steps. The functional groups are either introduced directly through the selection of suitable monomers or added in a postpolymerization step. The workflow for membrane functionalization and testing is shown in Figure 25.

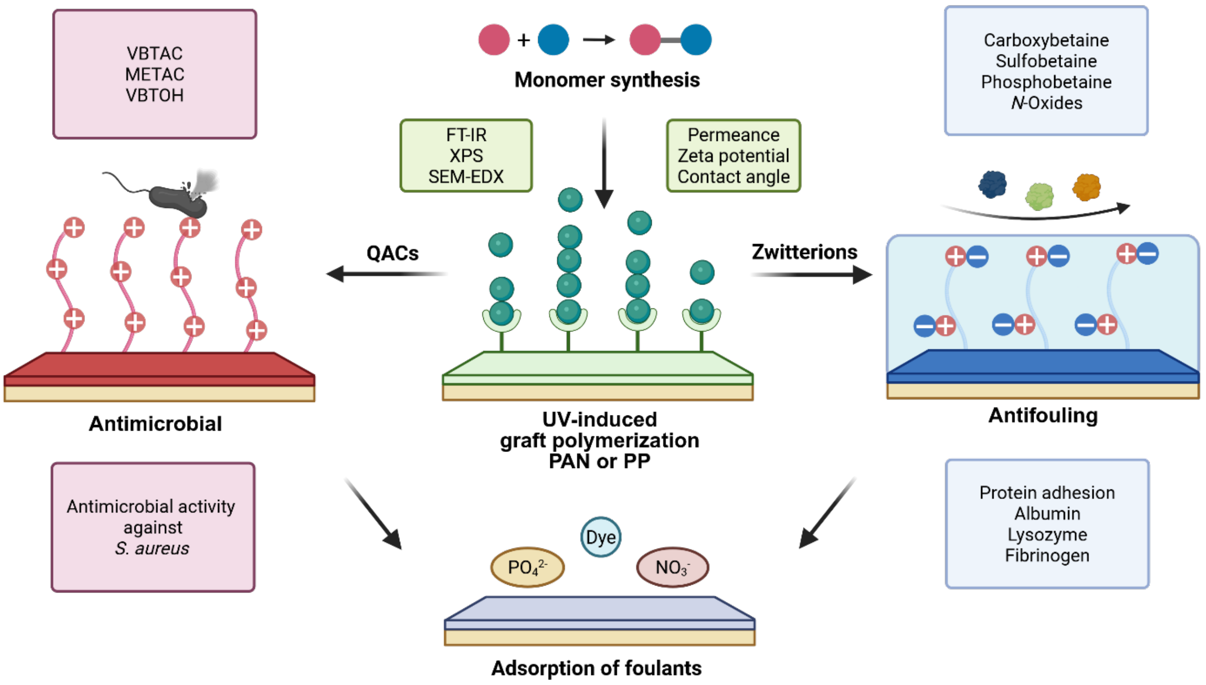

Figure 25: Workflow: (**1**) Synthesis, (**2**) UV-induced grafting modification, (**3**) characterization of membrane and (**4**) investigation of antimicrobial efficacy and antifouling properties, (**5**) removal of foulants such as dyes or salts.

The first part of the project focuses on the modification of PAN ultrafiltration membranes for drinking water and wastewater treatment. Different polycationic (*e.g.* ammonium and ammonium alcohol groups) and polyzwitterionic (including sulfobetaines, carboxybetaines, phosphobetaines and *N*-oxides groups) brush polymers based on polymethacrylate or polymethacrylamide scaffolds were grafted from the membrane surface. The modified membranes will be characterized by their physicochemical properties. In addition, functional tests are performed regarding the adsorption capacity for model contaminants such as dyes, proteins, nitrate and phosphate as well as the antibacterial effect.

The second part of the project involves transferring the UV-induced grafting method to inexpensive, widely used PP nonwoven membranes to investigate their suitability for use in water and air filtration applications. The aim is to modify the PP membranes with charged and zwitterionic polymer brushes containing quaternary ammonium compounds such as VBTAC and VBTOH, as well as zwitterions such as carboxybetaine derivatives with different carbon spacer lengths (C1 and C3). The modified membranes will be evaluated in terms of their protein adsorption, antimicrobial effect and dye adsorption capacity. Additionally, the feasibility of deriving active esters from carboxybetaine monomers will be investigated to create a foundation for the covalent binding of biomolecules. The efficiency of bioconjugation will be verified by exemplary immobilizing the model protein horseradish peroxidase (HRP) using EDC/NHS chemistry and quantified by enzymatic assays (pyrogallol conversion).

The overall aim of the work is to establish a flexible, easily scalable membrane modification system that can be used for applications in water treatment.

6 Results and Discussion

6.1 Functionalization of PAN membranes

PAN ultrafiltration membranes are characterized by high thermal and chemical stability and broad solvent resistance. However, their suitability for use is limited by their susceptibility to membrane fouling.[40] This leads to reduced flux or clogging of the pores, resulting in higher operating costs and the need for chemical cleaning of the membrane, for example by backwashing or chemical treatment with sodium hypochlorite or hydrogen peroxide.[89]

One promising strategy to improve membrane performance is to modify the membrane surface to minimize fouling and extend its lifetime. For example, hydrophilic groups are introduced to reduce the adsorption of foulants, or cationic groups are introduced to achieve antimicrobial properties.[12] PAN can be modified in a variety of ways, including plasma treatment[130], polymer blends[139], composites[140], grafting[141], deposition of polyelectrolytes[142], or chemically by hydrolysis with sodium hydroxide[143]. However, many of these methods are characterized by harsh reaction conditions and complex, multi-step synthetic processes.

In contrast, the UV-induced graft polymerization developed in this work is a gentle method in which the bulk material remains largely intact. Irradiation of a photoinitiator produces radicals that abstract hydrogen atoms from the membrane surface and thus serve as a starting point for the attachment of monomers. In a subsequent step, the polymer brushes can be further functionalized. The modification process is shown schematically in Figure 26.

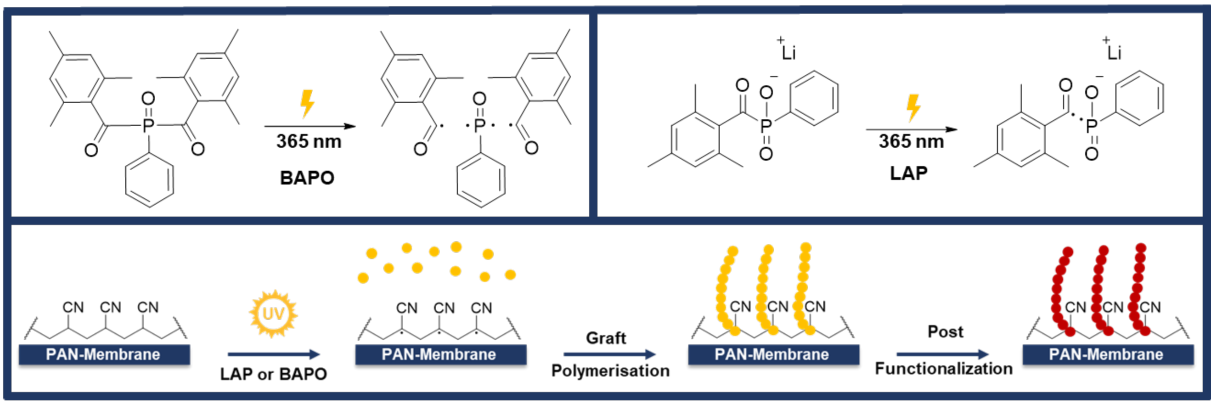

Figure 26: UV-induced graft polymerization using BAPO and LAP as photoinitiators at 365 nm. Monomers (yellow) react with surface-generated radicals to form polymer brushes, which can be postfunctionalized (red) in a subsequent step.

Irradiation is performed using an energy efficient LED light source with a narrow emission spectrum at 365 nm. Until now, only benzophenone has been used as a type II photoinitiator for UV-induced graft polymerization on PAN ultrafiltration membranes.[132] In this work, acylphosphine oxides such as BAPO (IRGACURE® 819) and LAP are used as type I photoinitiators for the first time. Radicals are formed by *α*-cleavage from the excited triplet state, which is achieved after photoexcitation and intersystem crossing.[144] A major advantage of these initiators is their absorption in the near UV (350–400 nm), high quantum yield of radicals, high reactivity of the resulting benzoyl and phosphinoyl radicals, fast photolysis, and good solubility in various formulations. In addition, acylphosphine oxides exhibit photobleaching, in which the chromophores are destroyed during irradiation, resulting in a colorless reaction environment. This allows deeper light penetration into the coating and promotes complete curing.[145] A disadvantage is the high cytotoxicity of certain acylphosphine oxides such as BAPO.[146] Interestingly, the corresponding acylphosphine oxide salts have been found to be non-toxic. LAP, for example, has been shown to have good biocompatibility.[147]

In general, the functional groups with antifouling behavior are introduced either directly through the monomer used or by post-functionalization of the polymer brush. An overview of all modifications is shown in Figure 27.

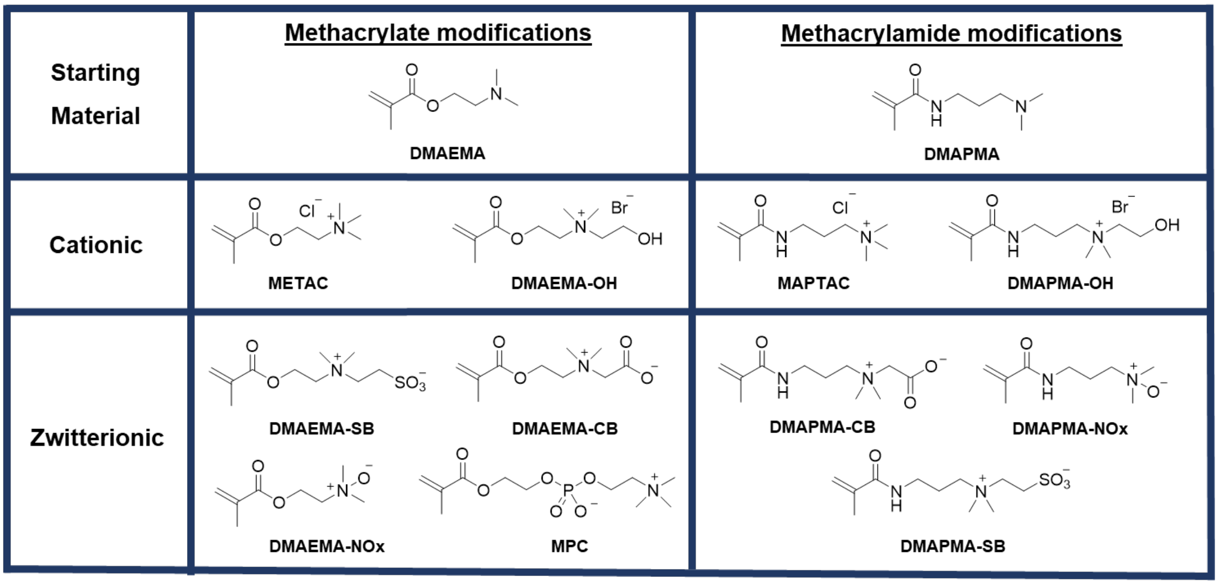

Figure 27: Polymer brush structures, including starting materials, cationic and zwitterionic modifications, based on methacrylates or methacrylamides scaffolds.

The inexpensive and commercially available compounds DMAEMA (methacrylate) and DMAPMA (methacrylamide) were selected as starting material. Many functional groups can be introduced *via* the tertiary amine by nucleophilic substitution or oxidation. SCHÖNEMANN *et al.* showed that the ester and amide functions of the corresponding polymers are not hydrolyzed or only to a negligible extent over a period of one year and at different pH values (0, 7.4 and 14). This ensures the long-term stability of the polymer backbone. The corresponding monomers, on the other hand, were hydrolyzed under the same conditions.[148]

To kill microorganisms, the membrane was coated with contact-active polymer brushes based on quaternary ammonium compounds (QACs).[109] The mechanism of action of polymeric QACs is not completely understood. Proposed mechanisms are the polymeric spacer effect[120], the phospholipid sponge effect[121] and an ion exchange[122] mechanism. Commercially available QAC monomers such as METAC and MAPTAC were used. DMAEMA was polymerized onto the membrane surface and then post-functionalized by reaction with 2-bromoethanol to form a quaternary ammonium alcohol (OH). The idea is to combine the contact-active effect with an anti-adhesive component. If a bacterium can penetrate the hydrated surface layer, it should be killed by the positive charge of the ammonium group. The positively charged polymer brushes serve not only to neutralize microorganisms, but also to adsorb negatively charged contaminants such as dyes or pharmaceuticals.

To prevent the accumulation of contaminants on the membrane surface, zwitterionic polymer brushes based on carboxybetaines, sulfobetaines, phosphobetaines and *N*-oxides are used. These are characterized by their high hydrophilicity. In order to maximize the antifouling properties, the distance between the positive and negative groups should be as short as possible. A lower dipole moment reduces electrostatic and dipole-dipole interactions with foulants and thus improves fouling resistance.[149] The functional groups *N*-oxide (NOx), carboxybetaines (CB), and sulfobetaines (SB) were introduced by post-functionalization of DMAEMA and DMAPMA, respectively. The commercial phosphobetaine monomer MPC was used because of the complexity of synthesizing the monomer and the lack of a suitable and inexpensive compounds for post-functionalization.

Two methods of grafting monomers onto PAN, referred to as method A and method B, have been developed and are illustrated in Figure 28 using DMAEMA and METAC as examples, along with the post-functionalization of tertiary amines.

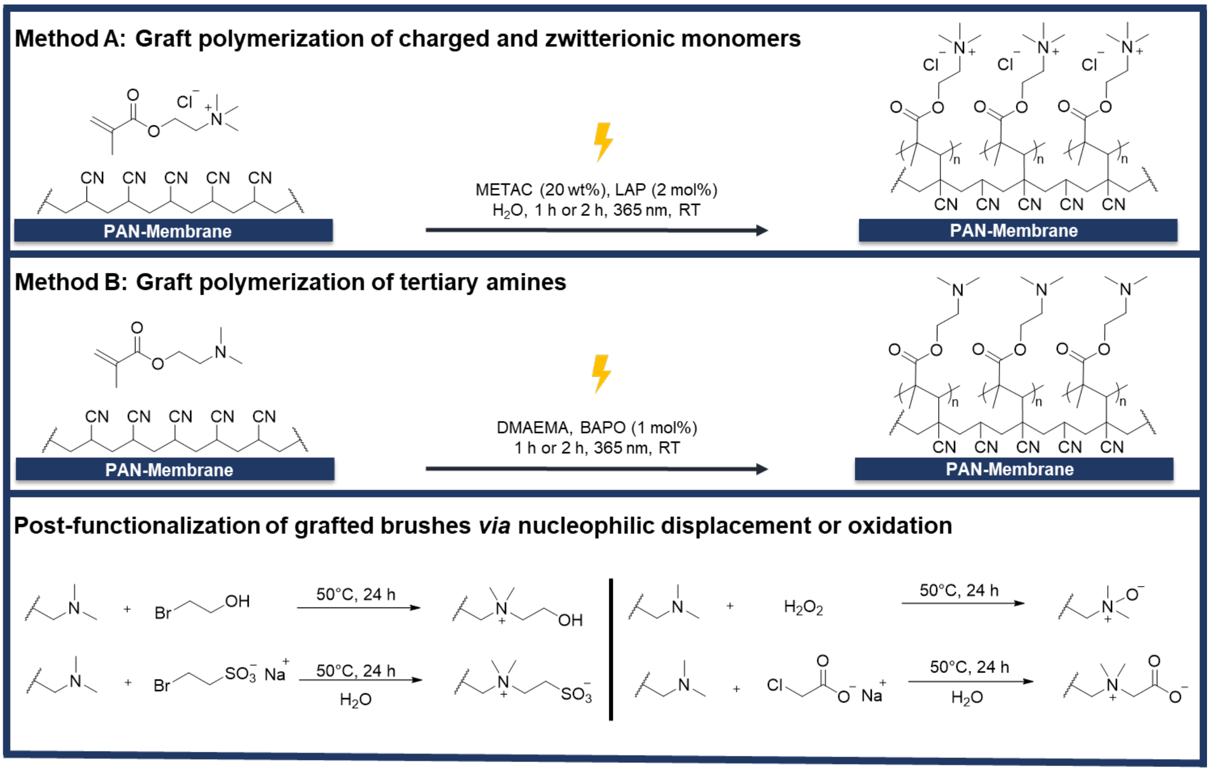

Figure 28: Reaction conditions for UV-induced graft polymerization: method A, applied to hydrophilic monomers (METAC), and method B, optimized for non-polar monomers (DMAEMA). Reaction schemes for the post-modification of polymer brushes with tertiary amines to obtain ammonium alcohols, sulfobetaines, carboxybetaines, and *N*-oxides.

UV-induced graft polymerization was performed in the absence of oxygen. On the one hand, oxygen can quench the excited state of the photoinitiator. On the other hand, it reacts with primary initiating or growing radicals to form peroxyl radicals (ROO·), which are energetically unsuitable to initiate methacrylate polymerization. Instead, these peroxyl radicals tend to terminate polymerization either by radical-radical recombination or by hydrogen abstraction from an adjacent molecule. The resulting radical often has too little reactivity with the methacrylate double bond to reinitiate the initiation process.[150]

The PAN membrane was cut into 1 cm^2 pieces and mixed with a solution of photoinitiator and monomer. This solution was degassed under nitrogen for 20 min. The soaked membranes were then irradiated for 2 h at a wavelength of 365 nm in the photoreactor. One advantage of soaking is that the excess solution can be reused, reducing monomer consumption. Method A was optimized for hydrophilic monomers. Here, LAP is used, which generates only two radicals. Method B was tailored for non-polar or hydrophobic monomers. It uses BAPO as the photoinitiator, which can form four radicals under irradiation. For this reason, 1 mol% of radical initiator is used in this case, compared to 2 mol% when LAP is used. The modification process does not require the use of environmentally harmful solvents. In the case of DMAEMA and DMAPMA, no additional solvent is required because the photoinitiator BAPO is soluble in both monomers. For all other modifications, water can be used as an environmentally friendly solvent in combination with the water-soluble photoinitiator LAP.

Post-functionalization is an attractive method for generating a large library of functional polymers. The advantage is that all polymers have identical chain lengths or a comparable chain length distribution. In addition, functional groups can be introduced that are not compatible with the polymerization conditions.

Direct graft polymerization is a simple and effective method that allows monomers to be grafted directly onto the membrane surface in one step. However, the chemical compatibility of certain monomers with the reaction conditions, such as pH, solvent, or light sensitivity, can limit this approach. Additionally, some zwitterionic or functional monomers require complex, time-consuming syntheses, which make direct grafting impractical. In contrast, post-modification enables the use of simple precursor monomers that can be easily grafted. Then, a second mild reaction step is performed to introduce the desired functionality. Although this increases the number of steps, it offers greater versatility and stability, particularly for sensitive or synthetically challenging structures.

It is important to note for this study that the amount of graft polymer in each modification can differ. Therefore, properties such as adsorption capacity, antimicrobial activity, protein adsorption, and phosphate and nitrate adsorption cannot be correlated. The primary goal of the modification process was to alter the membrane properties while maintaining adequate permeance of around 100 $L\ m^{-2}\ h^{-1}\ bar^{-1}$ to ensure sufficient water flow for applications in water and wastewater treatment. Additionally, the results suggest that the permeance can be tuned by adjusting the monomer concentration during the grafting process. This provides a mean to optimize membrane performance for specific applications by balancing functionalization with water transport properties.

6.1.1 Membrane characterization

To verify the success of the UV-induced polymerization, ATR-FTIR spectra of the modified materials were recorded. The introduced functional groups can be identified because of characteristic vibrations and in comparison, with the unmodified PAN membrane. Figure 29 shows the IR spectra of the DMAEMA-based polymer brushes.

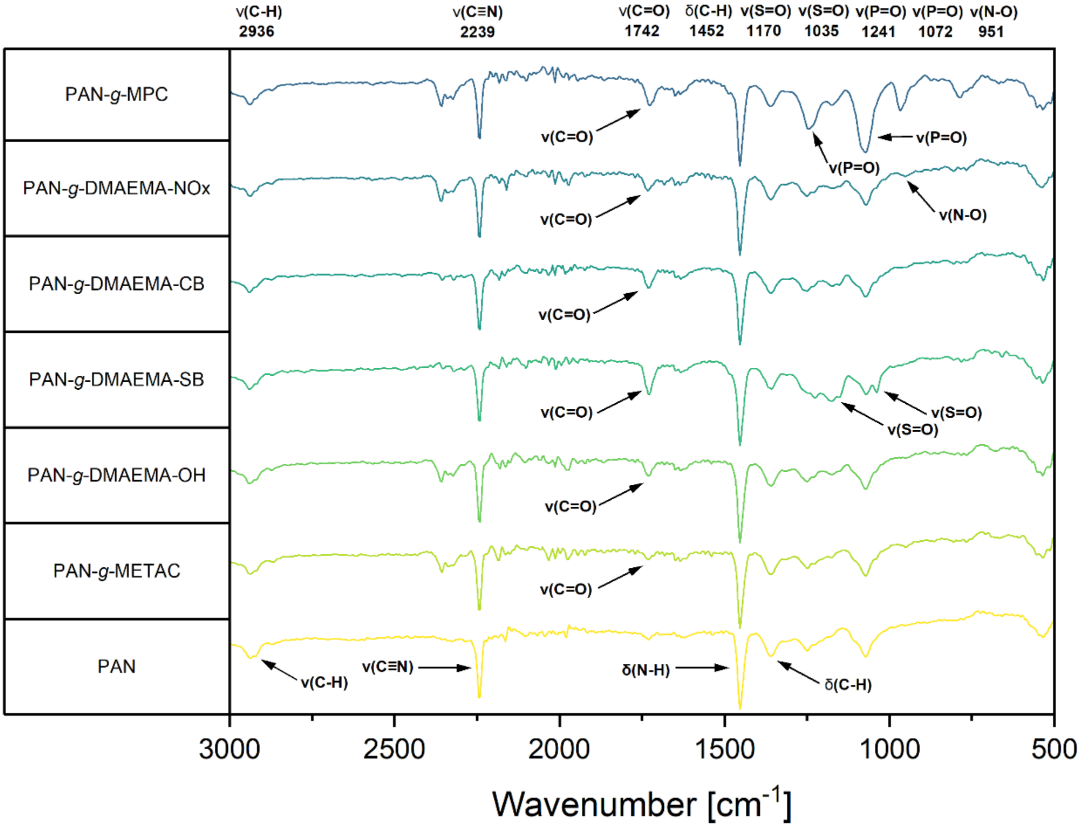

Figure 29: ATR-FTIR of unmodified PAN membranes and functionalized with DMEMA derivatives METAC, OH, SB, CB, NOx and MPC in the range from 3000–500 cm^{-1}.

The bands of the unmodified PAN membrane are visible in all spectra of the modified materials. The stretching vibration of the methylene groups ($-CH_2-$) of the polymer backbone appears at 2936 cm^{-1}. An intense band at 2239 cm^{-1} can be assigned to the stretching vibration of the nitrile group (-CN). In addition, a strong bending vibration of the methylene groups ($-CH_2-$) is observed at 1452 cm^{-1}. All modifications show the methacrylate specific carbonyl band at 1742 cm^{-1} (C-O). PAN-*g*-MPC is clearly identified by the characteristic bands at 1241 cm^{-1} (-O-P-O-) and 1072 cm^{-1} (-P-O-C-). In contrast, the band at 951 cm^{-1} (-N-O), which is typical for PAN-*g*-DMAEMA-NOx, is only weakly pronounced. PAN-*g*-DMAEMA-CB shows a specific but also weak band at 1634 cm^{-1}, which is assigned to the stretching vibration (C-O). The typical bands of PAN-*g*-DMAEMA-SB appear at 1170 and 1035 cm^{-1} (S-O). In the case of PAN-*g*-

METAC and PAN-*g*-DMEMA-OH, only the carbonyl band of the methacrylate is clearly visible; no other characteristic bands are detectable. In summary, all methacrylate membranes were successfully modified. Figure 30 shows the IR spectra of the DMAPMA-based polymer brushes.

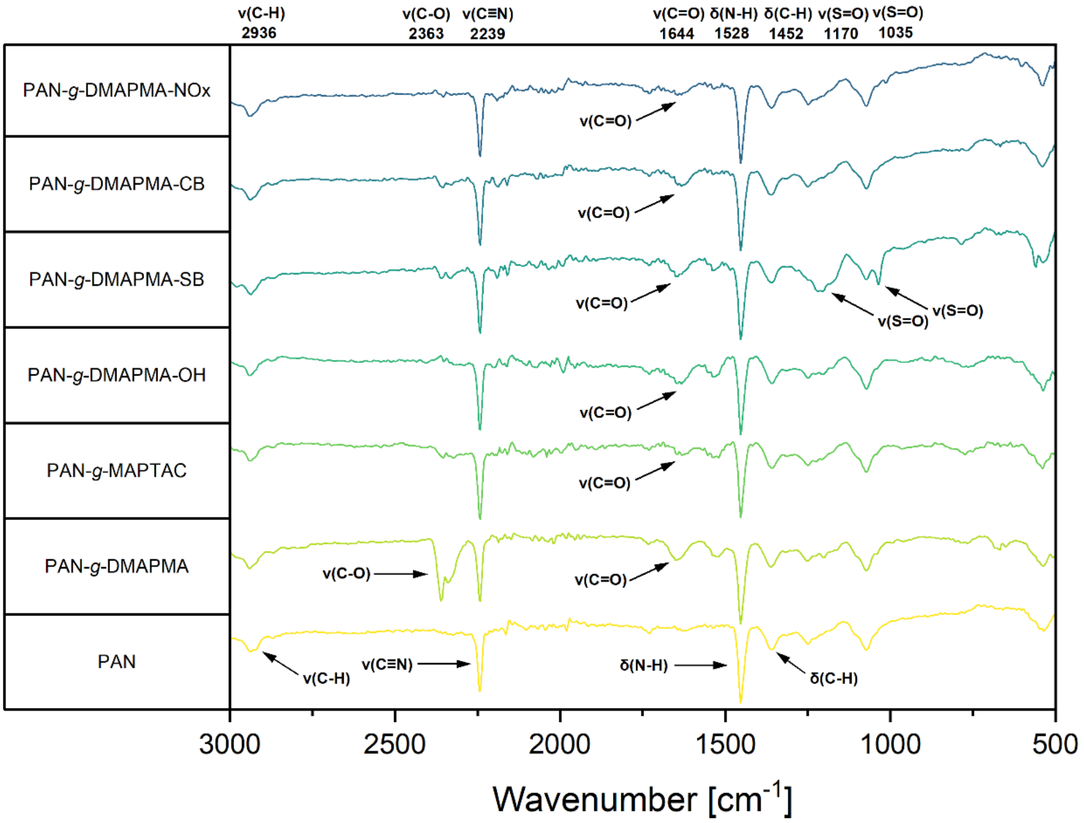

Figure 30: ATR-FTIR of unmodified PAN membranes and functionalized with DMAPMA derivatives METAC, OH, SB, CB, NOx and MPC in the range from 3000–500 cm^{-1}.

All DMAPMA-based membranes mainly display the PAN base material, as described above. The two signals of the methacrylamide group are visible in all materials, namely the amide I band at 1644 cm^{-1} (C-O) and the amide II band at 1452 cm^{-1} (N-H). Sulfobetaine is also clearly visible with characteristic bands at 1170 and 1035 cm^{-1} (S-O). However, the carboxybetaine cannot be clearly distinguished from the amide as both bands appear in the same region. In contrast to the DMAEMA membranes, other modifications such as PAN-*g*-NOx, PAN-*g*-DMAEMA-OH and PAN-*g*-MAPTAC cannot be clearly detected. However, all modified membranes are evidently different from untreated PAN, indicating that modification has occurred. Some spectra also show a signal at 2363 cm^{-1} (C-O), which can be attributed to CO$_2$.

Next, the water contact angles (WCA) of the membranes were determined. This method can be used to investigate whether a material surface has hydrophilic or hydrophobic properties. A contact angle of less than 90° indicates a hydrophilic surface, *i.e.* a surface with high surface energy. If the contact angle is greater than 90°, the surface is said to be hydrophobic with a correspondingly low surface energy.[151] The underlying principle is shown in Figure 31.

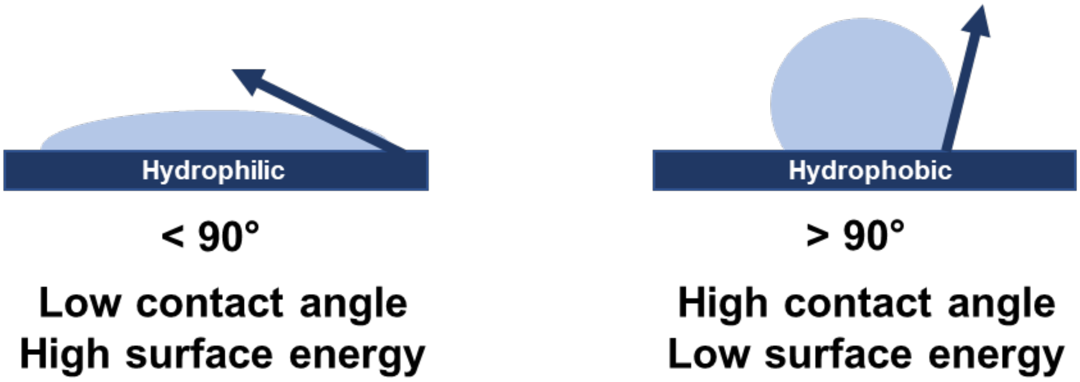

Figure 31: Principle of contact angle measurement to distinguish between hydrophilic and hydrophobic surfaces.

For evaluation of the dynamic water contact angle (WCA), independent triplicate measurements were obtained at three distinct locations on the surface. The measurement of contact angles was conducted using deionized water, employing the static sessile drop method. To obtain the contact angle, a 10-second video was recorded at a frequency of 10 Hz. The contact angle was then determined as the mean value of the first three contact angles. The results are shown in Figure 32.

WCA measurements provided indirect evidence of successful surface modification, as all modified membranes showed slight changes compared to the untreated PAN membrane. The untreated PAN membrane has a water contact angle of 44.8°, indicating that the material is already intrinsically hydrophilic. In general, the DMAPMA membranes have lower contact angles than the DMAEMA membranes. The lowest WCAs were measured for PAN-*g*-DMAPMA-OH (35.8°) and PAN-*g*-DMAPMA-NOx (35.9°). In contrast, PAN-*g*-DMAEMA-OH (61.0°) and PAN-*g*-DMAEMA-CB (55.9°) showed the highest contact angles. The other modifications did not differ significantly from the untreated membrane.

The observed differences are due to variations in porosity, surface roughness and introduced functional groups, as will be shown in later analyses. Despite these differences, all membranes absorb the WCA measurement droplet very quickly, indicating a generally hydrophilic surface.

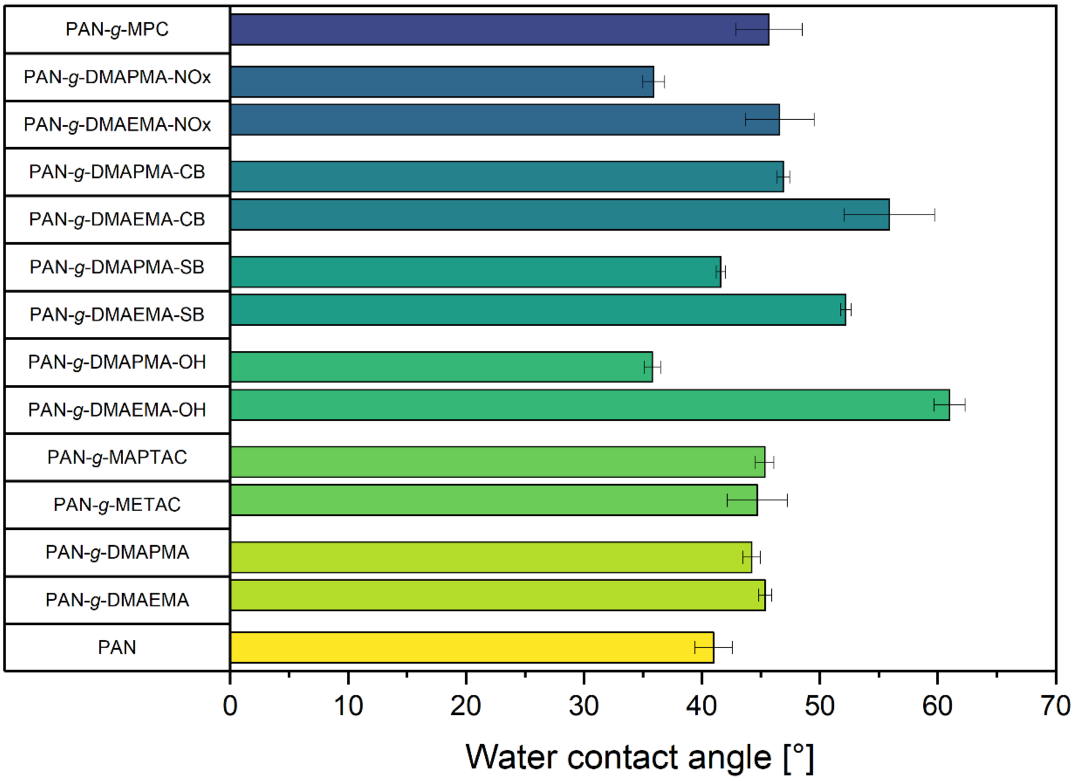

Figure 32: Average dynamic water contact angle (WCA) values of various modified and untreated PAN membranes. The data show differences in wettability because of surface modification.

Scanning electron microscopy combined with energy dispersive X-ray spectroscopy (SEM-EDX) provided detailed insights into the surface morphology and elemental composition of the membranes. Because the PAN membrane is non-conductive, it must be prepared prior to SEM examination. Without this preparation, electrons would accumulate on the surface, an effect known as charging, resulting in white areas in the SEM images. To obtain high-resolution images, a thin conductive layer is applied to the surface. This is done with a sputter coater using materials such as carbon or platinum. The coating improves the signal-to-noise ratio and prevents the sample from becoming charged.

The SEM images of DMAEMA, both top view and cross section, are shown in Figures 33–34. In the top view, the pores are clearly visible on all membranes. In addition, there are no impurities such as salt residues. The cross-sectional images also confirm that the pore structure is intact and has not been sealed by excessive polymerization. The qualitative surface composition of the membranes was investigated by EDX for PAN-*g*-DMAEMA-SB and PAN-*g*-MPC. Both survey spectra and cross-sectional elemental mapping were performed, with particular emphasis on carbon, nitrogen, sulfur and phosphorus (see appendix Figures A30–A33).

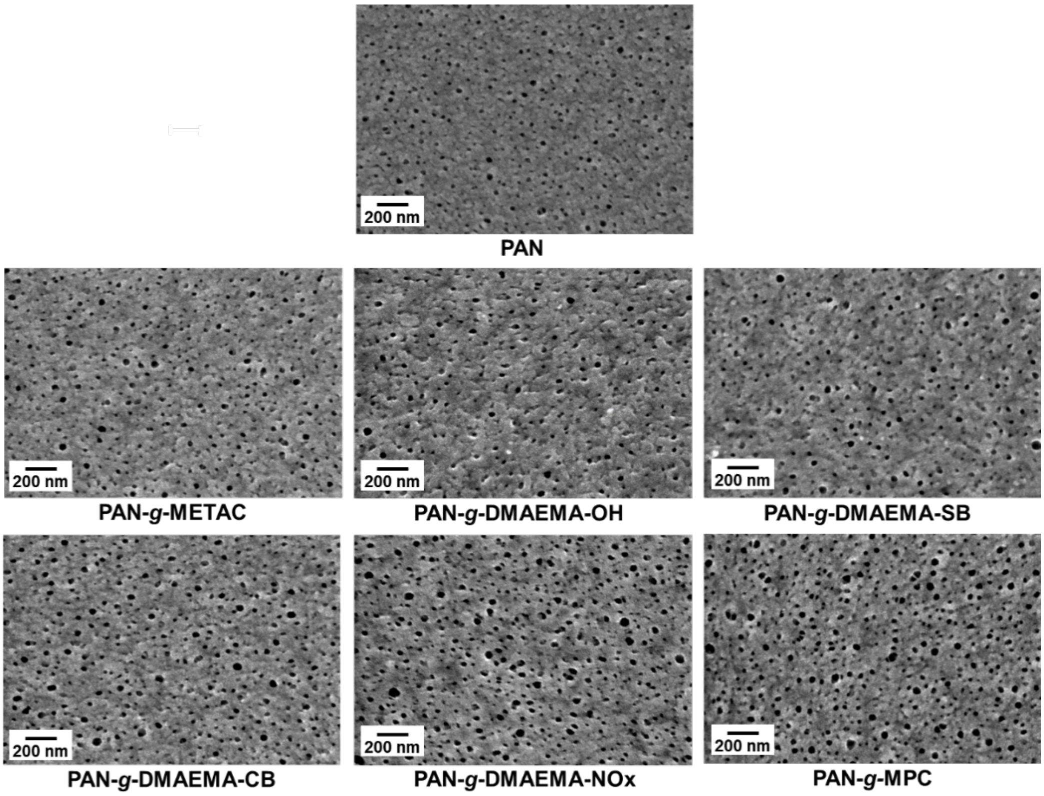

Figure 33: SEM images of the top view in a 100k magnification of pristine PAN and PAN modified with METAC, DMAEMA-OH, DMAEMA-SB, DMAEMA-CB, DMAEMA-NOx and MPC.

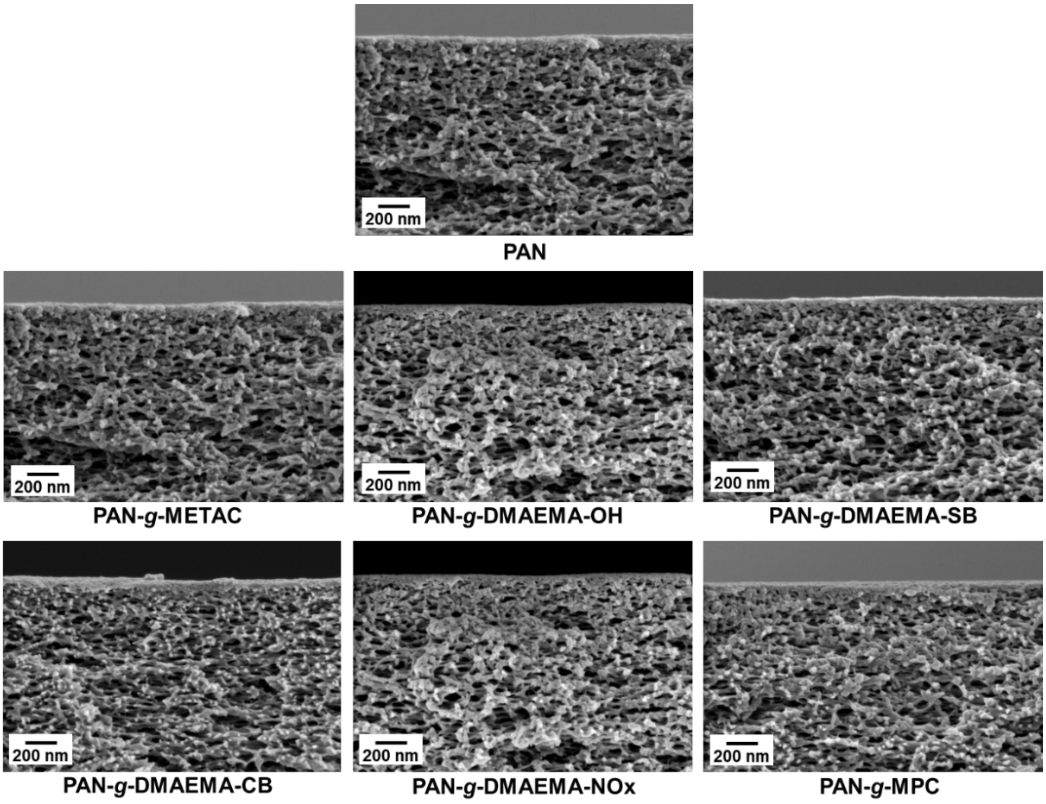

Figure 34: SEM images of the corresponding cross fractions in a 50k magnification of pristine PAN and PAN modified with METAC, DMAEMA-OH, DMAEMA-SB, DMAEMA-CB, DMAEMA-NOx and MPC.

The analysis clearly shows that sulfur atoms are detectable in the PAN-*g*-DMAEMA-SB membrane, while phosphorus atoms were detected in the PAN-*g*-MPC membrane. A platinum peak is also visible in the EDX spectrum of the PAN-*g*-DMAEMA-SB sample, which can be attributed to the previous platinum sputter coating. In the case of the PAN-*g*-MPC membrane, a carbon coating was used instead to avoid the superposition of the phosphor signal by platinum. The line scans are particularly informative because they show how the elements are distributed in the membrane cross section (Figure 35–36).

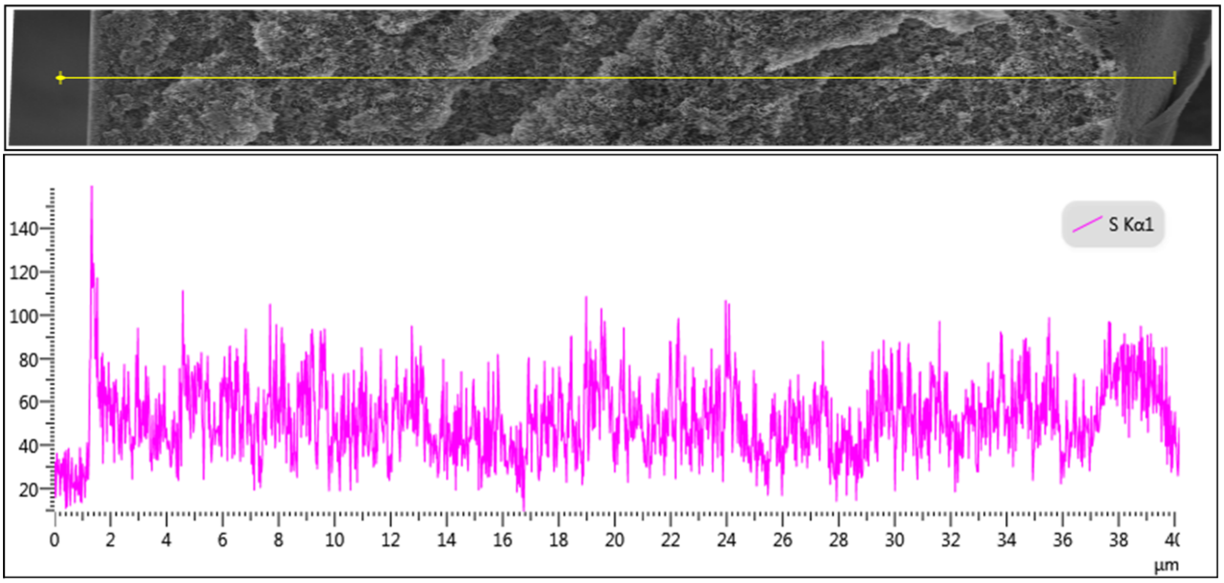

Figure 35: SEM image of the cross fraction (top) and line spectrum (bottom) of sulfur in the cross fraction of PAN modified with DMAEMA-SB.

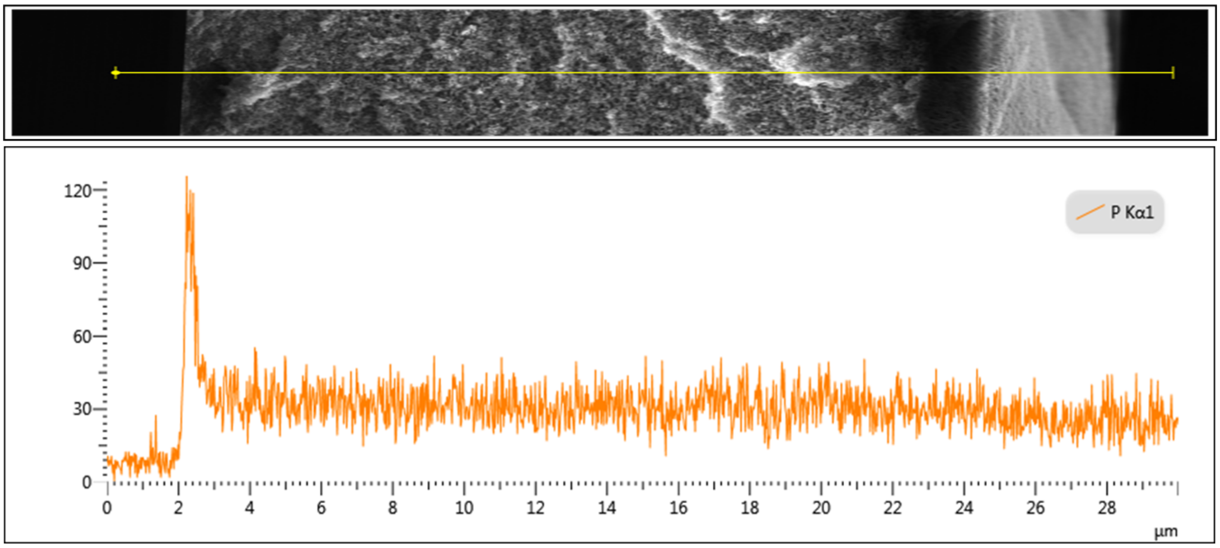

Figure 36: SEM image of the cross fraction (top) and line spectrum (bottom) of sulfur in the cross fraction of PAN modified with MPC.

The amount of functional groups is significantly higher at the membrane surface than in the interior. The distribution of phosphorus in the cross section appears to be more homogeneous than that of sulfur, where there are greater fluctuations, which is reflected in a higher standard deviation. It is noteworthy that a change in the interior of the membrane was detected at all, as this was not originally expected. This finding is a central result of this work. A possible explanation could be the photobleaching effect of the photoinitiators BAPO and LAP. The aforementioned effect could have allowed a deeper penetration of the reaction, which in turn leads to a modification of the membrane structure also in the interior. EDX analysis is not useful for PAN-*g*-METAC, PAN-*g*-DMAEMA-OH, PAN-*g*-DMAEMA-CB and PAN-*g*-DMAEMA-NOx membranes, as their elemental composition does not differ significantly from that of the untreated PAN membrane. In addition, oxygen is always present as an environmental impurity and is therefore difficult to unambiguously assign. EDX analysis is ideal for heavier elements, as they can be more clearly detected and distinguished.

For further characterization, an attempt was made to analyze the membrane using XPS. This method is much more sensitive than EDX and provides precise information about the elemental composition of the sample surface. XPS is particularly suitable for the study of thin layers, since only the top 20 nm of the surface is analyzed. For the measurement, a material was chosen that differs significantly from the elemental composition of the untreated PAN membrane. In this case it is PAN-*g*-DMAEMA-SB. The survey and region spectra of the untreated PAN membrane and the modified PAN-*g*-DMAEMA-SB membrane are shown in the appendix Figures 34–37. The evaluation of the measurements is shown in Tables 1 and 2.

Table 1: Elemental composition of the pristine PAN membrane based on XPS measurements.

Pristine PAN					
Survey (%)	Element	Energy (ev)	Peak Area	Concentration (at%)	Structure
76.10	C 1s 1	284.50	14485.19	27.71	$-CH_2$
	C 1s 2	285.48	12208.37	23.37	-CH-CN
	C 1s 3	286.24	25555.78	48.92	-C≡N
21.75	N 1s 1	398.46	6369.87	25.64	/
	N 1s 2	399.16	18470.18	74.36	-C≡N
1.5	O 1s 1	530.71	2600.50	82.87	CO_2
	O 1s 2	531.63	537.62	17.13	/

The spectra were evaluated using the NIST X-ray Photoelectron Spectroscopy Database.[152] The untreated PAN was successfully identified. The C1s peak can be deconvoluted into three components, which appear at 284.50 eV (-CH_2-), 285.48 eV (-CH-CN) and 286.24 eV (-C≡N). These signals correspond to the three carbon atoms from the monomer structure of PAN.[153] The nitrogen of the nitrile group shows a signal at a binding energy of 399.16 eV. The calculated N/C ratio of 0.29 is in good agreement with the theoretical value of 0.30. In addition, three other signals appear at 398.46 eV, 530.71 eV, and 531.63 eV, which are due to impurities from the manufacturing process or CO_2 adhering to the surface.

Table 2: Elemental composition of the PAN-*g*-DMAEMA-SB membrane based on XPS measurements.

PAN-*g*-DMAEMA-SB					
Survey %	Element	Energy (ev)	Peak Area	Concentration (at%)	Structure
75.58	C 1s 1	283.51	979.25	2.51	/
	C 1s 2	284.49	13125.25	33.68	/
	C 1s 3	285.72	20051.11	51.47	-C≡N
	C 1s 4	285.73	3678.06	9.44	/
	C 1s 5	288.05	1129.31	2.90	/
18.01	N 1s 1	398.69	4091.02	26.59	/
	N 1s 2	398.97	10822.60	70.36	-C≡N
	N 1s 3	401.18	468.97	3.05	NR_4
5.84	O 1s 1	529.66	700.18	8.96	CO_2
	O 1s 2	530.76	3842.66	49.17	SO_3
	O 1s 3	532.29	3270.96	41.87	SO_3
0.20	S 2p 1 3/2	166.23	144.87	56.94	SO_3
	S 2p 1 1/2	167.39	72.43	28.48	SO_3
	S 2p 2 3/2	167.72	24.72	9.72	SO_3
	S 2p 2 1/2	168.88	12.36	4.86	SO_3

The PAN membrane modified with sulfobetaine exhibits characteristic signals of the corresponding functional groups in the XPS spectrum. The ammonium group signal (NR_4) is clearly assigned to 3.05 eV. Additionally, the characteristic sulfur signals of sulfobetaine are detectable at 166.23 and 167.39 eV (SO_3). Signals appear at 167.72 eV and 168.88 eV, indicating the presence of a second sulfur species. These signals are most likely from 2-bromoethane sulfonate, which is present as the counterion of sulfobetaine, or from a protonated tertiary amine. This assumption is supported by the fact that the substance was used in excess during post-functionalization. The oxygen atoms of the sulfonate groups appear at 530.76 and

532.29 eV. The nitrile group signals from the PAN base material appear at 285.72 eV (C 1s) and 398.97 eV (N 1s). Additional carbon signals were detected at 283.51 eV, 284.49 eV, 285.73 eV, and 288.05 eV. These signals presumably originate from CH_3, CH_2, and CH groups. However, their exact assignment was not possible, due to the additional C species from the modification. Overall, the XPS analysis indicates that the functionalization was successful. However, the relatively low intensity of the corresponding signals in the survey spectrum suggests a rather thin functionalized layer. Pore size and porosity were assessed based on SEM images, with the results presented in Figures 37–38.

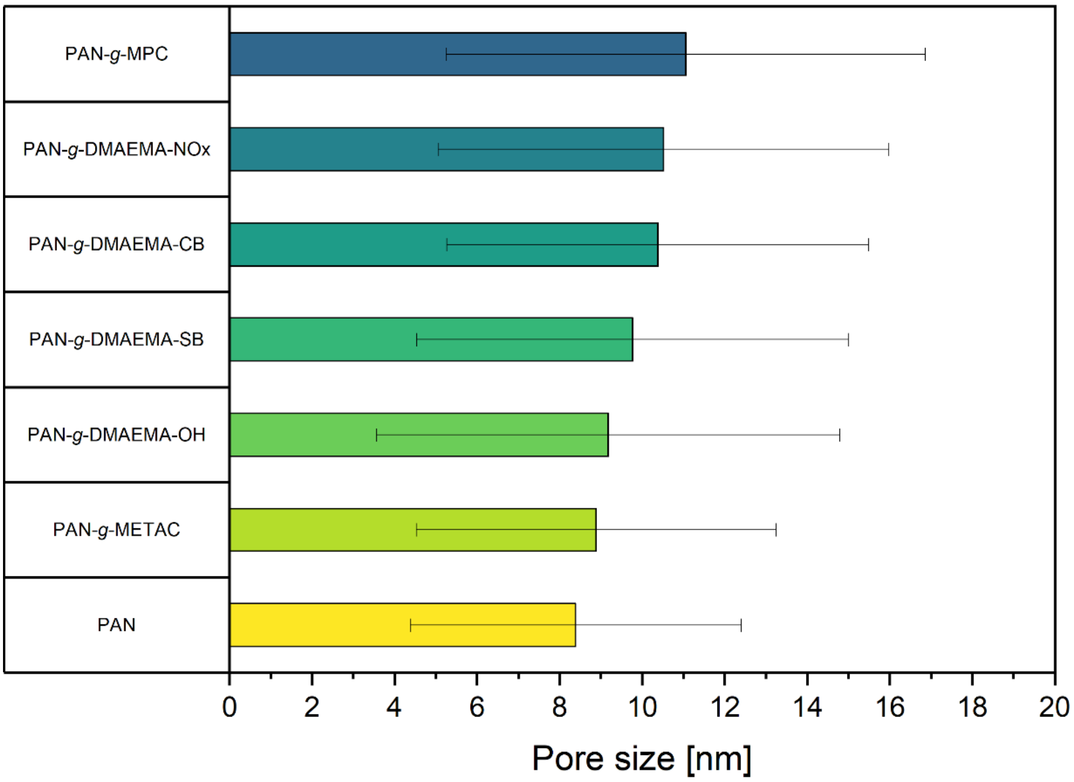

Figure 37: Average pore diameter of PAN membranes, determined from SEM images. Untreated PAN membranes are shown, as well as membranes modified with METAC, DMAEMA-OH, DMAEMA-SB, DMAEMA-CB, DMAEMA-NOx, and MPC.

For the untreated PAN membrane, an average pore size of 8.39 nm and a porosity of 1.79% were measured. In contrast, the membranes functionalized with methacrylate monomers showed a broader pore size distribution of 8.89 to 11.1 nm and a significantly higher porosity in the range of 1.65% to 5.40%. These results indicate that methacrylate modifications lead to a greater increase in pore size and porosity. This behavior can be explained by several factors. Grafting primarily occurs at the membrane surface and pore walls without fully closing the pores, which preserves the pore structure. Additionally, interactions with the solvent and temporary swelling effects during the grafting process can result in structural changes that lead to a slightly expanded, yet stable, pore network after drying. Furthermore, introducing functional groups, such as *N*-oxides, sulfobetaines, phosphobetaines, or carboxybetaines, can lead to electrostatic interactions that influence the conformation of polymer chains, thereby increasing the effective pore size. In conclusion, the results demonstrate that the grafting method affects the pore structure of polymers.

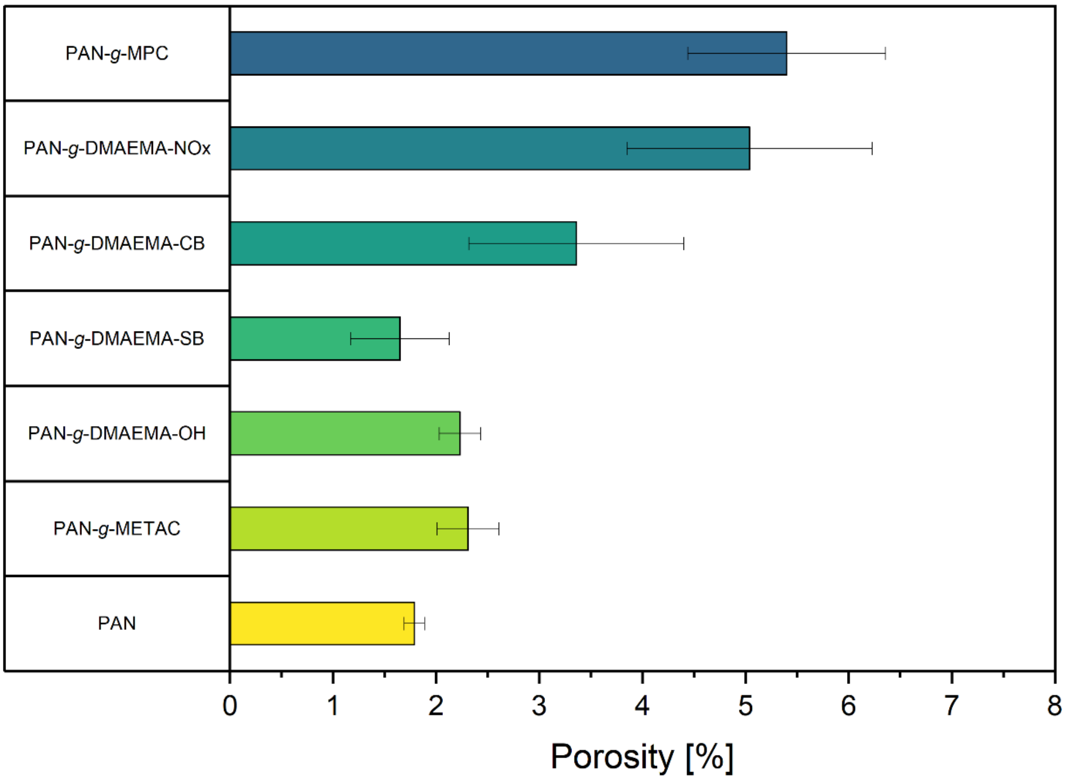

Figure 38: The porosity of the PAN membranes was determined from SEM images. Values are shown for both untreated and modified membranes. Modifications include METAC, DMAEMA-OH, DMAEMA-SB, DMAEMA-CB, DMAEMA-NOx, and MPC.

Pore size plays a key role in membrane fouling processes. When foulants are smaller than the pores, they can penetrate and adsorb onto the pore walls. This can lead to a narrowing of the pore diameter or complete blockage of individual pores. Conversely, if the foulants are larger than the pores, the selective layer of the membrane remains intact, and a cake layer forms on the membrane surface. In both cases, permeate flow decreases and transmembrane pressure (TMP) increases.[154] Thus, the optimal pore size of membranes with regard to fouling behavior is a key question. To date, only a few studies have systematically investigated the relationship between pore size and fouling. Jin *et al.* analyzed ceramic membranes with different pore sizes and found that the membrane with the largest pores was most susceptible to fouling.[155] However, Nittami *et al.* reported in a study on PTFE membranes that the membrane with the smallest pore size fouled the fastest.[156] These contradictory results suggest that the influence of pore size on fouling behavior depends heavily on the membrane material. This factor could be optimized further in the future, but the initial focus was on achieving acceptable permeability and separation performance.

The surface topography and roughness of the membranes were analyzed using AFM. Figure 39 shows the corresponding images of the untreated and functionalized membranes.

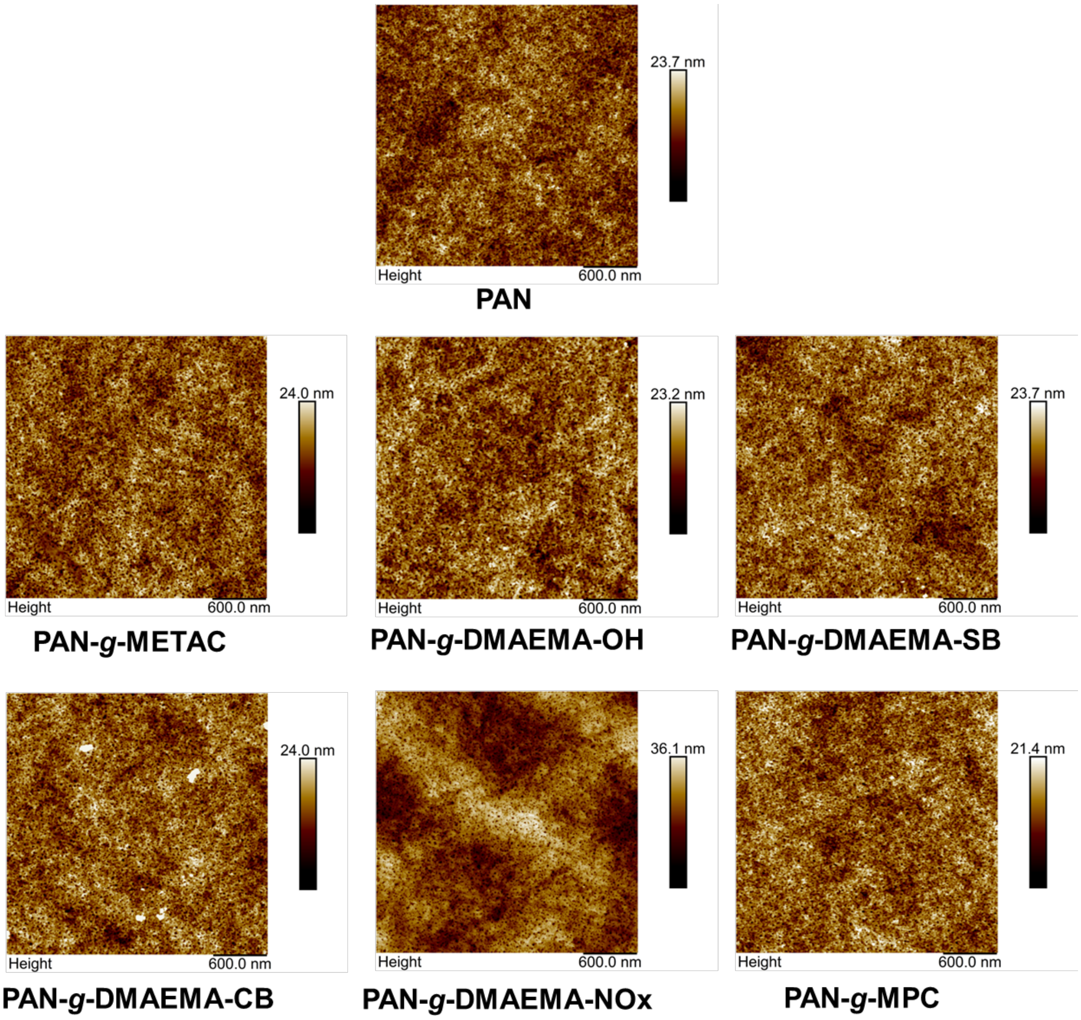

PAN

PAN-*g*-METAC **PAN-*g*-DMAEMA-OH** **PAN-*g*-DMAEMA-SB**

PAN-*g*-DMAEMA-CB **PAN-*g*-DMAEMA-NOx** **PAN-*g*-MPC**

Figure 39: AFM images of pristine PAN membrane and modified with METAC, DMAEMA-OH, DMAEMA-SB, DMAEMA-CB, DMAEMA-NOx, and MPC.

The untreated PAN membrane and the modified membranes PAN-*g*-METAC, PAN-*g*-DMAEMA-OH, PAN-*g*-DMAEMA-SB, and PAN-*g*-MPC have inconspicuous surface topographies without noticeable structures. In contrast, the PAN-*g*-DMAEMA-CB membrane exhibits bright spots that may be salt deposits, such as NaCl. The PAN-*g*-DMAEMA-NOx membrane's surface appears significantly more irregular, indicating increased roughness, which should be reflected in the roughness values. Figure 40 shows the surface roughness values R_a and R_q of the untreated PAN membrane and the modified membranes.

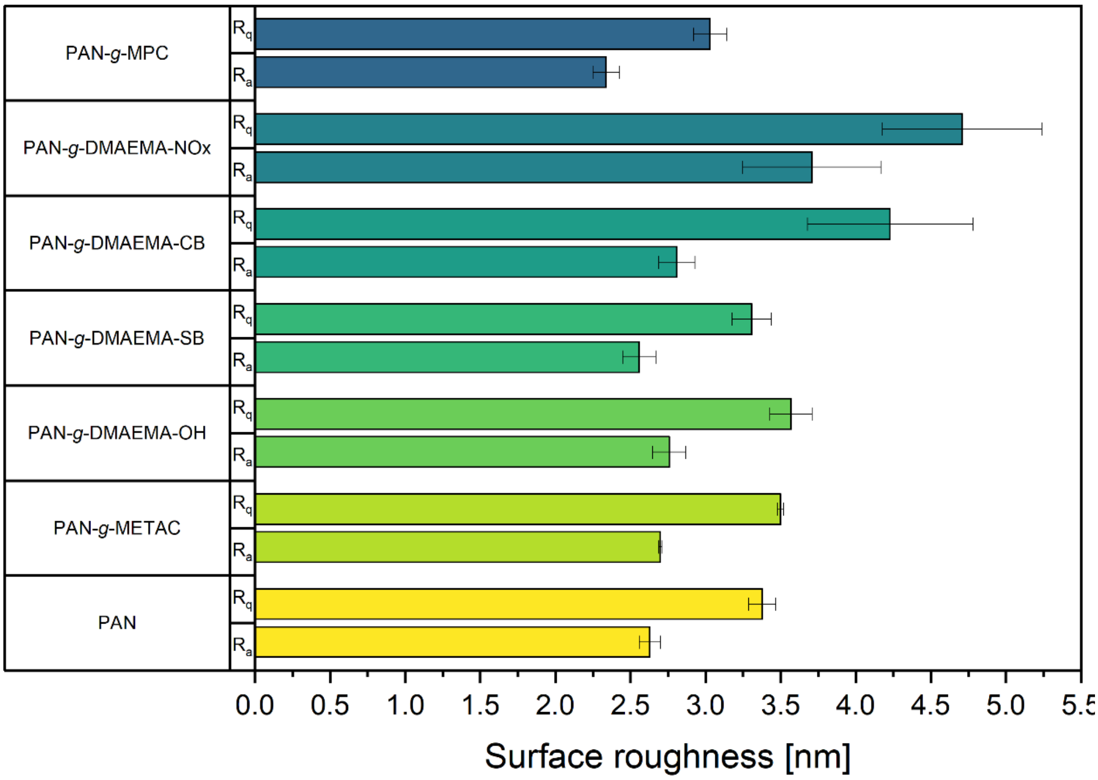

Figure 40: The surface roughness of the PAN membranes was quantified using the R_a (arithmetic mean of height deviations) and R_q (quadratic mean of height deviations) parameters, which were determined from the AFM images. The values shown are for untreated PAN membranes and membranes modified with METAC, DMAEMA-OH, DMAEMA-SB, DMAEMA-CB, DMAEMA-NOx, and MPC.

Surface roughness measurements confirm the properties of the respective membranes described above. The untreated PAN membrane and the membranes modified with PAN-*g*-METAC, PAN-*g*-DMAEMA-OH, PAN-*g*-DMAEMA-SB, and PAN-*g*-MPC exhibit similar surface structures, as indicated by their comparable values of R_a (2.63 nm) and R_q (3.38 nm). However, the membrane modified with PAN-*g*-DMAEMA-NOx has the highest roughness, with an R_a of 3.71 nm and an R_q of 4.71 nm. This might be attributed to the post-grafting treatment with hydrogen peroxide, a strong oxidizing agent that might alter the surface properties. As a result, irregularities form, leading to increased roughness. Water contact angle can be influenced by the surface roughness. QUÉRÉ *et al.* demonstrated that increased roughness is usually associated with increased hydrophilicity, which should result in a lower contact angle.[157] However, this effect could not be clearly confirmed in the present study because the differences in surface roughness were very small. Overall, all membranes have a smooth surface because the roughness values are in the low nanometer range.

The MWCO (molecular weight cut-off) is the molecular weight at which a membrane achieves approximately 90% retention of a dissolved substance. It is a measure of how selectively a membrane retains molecules based on their size, and it serves as a characteristic value for the separation limit of ultrafiltration or nanofiltration membranes.[158] The results for the MWCO measurements are shown in Figure 41.

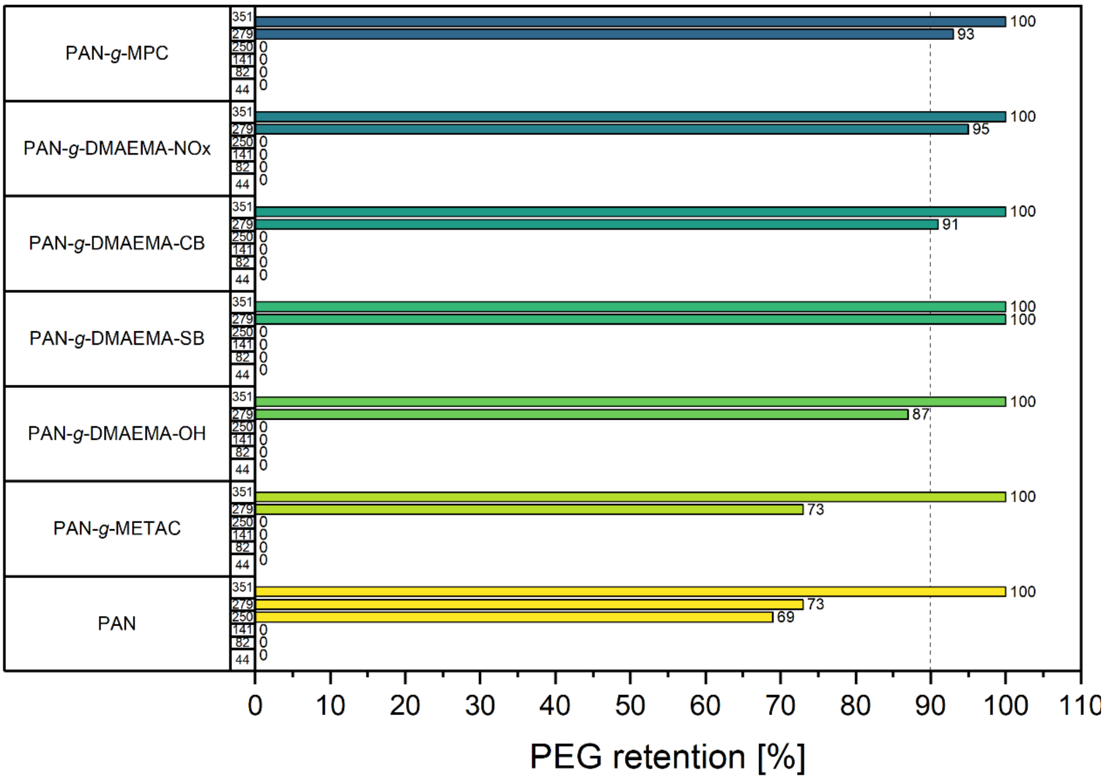

Figure 41: MWCO of the untreated PAN membrane and the modified membranes, determined using retention rates of a PEG standard with molecular weights of 44, 82, 141, 250, 279 and 351 kDa. The following were investigated: untreated PAN and membranes modified with METAC, DMAEMA-OH, DMAEMA-SB, DMAEMA-CB, DMAEMA-NOx and MPC.

The MWCO of the membranes remained largely unchanged after modification. The unmodified PAN membrane exhibits an MWCO of 351 kDa, while the modified membranes show MWCO values ranging from 351 kDa to 279 kDa. This indicates that the grafting process does not significantly alter the overall pore size distribution. The slight decrease in MWCO for some modifications suggests minimal pore narrowing due to the introduction of functional groups. The molecular mass of biomolecules such as proteins plays a crucial role in membrane fouling. High-molecular-weight proteins are often retained by the membrane, which can lead to accumulation on the membrane surface or in the pores. These deposits impair the permeability and efficiency of the membrane in the long term. This is particularly critical for membranes with lower MWCO, as they tend to accumulate larger biomolecules. Pure water permeance describes how permeable a membrane is to demineralized water. In other words, it indicates how much water flows through the membrane per unit of area and time in relation to the applied pressure. To evaluate their suitability for filtration applications, the pure water permeance of the membranes was determined in dead-end mode. The results are shown in Figure 42.

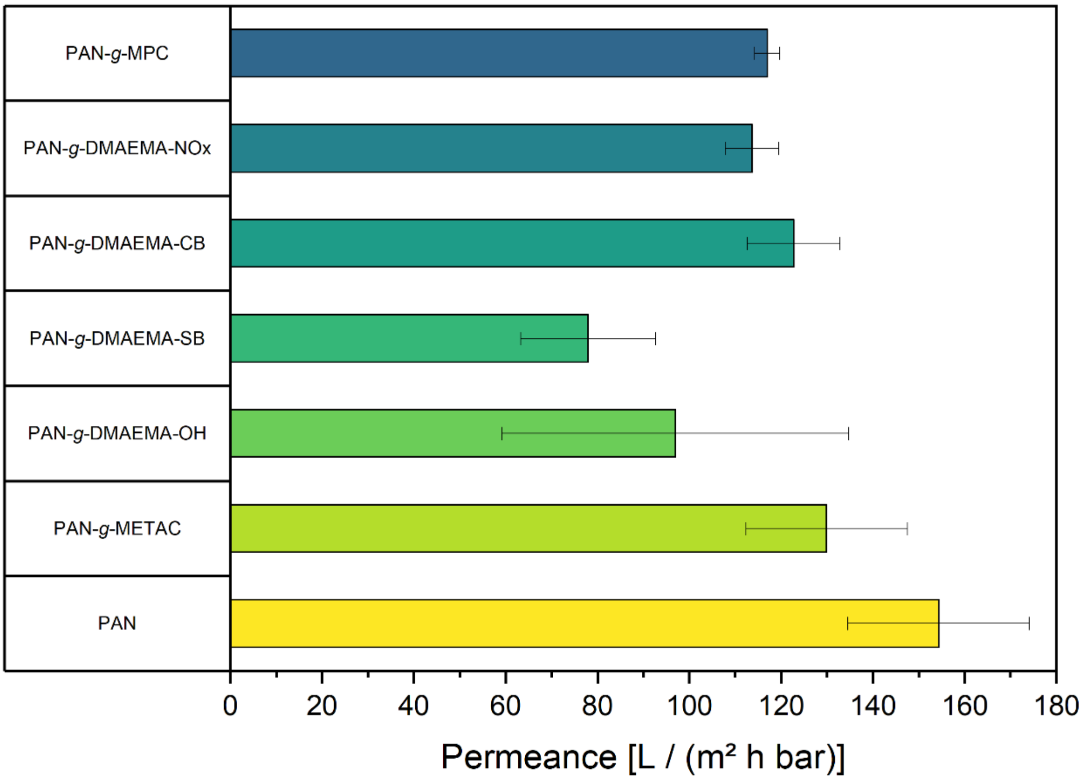

Figure 42: The pure water permeance was measured for the untreated PAN membrane and the modified membranes (METAC, DMAEMA-OH, DMAEMA-SB, DMAEMA-CB, DMAEMA-NOx, and MPC). Measurements were taken at a transmembrane pressure of 2 bar. The active membrane area was 3.14 cm².

The untreated PAN membrane exhibited the highest water permeance, at 154 L/(m^2 h bar). In contrast, the permeance decreased for all modified membranes. This decline is likely due to the introduction of different functional groups that influence the membrane's pore size, porosity, and swelling behavior, thereby changing their permeability. The membranes with PAN-*g*-DMAEMA-OH and PAN-*g*-DMAEMA-SB exhibited the lowest permeability, consistent with their low porosity. Despite the reductions observed, all membranes exhibited structural integrity and functional filtration behavior.

Zeta potential analysis was conducted to assess the charge of the formed layer on the surface, which is a crucial factor in antifouling performance and membrane interactions. The zeta potential measurements reveal significant differences in surface charge between the unmodified PAN membrane and the modified membranes. Figure 43 shows the zeta potentials for pristine PAN and the modified membranes.

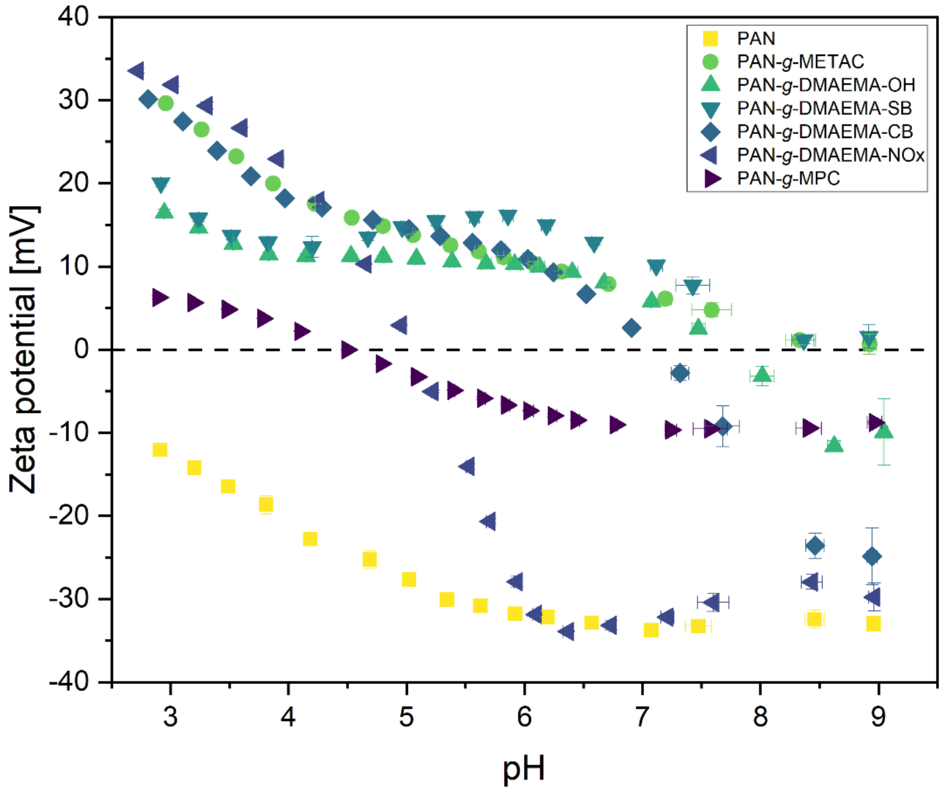

Figure 43: Zeta potential measurements of pristine PAN and PAN modified with METAC, DMAEMA-OH, DMAEMA-SB, DMAEMA-CB, DMAEMA-NOx and MPC.

The unmodified PAN membrane exhibits zeta potential values ranging from -12.05 mV to -33.01 mV across a pH range of 3 to 9. This negative charge results from the adsorption of hydroxyl ions onto the membrane surface. In contrast, all modified membranes display more positive values compared to unmodified PAN. PAN-*g*-METAC remains positively charged over the entire pH range, with a zeta potential ranging from 29.78 mV to 0.35 mV, which can be attributed to the presence of the positively charged nitrogen atom.

Similarly, PAN-*g*-DMAEMA-SB exhibits a positive zeta potential between 19.58 mV and 1.33 mV. This behavior deviates from literature reports, which indicate that sulfobetaine groups generally display negative zeta potential across all pH values.[159] A possible explanation for this discrepancy is the elimination of the sulfobetaine structure, leading to the formation of vinylsulfonate and a positively charged ammonium group. To test this hypothesis, a homopolymer of DMAEMA was synthesized and reacted with 2-bromoethanesulfonate. The reaction conditions were the same as for post-functionalization. NMR analysis confirmed the elimination reaction, resulting in the formation of vinylsulfonate (Figure A21). The vinylsulfonate could also have been formed by the elimination of 2-bromoethanesulfonate in aqueous solution at elevated temperature. Carboxybetaines with a C2 spacer have been reported to be unstable, existing in equilibrium with the ammonium acrylate salt formed through elimination.[160] In literature, this was not observed for C2 sulfobetaines. Further investigations of other post-modifications revealed no similar elimination products.

PAN-*g*-DMAEMA-NOx starts with a zeta potential of 33.18 mV and reaches its isoelectric point at pH 5.0, after which it becomes negative, reaching a potential of -30.46 mV. The *N*-oxide remains protonated above the isoelectric point, and its transition to a negative zeta potential aligns well with the pK_a of trimethylamine *N*-oxide (TMAO), which is approximately 4.7. This suggests that the change in protonation state is directly reflected in the zeta potential measurements.

PAN-*g*-DMAEMA-CB exhibits a starting zeta potential of 30.20 mV, reaching its isoelectric point at pH 7.1 before becoming negative at -24.0 mV. The carboxybetaine modification results in a positive charge at low pH due to protonation of the carboxylate group. At higher pH values, deprotonation occurs, leading to a decrease in zeta potential and a negative charge.

PAN-*g*-DMAEMA-OH starts at 16.45 mV, with an isoelectric point at pH 7.68, and becomes negative down to -10.15 mV at higher pH values. The consistently positive zeta potential across a broad pH range is attributed to the presence of a stable ammonium cation.

PAN-*g*-MPC displays a distinctly different behavior compared to the other modifications. It starts with a zeta potential of 5.7 mV, reaches its isoelectric point at pH 7.68, and becomes negative at -8.93 mV. Unlike the other modifications, PAN-*g*-

MPC remains mostly negative across the entire pH range, which aligns with expectations based on its zwitterionic structure. Overall, the results confirm that each modification introduces distinct surface charge properties. The successful shifts in zeta potential across different modifications further indicate that the functionalization process was effective and led to the expected chemical changes on the membrane surface. However, the magnitude of the charge effects cannot be directly compared due to differences in grafting efficiency as mentioned before.

6.1.2 Dye adsorption

Acid orange 7 and methylene blue were used as model substances to evaluate the dye adsorption properties of the modified membranes. Acid orange 7 is an anionic azo dye containing a sulfonate group, while methylene blue is a cationic phenothiazine dye with a positive charge delocalized over the sulfur and nitrogen atoms (Figure 44). These structural differences allow for the investigation of selective dye interactions with the membrane surface. To assess adsorption behavior, a static dye adsorption test was first performed, followed by measurements in the dead-end filtration mode. Static dye adsorption serves as an indirect method to determine surface charge, complementing the zeta potential analysis. By examining the extent of dye uptake, valuable insights can be gained into the electrostatic interactions between the modified membrane surfaces and the charged dye molecules.

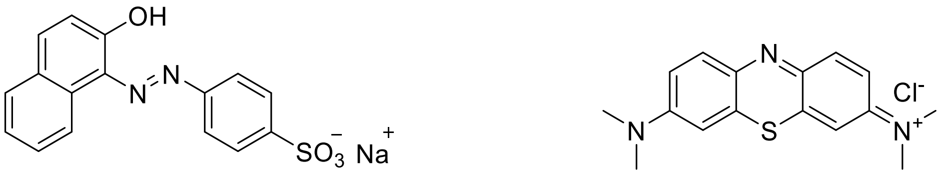

Acid orange 7

Methylene blue

Figure 44: Chemical structures of the anionic azo dye acid orange 7 and the cationic phenothiazine dye methylene blue.

Membrane samples with a diameter of 2.0 cm were immersed in a 50 µM acid orange 7 solution or 25 µm methylene blue solution adjusted to pH 7.4. The samples were incubated under static conditions for seven days to allow equilibrium adsorption. After incubation, the residual dye concentration in the solution was determined by measuring the absorbance, providing an indirect measure of the dye uptake by each membrane type. The results clearly show that the adsorption of acid orange 7 dye is influenced by various membrane modifications (Figure 45).

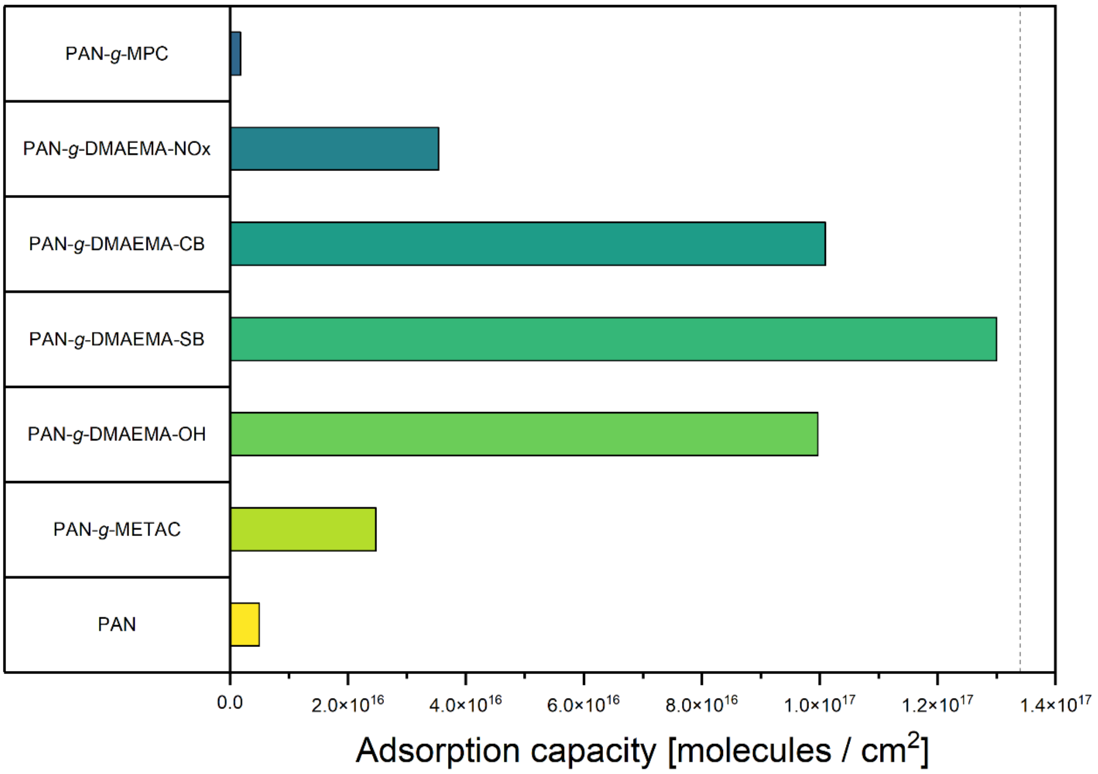

Figure 45: Acid orange 7 adsorption capacity of pristine PAN and PAN modified with METAC, DMAEMA-OH, DMAEMA-SB, DMAEMA-CB, DMAEMA-NOx and MPC. The membranes, each with a diameter of 2.0 cm, were placed in a 50 µM acid orange 7 solution at pH 7.4 and incubated for 7 days before measuring the absorbance. The dotted line represents the maximum adsorption capacity.

Pristine PAN exhibits low adsorption, which can be attributed to electrostatic interactions. Due to the negative zeta potential of the PAN membrane and the negative charge of the dye, adsorption is hindered.

The PAN-*g*-DMAEMA-SB membrane exhibits the highest adsorption of acid orange 7, which can be attributed to several factors. First, at pH 7.4, it exhibits the highest zeta potential of all the samples tested, *i.e.*, it is the most positive. This results in strong electrostatic interactions between the membrane's positively charged surface and the azo dye's negative charge. Another influencing factor is the presence of unconverted tertiary amines in the polymer. At pH 7.4, these amines become protonated and contribute to the positive surface charge. This explains why a positive zeta potential is measured despite the zwitterionic structure of sulfobetaine, which is formally electrically neutral. Static dye adsorption is an indirect method used to evaluate the surface charge accessible to the solvent. The high adsorption capacity of PAN-*g*-DMAEMA-SB indicates that a large amount of polymer has been immobilized on the membrane surface. Additionally, permeation and porosity measurements indicate that the sulfobetaine modified membrane exhibits the lowest water permeability and porosity. This finding supports the hypothesis that this membrane was functionalized with the greatest amount of polymer compared to the other modifications. Consequently, a greater surface area is available for dye binding, explaining the high adsorption performance.

Both PAN-*g*-DMAEMA-CB and PAN-*g*-DMAEMA-OH exhibit comparatively high adsorption of the azo dye acid orange 7. Both modifications have a positive zeta potential at pH 7.4, with that of PAN-*g*-DMAEMA-OH being slightly higher. Theoretically, carboxybetaine modification should show little or no dye adsorption due to its zwitterionic nature. The polymers net charge is neutral. However, the observed adsorption can be explained by the presence of unreacted tertiary amines that are protonated under physiological conditions, thereby contributing to the positive surface charge. PAN-*g*-DMAEMA-OH contains an ammonium functional group, which is also positively charged at neutral pH. Therefore, stronger dye adsorption would be expected compared to PAN-*g*-DMAEMA-CB. Nevertheless, the adsorption performance of both modifications is similar. This suggests that PAN-*g*-DMAEMA-OH exhibits more pronounced swelling behavior due to its hydrophilic hydroxy groups. This swelling could reduce the effective surface area for dye binding, resulting in a comparable adsorption capacity despite the higher charge. Lower permeability and porosity values for this modification support this assumption.

The PAN-*g*-DMAEMA-NOx modification exhibits significantly lower adsorption of acid orange 7 than other derivatives. This low adsorption is consistent with the *N*-oxide derivative's chemical structure. Due to its zwitterionic nature, the polymer has an almost neutral net charge at pH 7.4. However, in this case, it is a fully oxidized form of DMAEMA, in which the tertiary amines have been almost entirely converted to *N*-oxide groups. Consequently, there are hardly any protonatable nitrogen centers remaining that could generate a positive surface charge. The zeta potential measurement confirms this, as PAN-*g*-DMAEMA-NOx exhibits a negative zeta potential at pH 7.4. This results in an electrostatic repulsion between the negatively charged membrane surface and the anionic dye acid orange 7. The low dye binding can therefore be attributed mainly to this electrostatic repulsion. The low adsorption amount that is nevertheless detectable could be explained by non-specific interactions, such as van der Waals forces or hydrophobic effects. However, these factors play a minor role and do not result in significant dye retention.

Contrary to expectations, the PAN-*g*-METAC membrane exhibits low adsorption of the anionic dye acid orange 7, despite having the second highest zeta potential among the examined samples at pH 7.4. Theoretically, a higher zeta potential favors stronger electrostatic attraction to negatively charged dyes. This discrepancy suggests that either a small amount of polymer was immobilized during the direct polymerization of the METAC on the PAN surface or the graft density is significantly lower than in other modifications.

As expected, the PAN-*g*-MPC membrane exhibits the lowest adsorption of the anionic dye acid orange 7. At pH 7.4, the membrane exhibits slightly negative zeta potential, resulting in electrostatic repulsion between the membrane surface and the negatively charged dye. These interactions significantly inhibit adsorption.

The modified membranes PAN-*g*-DMAEMA-SB, PAN-*g*-DMAEMA-CB, and PAN-*g*-DMAEMA-OH show great potential for removing anionic impurities. Their positive zeta potentials at neutral pH and the strong adsorption of the model dye acid orange 7 indicate effective electrostatic interactions. For example, these materials could therefore be used specifically for the separation of anionic drug residues such as diclofenac or naproxen from drinking water. In contrast, PAN-*g*-MPC exhibits very low adsorption and a near neutral zeta potential, indicating pronounced antifouling properties. This membrane modification is therefore particularly suitable for applications where minimal interaction with dissolved substances is desired, for example in prefiltration or to improve the long-term stability of membrane systems.

The membranes were tested under realistic, dynamic filtration conditions. For this purpose, they were placed in an Amicon stirring cell with a membrane diameter of 2.0 cm and a constant pressure load of 1 bar. Filtration was carried out using a 50 µM solution of acid orange 7 or a 25 µM solution of methylene blue at pH 7.4. The conducted experiment aimed to evaluate the mechanical stability of the modified membranes under pressure and to determine if the dyes were adsorbed and effectively retained on the surface. Additionally, it was examined whether the adsorption tendencies observed in static tests could be confirmed under dynamic conditions (Figure 46).

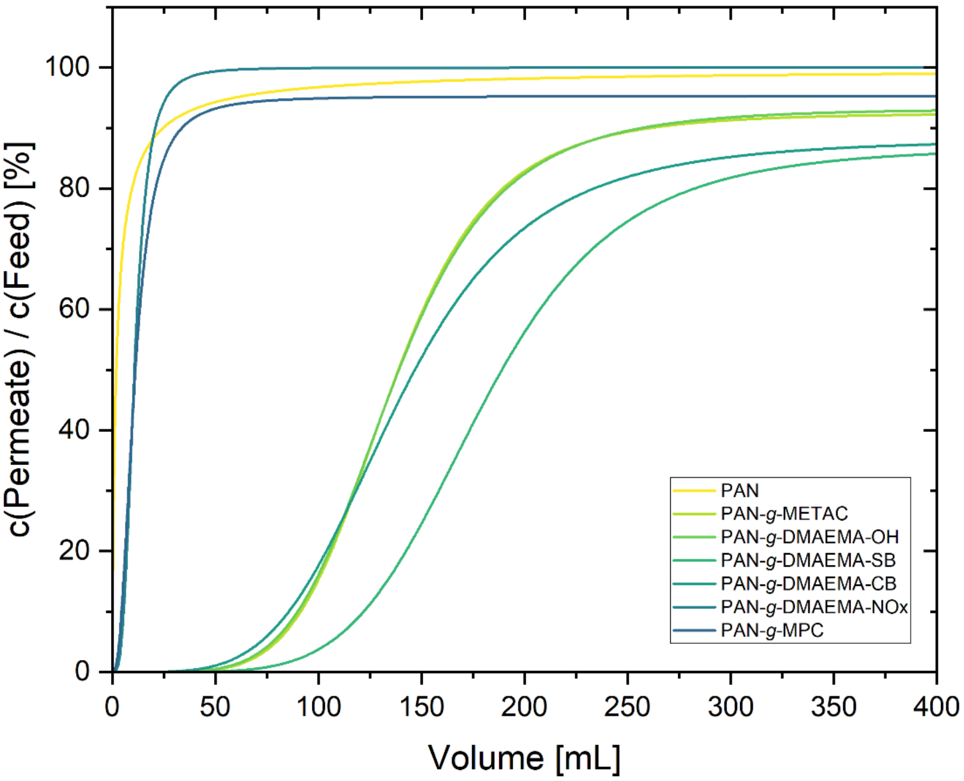

Figure 46: Dynamic dye adsorption in dead-end mode of acid orange 7 by pristine PAN and PAN modified with METAC, DMAEMA-OH, DMAEMA-SB, DMAEMA-CB, DMAEMA-NOx, and MPC. Membranes (diameter: 2.0 cm) were exposed to a 50 µM dye solution at pH 7.4 in an Amicon stirring cell operated at a constant pressure of 1 bar.

Under dynamic filtration conditions, unmodified PAN, PAN-*g*-DMAEMA-NOx, and PAN-*g*-MPC show no significant retention of acid orange 7, as expected. The dye permeates completely through the membrane. The concentration in the feed stream is roughly the same as in the permeate. Remarkably, a small amount of dye binding was still observed in the static adsorption tests with the *N*-oxide derivative. However, this behavior disappears completely under dynamic conditions, indicating that the adsorption in the static tests was based solely on weak, non-specific interactions. The lack of retention in flow mode thus confirms that there is no stable interaction between the dye and the membrane surface.

As expected, the PAN-*g*-METAC, PAN-*g*-DMAEMA-CB, and PAN-*g*-DMAEMA-OH membranes exhibit significant uptake of the anionic dye acid orange 7. These membranes reach their adsorption capacity after approximately 50 mL. Subsequently, the excess dye passes through the membrane and appears in the permeate. An interesting observation was made with the PAN-*g*-METAC membrane. Although a low dye uptake was observed in static tests, the membrane showed significant retention of acid orange 7 under dynamic conditions. This suggests that dynamic filtration tests offer a more accurate representation of the interactions between the dye and the membrane surface than static adsorption tests.

The PAN-*g*-DMAEMA-SB membrane has the highest adsorption capacity of the dye acid orange 7. Maximum adsorption is achieved at approximately 100 mL, after which the dye appears in the permeate. These results align with expectations, confirming the previously observed static adsorption data and the membranes high positive zeta potential at pH 7.4. The dominant mechanism for dye binding is the strong electrostatic interaction between the cationic surface and the anionic dye.

Subsequently, static and dynamic adsorption with methylene blue was performed (Figures 47–48). It was expected that the results will be largely reversed for the respective membrane modifications compared to acid orange 7.

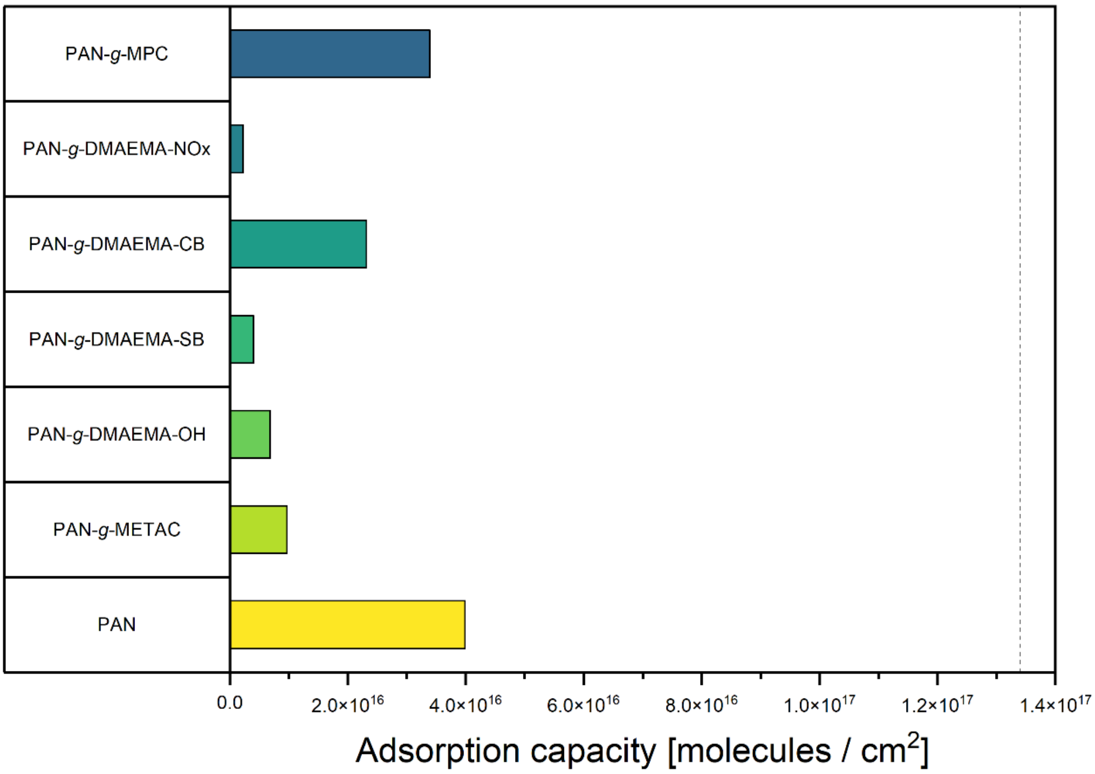

Figure 47: Methylene blue adsorption capacity of pristine PAN and PAN modified with METAC, DMAEMA-OH, DMAEMA-SB, DMAEMA-CB, DMAEMA-NOx and MPC. The membranes, each with a diameter of 2.0 cm, were placed in a 25 µM methylene blue solution at pH 7.4 and incubated for 7 days before measuring the absorbance. The dotted line represents the maximum adsorption capacity.

The highest methylene blue adsorption amounts were observed with unmodified PAN and PAN-*g*-MPC. Both membranes have a negative zeta potential at pH 7.4, favoring electrostatic attraction with the cationic dye. However, the total amount of dye adsorbed is significantly lower than that of the anionic dye acid orange 7. These findings suggest that interactions between the membrane surfaces and methylene blue are weaker, or that the binding capacity for cationic dyes is limited.

PAN-*g*-METAC, PAN-*g*-DMAEMA-SB, PAN-*g*-DMAEMA-OH, PAN-*g*-DMAEMA-CB and PAN-*g*-DMAEMA-NOx show only negligible adsorption of the cationic dye methylene blue. This behavior is expected for PAN-*g*-METAC, PAN-*g*-DMAEMA-SB, and PAN-*g*-DMAEMA-OH, as all three modifications exhibit a positive zeta potential at pH 7.4, which promotes electrostatic repulsion with the cationic dye. Notably, despite having a negative zeta potential at pH 7.4, PAN-*g*-DMAEMA-NOx exhibits no significant dye adsorption. The results suggest an alternative mechanism is at work. Studies have shown that polymer-bound *N*-oxides exhibit pronounced surface hydration largely independent of salt concentration. This strong hydrate shell distinguishes *N*-oxides from other polyzwitterions, whose properties depend heavily on ionic conditions. The dense water shell around the surface could effectively prevent dye molecule adsorption, thus explaining the observed behavior.

In summary, it can be concluded that the modified membranes investigated exhibit only a low affinity for positively charged contaminants such as methylene blue. This suggests that the surface modifications, particularly those involving zwitterionic or positively charged functional groups, effectively suppress the adsorption of cationic substances. This property could be advantageous in applications where selective rejection of positively charged molecules is desired.

In dynamic adsorption, only the unmodified PAN and the PAN-*g*-MPC show low uptake of the cationic dye methylene blue. Adsorption capacity is reached after about 15 mL for PAN and 5 mL for PAN-*g*-MPC, respectively. No significant adsorption of methylene blue was observed for any of the other membranes examined, including PAN-METAC, PAN-*g*-DMAEMA-SB, PAN-*g*-DMAEMA-OH, PAN-*g*-DMAEMA-CB and PAN-*g*-DMAEMA-NOx.

A remarkable observation is that the dye does not fully appear in the permeate rather, it accumulates in the feed reservoir. This means the adsorption curve never returns to 100%, indicating the feed stream is more concentrated than the permeate. This behavior can be explained by two physicochemical effects: concentration polarization and the Donnan effect.

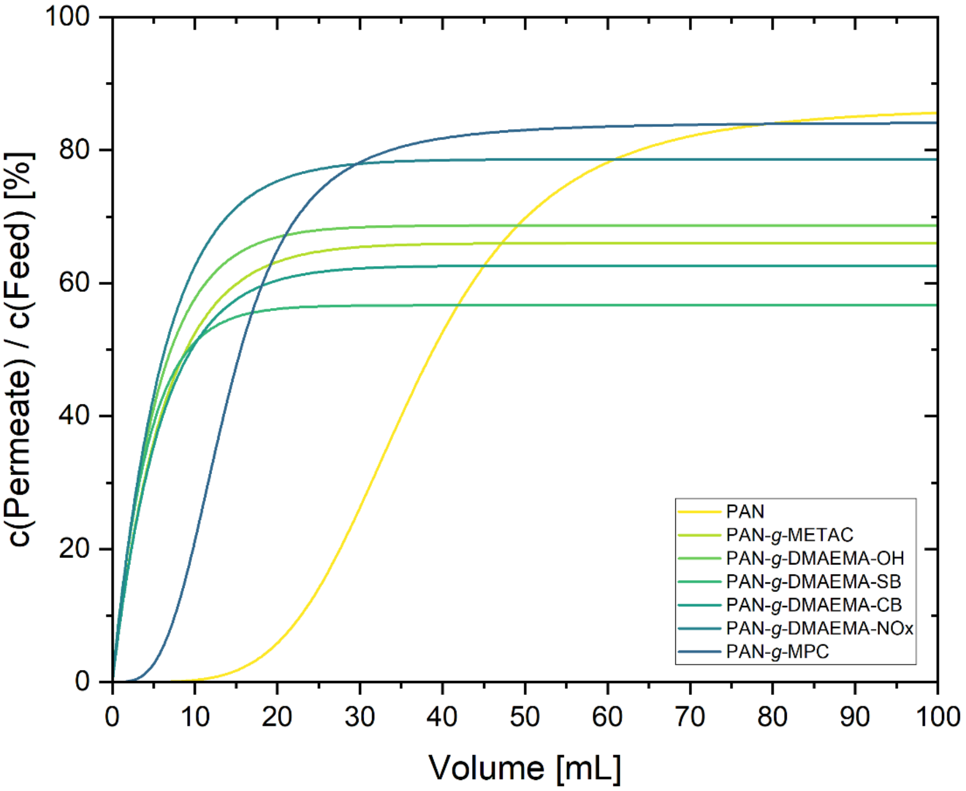

Figure 48: Dynamic dye adsorption in dead-end mode of methylene blue by pristine PAN and PAN modified with METAC, DMAEMA-OH, DMAEMA-SB, DMAEMA-CB, DMAEMA-NOx, and MPC. Membranes (diameter: 2.0 cm) were exposed to a 25 µM dye solution at pH 7.4 in an Amicon stirring cell operated at a constant pressure of 1 bar.

Concentration polarization is the phenomenon in which dissolved substances accumulate on the membranes surface during filtration because the membrane retains them while the solvent passes through. A concentration gradient is created, with a higher concentration of the dye directly at the membrane surface than in the rest of the feed.[65] Such a gradient can lead to local saturation, which reduces permeate flow. The effect was also observed in the experiment. Employing cross-flow filtration instead of dead-end filtration significantly reduces concentration polarization. The reduction occurs because the cross-flow generated along the membrane surface minimizes boundary layer formation. Increased flow velocity also promotes turbulence at the membrane surface, minimizing the adsorption of dissolved substances near the membrane and improving the performance of the membrane system.

Additionally, the Donnan effect is significant. It describes the electrostatic repulsion or attraction of ions to selectively charged membrane surfaces. Since many modified membranes have a positive zeta potential at pH 7.4, cationic dyes, such as methylene blue, are electrostatically repelled. This repulsion prevents effective adsorption and reduces transport through the membrane. This is why methylene blue does not appear completely in the permeate despite the lack of adsorption.

Overall, the results show that the membranes examined, especially those with positive surface potential, hardly interact with cationic dyes. At the same time, they illustrate how membrane surface charge, mass transport phenomena, and electrostatic effects can influence separation performance. These properties could enable selective removal of anionic components in mixtures of positively and negatively charged impurities.

6.1.3 Phosphate and nitrate adsorption

The ability of the produced modified membranes to adsorb inorganic anions, such as orthophosphate ($H_2PO_4^-$, HPO_4^{2-}, and PO_4^{3-}) and nitrate (NO_3^-), from aqueous solutions under static conditions was evaluated. Particular attention was paid to the membranes' possible selectivity toward the respective anions, given that most modifications have a positive surface charge or zeta potential. These positive surface properties generally favor electrostatic interactions with negatively charged anions.

Although phosphate and nitrate are essential plant nutrients, their excess in surface water leads to algal bloom. This phenomenon is a major driver of eutrophication, or the gradual aging of water bodies. The excessive growth of aquatic plants that results from this process leads to oxygen depletion, damages aquatic life forms, and disrupts the ecological balance.[161]

In addition to environmental issues, nitrates pose a particular health risk. High levels of nitrate in drinking water can lead to conditions such as blue baby syndrome (methemoglobinemia), which impairs the blood's ability to carry oxygen. Nitrate can also convert into nitrosamines, which are carcinogenic. Current studies also suggest links to various types of cancer, infectious diseases, and diabetes.[162] Because of these risks, removing nitrate and phosphate from drinking water or wastewater is very important. The goal is to reduce their concentrations below the limits specified in legal guidelines before discharging the treated water into the environment.

The concentrations of nitrate and orthophosphate were determined using Spectroquant test kits. In the nitrate method, nitrate ions in sulfuric and phosphoric acid solutions react with 2,6-dimethylphenol (DMP) to form 4-nitro-2,6-dimethylphenol, which is detected photometrically. The orthophosphate method is based on the reaction of orthophosphate ions with molybdate in sulfuric acid solution to form molybdophosphoric acid. This is reduced by ascorbic acid to form phosphomolybdenum blue (PMB) and quantified photometrically. The results show that some of the functionalized membranes exhibit a low adsorption of orthophosphate or nitrate (Figure 49).

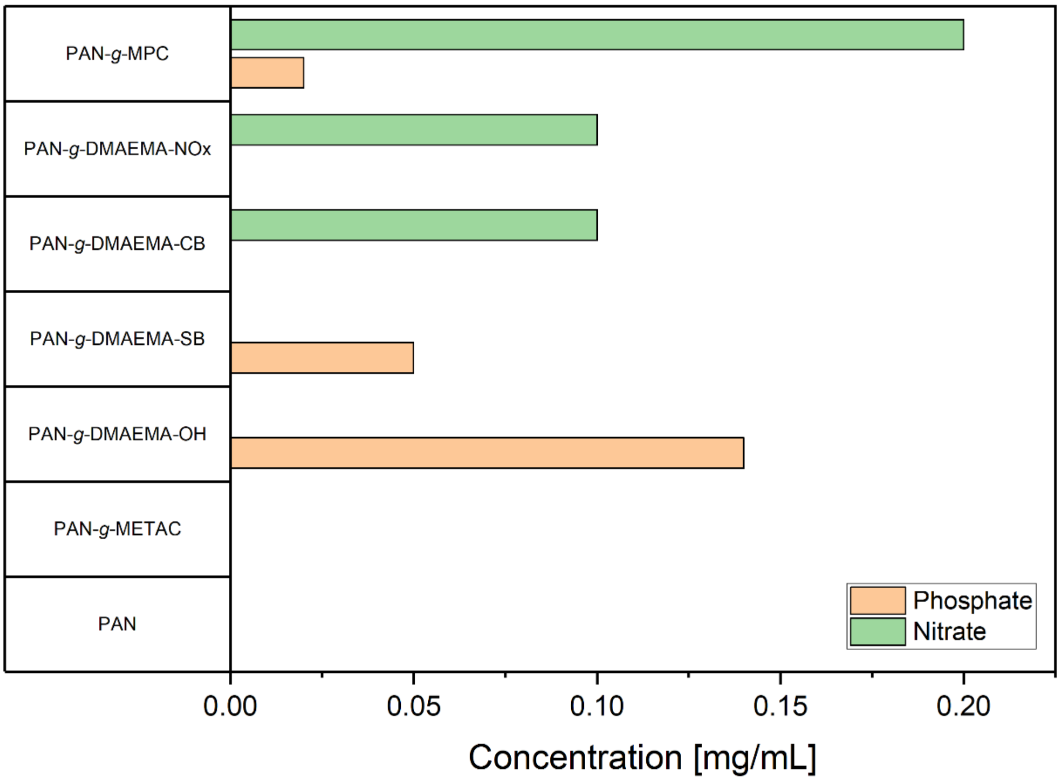

Figure 49: Static adsorption of orthophosphate ($H_2PO_4^-$, HPO_4^{2-}, and PO_4^{3-}) and nitrate (NO_3^-) on modified PAN membranes. The membranes were incubated for 72 h in solutions with a defined concentration (5 mg/L each) of the respective anions at pH 7.4. The residual concentrations were determined photometrically using Spectroquant test kits.

The measuring range of the Spectroquant test kit for nitrate and phosphate is 0.5 to 12.5 mg/L. Pristine PAN and METAC exhibited no detectable adsorption of phosphate or nitrate. A slight adsorption of nitrate was observed for PAN-*g*-DMAEMA-NOx, PAN-*g*-DMAEMA-CB, and PAN-*g*-MPC, while PAN-*g*-METAC, PAN-*g*-DMAEMA-SB, and PAN-*g*-DMAEMA-OH adsorbed small amounts of orthophosphate. This trend does not align with theoretical expectations. Specifically, cationic modifications such as PAN-*g*-METAC and PAN-*g*-DMAEMA-OH were expected to exhibit stronger adsorption of anionic species, such as nitrate or phosphate, due to electrostatic interactions.

However, the observed effects can probably be attributed to weakly bound, superficially adhering ions that do not remain on the membrane surface under dynamic filtration conditions.

Another relevant aspect is the pore size of the modified ultrafiltration membranes used. This is around 10.0 nm, while the effective diameters of phosphate (approx. 0.238 nm, PO_4^{3-}) and nitrate ions (approx. 0.179 nm, NO^{3-}) are significantly smaller.[163] As a result, it is very likely that the ions pass through the membrane unhindered without interacting with the membrane surface in any relevant way. Therefore, it would be interesting to conduct similar experiments with modified PAN nanofiltration membranes that have a pore size comparable to the size of the ions. Additionally, future studies should select an analytical method that can reliably quantify very low ion concentrations.

In addition to nitrates and phosphates, wastewater typically contains numerous other ions that compete with these anions for adsorption sites. The most significant of these are bicarbonate (HCO^{3-}), chloride (Cl^-), and sulfate (SO_4^{2-}). These ions can significantly reduce the adsorption capacity for nitrates and phosphates because they bind preferentially to the active sites of the membrane.[164] However, this effect was not relevant in the static tests performed here because the test solutions did not contain competing anions. When using this method in real wastewater systems, though, such interactions must be considered because they can significantly impact the selectivity and efficiency of adsorption.

In summary, no clear selectivity toward nitrate or phosphate was observed with the membrane modifications investigated.

6.1.4 Antimicrobial activity

The antimicrobial activity of the modified PAN membranes was investigated using a modified ASTM E2149 assay. The goal was to determine if the functionalized membrane surfaces could suppress biofilm formation and prevent biofouling and associated flux decline. The test organism was *S. aureus*, a gram-positive bacterium. The bacteria were cultured on Columbia agar for 12 h, after which they were adjusted to a target concentration of 10^5 CFU/mL in a 0.9% NaCl solution. Membrane samples, each with an area of 1.0 cm^2, were incubated in 2 mL of this bacterial suspension for 2 h at 37 °C and 300 rpm. These conditions correspond to a microbial load of 2.0 × CFU/cm^2. After incubation, 100 µL of the original suspension, as well as 1:10 and 1:100

dilutions, were spread onto Columbia agar plates and incubated for 18 h at 37 °C. Colony-forming units (CFUs) were counted to determine the bacterial survival rate. The results are shown in Figure 50.

Due to their positive surface charge, PAN-*g*-METAC and PAN-*g*-DMAEMA-OH were expected to exhibit pronounced antimicrobial effects. Most bacteria have a negative cell surface zeta potential at pH values above 2 due to the prevalence of negatively charged functional groups, such as peptidoglycan, teichoic acid, and teichuronic acid in gram-positive bacteria and lipopolysaccharides, phospholipids, and proteins in gram-negative bacteria.[165] Thus, electrostatic interactions and mechanisms, such as the polymeric spacer effect, the phospholipid sponge effect, and ion exchange processes, could contribute to the antimicrobial effect.

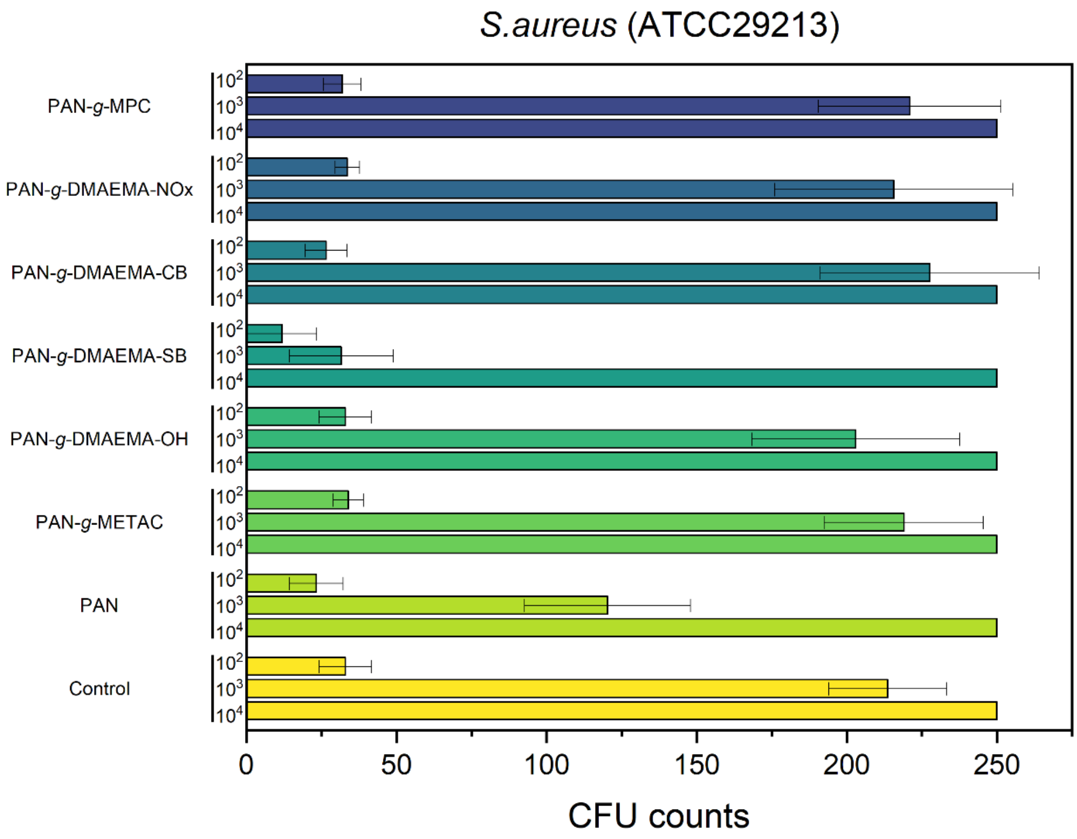

Figure 50: Determination of the antimicrobial activity of modified PAN membranes using a modified ASTM E2149 assay. The membrane samples (1.0 cm^2) were incubated in 2 mL of a *S. aureus* suspension (10^5 CFU/mL in 0.9% NaCl) for 2 h at 37 °C and 300 rpm. The colony-forming units (CFU) were then determined by plating the suspension and its dilutions on Columbia agar.

Zwitterionic functionalized membranes such as PAN-*g*-DMAEMA-SB and PAN-*g*-DMAEMA-CB should theoretically not exhibit any antimicrobial effect, as their surface charge is neutral. Interestingly, however, zeta potential measurements show that both membrane modifications exhibit a positively charged zeta potential at pH 7.4, which could nevertheless enable some electrostatic interaction with bacterial cell walls.

The results show that none of the examined membrane modifications have a significant antimicrobial effect against *S. aureus*. MURATA *et al.* postulated that a positive charge density of at least 5 × 10^{15} N^+/cm^2 is required on planar surfaces to achieve an antimicrobial effect.[166] For PAN-*g*-DMAEMA-SB, an adsorption capacity of 1.3 × 10^{17} acid orange 7 molecules per cm^2 was determined, which indirectly indicates the membrane's solvent-accessible positive charge.

However, previous results indicate that the polymer is not only on the membrane surface but also penetrates the pore structure of the PAN ultrafiltration membrane (pore diameter approximately 10 nm). This distributes the positive charge over a larger volume, reducing the effective surface charge. Since *S. aureus* is 0.5–1.5 µm in size, the bacteria cannot penetrate the pores.[167] This means that interaction is limited to the membrane surface.

Additionally, the zeta potential of various *S. aureus* strains generally falls within the range of -8 mV to -18 mV, averaging approximately -13.2 mV.[168] This negative surface charge enables electrostatic attraction to the positively charged membrane in principle. However, when interpreting the results, it should be noted that different strains sometimes exhibit widely varying surface properties, which can limit their comparability.

Another possible explanation for the lack of antimicrobial activity despite the positive zeta potential at pH 7.4, is the strong hydration of the membrane surfaces, particularly with zwitterionic modifications, such as PAN-*g*-DMAEMA-SB, PAN-*g*-DMAEMA-CB, PAN-*g*-DMAEMA-NOx, and PAN-*g*-MPC. These hydration shells may prevent direct bacterial contact with the membrane surface. This behavior is desirable in terms of antifouling properties because it inhibits the accumulation of microorganisms and minimizes flux losses due to biofouling.

To further elucidate the mechanism of action, future investigations should focus on bacterial adhesion to analyze the influence of surface properties more precisely.

6.1.5 Protein adsorption

Proteins are among the main causes of biofouling and membrane fouling, as they can lead to the formation of a cake layer on the membrane surface, which reduces permeate flow and impairs membrane performance in the long term. The aim of the present investigations was to determine whether the modified PAN membranes exhibit reduced protein adsorption due to increased surface hydration and are therefore potentially effective in preventing fouling.

Three proteins with different physicochemical properties were selected for static adsorption experiments: bovine serum albumin (BSA), lysozyme, and fibrinogen. They differ significantly in molecular weight, hydrodynamic radius, charge at pH 7.4, and isoelectric point (Table 3). The selection of these proteins is intended to evaluate the adsorption behavior towards both small and large, as well as negatively and positively charged macromolecules.

For each experiment, a membrane sample (diameter: 2.0 cm) was incubated in 2 mL of a protein solution (1 g/L in PBS buffer, pH 7.4). The samples were stored in sealed containers at 25 °C and a shaking speed of 100 rpm for 24 h to achieve adsorption equilibrium. Subsequently, the remaining protein concentration in the solution was determined by UV-Vis spectroscopy to indirectly quantify the adsorbed amount.

Table 3: Molecular weight, isoelectric point, hydrodynamic radius (R_h), dimensions, and protein charge at pH 7.4 of bovine serum albumin, lysozyme, and fibrinogen.

Protein	Molecular weight [kDa]	Isoelectric point [IEP]	R_h [nm]	Dimensions [nm x nm x nm]	Protein charge at pH 7.4
Bovine serum albumin[169, 170]	67.0	4.7	3.3	9.5 × 5 × 5	-20.5
Lysozyme[171-173]	14.3	11	1.9	3 × 3 × 4.5	+8
Fibrinogen[174-176]	340	5.8	10.7	9 × 47.5 × 6	-8

The results of the adsorption of BSA, lysozyme, and fibrinogen onto modified PAN membranes are shown in Table 4. No significant adsorption of BSA was observed for any of the examined membranes. Unmodified PAN does not adsorb BSA due to electrostatic repulsion from its negative zeta potential, supported by its hydrophilic character and smooth surface. For the zwitterionic modifications PAN-*g*-DMAEMA-SB, PAN-*g*-DMAEMA-CB, PAN-*g*-DMAEMA-NOX, and PAN-*g*-MPC, this behavior is plausible and can be attributed to a highly hydrated surface, which is characteristic of zwitterions. This hydration shell acts as a barrier to protein adsorption by preventing interaction between the protein and the membrane surface. No BSA adsorption was observed for PAN-*g*-DMAEMA-OH, either. This suggests that the hydroxyl groups create a strongly hydrated interface as well. Despite the presence of ammonium groups, this modification behaves more like polyethylene glycol (PEG), which is known for its protein-repellent properties. This interpretation is consistent with the previously observed lack of antimicrobial effects of this membrane. On the other hand, adsorption of BSA would be expected for PAN-*g*-METAC due to electrostatic interactions. At pH 7.4, BSA is negatively charged, while PAN-*g*-METAC has a positive zeta potential. Additionally, the hydrodynamic radius of BSA is significantly smaller than the pore size of the membrane (~10 nm), therefore adsorption on the surface or in the pore area could occur. One possible explanation for the lack of adsorption is a low modification density. This is supported by the comparatively low adsorption capacity toward acid orange 7, which is an indirect measure of the number of solvent-accessible positive charges. As expected, the unmodified PAN membrane, which has a negative zeta potential, also shows no adsorption of BSA, as it is also negatively charged. The resulting electrostatic repulsion prevents any significant interaction between the protein and the membrane surface.

Table 4: Static adsorption of bovine serum albumin, lysozyme, and fibrinogen on modified PAN membranes.

Membrane	Bovine serum albumin [µg]	Lysozyme [µg]	Fibrinogen [µg]
PAN	0	23	27
PAN-*g*-METAC	0	21	164
PAN-*g*-DMAEMA-OH	0	0	97
PAN-*g*-DMAEMA-SB	0	0	34
PAN-*g*-DMAEMA-CB	0	0	28
PAN-*g*-DMAEMA-NOx	0	22	46
PAN-*g*-MPC	0	0	72

The results show that lysozyme is not adsorbed by most modified membranes, or only in very small quantities. Specifically, zwitterionic modifications such as PAN-*g*-DMAEMA-SB, PAN-*g*-DMAEMA-CB, PAN-*g*-DMAEMA-OH, and PAN-*g*-MPC demonstrate no measurable adsorption. This behavior can be attributed to the highly hydrated surfaces of these modifications, which prevent protein adsorption. The unmodified PAN membrane shows low adsorption of lysozyme. The results can be explained by the electrostatic attraction between the negatively charged membrane surface and the positively charged lysozyme at pH 7.4. PAN-*g*-METAC also exhibits low lysozyme adsorption. One possible explanation is that only a small amount of METAC was immobilized on the surface. This allowed the properties of the original PAN material to predominate, resulting in an interaction similar to that of the unmodified membrane. The low adsorption by PAN-*g*-DMAEMA-NOx is also unexpected, although this modification is normally characterized by a highly hydrated surface that should prevent protein adsorption. One possible explanation is the strikingly low zeta potential of the membrane at pH 7.4, which indicates a negative surface charge and could therefore enable interactions with lysozyme.

All examined membranes show significant fibrinogen adsorption. This is especially evident in the PAN-*g*-METAC modification. The results are likely due to the surface's lower hydration compared to other modifications, which reduces protein adsorption effectiveness. Additionally, the positive surface charge of cationic modifications increases adsorption because fibrinogen is negatively charged at pH 7.4, favoring electrostatic interactions with cationic surfaces. Another decisive factor is the molecular size of fibrinogen, which is significantly larger than BSA and lysozyme. Due to its extended structure and hydrodynamic radius of 10.7 nm, fibrinogen may partially become stuck or accumulate in the membrane's pores. This could lead to higher apparent adsorption. To validate this hypothesis, further investigation of the membrane surface by AFM would be useful. An increase in surface roughness after contact with fibrinogen could indicate whether the protein is adsorbed in the pores. In addition, it should be investigated whether the adsorption is reversible. Since the present static tests do not allow any conclusions to be drawn about desorption or redissolution, a supplementary experiment with fluorescence-labeled proteins in combination with a backwashing step would be advantageous. Subsequent analyses using confocal laser scanning microscopy could visually determine whether and to what extent proteins remain on or in the membrane.

In summary, it can be said that the modified membranes show a significant antifouling effect against BSA and lysozyme under static conditions. However, to validate these results, further investigations under dynamic conditions should be carried out to confirm the behavior under more realistic application scenarios.

6.1.6 Polymer synthesis

Since many properties of the graft polymers cannot be determined directly on the surface due to their low quantity and anchoring in the membrane pores, the corresponding homopolymers were synthesized independently. These serve as model substances to evaluate the efficiency of the respective post-functionalization and the thermal stability of the modified layers. By comparing the properties of the free polymers with those of the modified membranes, conclusions can be drawn about the chemical composition and behavior of the surface modification. DMAEMA, MPC, and METAC were each polymerized in solution under an inert gas atmosphere using ammonium persulfate (APS) as a radical initiator (Figure 51).

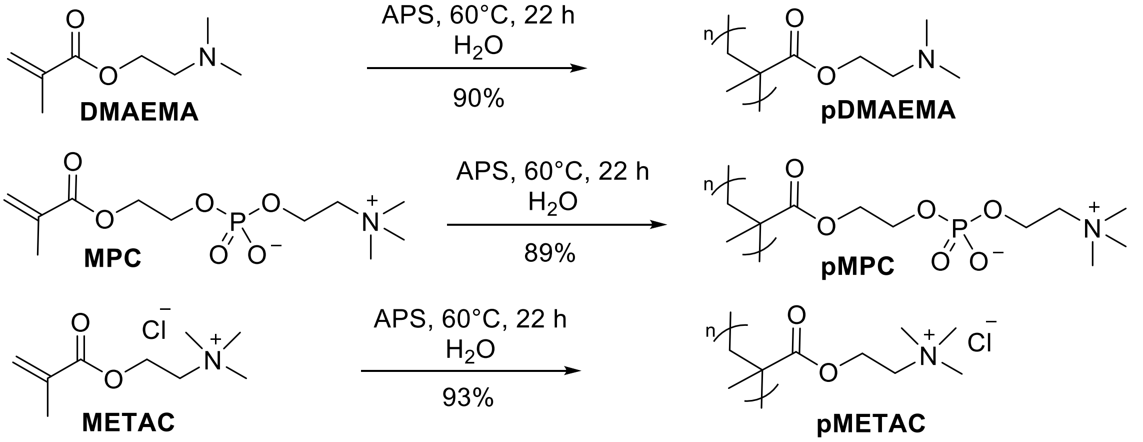

Figure 51: Polymerization of DMAEMA, MPC, and METAC in solution with APS as radical initiator.

The resulting homopolymers were then purified by dialysis using ultrapure water. A yield of 90% was achieved for pDMAEMA. Trace amounts of DMAEMA remain detectable in the ^{1}H-NMR spectrum, but the polymer itself is clearly identifiable. Repeated dialysis could help completely remove any remaining monomers. The polymerization of MPC and METAC gave 89% and 93% yield of the polymer, respectively. The corresponding ^{1}H-NMR spectra show no significant impurities, indicating a successful and clean synthesis.

To post-functionalize pDMAEMA and produce its derivatives, pDMAEMA-OH, pDMAEMA-SB, and pDMAEMA-CB, the polymer's tertiary amine was converted in a classic Menshutkin reaction (Figure 52). 2-Bromoethanol, sodium 2-bromosulfonate, and sodium chloroacetate were used as alkylating agents for this purpose. The resulting quaternary ammonium salts were purified by dialysis with ultrapure water to eliminate the unreacted reagents and byproducts. To determine the degree of functionalization, the ratio of the integrals of the tertiary to quaternary ammonium signals in the ^{1}H-NMR spectrum was evaluated. This made it possible to quantify the proportion of available tertiary amine groups that were successfully converted into quaternary groups.

The degree of functionalization of pDMAEMA-OH is approximately 80%. The remaining 20% is attributed to unreacted tertiary amine, as determined by the ^{1}H-NMR spectrum. The relatively high viscosity of the reaction solution may have impaired the reaction.

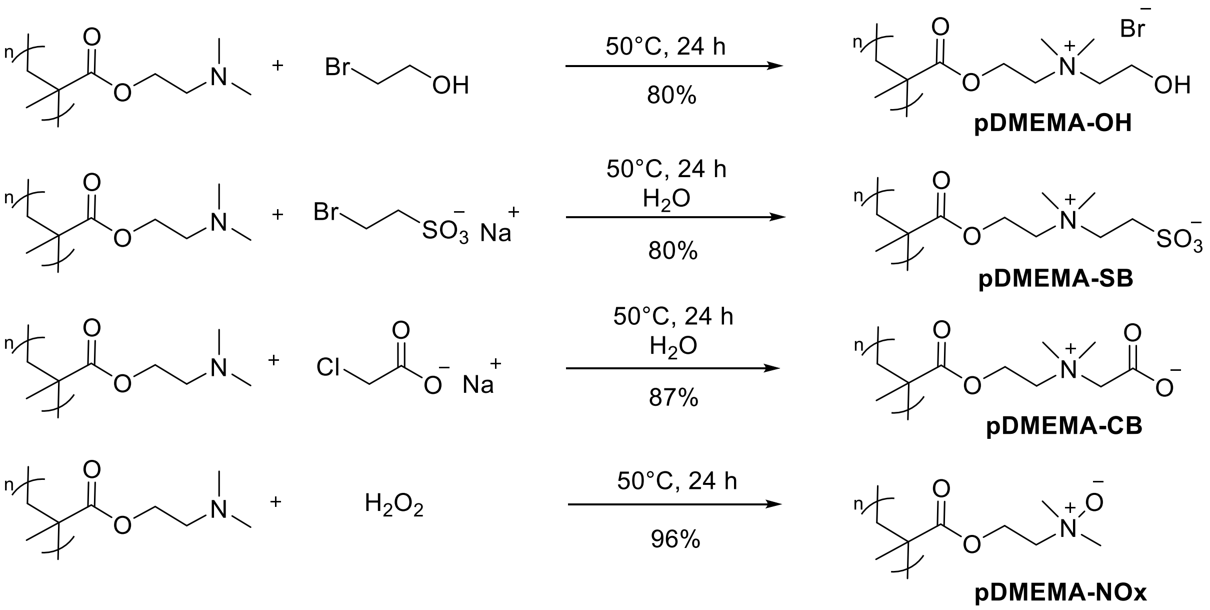

Figure 52: Post-functionalization of pDMAEMA with 2-bromoethanol, sodium 2-bromethansulfonate, sodium chloroacetate and hydrogen peroxide.

pDMAEMA-SB showed approximately 80% functionalization. Signals from a vinyl sulfonate were detected in the ^{1}H-NMR spectrum. This byproduct may have formed through the hydrolysis of the sodium 2-bromomethanesulfonate starting material or through elimination from the product. The former is considered more likely, especially at elevated temperature. Therefore, the observed degree of functionalization includes the conversion to the sulfobetaine and the formation of a protonated tertiary amine with vinyl sulfonate as the counterion. To suppress hydrolysis of the starting material and increase the selectivity of the reaction, it should be carried out in an aprotic solvent, such as DMF.

pDMAEMA-CB exhibits 87% functionalization. The remaining 13% were identified as unreacted tertiary amine in the ^{1}H-NMR. Using an aprotic solvent could increase the yield further. However, since pDMAEMA is soluble in water, it is challenging to find a suitable aprotic solvent that dissolves both reactants well.

pDMAEMA-NOx was functionalized through the oxidative conversion of the tertiary amine using hydrogen peroxide. The reaction proceeded almost quantitatively, as evidenced by a clean ^{1}H-NMR spectrum without byproducts. This indicates the oxidation was highly efficient and selective under the chosen conditions. The post functionalization of membranes should therefore have similar results.

Thermal stability was investigated by analyzing the samples pDMAEMA-OH, pDMAEMA-SB, pDMAEMA-CB, pDMAEMA-NOx and pMPC using thermogravimetric analysis (TGA). The mass loss of the materials was determined as a function of temperature to draw conclusions about their decomposition profiles and thermal stability. The aim was to evaluate how the different chemical modifications affect the thermal behavior of the polymers. The results are shown in Figure 53.

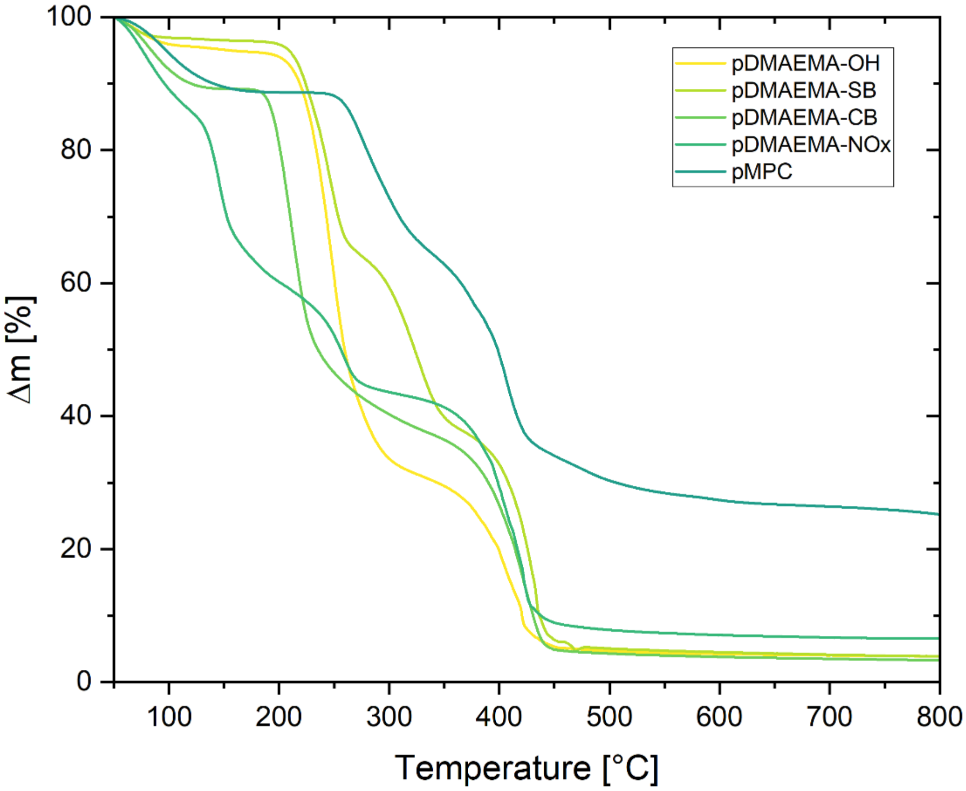

Figure 53: Thermogravimetric analysis (TGA) of the polymers pDMAEMA-SB, pDMAEMA-CB, pDMAEMA-OH, pMPC, and pDMAEMA-NOx to investigate their thermal stability and decomposition processes under a nitrogen atmosphere.

pDMAEMA-SB undergoes a multi-stage mass loss, indicating various thermal decomposition processes. The sample is thermally stable up to approximately 205 °C, which is considered the onset temperature of thermal decomposition. Between 50 °C and 204 °C, an initial mass loss can be observed, which is due to the crystal water. Between 205 °C and 262 °C, the functional groups begin to decompose, presumably eliminating the vinyl sulfonate and ester groups. In the subsequent temperature range of 263 °C to 350 °C, the polymer backbone degrades. A significant amount of mass is lost between 351 °C and 450 °C, which is attributed to the degradation of quaternary ammonium and sulfonic acid groups. Literature data is available for C3 derivative of pDMAEMA-SB.[177]

The onset of the thermal decomposition of pDMEMA-CB occurs at around 184 °C, which indicates that the polymer is thermally stable up to this temperature. In the range from 50 °C to 183 °C, an initial, slight loss of mass can be observed, which is due to the release of crystal water. Subsequently, between 184 °C and 345 °C, functional groups undergo decomposition. In this temperature range, ester groups, carboxylate groups, and parts of the polymer backbone are presumably eliminated. A further significant loss of mass occurs in the range from 345 °C to 446 °C, which can be attributed to the thermal degradation of the quaternary ammonium groups.

Thermal decomposition of pDMAEMA-OH begins at approximately 203 °C, which indicates good thermal stability up to this temperature. An initial loss of mass can be observed in the temperature range from 50 °C to 202 °C, which is attributed to the release of crystal water. Between 203 °C and 323 °C, the decomposition of functional groups occurs. During this period, hydroxyl and ester groups are likely to be eliminated, initiating the first degradation reactions in the polymer backbone. In the next section, from 324 °C to 449 °C, the tertiary ammonium groups undergo thermal degradation.

The decomposition of pMPC begins at 254 °C, and the polymer exhibits comparatively high thermal stability. An initial loss of mass can be observed in the temperature range from 50 °C to 253 °C, which is due to the removal of water. Between 254 °C and 349 °C, the ester groups are expected to decompose, and the polymer backbone is expected to break down. From 349 °C to 429 °C, thermo-oxidative decomposition of the phosphate groups occurs. This produces phosphoric acid, which forms a protective layer that delays further thermal degradation. Importantly, switching from a nitrogen atmosphere to an air atmosphere would result in the polymer-based residue undergoing complete oxidation.

The thermal decomposition of pDMAEMA-NOx begins at 124 °C, which is in good agreement with literature values.[178] It is not thermally stable compared to the other examined polymers. In the range from 50 °C to 124 °C, crystal water is first removed from the polymer. Between 125 °C and 273 °C, the elimination of the *N*-oxide functionality *via* Cope elimination and the degradation of the ester groups are expected to occur. In the subsequent phase, from 274 °C to 434 °C, the polymer backbone and the ammonium groups undergo thermal degradation.

The *N*-oxide has low thermal stability, limiting its potential applications. In contrast, phosphobetaine exhibits excellent thermal stability. Additionally, TGA results confirm the hypothesis that vinyl sulfonate forms in PAN-*g*-DMAEMA-SB. The synthesis of the homopolymers therefore provided valuable insights that would be difficult to obtain directly from the membrane surface.

6.2 Functionalization of PP membranes

In addition to their use in water treatment, nonwoven PP materials are widely applied in air filtration, such as in respiratory masks and indoor air purification systems. PP is a thermoplastic polymer that can be processed cost-effectively and offers high crystalline, good chemical resistance, low density, and adequate mechanical strength.[179] In recent years, the demand for air filter materials with antimicrobial properties has grown significantly, particularly in response to the global health crisis caused by the SARS-CoV-2 virus.[180] Although this work primarily focuses on membranes for water treatment, the developed surface modifications are also highly relevant for air filtration applications aimed at reducing airborne bacterial and viral contamination.

The PP surface was modified using a grafting method that has already proven effective in the modification of PAN. In this study, styrene-based monomers were employed to introduce specific functional groups to the surface. Three different strategies were pursued (Figure 54). The first approach aimed to achieve antimicrobial properties using the well-established monomer VBTAC and the newly synthesized monomer VBTOH. Additionally, C1 and C3 esters were investigated. These esters primarily serve as intermediates for the synthesis of carboxybetaine, but they were also tested for potential antimicrobial effects.

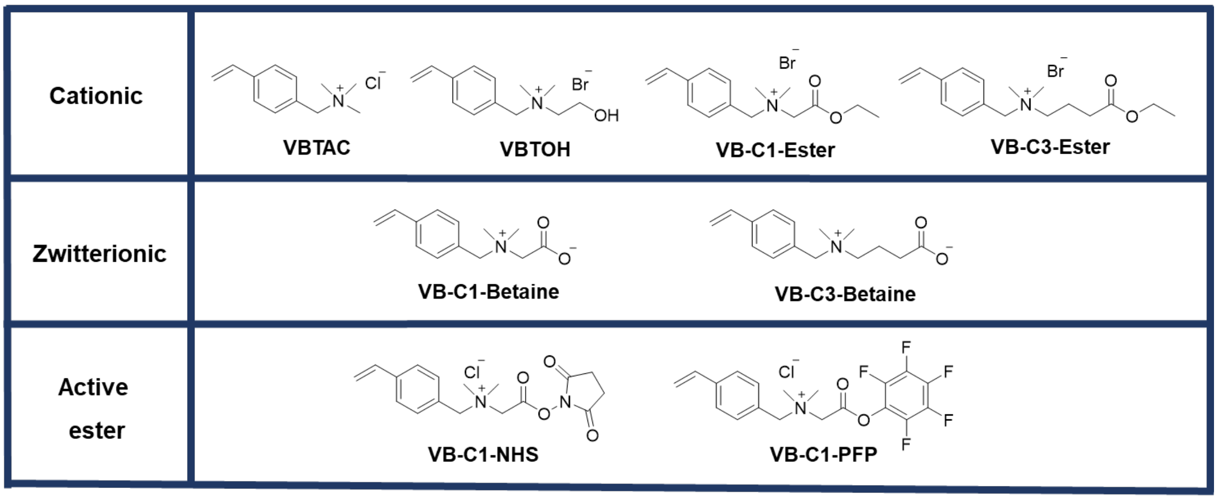

Figure 54: Chemical structures of the styrene-based cationic, zwitterionic and active ester monomers.

The second approach focused on imparting antifouling properties by developing novel styrene-based carboxybetaine compounds, differing in the spacer length between the ammonium group and the carboxylate moiety (C1 and C3). These structures are designed to prevent protein and microorganism adsorption through steric repulsion and strong surface hydration.

The third approach focused on enabling further surface functionalization (Figure 55). To achieve this, carboxybetaine molecules were converted into reactive esters, such as NHS or PFP esters, to allow covalent attachment of antimicrobial peptides (AMPs) or other bioactive compounds. This strategy can be implemented in two ways: either by direct graft polymerization of active ester monomers, or *via* a two-step process in which carboxybetaine is first grafted onto the surface and subsequently converted into reactive esters through an EDC-mediated reaction. A key advantage of this approach lies in the fact that any excess, unreacted active esters hydrolyze after functionalization, reverting to antifouling carboxybetaine groups. This enables the creation of membrane surfaces with dual functionality, combining antimicrobial activity with antifouling properties.

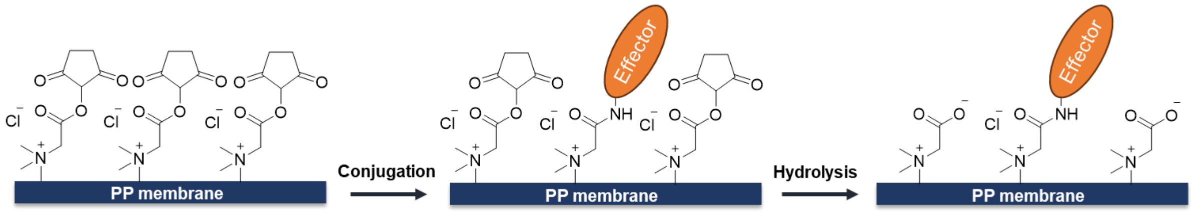

Figure 55: Two-step functionalization process: Carboxybetaine is converted into active esters to couple bioactive molecules such as AMPs. Unreacted esters hydrolyze back to carboxybetaine, creating a surface with antimicrobial and antifouling properties.

6.2.1 Synthesis

Vinylbenzyl chloride (VBC) was used as the starting material to synthesize VBTOH (Figure 56). In a nucleophilic substitution reaction, VBC was first converted to VBDMA with dimethylamine and potassium carbonate as the base. The reaction gave 67% VBDMA. While the conversion was nearly quantitative, it is likely that not all the product was recovered from the column during chromatography. Then, VBDMA underwent alkylation with 2-bromoethanol in a Menshutkin reaction to give 96% VBTOH. This monomer's design is based on combining the antimicrobial properties of QACs with the antifouling properties of a PEG-like OH group.

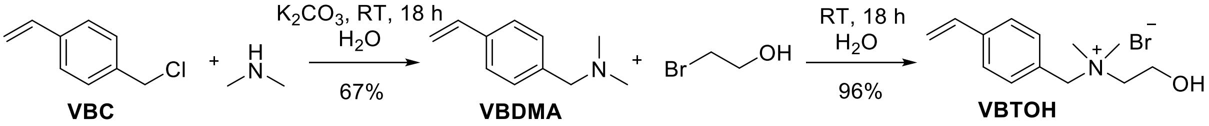

Figure 56: Synthesis of VBTOH monomer with antimicrobial and antifouling properties.

When designing styrene-based carboxybetaine compounds with antifouling properties, it is important to consider key molecular parameters such as hydrogen bonding, net charge, and dipole moment. In particular, the spacing between the ammonium and carboxylate groups significantly influences the antifouling properties. Varying the spacer length only slightly affects the hydration of the ammonium group but significantly impacts the hydration of the carboxylate group. Notably, significant differences in hydration are observed between C1 and C3 carboxybetaine.[181] C1 betaine exhibits superior antifouling activity despite lower hydration than its C3 analogues. Compared to C3, C1 has a lower dipole moment, leading to reduced electrostatic interactions with fouling molecules. In addition to protective surface hydration, the dipole moment and net charge of the surface are also important factors contributing to antifouling properties.[149] C2 carboxybetaine compounds are not suitable for practical applications because they are thermodynamically unstable. They tend to undergo Hofmann elimination at high temperatures and pH values. This results in the formation of an ammonium acrylate salt, with which they exist in equilibrium.[160] Another important aspect is that, unlike sulfobetaines, carboxybetaines do not exhibit self-aggregation. Consequently, they do not exhibit temperature- or salt-dependent behavior. The C1 and C3 betaines were synthesized in two steps (Figure 57). First, the tertiary amines of VBDMA were alkylated with a *α*-bromoethyl ester using a Meshutkin reaction.

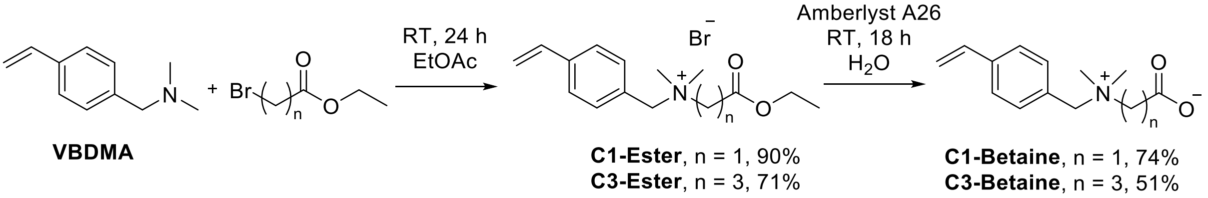

Figure 57: Synthesis of styrene based C1 and C3 carboxybetaines.

The C1 and C3 esters were then synthesized with yields of 90% and 71%, respectively. As these are QAC compounds, their antimicrobial properties were also tested later. The esters were hydrolyzed with a hydroxide-loaded anion exchange resin, Amberlyst A26, to release the C1 and C3 betaines. Amberlyst A26 makes it possible to remove salts directly, which would otherwise be difficult. Additionally, deprotection is sensitive to the amount of resin and reaction time used otherwise, polymerization may occur. This resulted in yields of 74% and 51%, respectively. Not all of the carboxybetaine could be recovered. Additionally, the larger dipole of the C3 carboxybetaine leads to a stronger interaction with the resin, explaining the moderate yield. This reaction is only suitable for large-scale production to a limited extent. Nevertheless, C3 carboxybetaine was primarily synthesized as a reference substance due to the expected difference in its antifouling properties compared to C1. The active ester monomers of C1 carboxybetaine were synthesized from C1 betaine through a reaction with EDC and NHS (Figure 58). However, no product was obtained, as uncontrolled polymerization occurred instead. One possible explanation for this behavior is that the neighboring quaternary ammonium group pulls electron density away from the carboxyl group, resulting in a less electron-rich and more reactive carbonyl group. This trend is also evident in the significantly different pK$_a$ values of the betaine groups (pK$_a$ ≈ 1.84)[182] compared to acetic acid (pK$_a$ ≈ 4.75)[183]. Similar behavior has been previously reported for betaine esters, which undergo significantly accelerated hydrolysis under neutral or slightly basic conditions compared to conventional esters.[184] Therefore, it can be deduced that C1 carboxybetaine-based active ester monomers are not bench-stable. Thus, derivatization of carboxybetaine *via* EDC/NHS chemistry is only possible *in situ*.

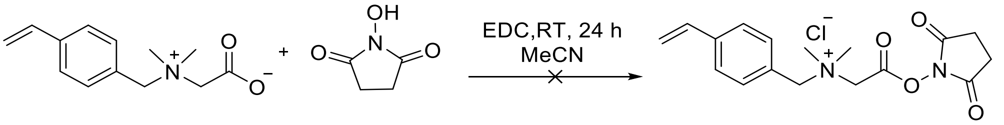

Figure 58: Synthesis attempt of active ester VB-C1-NHS.

In addition to NHS esters, alternative activating groups such as *N*-hydroxyphthalimide (NHPI), *p*-nitrophenol (PNP), trichlorophenol (TCP), and 1,1′-carbonyldiimidazole (CDI) were also investigated. These also failed to produce stable, isolatable active esters. These findings underscore the reactivity and instability of C1 carboxybetaine esters. TFP- and PFP-based active esters exhibit reactivity similar to that of classic NHS esters but demonstrate significantly greater hydrolysis stability.[185] To take advantage of this property for functionalization, the synthesis route was adapted (Figure 59). Starting with dimethylglycine, the corresponding active ester was produced with a very high yield using EDC and pentafluorophenol (PFP).

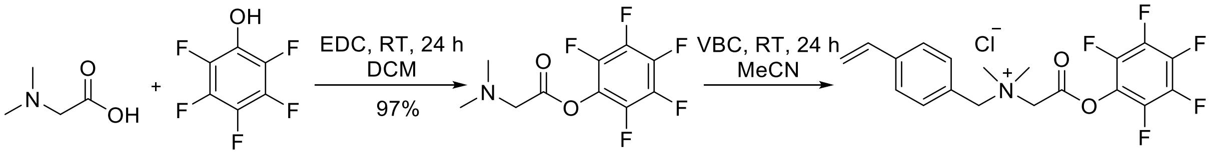

Figure 59: Synthesis attempt of active ester VB-C1-PFP.

In the second step, the tertiary amine of the dimethylglycine PFP ester underwent alkylation *via* a Menshutkin reaction. The resulting product was an orange-colored, viscous oil that was identified using both ^{1}H-NMR and mass spectrometry. However, isolation in pure form was not possible. Nevertheless, the product proved to be sufficiently stable. This approach was not pursued further due to the complex synthesis. Instead, it was decided to generate active esters exclusively *in situ* for future applications in the field of bioconjugation.

6.2.2 UV-Grafting

PP is significantly more difficult to modify than PAN due to its chemical inertness. However, successfully functionalizing PP membranes using UV-initiated graft polymerization would greatly expand the potential applications of this method, especially with regard to cost-effective filter materials.

In this study, only styrene-based monomers were employed for the modification process. Although styrene derivatives are less reactive than methacrylates, their aromatic structure enables them to form stable polymer networks. This stability is supported by π-π interactions in the polymer backbone, which can lead to robust, well-adhering layers. However, the low biodegradability of polystyrene poses an ecological problem.[186] Nevertheless, investigating the compatibility of styrene monomers with UV-induced graft polymerization is of fundamental interest. A direct grafting approach was chosen for the modification (Figure 60).

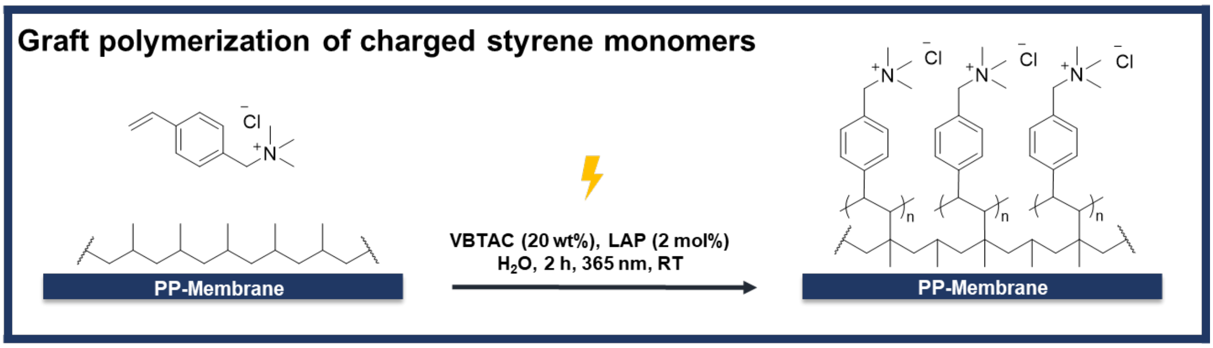

Figure 60: The reaction conditions for UV-induced graft polymerization on PP used for hydrophilic monomers, such as VBTAC.

The target monomers were either prepared (*e.g.* carboxybetaine monomers), or the monomers were commercially available (*e.g.* VBTAC). Post-functionalization would not be economically or chemically feasible in these cases. To carry out the graft polymerization, the PP nonwoven membranes were cut into 1 cm^2 pieces and placed in a solution of photoinitiator and monomer. The solution was purged with nitrogen for 20 min to ensure a radical reaction in the absence of oxygen. This was followed by UV irradiation at 365 nm for 2 h in a photoreactor. After irradiation, the membranes were thoroughly washed to remove non-covalently bound polymer.

6.2.3 Membrane characterization

To verify the success of the UV-induced polymerization, IR spectra of the modified materials were recorded. The introduced functional groups can be identified because of characteristic vibrations and in comparison, with the unmodified PP membrane. Figure 61 shows the IR spectra of the styrene-based polymer brushes.

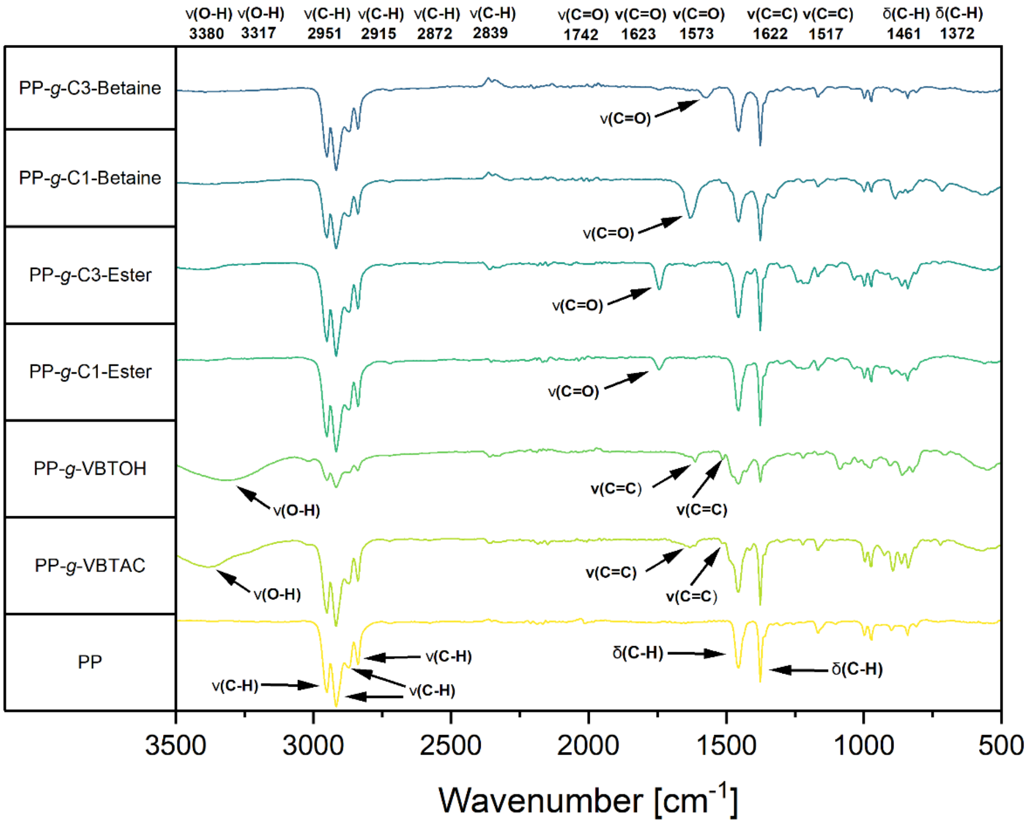

Figure 61: ATR-FTIR of unmodified PP membranes and functionalized with styrene derivatives VBTAC, VBTOH, C1-ester, C3-ester, C1-betaine and C3-betaine in the range from 3500-500 cm^{-1}.

The characteristic bands of the unmodified PP membrane are clearly visible in the IR spectrum. The signals at 2951, 2915, 2872, and 2839 cm^{-1} are attributable to the stretching vibrations of methyl and methylene groups. The bands at 1461 and 1372 cm^{-1} correspond to the deformation vibrations (bending) of the methyl groups. The band at 1116 cm^{-1} can be attributed to the wagging and rocking modes of methyl and C-H bonds, respectively. The modified membranes with PP-*g*-C1-ester and PP-*g*-

C3-ester can be easily identified by their characteristic carbonyl band at 1741 cm^{-1}. The unprotected PP-*g*-C1-betaine and PP-*g*-C3-betaine show bands at lower wave numbers, namely at 1619 and 1573 cm^{-1}, which can be attributed to the carboxylate groups. PP-*g*-VBTOH shows a pronounced OH band at 3317 cm^{-1}. In addition, the signals at 1622 and 1517 cm^{-1} can be attributed to the aromatic ring system, although these bands are only weakly pronounced. In the esters and betaines, these aromatic bands are only partially visible because they are masked by overlapping peaks. For PP-*g*-VBTAC, a band at 3380 cm^{-1} is visible, indicating residual water. The aromatic vibrations appear clearly at 1622 and 1517 cm^{-1}. Overall, the IR spectroscopic results confirm that the membranes were successfully modified with the respective monomers. Additionally, attempts were made to graft the VB-C1-PFP crude product onto PP. The results for IR spectroscopy analysis are shown in Figure 62.

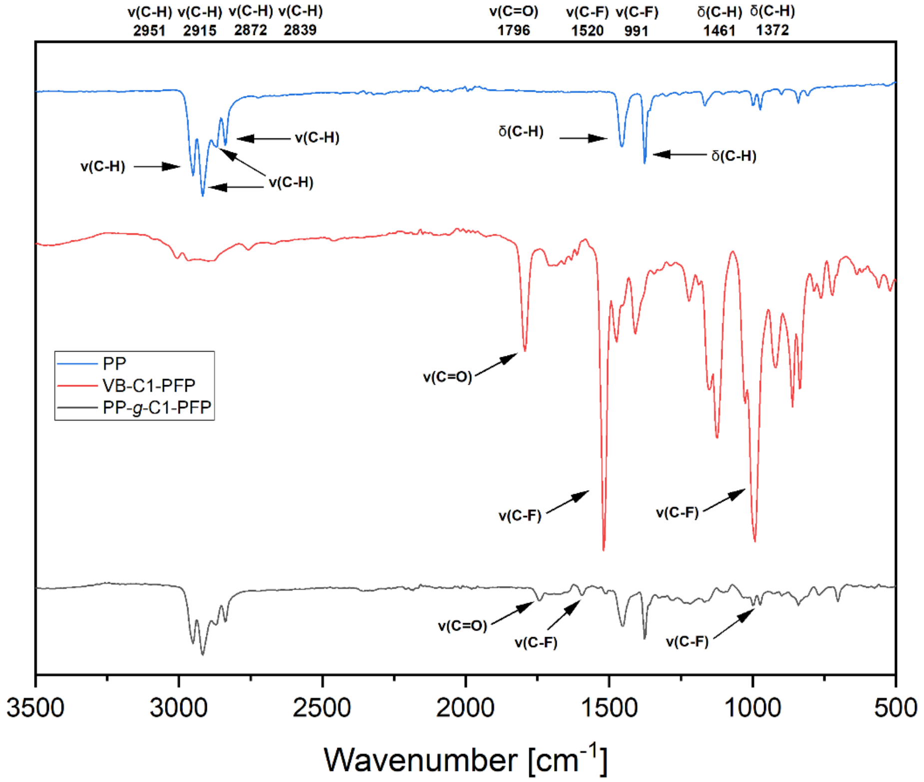

Figure 62: ATR-FTIR of unmodified PP membrane (blue), VB-C1-PFP monomer (red) and the PP modified VB-C1-PFP membrane (black) in the range from 3500-500 cm^{-1}.

The monomer exhibits characteristic IR bands at 1520 cm^{-1} and 922 cm^{-1}, which can be attributed to the ring vibrations of the PFP group and the C-F bonds, respectively. In addition, the carbonyl band of the PFP ester is clearly visible at 1796 cm^{-1}. A comparison of the IR spectra of untreated PP, the monomer VB-C1-PFP, and the modified membrane PP-*g*-C1-PFP shows that the aforementioned bands are also present in the membrane, indicating successful modification. The detectable fluorine bands indicate that the PFP ester remained intact during the grafting reaction. To confirm the IR spectroscopy results, supplementary analyses using XPS, SEM-EDX, and zeta potential measurements would be useful. Dynamic water contact angle measurements were performed to evaluate surface wettability (Figure 63).

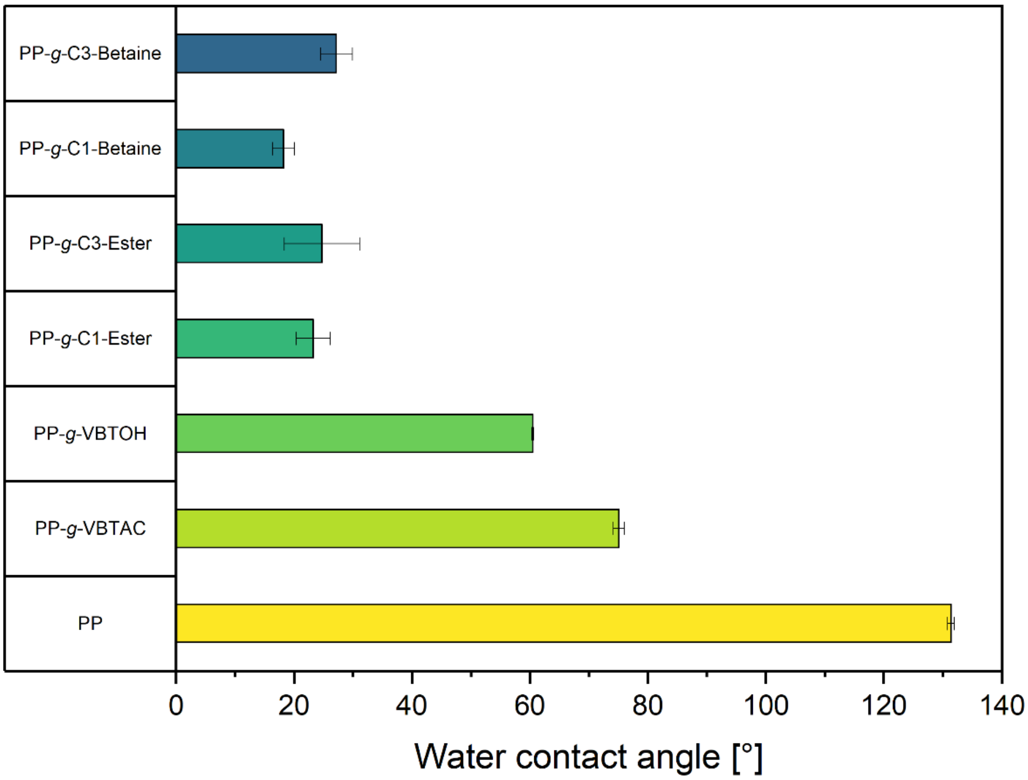

Figure 63: Average dynamic water contact angle (WCA) values of pristine PP and PP modified with VBTAC, VBTOH, C1-ester, C3-ester, C1-betaine and C3-betaine.

The goal of the modification was to make the originally hydrophobic PP surface more hydrophilic. Unmodified PP had a high contact angle of 131°, indicating a highly hydrophobic surface. Water droplets were not absorbed by this surface. After modification, the C1 and C3 carboxybetaines had significantly lower contact angles of 18° and 27°, respectively, indicating increased hydrophilicity. The corresponding C1 and C3 esters had similar contact angles of 23° and 24°, respectively. While these values are comparable, the surfaces differ fundamentally in their interaction with foulants. The esters are cationic, while the betaine surfaces are zwitterionic, which can lead to antimicrobial or antifouling behavior. PP-*g*-VBTAC and PP-*g*-VBTOH had contact angles of 75° and 60°, respectively, indicating lower hydrophilicity than the esters and betaines. This behavior can be explained by the shorter, more hydrophobic side chains that allow the hydrophobic properties of the styrene polymer backbone to be expressed more strongly. In summary, all modifications demonstrate significantly altered wettability compared to the unmodified PP membrane, confirming the successful surface modification. Next, the surface of the modified membranes was analyzed using laser scanning microscopy to check for intact fiber structure and excessive surface polymerization. The results are displayed in Figure 64.

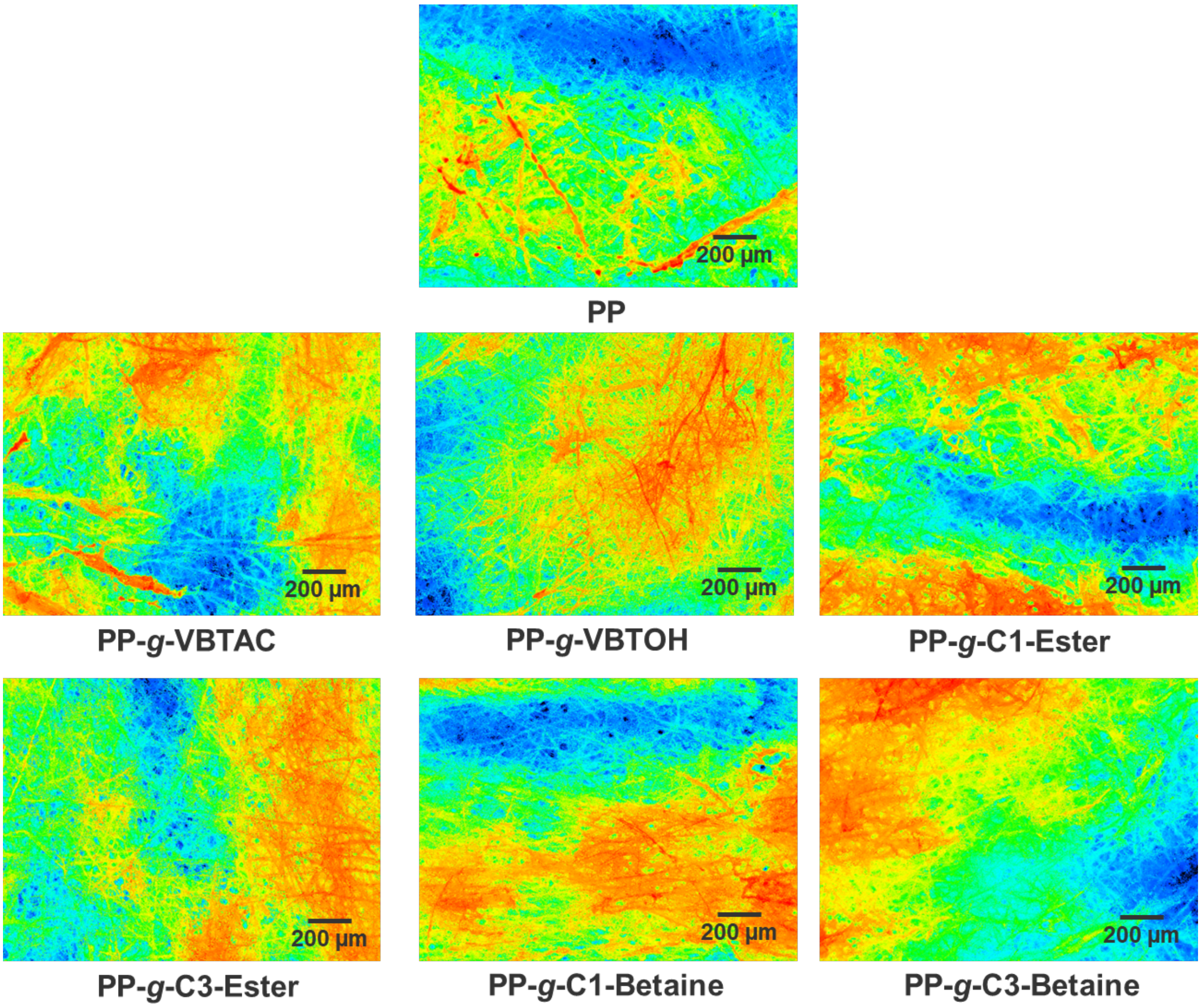

PP

PP-*g*-VBTAC **PP-*g*-VBTOH** **PP-*g*-C1-Ester**

PP-*g*-C3-Ester **PP-*g*-C1-Betaine** **PP-*g*-C3-Betaine**

Figure 64: Laser scan images of the top view in a 100k magnification of pristine PP and PP modified with VBTAC, VBTOH, C1-ester, C3-ester, C1-betaine and C3-betaine.

The PP membrane has a microstructured surface that is not completely flat explaining the visible differences in height. The characteristic fiber structure resulting from the meltblown process is clearly visible in all images. Samples PP, PP-*g*-VBTAC, PP-*g*-VBTOH, PP-*g*-C1-ester, and PP-*g*-C3-ester have similar surface morphologies, suggesting that UV-initiated graft polymerization largely retains the bulk structure. In contrast, areas with fewer pores can be identified in the PP-*g*-C1-betaine and PP-*g*-C3-betaine. This suggests that polymer immobilization was stronger in these areas than in the other modifications. The measured contact angles support this observation. One possible consequence of this stronger coating is reduced water or airflow through the membrane The surface roughness of the membranes was analyzed to assess potential interactions with foulants, particularly microorganisms. The results are shown in Figure 65.

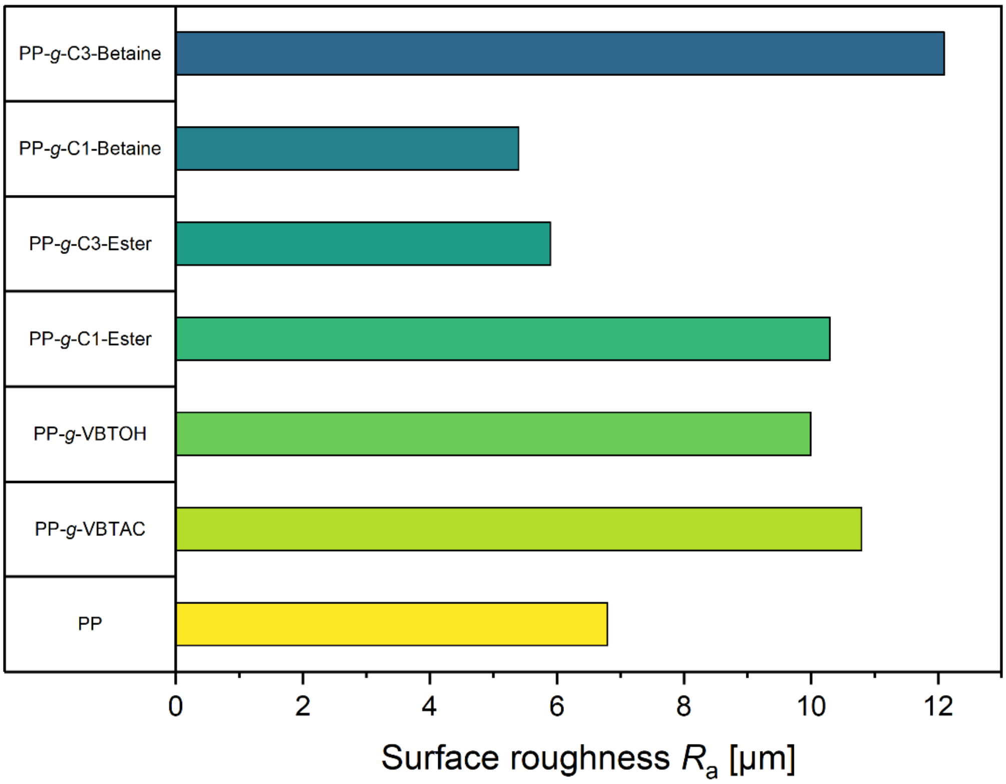

Figure 65: The surface roughness of the PAN membranes was quantified using the R_a (arithmetic mean of height deviations), which were determined from the laser scan images. The values shown are for untreated PP membranes and membranes modified with VBTAC, VBTOH, C1-ester, C3-ester, C1-betaine and C3-betaine.

The pristine PP membrane had an average roughness value of 6.8 µm. After modification, roughness values ranged from 5.4 to 10.0 µm, indicating that the membrane surface's microstructure was largely preserved. The slight differences in surface roughness can be explained by variations in swelling behavior and the amount of immobilized polymer. Micrometer-structured surfaces can promote the adhesion of microorganisms because bacteria can become trapped in the recesses and protected from shear forces. Therefore, for antimicrobial properties, it would be advantageous to use a nanostructured surface. These structures reduce the effective contact area between microorganisms and the surface, hindering initial adhesion. To fully characterize the membrane, XPS, zeta potential, and airflow measurements should also be carried out in the future, as the results obtained so far are promising.

6.2.4 Dye adsorption

Adsorption capacity was determined under static conditions and served as an indirect measure of solvent-accessible positive charge or immobilized polymer amount on the membrane surface (Figure 66).

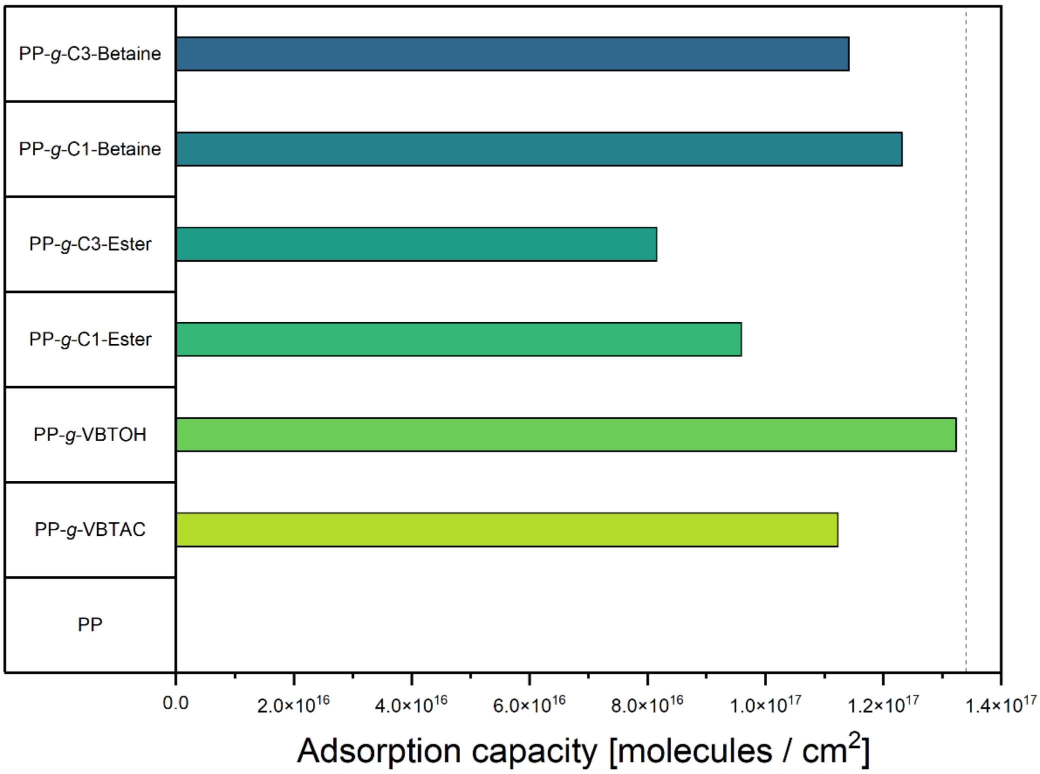

Figure 66: Acid orange 7 adsorption capacity of pristine PP and PP modified with VBTAC, VBTOH, C1-ester, C3-ester, C1-betaine and C3-betaine. The membranes, each with a diameter of 2.0 cm, were placed in a 50 µM acid orange 7 solution at pH 7.4 and incubated for 7 days before measuring the absorbance. The dotted line represents the maximum adsorption capacity.

Two dyes were used in the study: acid orange 7, a negatively charged azo dye, and methylene blue, a cationic phenothiazine dye. Pristine PP has no functional groups and is highly hydrophobic. This is reflected in its dye uptake. It showed no adsorption of acid orange 7. In contrast, all modified membranes showed significant adsorption of the anionic dye. The PP-*g*-C1-ester and PP-*g*-C3-ester had the lowest dye uptake, which is attributable to their hydrophobic ethyl groups. The carboxybetaine adsorbed significantly more dye, a behavior that has been observed with PAN carboxybetaine too. These results suggest that interactions are primarily determined by functional groups rather than the polymer backbone. There is likely a positive zeta potential here as well, which promotes electrostatic attraction with the negatively charged dye. Both PP-*g*-VBTAC and PP-*g*-VBTOH showed strong adsorption of acid orange 7 due to electrostatic interactions with their positively charged groups. Therefore, the membranes are potentially suitable for removing anionic contaminants. Due to their strong cationic surface, they possibly also exhibit antimicrobial properties. On the other hand, unmodified PP showed slight adsorption of the positive dye (Figure 67).

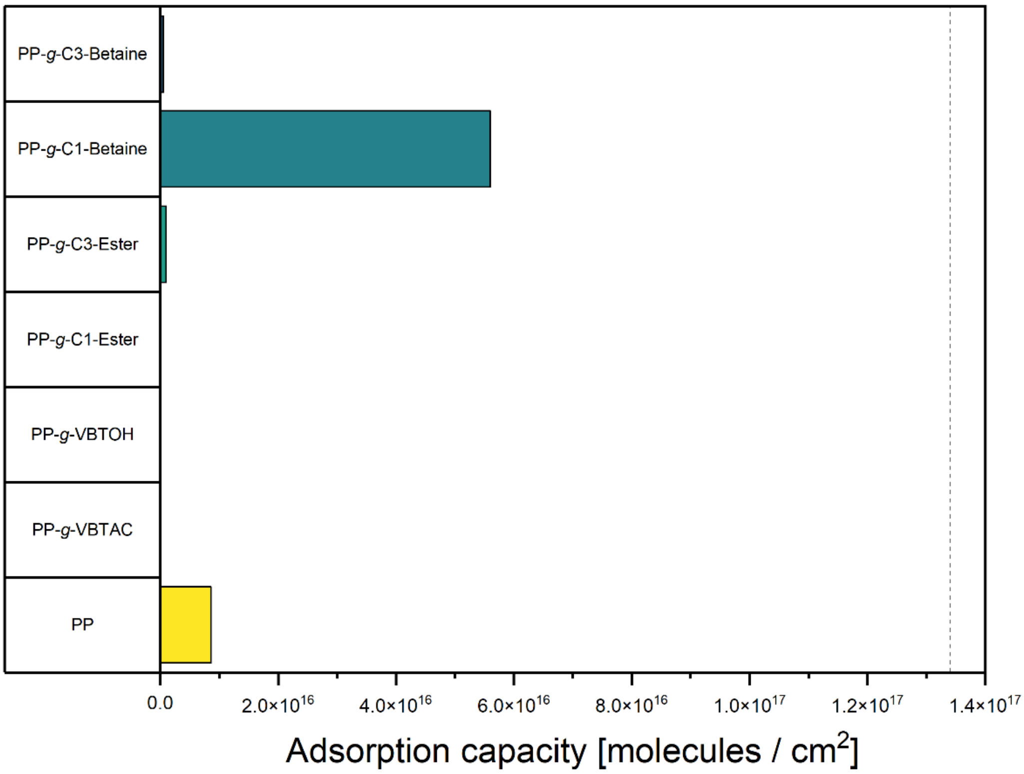

Figure 67: Methylene blue adsorption capacity of pristine PP and PP modified with VBTAC, VBTOH, C1-Ester, C3-Ester, C1-Betaine and C3-Betaine. The membranes, each with a diameter of 2.0 cm, were placed in a 25 µM methylene blue solution at pH 7.4 and incubated for 7 days before measuring the absorbance. The dotted line represents the maximum adsorption capacity.

This is because many polymers have slightly negative zeta potential, which can cause electrostatic attraction. In summary, the modifications tested are not suitable for removing cationic contaminants. However, they show promising potential for removing anionic species and for antimicrobial applications. Dynamic adsorption should be tested in the future.

6.2.5 Antimicrobial activity

The antimicrobial activity of the modified PP membranes was investigated using a modified ASTM E2149 assay.[187] The goal was to determine if the functionalized membrane surfaces suppress biofilm formation and prevent biofouling and associated flux decline. The test organism was *S. aureus*, a gram-positive bacterium. The results are presented in Figure 68.

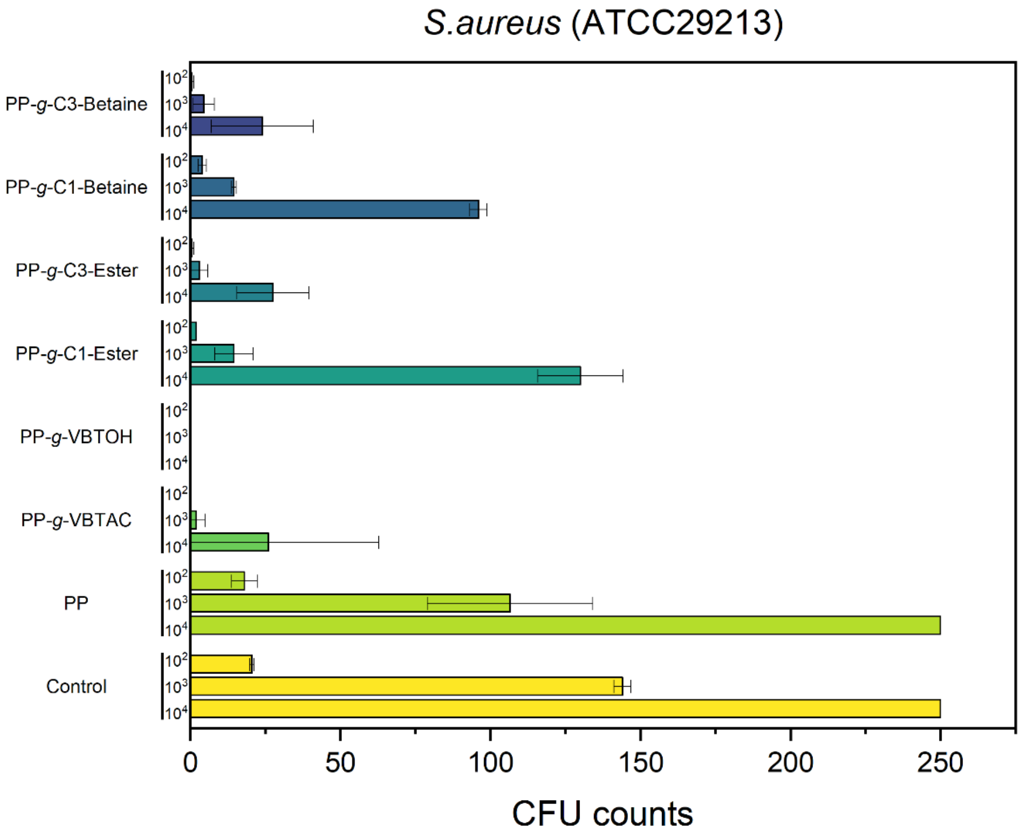

Figure 68: Determination of the antimicrobial activity of modified PAN membranes using a modified ASTM E2149 assay. The membrane samples (1.0 cm^2) were incubated in 2 mL of a *S. aureus* suspension (10^5 CFU/mL in 0.9% NaCl) for 2 h at 37 °C and 300 rpm. The colony-forming units (CFU) were then determined by plating the suspension and its dilutions on Columbia agar.

The growth control consisted of a bacterial suspension without a membrane. As expected, both the control and pristine PP showed strong, comparable bacterial growth. In contrast, the PP-*g*-C1-Ester and PP-*g*-C3-Ester and their corresponding carboxybetaine compounds exhibited significantly reduced bacterial growth.

Remarkably, the C3 derivatives both the esters and the betaines, led to a greater reduction in bacterial growth than their C1 counterparts. This suggests that the length of the spacer between functional groups influences the antimicrobial effect. For the cationic esters, this could be explained by polymeric spacer effects or a positive zeta potential. However, it was unexpected that the zwitterionic carboxybetaine would also show a reduction, as they are not expected to have an antimicrobial effect. One possible explanation could be the structural difference between PP-*g*-C1-Betaine and PP-*g*-C3-Betaine. The C3 derivatives have a greater distance between positive and negative charges, leading to a more pronounced dipole moment. This could promote specific interactions with bacterial cell walls, such as a phospholipid sponge effect or ion exchange effects. Of particular note, PP-*g*-VBTOH showed complete inhibition of bacterial growth. PP-*g*-VBTAC also led to nearly complete inhibition. These results demonstrate that PP-*g*-VBTOH exhibits antimicrobial properties comparable to PP-*g*-VBTAC, making it suitable for similar applications. To further evaluate the practical suitability of these materials, their long-term stability and potential leaching behavior should be investigated.

6.2.6 Protein adsorption

The modified membranes were tested for their antifouling properties against proteins. For this purpose, BSA, lysozyme, and fibrinogen were used as model proteins. Their specific properties are listed in Table 3. Protein adsorption was analyzed under static conditions. In particular, PP-*g*-C1-Betaine and PP-*g*-C3-Betaine were tested, as their structural characteristics suggest antifouling effects. The results are shown in Table 5. The untreated PP membrane exhibited significant adsorption of all three proteins due to its hydrophobic, unmodified surface. In contrast, the PP-*g*-C1-Betaine and PP-*g*-C3-Betaine membranes showed no adsorption of BSA or lysozyme. This behavior is explained by the strong hydration of the zwitterionic surface and steric repulsion effects, which prevent non-specific protein binding.

Table 5: Static adsorption of bovine serum albumin, lysozyme, and fibrinogen on modified PP membranes.

Membrane	Bovine serum albumin [µg]	Lysozyme [µg]	Fibrinogen [µg]
PP	141	56	132
PP-*g*-C1-Betaine	0	0	32
PP-*g*-C3-Betaine	0	0	47

Interestingly, however, significant adsorption of fibrinogen was observed on both membranes. Fibrinogen is a much larger protein than BSA and lysozyme, and it could accumulate in recesses due to its size and the microstructured surface of the membrane. These recesses protect the protein from the shear forces that occur during the rinsing process, which makes it more difficult to remove.

This behavior is consistent with previous observations of PAN membranes modified with carboxybetaine. While effective protection against smaller proteins is possible, large proteins such as fibrinogen pose a particular challenge. Further studies on pore size and surface structure could be useful in this regard.

6.2.7 Bioconjugation

The experiments with activated esters aimed to evaluate the fundamental possibility of covalently immobilizing antimicrobial substances, such as antimicrobial peptides. Because comprehensive surface analysis is complex and time-consuming, a simple test method was used to verify the success of the modification indirectly.[188] The enzyme horseradish peroxidase (HRP) was used as a model substance for this purpose. The functionality and successful immobilization were verified using a colorimetric HRP assay, in which HRP produces the dye purpurogallin when H_2O_2 and pyrogallol are present (Figure 69). Purpurogallin formation can be detected spectrophotometrically at 420 nm.

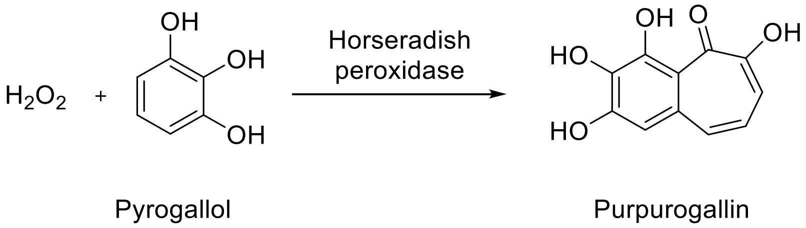

Figure 69: Enzymatic oxidation of pyrogallol, which results in the formation of the dye purpurogallin.

Two strategies for enzyme immobilization were tested (Figure 70). Prior to the experiments, the membranes were cut into pieces of 0.5 × 2.0 cm.

In the first method (*in situ* activation), PP-*g*-C1-betaine membranes were incubated in PBS buffer (pH 7.4) containing HRP (0.2 mg/ml), EDC (0.6 M), and NHS (0.4 M). The samples were shaken at 300 rpm for 18 h to enable covalent attachment of the enzyme via activated ester groups on the membrane surface.

In the second strategy, the membranes were pre-functionalized with PP-*g*-C1-PFP, as previously described, and subsequently incubated with the HRP solution under identical conditions, without the addition of EDC/NHS.

After incubation, the membranes were washed with PBS to remove unbound protein. It is important to store the HRP-functionalized membranes in buffer to prevent enzyme denaturation.

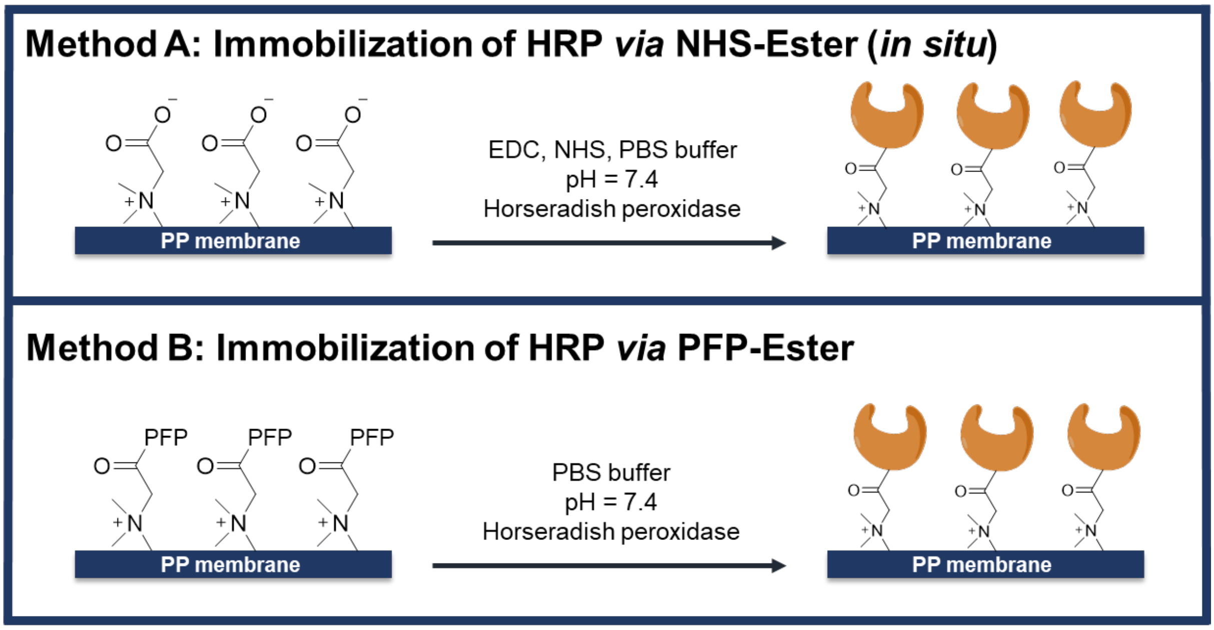

Figure 70: Schematic representation of enzyme immobilization by means of (**A**) *in situ* activation of carboxybetaine surfaces with EDC/NHS and (**B**) direct coupling to PFP-active polymer brushes.

The HRP activity test demonstrated that membranes prepared by both methods exhibited enzymatic activity, as evidenced by purpurogallin formation. The results are presented in Figures 71–72. In the EDC/NHS method, the absorption values ranged from 0.4935 to 0.5834, indicating immobilization and functional enzyme activity.

A study by Higaki *et al.* shows that the functionalization of C1 carboxybetaine is most effective when only EDC is used in combination with a MES buffer (pH = 5.0).[189] This simplified activation protocol could be adopted in future work to achieve more efficient coupling and reproducibly better results. The findings also suggest that the *O*-acylisourea ester is inherently unstable and is rapidly hydrolyzed under PBS buffer conditions.

The PFP-modified membranes exhibited even higher absorption values, ranging from 1.0383 to 1.2711. These results suggest more effective enzyme binding or higher catalytic activity. The slightly yellowish color of the negative control can be explained by pyrogallol's known auto-oxidation. Additionally, the enzymatic activity of the membranes remained intact after prolonged storage in PBS, suggesting covalent bonds and stable immobilization.

Overall, these results demonstrate the successful implementation of the concept of covalently bonding bioactive molecules *via* active esters, representing a suitable strategy for functionalizing antimicrobial membrane surfaces.

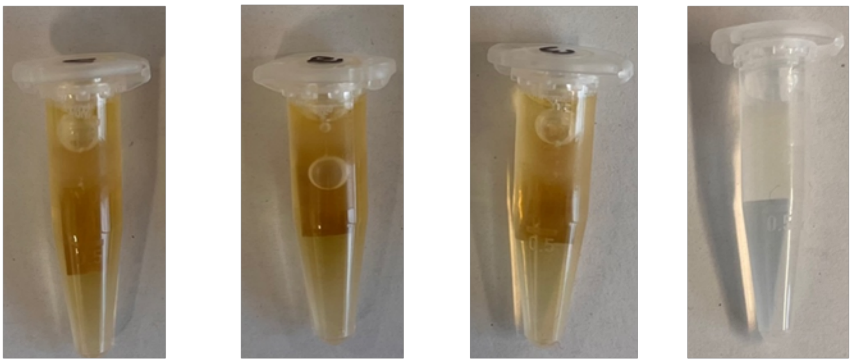

HRP 1 **HRP 2** **HRP 3** **negative**

Sample	Absorption [a.u.]			Average [a.u.]
PP-*g*-NHS-HRP 1	0.5116	0.5116	0.5116	0.5116
PP-*g*-NHS-HRP 2	0.5834	0.5834	0.5834	0.5834
PP-*g*-NHS-HRP 3	0.4935	0.4935	0.4936	0.4935
negative	0.0000	0.0000	0.0000	0.0000

Figure 71: Tubes 1–3 contain PP-*g*-NHS-HRP membranes that have converted pyrogallol to purpurogallin (yellow). Tube 4 shows negative control without HRP. The table opposite summarizes the measured absorption values from a triple determination.

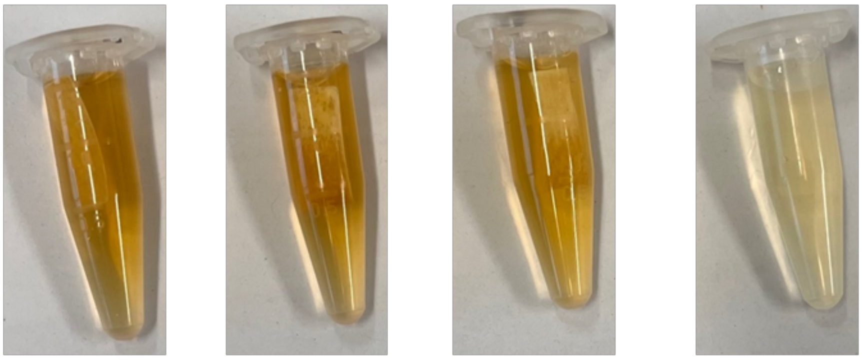

HRP 1 **HRP 2** **HRP 3** **negative**

Sample	Absorption [a.u.]			Average [a.u.]
PP-*g*-PFP-HRP 1	1.2707	1.2712	1.2715	1.2711
PP-*g*-PFP-HRP 2	1.1879	1.1885	1.1889	1.1884
PP-*g*-PFP-HRP 3	1.0383	1.0383	1.0383	1.0383
negative	0.0211	0.0211	0.0213	0.0212

Figure 72: Tubes 1–3 contain PP-*g*-PFP-HRP membranes that have converted pyrogallol to purpurogallin (yellow). Tube 4 shows negative control without HRP. The table opposite summarizes the measured absorption values from a triple determination.

7 Outlook

The UV-initiated graft polymerization method developed is versatile and mild for immobilizing functional groups on PAN ultrafiltration membranes. Notably, zwitterionic groups were successfully introduced into the membrane's pore structure without significant loss of permeability. Future work should focus on controlling the functionalization process in a more targeted manner. To improve comparability of the coatings, the method should be further developed so that the membranes have a defined, uniform amount of polymer. One way to achieve this would be to covalently immobilize photoinitiators or ATRP initiators on the surface to enable a controlled SI-ATRP reaction. Additionally, the long-term stability of the functionalization, behavior under real process conditions, and targeted separation of specific pollutants such as pharmaceuticals could be investigated. Combining several functional groups on a membrane surface could enable new applications, such as selectively separating or targeting the adsorption of molecules.

Transferring the grafting method to inexpensive, widely used PP nonwoven membranes shows promise for applications in water and air filtration. In particular, combining antimicrobial QACs with antifouling-effective zwitterions offers great potential for developing multifunctional filter materials. Future work should investigate the long-term stability and effectiveness of this antimicrobial treatment in more detail. Further analytical investigations, such as SEM-EDX, XPS, zeta potential measurements, and the determination of pore size and porosity, are still necessary. In addition, the permeability of the membranes to water and air should be systematically tested. Functionalization using active esters is fundamentally possible. Although the approach using PFP esters showed better results than the NHS method, it should not be pursued further due to environmental concerns. Nevertheless, both methods offer the possibility of immobilizing antimicrobial peptides (AMPs) on the membrane surface in the future, for example.

UV-induced functionalization is a powerful platform technology for customized membrane materials in various fields of application from water treatment to air filtration.

8 Material and methods

8.1 General procedures

All chemicals and solvents used were purchased in reagent grade from the manufacturers Sigma-Aldrich, Merck, BLDpharm, abcr, Grüssing, Carl Roth, Thermo Fisher, TCI, VWR and Eurisotop and, unless otherwise stated, were used without further purification. PAN membranes were provided by the Helmholtz-Zentrum Hereon. PP membranes were purchased from kindnessX. All reactions under inert conditions were performed in glassware dried with a heat gun under vacuum, and with anhydrous solvents.

8.2 Chromatography

Column chromatography

Silica gel 60 (particle size 0.040–0.063 mm, 230–400 mesh) from Machery-Nagel was used for column chromatography.

Thin-layer chromatography (TLC)

Prefabricated TLC plates (ALUGRAM® Xtra SIL G/UV254) from Machery-Nagel were used. R_f values were determined at chamber saturation. UV-active substances were detected at a wavelength of 254 nm. A potassium permanganate solution was used as TLC stain, which consists of 1.5 g $KMnO_4$, 10 g K_2CO_3, 1.25 mL 10% NaOH and 200 mL ultrapure water.

Gel permeation chromatography (GPC)

The molar mass distribution was determined using gel permeation chromatography (GPC). A SUPREMA column (3000 Å, 8 × 300 mm, 10 µm particle size; suitable for the range from 1 kDa to 3 MDa) was used for this purpose. Water with 0.5% $NaNO_3$ served as the mobile phase. The flow was controlled by a VWR Hitachi L-2130 pump. The samples were injected using a VWR Hitachi Autosampler 5280, while detection was performed using a VWR Hitachi Chromaster 5450 refractive index (RI) detector. A PEG ReadyCal standard from PSS Polymer Standards Service was used for calibration.

8.3 Instrumental analytics

Nuclear magnetic resonance spectroscopy (NMR)

The NMR spectra were recorded by the spectroscopy department of the Institute of Organic Chemistry at the University of Hamburg. The ^{1}H, ^{13}C spectra were recorded on the Bruker Avance III 400 and Avance III 600 instruments. The COSY, HSQC and HMBC correlation spectra were also measured on these instruments. The chemical shift of the obtained spectra was calibrated to the solvent signal of $CDCl_3$ (^{1}H: 7.26 ppm; ^{13}C: 77.16 ppm) or D_2O (^{1}H: 4.80 ppm).

Mass spectrometry (MS)

The MS spectra were recorded by the mass spectrometry department of the Institute of Organic Chemistry at the University of Hamburg. HRMS-ESI spectra of all synthesized compounds were recorded on a mass spectrometer model 6224 ESI-TOF from Agilent. For reaction control, ESI spectra were measured on the amaZon SL model from Bruker.

Infrared spectroscopy (IR)

The IR spectra were measured on an FT-IR spectrometer of the IRAffinity-1S model from SHIMADZU. The ATR unit used is the Quest model from Specac. It was measured at room temperature and in a range of 400–4000 cm^{-1}.

Ultraviolet–visible spectroscopy (UV-Vis)

The UV/Vis spectra were measured on the BioMate-3S model from Thermo Scientific. The evaluation was carried out using the VISIONlite software.

Scanning electron microscopy (SEM)

SEM images were recorded on a Merlin from ZEISS at an accelerating voltage of 5 keV using an InLens secondary electron detector. Prior to the measurement, the samples underwent a drying process under vacuum at a temperature of 50 °C for a duration of 48–72 h. Thereafter, the samples were sputter-coated with 1 nm platinum using a CCU-010 coating device from Safematic. The pore size and porosity of the membrane surface were analysed with the IMS software from Imagic Bildverarbeitung AG.

Energy-dispersive X-ray spectroscopy (EDX)

The EDX analysis was conducted with an accelerating voltage of 5 keV, a probe current of 150 pA, and a working distance of 5.6–5.8 mm. The detection of signals was facilitated by employing an X-Max Extreme as the primary EDX detector and an X-Max 150 as the secondary EDX detector. Prior to measurement, the samples were subjected to vacuum drying at 50 °C for a duration of 48–72 h, followed by sputter coating with 1.5 nm platinum using a CCU-010 coating device from Safematic.

X-ray photoelectron spectroscopy (XPS)

XPS measurements were performed with a KRATOS AXIS Ultra DLD from Kratos Analytical, equipped with a monochromatic Al-Kα anode and operated at 15 kV (225 W). A pass energy of 160 eV was used for the survey spectra, while a pass energy of 20 eV was used for the region spectra. The area investigated was 700 µm × 300 µm. The CASA-XPS software was used to evaluate and validate the data. The spectra were calibrated by adjusting the C 1s signal to 284.5 eV. A background subtraction (Tougaard or Shirley) was performed for the deconvolution of the region files before the calculation.

Atomic force microscopy (AFM)

The surface roughness of the samples was determined with the Multimode 8 atomic force microscope from Bruker in the PeakForce QNM mode. ScanAsyst Air, with a spring constant of 0.4 N/m and a radius of 2 nm, was utilised as the tip. The maximum force recorded was 500 pN, with a frequency of 1 kHz and a scanning velocity of 0.47 Hz. The arithmetic average roughness (R_a) and quadratic mean of height deviations (Rq)was then determined.

Water contact angle (WCA)

Contact angles were obtained using an OCA 20 goniometer from DataPhysics. For evaluation, independent triplicate measurements were obtained at three distinct locations on the surface. The measurement of contact angles was conducted using deionized water, employing the static sessile drop method with a dispensing volume of 2 µL. The dispensing rate of the automatic syringe was set at 1 µL min^{-1}. To obtain the contact angle, a 10-second video was recorded at a frequency of 10 Hz. The contact angle was then determined as the mean value of the first three contact angles. The obtained angle was calculated with the OCA software.

Zeta potential measurement

The zeta potential was measured using the SurPASS Eco 3 from Anton Paar. The streaming potential method was employed to assess the zeta potential. The electrolyte solution employed was a 0.01 M NaCl solution, and the pH was adjusted using 0.05 M NaOH and 0.05 M HCl. All solutions were prepared using ultrapure Milli-Q water. Before starting the zeta potential measurement, the membranes were thoroughly rinsed with the electrolyte solution to ensure cleanliness and consistency. The zeta potential measurements were conducted within the pH range of 9 to 3, with four replicates being obtained at each pH value.

Thermogravimetric analysis (TGA)

Thermogravimetric analysis was performed using TGA 2 from Mettler-Toledo. The sample was first heated to 80 °C at a rate of 10 K/min and held at this temperature for 10 min. It was then heated at a rate of 10 K/min to 700 °C.

Laser scanning microscope

The VK-X260K laser scanning microscope and the corresponding VK-X250K control unit from Keyence were used to examine the surface morphology. A violet semiconductor laser with a wavelength of 408 nm was used as the light source for the measurement. The VK recording module software was used to analyze the data.

8.4 Laboratory devices

Photoreactor

The PhotoRedOx Box from EvoluChem with built-in room temperature cooling was used for photopolymerization. An LED lamp (30 W) with a wavelength of 365 nm was used as an irradiation source.

Freeze Dryer

The “Alpha 2-4 LDplus” freeze-drying system from Christ was used for lyophilization.

8.5 Performance evaluation

Pure water permeance

The permeance was determined using a device from Hereon in dead-end mode. It was measured on a circular piece of the membrane with a diameter of 2.0 cm corresponding to an active area (A) of 3.14 cm^2, using ultrapure water. A transmembrane pressure of 2 bar was applied. The permeance (J) was calculated using the following equation (1), where ΔV is the volume difference, Δp the pressure difference and Δt the time difference.

$$J = \frac{\Delta V}{\Delta p \cdot \Delta t \cdot A} \quad \text{(Equation 1)}$$

Molecular weight cut-off (MWCO)

The retention of four PEG solutions with different molecular weights (44 k, 82.8 k, 141.7 k, 219.4 k, 250 k and 351 k) was investigated. For sample preparation, 50 mg of each of the PEGs with a molecular weight of 44 k, 82.8 k and 141.7 k were dissolved together in 500 mL of ultrapure water. The PEGs with higher molecular weights (219.4 k, 250 k and 351 k) were dissolved individually at 50 mg each in 500 mL ultrapure water. Membranes with a diameter of 2.0 cm (active membrane area: 3.14 cm^2) were used for filtration. To avoid swelling processes during the measurement, the membranes were pre-filtered with pure water at a transmembrane pressure of 2 bar for 1.5 h before starting the adsorption tests. The PEG solutions were then filtered using an Amicon cell in dead-end mode with stirring and a constant transmembrane pressure of 2 bar. After a filtration time of 1.5 h, samples of the permeate and retentate were taken. In addition, a sample of the initial solution (feed) was taken. The concentrations of the PEGs in the respective samples were determined using gel permeation chromatography (PSS Polymer Standards Service). Two measurements were carried out for each membrane modification, with the values shown as mean values. The retention was calculated according to equation (2). Where C_p is the PEG concentration in the permeate, C_f is the concentration in the feed and C_r is the concentration in the retentate. These values can be used to determine the MWCO of the membrane.

$$\text{Retention} = 1 - \frac{\left(c(\text{P}) + c(\text{F})\right)}{2 \cdot c(\text{R})} \cdot 100 \quad \text{(Equation 2)}$$

Static dye adsorption

The adsorption behavior of two dyes with opposite charges was investigated. Acid orange 7 was selected as the negatively charged dye and methylene blue as the positively charged dye. For this purpose, a 50 µM solution of acid orange 7 (corresponding to 17.6 mg/L) and a 25 µM solution of methylene blue (corresponding to 9.8 mg/L) were prepared separately in ultrapure water. Membranes with a diameter of 2.0 cm were used for the static adsorption tests, which corresponds to an active membrane area of 3.14 cm^2. The membranes previously used for water flux measurements were each placed in a vial containing 10 mL of the respective dye solution. The samples were left to rest for seven days at room temperature. The concentration of non-adsorbed dye in the solution was then determined by UV-Vis spectroscopy. The amount of adsorbed dye was calculated using equation (3). In this equation, N represents the number of adsorbed molecules, A for the membrane area, C_0 for the initial concentration of the dye, C for the measured concentration after adsorption, V for the volume and N_a for the Avogadro constant.

$$\text{Adsorbed dye} = \frac{N}{A} = \frac{(C_0 - C) \cdot V \cdot N_A}{A} \quad \text{(Equation 3)}$$

Dynamic dye adsorption

For the dynamic adsorption tests, membranes with a diameter of 2.0 cm were used, which corresponds to an active membrane area of 3.14 cm^2. To avoid swelling processes, each membrane was pre-filtered with ultrapure water at a transmembrane pressure of 1 bar for one hour prior to dye adsorption. Dye solutions of acid orange 7 (250 mL, 2.0 µM) or methylene blue (250 mL, 1.0 µM) were then filtered through the membrane. The filtration was carried out with stirring in dead-end mode using an Amicon cell at a constant transmembrane pressure of 1 bar. During the process, 10 mL samples of the permeate were continuously taken until the dye concentration of the original feed solution was reached. In addition, a sample of the starting solution was taken at the beginning and a sample of the retentate at the end. The dye concentrations in the individual samples were determined using UV-Vis spectroscopy. The absorbance of methylene blue was measured at a wavelength of 665 nm, that of acid orange 7 at 482 nm. The concentration was determined by comparing the measured absorbance with previously prepared calibration curves. Two samples per modified membrane were analyzed for the dynamic adsorption experiment. The results of the dynamic experiment are given as a logistic fit of the mean ± standard deviation.

Phosphate and Nitrate adsorption

Orthophosphate ($H_2PO_4^-$, HPO_4^{2-}, PO_4^{3-}) and nitrate ions (NO_3^-) were determined using the Merck Spectroquant® NOVA 60 photometer with the corresponding Spectroquant® test kits. For the static adsorption test, the membranes were incubated in glass vials containing 20 mL of a test solution with the following concentrations: phosphate (5 mg/L PO_4^{3-}) and nitrate (5 mg/L NO_3^-), at a pH of 7.4. The incubation period was three days at room temperature. After incubation, the concentration of remaining ions in the solution was determined photometrically.

8.6 Microbiological evaluation

Protein adhesion

The assay was carried out according to a procedure described by ZHANG *et al.*[190] Adsorption was investigated for three selected proteins: Bovine serum albumin, lysozyme and fibrinogen. For each experiment, a membrane with a diameter of 2.0 cm, corresponding to an active membrane area of 3.14 cm^2, was placed in 2 mL of a protein concentration of 1 g/L in PBS buffer (pH 7.4). The samples incubated for 24 h at 25 °C and a shaking speed of 100 rpm to reach adsorption equilibrium. The membranes were then washed with 2 mL of pure PBS solution (pH 7.4) for 10 min at 25 °C and 100 rpm. This washing procedure was repeated twice to remove unbound or only weakly bound proteins. The amount of protein adsorbed on the membrane was calculated from equation (4), where m_0 is the protein mass in the solution before the start of the adsorption experiment, m_1 is the remaining protein mass in the solution after the experiment, m_{w1} and m_{w2} are the protein masses in the two wash solutions, and A is the active area of the membrane. The concentrations of the proteins in the individual samples were determined using a UV/Vis spectroscopy, whereby the evaluation was carried out based on previously prepared calibration curves.

$$\text{Adsorbed protein} = \frac{m}{A} = \frac{m_0 - (m_1 + m_{w1} + m_{w2})}{A} \quad \text{(Equation 4)}$$

Antimicrobial activity

The ASTM E2149-13a assay was carried out according to a modified procedure by BURMEISTER *et al.*[187] Before starting the tests, all membranes were disinfected with

70 vol% isopropyl alcohol and dried at room temperature. *S. aureus* (ATCC 29213 and 25923) was used as test organisms. The bacteria were cultured on Columbia agar for 12 h and then adjusted to a target concentration of 10^5 CFU/mL in a 0.9 wt% NaCl chloride solution. Membranes with a surface area of 1.0 cm^2 were treated in an Eppendorf tube with 2 mL each of the diluted bacterial suspension (10^5 CFU/mL). Incubation was carried out for 2 h at 37 °C with shaking at 300 rpm. These test conditions correspond to a challenge of 2.0×10^5 CFU/cm^2. After incubation, 100 µL of the original bacterial suspension and two dilution levels (1:10 and 1:100) were spread onto Columbia agar plates and incubated at 37 °C for 18 h. The CFU were then counted.

Protein immobilization

Method A: The following procedure was chosen for HRP on PP-*g*-C1-Betaine: A 0.5 × 2.0 cm piece of membrane was transferred to a 1.5 mL tube and mixed with 1.5 mL of a HRP solution (0.2 mg/mL in 50 mM PBS buffer, pH 7.4), EDC (0.6 M in 50 mM PBS buffer, pH 7.4), NHS (0.4 M in 50 mM PBS buffer, pH 7.4). Incubation was carried out for 18 h at 4 °C with constant shaking at 300 rpm to enable covalent binding of the enzyme to the activated ester groups of the membrane. The membrane was then washed four times with 1.5 mL fresh phosphate buffer to remove unbound protein.

Method B: The following procedure was chosen for immobilizing HRP on PP-*g*-C1-PFP: A 0.5 × 2 cm piece of membrane was transferred to a 1.5 mL tube and mixed with 1.5 mL of an HRP solution (0.2 mg/mL in 50 mM phosphate buffer, pH 7.4). Incubation was carried out for 18 h at 4 °C with constant shaking at 300 rpm to enable covalent binding of the enzyme to the activated ester groups of the membrane. The membrane was then washed four times with 1.5 mL fresh phosphate buffer to remove unbound protein.

Horseradish peroxidase activity

The assay was carried out according to a procedure described by TEMOCIN *et al.*[188] The activities of the free and immobilized horseradish peroxidase were determined using pyrogallol and H_2O_2 as substrates. The reaction mixtures consisted of 2 mL of a pyrogallol solution (20 mmol L^{-1}) and 1.5 mL of a PBS buffer solution (0.1 mol L^{-1}), to which either 0.1 mL of free HRP (0.01 mg mL^{-1}) or a defined amount of immobilized HRP was added. The reaction was started by adding 0.5 mL H_2O_2 solution

(10 mmol L^{-1}). Product formation was evaluated based on color development and measured spectrophotometrically at 420 nm. The measurement was carried out for the free enzyme one minute after the addition of H_2O_2 and for the immobilized enzyme 5 min after the addition. The values measured for control preparations without enzyme, but with H_2O_2, were used as blank values and subtracted from all measurements.

8.7 UV-Grafting of PAN and PP membranes

PAN-*g*-DMAEMA

2-(Dimethylamino)ethyl methacrylate (5.00 mL, 29.8 mmol) and BAPO (125 mg, 0.298 mmol, 1 mol%) were dissolved. The PAN membrane, measuring 1.0 cm^2, was then added to the solution and degassed with nitrogen for a period of 20 min. The soaked PAN membrane was then transferred to a new vial and irradiated with UV light (365 nm, 30 W) for 1 h at room temperature. The modified PAN membrane was cleaned with 10 mL ultrapure water *via* three 10-minute ultrasonication cycles, then vacuum-dried at 50 °C.

PAN-*g*-DMAPMA

N-[3-(Dimethylamino)propyl]methacrylamide (5.00 mL, 27.6 mmol) and BAPO (120 mg, 0.276 mmol, 1 mol%) were dissolved. The PAN membrane, measuring 1.0 cm^2, was then added to the solution and degassed with nitrogen for a period of 20 min. The soaked PAN membrane was then transferred to a new vial and irradiated with UV light (365 nm, 30 W) for 1 h at room temperature. The modified PAN membrane was cleaned with 10 mL ultrapure water *via* three 10-minute ultrasonication cycles, then vacuum-dried at 50 °C.

PAN-*g*-METAC

2-(Methacryloyloxy)ethyl trimethylammonium chloride (75% in H_2O, 1.33 mL, 4.81 mmol) and LAP (28.3 mg, 0.096 mmol, 2.0 mol%) were dissolved in 3.67 mL demineralized water. The PAN membrane, measuring 1.0 cm^2, was then added to the solution and degassed with nitrogen for a period of 20 min. The soaked PAN membrane was then transferred to a new vial and irradiated with UV light (365 nm, 30 W) for 1 h at room temperature. The modified PAN membrane was cleaned with 10 mL ultrapure water *via* three 10-minute ultrasonication cycles, then vacuum-dried at 50 °C.

PAN-*g*-MAPTAC

[3-(Methacryloylamino)propyl]trimethylammonium chloride (50% in H_2O, 2.0 mL, 4.53 mmol) and LAP (26.7 mg, 0.091 mmol, 2.0 mol%) were dissolved in 3.0 mL demineralized water. The PAN membrane, measuring 1.0 cm^2, was then added to the solution and degassed with nitrogen for a period of 20 min. The soaked PAN membrane was then transferred to a new vial and irradiated with UV light (365 nm, 30 W) for 1 h at room temperature. The modified PAN membrane was cleaned with 10 mL ultrapure water *via* three 10-minute ultrasonication cycles, then vacuum-dried at 50 °C.

PAN-*g*-MPC

2-(Methacryloyloxy)ethyl phosphorylcholine (1.00 g, 3.38 mmol) and LAP (0.020 g, 0.068 mmol, 2.0 mol%) were dissolved in 4.0 mL demineralized water. PAN membrane with an area of 1.0 cm^2 was added to the solution and was degassed with nitrogen for 20 min. The soaked PAN membrane was transferred to a new vial and was irradiated with UV light (365 nm, 30 W) for 1 h at room temperature. The modified PAN membrane was cleaned with 10 mL ultrapure water *via* three 10-minute ultrasonication cycles, then vacuum-dried at 50 °C.

PP-*g*-VBTAC

(Vinylbenzyl)trimethylammonium chloride (1.00 g, 4.72 mmol) and LAP (27.7 mg, 0.094 mmol, 2.0 mol%) were dissolved in 4.0 mL demineralized water. The PAN membrane, measuring 5.0 cm^2, was then added to the solution and degassed with nitrogen for a period of 20 min. The soaked PAN membrane was then transferred to a new vial and irradiated with UV light (365 nm, 30 W) for 1 h at room temperature. The modified PP membrane was cleaned with 10 mL ultrapure water *via* three 10-minute ultrasonication cycles, then vacuum-dried at 50 °C.

PP-*g*-VBTOH

2-Hydroxy-*N*,*N*-dimethyl-*N*-(4-vinylbenzyl)ethan-1-aminium bromide (1.00 g, 3.50 mmol) and LAP (25.6 mg, 0.070 mmol, 2.0 mol%) were dissolved in 4.0 mL demineralized water. The PAN membrane, measuring 5.0 cm^2, was then added to the solution and degassed with nitrogen for a period of 20 min. The soaked PAN membrane was then transferred to a new vial and irradiated with UV light (365 nm, 30 W) for 1 h at room temperature. The modified PP membrane was cleaned with 10 mL ultrapure water *via* 3x10 min ultrasonication cycles, then vacuum-dried at 50 °C.

PP-*g*-C_1-Ester

2-Ethoxy-*N*,*N*-dimethyl-2-oxo-*N*-(4-vinylbenzyl)ethan-1-aminium bromide (1.00 g, 3.05 mmol) and LAP (17.7 mg, 0.061 mmol, 2.0 mol%) were dissolved in 4.0 mL demineralized water. The PAN membrane, measuring 5.0 cm^2, was then added to the solution and degassed with nitrogen for a period of 20 min. The soaked PAN membrane was then transferred to a new vial and irradiated with UV light (365 nm, 30 W) for 1 h at room temperature. The modified PP membrane was cleaned with 10 mL ultrapure water *via* three 10-minute ultrasonication cycles, then vacuum-dried at 50 °C.

PP-*g*-C_3-Ester

4-Ethoxy-*N*,*N*-dimethyl-4-oxo-*N*-(4-vinylbenzyl)butan-1-aminium bromide (1.00 g, 2.81 mmol) and LAP (16.5 mg, 0.056 mmol, 2.0 mol%) were dissolved in 4.0 mL demineralized water. The PAN membrane, measuring 5.0 cm^2, was then added to the solution and degassed with nitrogen for a period of 20 min. The soaked PAN membrane was then transferred to a new vial and irradiated with UV light (365 nm, 30 W) for 1 h at room temperature. The modified PP membrane was cleaned with 10 mL ultrapure water *via* 3x10 min ultrasonication cycles, then vacuum-dried at 50 °C.

PP-*g*-C_1-Betaine

2-(Dimethyl(4-vinylbenzyl)ammonio)acetate (1.00 g, 4.56 mmol) and LAP (26.8 mg, 0.091 mmol, 2.0 mol%) were dissolved in 4.0 mL demineralized water. The PAN membrane, measuring 5.0 cm^2, was then added to the solution and degassed with nitrogen for a period of 20 min. The soaked PAN membrane was then transferred to a new vial and irradiated with UV light (365 nm, 30 W) for 1 h at room temperature. The modified PP membrane was cleaned with 10 ml ultrapure water *via* 3x10 min ultrasonication cycles, then vacuum-dried at 50 °C.

PP-*g*-C_3-Betaine

4-(Dimethyl(4-vinylbenzyl)ammonio)butanoate (1.00 g, 4.03 mmol) and LAP (23.7 mg, 0.081 mmol, 2.0 mol%) were dissolved in 4.0 mL demineralized water. The PAN membrane, measuring 5.0 cm^2, was then added to the solution and degassed with nitrogen for a period of 20 min. The soaked PAN membrane was then transferred to a new vial and irradiated with UV light (365 nm, 30 W) for 1 h at room temperature. The modified PP membrane was cleaned with 10 mL ultrapure water *via* 3x10 min ultrasonication cycles, then vacuum-dried at 50 °C.

8.8 Post-modification

N-Oxides

PAN-*g*-DMAEMA or PAN-*g*-DMAPMA with an area of 1.0 cm^2 was oxidized with H_2O_2 (2 mL, 30% w/w) for 24 h at 50 °C. The membrane was washed with deionized water and was shaken in a thiosulfate solution (2.0 mL, 1 M) for 30 min to quench the excess of H_2O_2. The modified PAN membrane was subsequently cleaned with deionized water (10 mL) in an ultrasonic bath three times 10 min and dried in vacuo at 50 °C.

Carboxybetaines

PAN-*g*-DMAEMA or PAN-*g*-DMAPMA with an area of 1.0 cm^2 was alkylated with sodium chloroacetate solution (2.0 mL, 1 M) for 24 h at 50 °C. The modified PAN membrane was subsequently cleaned with deionized water (10 mL) in an ultrasonic bath three times 10 min and dried in vacuo at 50 °C.

Sulfobetaines

PAN-*g*-DMAEMA or PAN-*g*-DMAPMA with an area of 1.0 cm^2 was alkylated with sodium 2-bromoethanolsulfonate solution (2.0 mL, 1 M) for 24 h at 50 °C. The modified PAN membrane was subsequently cleaned with deionized water (10 mL) in an ultrasonic bath three times 10 min and dried in vacuo at 50 °C.

Ammonium alcohols

PAN-*g*-DMAEMA or PAN-*g*-DMAPMA membrane with an area of 1.0 cm^2 was alkylated with 2-bromoethanol (2.0 mL, 28.2 mmol) for 24 h at 50 °C. The modified PAN membrane was subsequently cleaned with ethanol (10 mL) in an ultrasonic bath three times 10 min and dried in vacuo at 50 °C.

8.9 Synthesis

N,*N*-dimethyl-1-(4-vinylphenyl)methanamine

The reaction was carried out according to a modified synthesis by DAN *et al.*[191] Under an inert gas atmosphere, 11.00 mL (64.87 mmol,1 eq.) vinylbenzyl chloride, 16.43 mL dimethylamine solution (40% in ethanol, 129.73 mmol, 2 eq.) and 17.93 g (129.73 mmol, 2 eq.) potassium carbonate were added to 60.0 mL dry ethanol. The solution was stirred at room temperature overnight. The suspension was filtered and washed with 120 mL of ethanol. The solvent was removed under reduced pressure. The crude product was purified by column chromatography on silica gel (PE/EE 4:1 v/v).

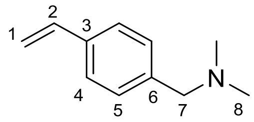

Yield: 7.01 g (43.47 mmol, 67%) of a clear colourless liquid was obtained. **Chemical formula:** $C_{11}H_{15}N$ **Molar mass:** 161.25 g/mol.

HRMS-ESI (m/z): $[M+H]^+$ calculated 161.1204; found 162.1281.

^{1}H-NMR: (500 MHz, $CDCl_3$, 25 °C) δ [ppm] = 7.37 (d, $^3J_{HH}$ = 8.0 Hz, 2H, **4-H**), 7.28 (d, $^3J_{HH}$ = 8.0 Hz, 2H, **5-H**), 6.71 (dd, $^3J_{HH}$ = 17.6, 10.9 Hz, 1H, **2-H**), 5.74 (d, $^3J_{HH}$ = 17.6 Hz, 1H, **1-Ha**), 5.23 (d, $^3J_{HH}$ = 10.8 Hz, 1H, **1-Hb**), 3.45 (s, 2H, **7-H**), 2.27 (s, 6H, **8-H**).

^{13}C-NMR: (126 MHz, $CDCl_3$, 25 °C) δ [ppm] = 138.0 (**C3**), 136.8 (**C6**),136.7 (**C2**), 129.5 (**C5**), 126.3 (**C4**), 113.7 (**C1**), 64.0(**C7**), 45.3 (**C8**).

FTIR (ATR): $\tilde{\nu}$ [cm^{-1}] = 2974, 2943, 2854, 2812, 2765, 1627, 1508, 1454, 1404, 1361, 1257, 1172, 1145, 1029, 1018, 987, 902, 856, 817, 725, 459.

2-Hydroxy-*N*,*N*-dimethyl-*N*-(4-vinylbenzyl)ethan-1-aminium bromide

5.00 g (31.00 mmol, 1 eq.) VBDMA were dissolved in 10.0 mL acetonitrile and cooled to 0 °C. Then 5.81 g (46.49 mmol, 1.5 eq.) 2-bromoethanol were added. The solution was stirred at room temperature for 24 h. The conversion of the reactant was checked by ESI-MS. The precipitated solid was filtered and then washed 3 times with 30 mL diethyl ether. The product was dried in an oil pump vacuum.

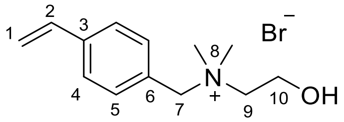

Yield: 8.48 g (29.64 mmol, 96%) of a colourless solid was obtained. **Chemical formula:** $C_{13}H_{20}BrNO$ **Molar mass:** 286.21 g/mol.

HRMS-ESI (m/z): $[M]^+$ calculated 206.1539; found 206.1544.

^{1}H-NMR: (600 MHz, D_2O, 25 °C) δ [ppm] = 7.64 (d, $^3J_{HH}$ = 8.3 Hz, 2H, **4-H**), 7.54 (d, $^3J_{HH}$ = 8.3 Hz, 2H, **5-H**), 6.86 (dd, $^3J_{HH}$ = 17.7, 11.0 Hz, 1H, **2-H**), 5.97 (d, $^3J_{HH}$ = 17.7 Hz, 1H, **1-Ha**), 5.45 (d, $^3J_{HH}$ = 10.9 Hz, 1H, **1-Hb**), 4.57 (s, 2H, **7-H**), 4.18–4.10 (m, 2H,**10-H**), 3.58–3.49 (m, 2H, **9-H**), 3.11 (s, 3H, **8-H**).

^{13}C-NMR: (101 MHz, D_2O, 25 °C) δ [ppm] = 139.7 (**C3**), 135.7 (**C2**), 133.4 (**C5**), 126.7 (**C4**), 126.4 (**C6**), 116.3 (**C1**), 68.9 (**C7**), 65.2 (**C9**), 55.4 (**C10**), 50.3 (**C8**).

FTIR (ATR): $\tilde{\nu}$ [cm^{-1}] = 3340, 2970, 1512, 1473, 1411, 1300, 1219, 1184, 1068, 1022, 987, 925, 891, 852, 813, 717, 543, 513, 451, 424.

2-Ethoxy-*N*,*N*-dimethyl-2-oxo-*N*-(4-vinylbenzyl)ethan-1-aminium bromide

3.00 g (18.60 mmol, 1 eq.) of VBDMA were dissolved in 20 mL ethyl acetate. The solution was cooled to 0 °C. Then 4.66 g (27.91 mmol, 1.5 eq.) ethyl bromoacetate were then slowly added. The solution was stirred for 24 h at room temperature and a colourless solid precipitated. The solid was filtered and washed 3 times with 20 mL of ethyl acetate. The product was dried under vacuum with an oil pump.

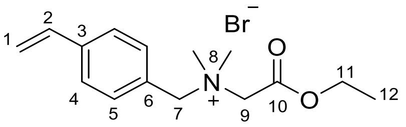

Yield: 5.54 g (16.87 mmol, 90%) of a colourless solid was obtained. **Chemical formula:** $C_{15}H_{22}BrNO_2$ **Molar mass:** 328.25 g/mol.

HRMS-ESI (m/z): $[M]^+$ calculated 248.1645; found 248.1650.

^{1}H-NMR: (400 MHz, D_2O, 25 °C) δ [ppm] = 7.64 (d, $^3J_{HH}$ = 8.3 Hz, 2H, **4-H**), 7.51 (d, $^3J_{HH}$ = 8.3 Hz, 2H, **5-H**), 6.86 (dd, $^3J_{HH}$ = 17.7, 11.0 Hz, 1H, **2-H**), 5.98 (d, $^3J_{HH}$ = 18.0 Hz, 1H, **1-Ha**), 5.46 (d, $^3J_{HH}$ = 11.7 Hz, 1H, **1-Hb**), 4.74 (s, 2H, **7-H**), 4.36 (q, $^3J_{HH}$ = 7.2 Hz, 2H,**11-H**), 4.21 (s, 2H, **9-H**), 3.30 (s, 6H, **8-H**), 1.34 (t, $^3J_{HH}$ = 7.2 Hz, 2H, **12-H**).

^{13}C-NMR: (101 MHz, D_2O, 25 °C) δ [ppm] = 165.4 (**C10**), 140.1 (**C3**), 135.7 (**C2**), 133.2 (**C5**), 126.9 (**C4**), 125.9 (**C6**), 116.5 (**C1**), 68.4 (**C7**), 63.5 (**C11**), 60.7 (**C9**), 51.2 (**C8**), 13.2 (**C12**).

FTIR (ATR): $\tilde{\nu}$ [cm^{-1}] = 3001, 2978, 2897, 2754, 1743, 1481, 1454, 1408, 1384, 1296, 1276, 1207, 1138, 1122, 1037, 1010, 979, 918, 887, 860, 837, 759, 721, 493.

4-Ethoxy-*N*,*N*-dimethyl-4-oxo-*N*-(4-vinylbenzyl)butan-1-aminium bromide

3.00 g (18.60 mmol, 1 eq.) of VBDMA were dissolved in 20 mL ethyl acetate. The solution was cooled to 0 °C. Then 5.44 g (27.91 mmol, 1.5 eq.) ethyl 4-bromobutyrate were then slowly added. The solution was stirred for 24 h at room temperature and a colorless solid precipitated. The solid was filtered and washed 3 times with 20 mL of ethyl acetate. The product was dried under vacuum with an oil pump.

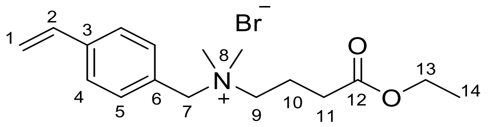

Yield: 4.71 g (13.21 mmol, 71%) of a colorless solid was obtained. **Chemical formula:** $C_{17}H_{26}BrNO_2$ **Molar mass:** 356.30 g/mol.

HRMS-ESI (m/z): $[M]^+$ calculated 276.1958; found 276.1964.

^{1}H-NMR: (500 MHz, D_2O, 25 °C) δ [ppm] = 7.61 (d, $^3J_{HH}$ = 8.1 Hz, 2H, **4-H**), 7.50 (d, $^3J_{HH}$ = 8.1 Hz, 2H, **5-H**), 6.83 (dd, $^3J_{HH}$ = 17.7,f 11.0 Hz, 1H, **2-H**), 5.94 (d, $^3J_{HH}$ = 17.6 Hz, 1H, **1-Ha**), 5.42 (d, $^3J_{HH}$ = 11.0 Hz, 1H, **1-Hb**), 4.48 (s, 2H, **7-H**), 4.16 (q, $^3J_{HH}$ = 7.1 Hz, 2H, **13-H**), 3.34–3.27 (m, 2H, **9-H**), 3.04 (s, 6H, **8-H**), 2.50 (t, $^3J_{HH}$ = 7.0 Hz, 2H, **11-H**), 2.22–2.12 (m, 2H, **10-H**), 1.23 (t, $^3J_{HH}$ = 7.2 Hz, 3H, **14-H**).

^{13}C-NMR: (126 MHz, D_2O, 25 °C) δ [ppm] = 174.9 (**C12**), 140.2 (**C3**), 136.1 (**C2**), 133.6 (**C5**), 127.1 (**C4**), 126.7 (**C6**), 116.7 (**C1**), 68.2 (**C7**), 63.2 (**C9**), 62.4 (**C13**), 50.0 (**C8**), 30.7 (**C11**), 18.1 (**C10**), 13.7 (**C14**).

FTIR (ATR): $\tilde{\nu}$ [cm^{-1}] = 2966, 1720, 1516, 1481, 1442, 1419, 1392, 1365, 1334, 1249, 1141, 1068, 1033, 999, 918, 902, 875, 856, 844, 829, 786, 729, 590, 462.

2-(Dimethyl(4-vinylbenzyl)ammonio)acetate

5.0 g (15.52 mmol, 1 eq.) ester was dissolved in 30 mL water. For deprotection, 14.59 g (1.25 eq.) Amberlyst A26 with an exchange capacity of 0.90 eq/L (for OH^-) and a density of 0.675 g/mL was added. After 18 h, the resin was filtered off and washed with 3 × 10 mL of water. The filtrate was lyophilized for work-up.

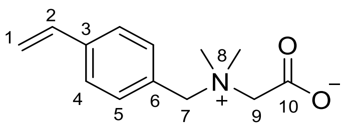

Yield: 2.52 g (11.49 mmol, 74%) of a colorless solid was obtained. **Chemical formula:** $C_{13}H_{17}NO_2$ **Molar mass:** 219.28 g/mol

HRMS-ESI (m/z): $[M+H]^+$ calculated 220.1332; found 220.1336.

^{1}H-NMR: (600 MHz, D_2O, 25 °C) δ [ppm] = 7.57 (d, $^3J_{HH}$ = 8.1 Hz, 2H, **4-H**), 7.44 (d, $^3J_{HH}$ = 8.3 Hz, 2H, **5-H**), 6.81 (dd, $^3J_{HH}$ = 17.7, 10.9 Hz, 1H, **2-H**), 5.93 (d, $^3J_{HH}$ = 17.7 Hz, 1H, **1-Ha**), 5.41 (d, $^3J_{HH}$ = 11.7 Hz, 1H, **1-Hb**), 4.68 (s, 2H, **H-7**), 3.69 (s, 2H, **H-9**), 3.16 (s, 6H, **8-H**).

^{13}C-NMR: (151 MHz, D_2O, 25 °C) δ [ppm] = 169.3 (**C10**), 139.6 (**C3**), 135.7 (**C2**), 133.0 (**C5**), 126.8 (**C4**), 126.7 (**C6**), 116.2 (**C1**), 66.5 (**C7**), 62.8 (**C9**), 50.8 (**C8**).

FTIR (ATR): $\tilde{\nu}$ [cm^{-1}] = 3479, 3325, 3078, 3001, 2970, 1651, 1469, 1435, 1377, 1323, 1222, 1184, 995, 956, 933, 914, 871, 856, 829, 767, 732, 709, 543, 408.

4-(Dimethyl(4-vinylbenzyl)ammonio)butanoate

5.0 g (14.03 mmol, 1 eq.) ester was dissolved in 30 mL water. For deprotection, 13.18 g (1.25 eq.) Amberlyst A26 with an exchange capacity of 0.90 eq/L (for OH^-) and a density of 0.675 g/mL was added. After 18 h, the resin was filtered off and washed with 3 × 10 mL of water. The filtrate was lyophilized for work-up.

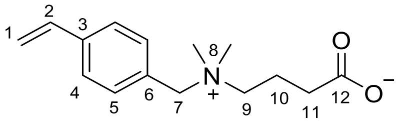

Yield: 1.77 g (7.16 mmol, 51%) of a colorless solid was obtained. **Chemical formula:** $C_{15}H_{21}NO_2$ **Molar mass:** 247.34 g/mol

HRMS-ESI (m/z): $[M+H]^+$ calculated 248.1645; found 248.1651.

^{1}H-NMR: (400 MHz, D_2O, 25 °C) δ [ppm] = 7.62 (d, $^3J_{HH}$ = 8.3 Hz, 2H, **4-H**), 7.51 (d, $^3J_{HH}$ = 8.3 Hz, 2H, **5-H**), 6.84 (dd, $^3J_{HH}$ = 17.7, 11.0 Hz, 1H, **2-H**), 5.96 (d, $^3J_{HH}$ = 16.9 Hz, 1H, **1-Ha**), 5.43 (d, $^3J_{HH}$ = 11.7 Hz, 1H, **1-Hb**), 4.47 (s, 2H, **H-7**), 3.33–3.24 (m, 2H, **9-H**), 3.02 (s, 6H, **H-8**), 2.27 (t, $^3J_{HH}$ = 7.3 Hz, 2H, **11-H**), 2.17–2.05 (m, 2H, **10-H**).

^{13}C-NMR: (101 MHz, D_2O, 25 °C) δ [ppm] = 180.7 (**C12**), 139.7 (**C3**), 135.7 (**C2**), 133.2 (**C5**), 126.7 (**C5**), 126.4 (**C6**), 116.3 (**C1**), 67.5 (**C7**), 63.7 (**C9**), 49.5 (**C8**), 33.6 (**C11**), 19.2 (**C10**).

FTIR (ATR): $\tilde{\nu}$ [cm^{-1}] = 3379, 3008, 1573, 1512, 1481, 1408, 1338, 1319, 1222, 995, 914, 860, 833, 759, 721, 405.

Poly(2-(dimethylamino)ethyl methacrylate)

The reaction was carried out according to a modified synthesis by VAN DE WETERING *et al.*[192] 10 mL (9.33 g, 59.3 mmol) 2-(dimethylamino)ethyl methacrylate were dissolved in 40 mL ultrapure water (20% v/v) in an inert gas atmosphere. Then 135 mg ammonium persulfate (0.593 mmol, M/I 100, mol/mol) were added, and the solution was stirred for 22 h at 60 °C. The resulting polymer was purified by extensive dialysis against water and isolated by lyophilization.

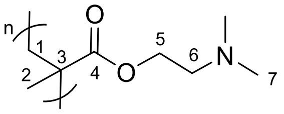

Yield: 8.40 g (90%) of a colorless solid was obtained. **Chemical formula:** $(C_8H_{15}NO_2)_n$ **Molecular weight distribution (M$_w$):** 20300 g/mol.

^{1}H-NMR: (400 MHz, D_2O, 25 °C) δ [ppm] = 4.38–3.99 (m, 2H, **5-H**), 2.97–2.64 (m, 2H, **6-H**), 2.45–2.31 (m, 6H, **7-H**), 2.19–1.79 (m, 2H, **1-H**), 1.26–0.812 (m, 3H, **2-H**).

FTIR (ATR): $\tilde{\nu}$ [cm^{-1}] = 3305, 2954, 2360, 2341, 2160, 2048, 1998, 1724, 1635, 1558, 1473, 1384, 1265, 1234, 1145, 1080, 991, 956, 887, 748, 451.

Poly(2-(methacryloyloxy)-*N*,*N*,*N*-trimethylethan-1-aminium chloride)

10.0 (75% in H_2O, 7.50 g, 36.1 mmol) METAC were dissolved in 35 mL ultrapure water (20% w/w) in an inert gas atmosphere. Then 82.4 mg ammonium persulfate (0.361 mmol, M/I 100, mol/mol) were added, and the solution was stirred for 22 h at 60 °C. The resulting polymer was purified by extensive dialysis against water and isolated by lyophilization.

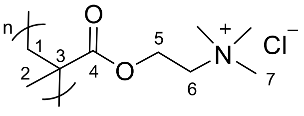

Yield: 6.98 g (93%) of a colorless solid was obtained. **Chemical formula:** $(C_9H_{18}ClNO_2)_n$ **Molecular weight distribution (M$_w$):** 5230 g/mol.

^{1}H-NMR: (400 MHz, D_2O, 25 °C) δ [ppm] = 4.72–4.29 (m, 2H, **5-H**), 4.02–3.64 (m, 2H, **6-H**), 3.39–3.19 (m, 9H, **7-H**), 2.37–1.63 (m, 2H, **1-H**), 1.49–0.89 (m, 3H, **2-H**).

^{13}C-NMR: (101 MHz, D_2O, 25 °C) δ [ppm] = 179.1 (**C4**), 64.5 (m, 2H, **C5**), 59.8 (m, 2H, **C6**), 54.3 (m, 9H, **C7**), 46.5 (**C1**), 19.0 (**C2**).

FTIR (ATR): $\tilde{\nu}$ [cm^{-1}] = 3371, 3016, 1720, 1639, 1477, 1261, 1234, 1145, 1041, 948, 898, 871, 748, 466.

Poly(2-(methacryloyloxy)-*N*,*N*-dimethylethan-1-amine oxide)

2.00 g Poly(2-(dimethylamino)ethyl methacrylate) was oxidized with H_2O_2 (10 mL, 30% w/w) for 24 h at 50 °C. The resulting polymer was purified by extensive dialysis against water and isolated by lyophilization.

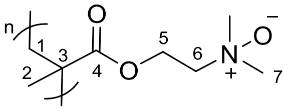

Yield: 2.12 g (96%) of a colorless solid was obtained. **Chemical formula:** $(C_8H_{15}NO_3)_n$ **Molecular weight distribution (M_w):** 213580 g/mol.

^{1}H-NMR: (400 MHz, D_2O, 25 °C) δ [ppm] = 4.45–4.34 (m, 2H, **5-H**), 3.82–3.57 (m, 2H, **6-H**), 3.36–3.57 (m, 6H, **7-H**), 22.2–1.51 (m, 2H, **1-H**), 1.23–0.77 (m, 3H, **2-H**).

^{13}C-NMR: (101 MHz, D_2O, 25 °C) δ [ppm] = 178.7 (**C4**), 68.3 (**C5**), 60.0 (**C6**), 58.9 (**C7**), 45.2 (**C1**), 18.3 (**C2**).

FTIR (ATR): $\tilde{\nu}$ [cm^{-1}] = 3224, 1720, 1454, 1396, 1319, 1234, 1153, 1060, 1033, 956, 898, 748, 725, 493, 462, 439.

Poly(2-((2-(methacryloyloxy)ethyl)dimethylammonio)ethane-1-sulfonate)

2.0 g Poly(2-(dimethylamino)ethyl methacrylate) was alkylated with 2-bromoethanolsulfonate solution (2.0 mL, 1 M) for 24 h at 50 °C. The resulting polymer was purified by extensive dialysis against water and isolated by lyophilization.

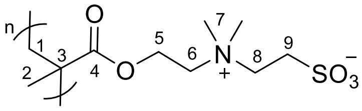

Yield: 2.70 g (80%) of a colorless solid was obtained. **Chemical formula:** $(C_{10}H_{19}NO_5S)_n$ **Molecular weight distribution (M_w):** 11600 g/mol.

^{1}H-NMR: (400 MHz, D_2O, 25 °C) δ [ppm] = 4.61–4.10 (m, 2H, **5-H**), 3.95–3.80 (m, 2H, **9-H**), 3.55–3.42 (m, 2H, **8-H**), 3.39–3.02 (m, 6H, **H-6**, **7-H**), 2.87–2.48 (m, -**N(Me)₂**), 2.29–1.61 (m, 2H, **1-H**),1.32–0.60 (m, 3H, **2-H**).

FTIR (ATR): $\tilde{\nu}$ [cm^{-1}] = 3421, 2951, 2823, 2769, 1724, 1465, 1388, 1145, 1037, 964, 852, 748, 601, 520.

Poly(2-((2-(methacryloyloxy)ethyl)dimethylammonio)acetate)

2.00 g Poly(2-(dimethylamino)ethyl methacrylate) was alkylated with chloroacetate solution (2.0 mL, 1 M) for 24 h at 50 °C. The resulting polymer was purified by extensive dialysis against water and isolated by lyophilization.

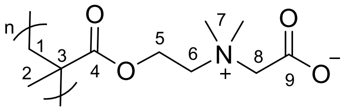

Yield: 2.38 g (87%) of a colorless solid was obtained. **Chemical formula:** $(C_{10}H_{17}NO_4)_n$ **Molecular weight distribution (M_w):** 223980 g/mol.

^{1}H-NMR: (400 MHz, D_2O, 25 °C) δ [ppm] = 4.67–3.86 (m, 6H, **8-H**, **6-H**, **5-H**), 3.54–3.22 (m, 6H, **7-H**), 3.04–2.87 (m, -**N(Me)$_2$**), 2.35–1.64 (m, 2H, **1-H**), 1.23–0.83 (m, 3H, **2-H**).

^{13}C-NMR: (101 MHz, D_2O, 25 °C) δ [ppm] = 178.5 (**C4**), 168.7 (**C9**), 64.7 (**C8**), 61.6 (**C5**), 59.8 (**C6**), 52.7 (**C7**), 45.3 (**C1**), 43.6 (-**N(Me)$_2$**), 18.7 (**C2**).

FTIR (ATR): $\tilde{\nu}$ [cm^{-1}] = 3387, 1720, 1624, 1473, 1388, 1327, 1265, 1230, 1145, 995, 960, 933, 891, 860, 833, 709, 493.

Poly(2-hydroxy-*N*-(2-(methacryloyloxy)ethyl)-*N*,*N*-dimethylethan-1-aminium bromide)

2.00 g Poly(2-(dimethylamino)ethyl methacrylate) was alkylated with 2-bromoethanol (2.0 mL, 28.2 mmol) for 24 h at 50 °C. The resulting polymer was purified by extensive dialysis against water and isolated by lyophilization.

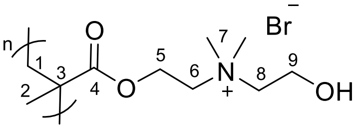

Yield: 2.87 g (80%) of a colorless solid was obtained. **Chemical formula:** $(C_{10}H_{20}BrNO_3)_n$ **Molecular weight distribution (M_w):** 26400 g/mol.

^{1}H-NMR: (400 MHz, D_2O, 25 °C) δ [ppm] = 4.68–4.28 (m, 2H, **5-H**), 4.23–4.09 (m, 2H, **9-H**), 4.07–3.77 (m, 2H, **6-H**), 3.75–3.53 (m, 2H, **8-H**), 3.40–3.25 (m, 6H, **7-H**), 2.92–2.78(-**N(Me)$_2$**), 2.29–1.68 (m, 2H, **1-H**), 1.24–0.89 (m, 2H, **2-H**).

FTIR (ATR): $\tilde{\nu}$ [cm^{-1}] = 3305, 2954, 1724, 1635, 1558, 1473, 1384, 1265, 1234, 1145, 1080, 991, 956, 748, 451.

Poly(2-(methacryloyloxy)ethyl (2-(trimethylammonio)ethyl) phosphate)

5.00 (16.9 mmol) phosphobetaine were dissolved in 25 mL ultrapure water (20% w/w) in an inert gas atmosphere. Then 38.6 mg ammonium persulfate (0.169 mmol, M/I 100, mol/mol) were added, and the solution was stirred for 22 h at 60 °C. The resulting polymer was purified by extensive dialysis against water and isolated by lyophilization.

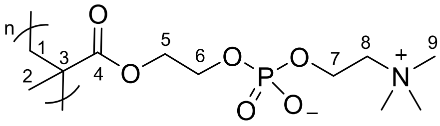

Yield: 4.45 g (89%) of a colorless solid was obtained. **Chemical formula:** $(C_{11}H_{22}NO_6P)_n$ **Molecular weight distribution (M_w):** 461640 g/mol.

^{1}H-NMR: (400 MHz, D_2O, 25 °C) δ [ppm] = 4.40–4.03 (m, 6H, **7-H**, **6-H**, **5-H**), 3.76–3.64 (m, 2H, **8-H**), 3.33–3.19 (m, 9H, **9-H**), 2.39–1.48 (m, 2H, **1-H**), 1.39–0.70 (m, 3H, **2-H**).

^{13}C-NMR: (101 MHz, D_2O, 25 °C) δ [ppm] = 179.7 (**C4**), 66.4 (**C6**), 65.6 **(C5**), 63.7 (**C7**), 59.9 (**C8**), 54.4 (**C9**), 45.2 (**C1**), 18.5 (**C2**).

FTIR (ATR): $\tilde{\nu}$ [cm^{-1}] = 3421, 2951, 2823, 2769, 1724, 1647, 1465, 1388, 1145, 1037, 964, 852, 748, 601, 520, 462.

Perfluorophenyl dimethylglycinate

3.65 g (32.4 mmol, 1.3 eq.) dimethylglycine were dissolved in 65 mL of CH_2Cl_2. The solution was cooled to 0 °C in an ice bath. While stirring continuously, 4.60 g (25.0 mmol, 1.0 eq.) PFP and 7.19 g (37.5 mmol, 1.5 eq.) EDC·HCl were added successively. The reaction mixture was left to stand overnight at room temperature with continuous stirring. The reaction was then terminated by adding 65 mL of a saturated $NaHCO_3$ solution. The aqueous phase was extracted three times with 65 mL CH_2Cl_2 each time. The combined organic phases were washed twice with 260 mL of saturated NaCl solution each, dried over anhydrous $MgSO_4$, and filtered. The solvent was removed under reduced pressure to isolate the product.

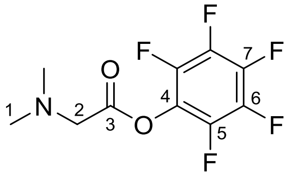

Yield: 6.58 g (24.4 mmol, 97%) of an orange oil was obtained. **Chemical formula:** $C_{10}H_8F_5NO_2$ **Molar mass:** 269.17 g/mol.

HRMS-ESI (m/z): $[M+H]^+$ calculated 270.0548; found 270.0523.

^{1}H-NMR: (600 MHz, $CDCl_3$, 25 °C) δ [ppm] = 3.57 (s, 2H, **2-H**), 2.45 (s, 6H, **1-H**).

^{13}C-NMR: (151 MHz, D_2O, 25 °C) δ [ppm] = 166.7 (**C3**), 142.1 (**C6**), 140.3 (**C4**), 138.9 (**C7**), 137.2 (**C5**), 59.5 (**C2**), 45.0 (**C1**).

^{19}F-NMR: (151 MHz, D_2O, 25 °C) δ [ppm] = -152.3 (**5-F**), -157.8 (**7-F**), -162.19 (**6-F**).

FTIR (ATR): $\tilde{\nu}$ [cm^{-1}] = 3012, 2963, 2878, 2759, 1796, 1517, 1475, 1409, 1225, 1146, 1126, 1013, 991, 916, 860, 830, 781, 758, 725, 630, 558, 521.

9 Literature

[1] Gleick, P. H.; Cooley, H. Freshwater Scarcity. *Annu. Rev. Environ. Resour.* **2021**, *46* (1), 319-348.

[2] Stephens, G. L.; Slingo, J. M.; Rignot, E.; Reager, J. T.; Hakuba, M. Z.; Durack, P. J.; Worden, J.; Rocca, R. Earth's water reservoirs in a changing climate. *Proc. R. Soc. A: Math. Phys. Eng. Sci.* **2020**, *476* (2236), 20190458.

[3] Biswas, A.; Sarkar, S.; Das, S.; Dutta, S.; Roy Choudhury, M.; Giri, A.; Bera, B.; Bag, K.; Mukherjee, B.; Banerjee, K.; et al. Water scarcity: A global hindrance to sustainable development and agricultural production – A critical review of the impacts and adaptation strategies. *Camb. Prism. Water* **2025**, *3*, 1-22.

[4] *Statista*. https://www.statista.com/chart/26140/water-stress-projections-global/ (accessed 24.07.25).

[5] Clarke, B.; Otto, F.; Stuart-Smith, R.; Harrington, L. Extreme weather impacts of climate change: an attribution perspective. *Environ. Res.: Climate* **2022**, *1* (1), 012001.

[6] van Vliet, M. T. H.; Jones, E. R.; Flörke, M.; Franssen, W. H. P.; Hanasaki, N.; Wada, Y.; Yearsley, J. R. Global water scarcity including surface water quality and expansions of clean water technologies. *Environ. Res. Lett.* **2021**, *16*, 024020.

[7] UNESCO. The United Nations World Water Development Report 2018: Nature-Based Solutions for Water; *UNESCO*: Paris, **2018**; 38-50.

[8] Schwarzenbach, R. P.; Egli, T.; Hofstetter, T. B.; von Gunten, U.; Wehrli, B. Global Water Pollution and Human Health. *Annu. Rev. Environ. Resour.* **2010**, *35* (1), 109-136.

[9] UNESCO. The United Nations World Water Development Report 2024: Water for prosperity and peace; *UNESCO*: Paris, **2024**; 27-40.

[10] Obotey Ezugbe, E.; Rathilal, S. Membrane Technologies in Wastewater Treatment: A Review. *Membranes (Basel)* **2020**, *10* (5), 89.

[11] Baker, J. S.; Dudley, L. Y. Biofouling in membrane systems — A review. *Desalination* **1998**, *118* (1-3), 81-89.

[12] Rana, D.; Matsuura, T. Surface modifications for antifouling membranes. *Chem. Rev.* **2010**, *110* (4), 2448-2471.

[13] Baker, R. W. Membrane Technology and Applications, 3rd ed.; *Wiley*, **2012**, 1-14.

[14] Tranchant, C. C.; Selvamuthukumaran, M. Applications of Membrane Technology for Food Processing Industrie, 1st ed.; *CRC Press*, Boca Raton, **2020**, 1-27.

[15] Lee, A.; Elam, J. W.; Darling, S. B. Membrane materials for water purification: design, development, and application. *Environ. Sci.: Water Res. Technol.* **2016**, *2* (1), 17-42.

[16] Strathmann, H. Membranes and Membrane Separation Processes, 1. Principles. In *Ullmann's Encyclopedia of Industrial Chemistry*. *Wiley* **2011**, 420-422.

[17] Ji, Y.-L.; Gu, B.-X.; An, Q.-F.; Gao, C.-J. Recent Advances in the Fabrication of Membranes Containing “Ion Pairs” for Nanofiltration Processes. *Polymers* **2017**, *9* (12), 715.

[18] Bazinet, L.; Moalic, M. Coupling of porous filtration and ion-exchange membranes in an electrodialysis stack and impact on cation selectivity: A novel approach for sea water demineralization and the production of physiological water. *Desalination* **2011**, *277* (1-3), 356-363.

[19] Selatile, M. K.; Ray, S. S.; Ojijo, V.; Sadiku, R. Recent developments in polymeric electrospun nanofibrous membranes for seawater desalination. *RSC Adv.* **2018**, *8* (66), 37915-37938.

[20] Anis, S. F.; Hashaikeh, R.; Hilal, N. Microfiltration membrane processes: A review of research trends over the past decade. *J. Water Process Eng.* **2019**, *32*, 100941.

[21] Al Aani, S.; Mustafa, T. N.; Hilal, N. Ultrafiltration membranes for wastewater and water process engineering: A comprehensive statistical review over the past decade. *J. Water Process Eng.* **2020**, *35*, 101241.

[22] Mohammad, A. W.; Teow, Y. H.; Ang, W. L.; Chung, Y. T.; Oatley-Radcliffe, D. L.; Hilal, N. Nanofiltration membranes review: Recent advances and future prospects. *Desalination* **2015**, *356*, 226-254.

[23] Malaeb, L.; Ayoub, G. M. Reverse osmosis technology for water treatment: State of the art review. *Desalination* **2011**, *267* (1), 1-8.

[24] Melin, T.; Rautenbach, R. Membranverfahren, 3rd ed.; *Springer* **2007**, 309-322.

[25] Vogel, H. C.; Todaro, C. M. Fermentation and Biochemical Engineering Handbook. *Noyes Publications* **1996**, (2), 271-283.

[26] Matsuura, T. Progress in membrane science and technology for seawater desalination — a review. *Desalination* **2001**, *134* (1-3), 47-54.

[27] Tsai, H. Effect of surfactant addition on the morphology and pervaporation performance of asymmetric polysulfone membranes. *J. Membr. Sci.* **2000**, *176* (1), 97-103.

[28] Chaturvedi, B. K.; Ghosh, A. K.; Ramachandhran, V.; Trivedi, M. K.; Hanra, M. S.; Misra, B. M. Preparation, characterization and performance of polyethersulfone ultrafiltration membranes. *Desalination* **2001**, *133* (1), 31-40.

[29] Scharnagl, N.; Buschatz, H. Polyacrylonitrile (PAN) membranes for ultra- and microfiltration. *Desalination* **2001**, *139* (1-3), 191-198.

[30] Arthanareeswaran, G.; Sriyamunadevi, T.; Raajenthiren, M. Effect of silica particles on cellulose acetate blend ultrafiltration membranes: Part I. *Sep. Purif. Technol.* **2008**, *64* (1), 38-47.

[31] Wang, D.; Li, K.; Teo, W. K. Preparation and characterization of polyvinylidene fluoride (PVDF) hollow fiber membranes. *J. Membr. Sci.* **1999**, *163* (2), 211-220.

[32] Yoo, S. H.; Kim, J. H.; Jho, J. Y.; Won, J.; Kang, Y. S. Influence of the addition of PVP on the morphology of asymmetric polyimide phase inversion membranes: effect of PVP molecular weight. *J. Membr. Sci.* **2004**, *236* (1-2), 203-207.

[33] Zeni, M.; Riveros, R.; de Souza, J. F.; Mello, K.; Meireles, C.; Filho, G. R. Morphologic analysis of porous polyamide 6,6 membranes prepared by phase inversion. *Desalination* **2008**, *221* (1-3), 294-297.

[34] Wang, H. H.; Jung, J. T.; Kim, J. F.; Kim, S.; Drioli, E.; Lee, Y. M. A novel green solvent alternative for polymeric membrane preparation via nonsolvent-induced phase separation (NIPS). *J. Membr. Sci.* **2019**, *574*, 44-54.

[35] Dong, X.; Lu, D.; Harris, T. A. L.; Escobar, I. C. Polymers and Solvents Used in Membrane Fabrication: A Review Focusing on Sustainable Membrane Development. *Membranes (Basel)* **2021**, *11* (5), 309.

[36] Cornelissen, E. R.; van den Boomgaard, T.; Strathmann, H. Physicochemical aspects of polymer selection for ultrafiltration and microfiltration membranes. *Colloids Surf. A* **1998**, *138* (2-3), 283-289.

[37] Nouzaki, K.; Nagata, M.; Arai, J.; Idemoto, Y.; Koura, N.; Yanagishita, H.; Negishi, H.; Kitamoto, D.; Ikegami, T.; Haraya, K. Preparation of polyacrylonitrile ultrafiltration membranes for wastewater treatment. *Desalination* **2002**, *144* (1-3), 53-59.

[38] Yoon, K.; Hsiao, B. S.; Chu, B. High flux nanofiltration membranes based on interfacially polymerized polyamide barrier layer on polyacrylonitrile nanofibrous scaffolds. *J. Membr. Sci.* **2009**, *326* (2), 484-492.

[39] Klaysom, C.; Hermans, S.; Gahlaut, A.; Van Craenenbroeck, S.; Vankelecom, I. F. J. Polyamide/Polyacrylonitrile (PA/PAN) thin film composite osmosis membranes: Film optimization, characterization and performance evaluation. *J. Membr. Sci.* **2013**, *445*, 25-33.

[40] Maske, V. A.; Kokate, A. M.; More, P. A.; Salunkhe, R. S.; More, A. P. A comprehensive review of polyacrylonitrile membranes: modifications and applications. *Polym. Bull.* **2024**, *81* (18), 16415-16455.

[41] Wente, V. A. Superfine Thermoplastic Fibers. *Ind. Eng. Chem.* **1956**, *48* (8), 1342-1346.

[42] Sun, F.; Li, T. T.; Zhang, X.; Shiu, B. C.; Zhang, Y.; Ren, H. T.; Peng, H. K.; Lin, J. H.; Lou, C. W. In situ growth polydopamine decorated polypropylen melt-blown membrane for highly efficient oil/water separation. *Chemosphere* **2020**, *254*, 126873.

[43] Deng, N.; He, H.; Yan, J.; Zhao, Y.; Ben Ticha, E.; Liu, Y.; Kang, W.; Cheng, B. One-step melt-blowing of multi-scale micro/nano fabric membrane for advanced air-filtration. *Polymer* **2019**, *165*, 174-179.

[44] González-Sánchez, A.; Rosas-Macías, R.; Hernández-Bautista, J. E.; Valdez-Garza, J. A.; Rodríguez-Fuentes, N.; Soriano-Corral, F.; Ledezma-Pérez, A. S.; Ávila-Orta, C. A.; Cruz-Delgado, V. J. Antimicrobial Properties of Polyester/Copper Nanocomposites by Melt-Spinning and Melt-Blowing Techniques. *Textiles* **2023**, *4* (1), 1-16.

[45] Yesil, Y.; Bhat, G. S. Porosity and barrier properties of polyethylene meltblown nonwovens. *J. Text. Inst.* **2016**, *108* (6), 1035-1040.

[46] Lee, Y. E.; Wadsworth, L. C. Fiber and web formation of melt-blown thermoplastic polyurethane polymers. *J. Appl. Polym. Sci.* **2007**, *105* (6), 3724-3727.

[47] Drabek, J.; Zatloukal, M. Meltblown technology for production of polymeric microfibers/nanofibers: A review. *Phys. Fluids* **2019**, *31* (9), 091301.

[48] Dutton, K. C. Overview and analysis of the meltblown process and parameters. *J. Text. Apparel, Technol. Manage.* **2009**, *6* (1), 1-25.

[49] Drabek, J.; Zatloukal, M. Influence of long chain branching on fiber diameter distribution for polypropylene nonwovens produced by melt blown process. *J. Rheol.* **2019**, *63* (4), 519-532.

[50] Ellison, C. J.; Phatak, A.; Giles, D. W.; Macosko, C. W.; Bates, F. S. Melt blown nanofibers: Fiber diameter distributions and onset of fiber breakup. *Polymer* **2007**, *48* (11), 3306-3316.

[51] Fang, Z.; Wang, J.; Xie, S.; Lian, Z.; Luo, Z.; Du, Y.; Zhang, X. Advancements in Research and Applications of PP-Based Materials Utilizing Melt-Blown Nonwoven Technology. *Polymers (Basel)* **2025**, *17* (8), 1013.

[52] Sun, Y.; Sun, H.; Yu, B.; Yang, X.; Xu, T. Preparation of CCO@M-PP MB for Oil–Water Separation. *Fibers Polym.* **2024**, *25* (2), 725-735.

[53] Chen, H.; Guo, M.; Yao, X.; Luo, Z.; Dong, K.; Lian, Z.; Wei, W. Green and Efficient Synthesis of an Adsorbent Fiber by Plasma-induced Grafting of Glycidyl Methacrylate and Its Cd(II) Adsorption Performance. *Fibers Polym.* **2018**, *19* (4), 722-733.

[54] Guo, M.; Chen, H.; Luo, Z.; Lian, Z.; Wei, W. Selective removal of Pb(II) ions from aqueous solutions by acrylic acid/acrylamide comonomer grafted polypropylene fibers. *Fibers Polym.* **2017**, *18* (8), 1459-1467.

[55] Liu, C.; Shi, J.; Luo, F.; Zhang, X. Preparation, characterization and antibacterial properties of hydro-charged melt-blown nonwovens coated with an N-halamine. *New J. Chem.* **2024**, *48* (45), 19355-19363.

[56] Lin, C.-J.; Shirazi, S.; Rao, P. Mechanistic Model for CaSO4 Fouling on Nanofiltration Membrane. *J. Environ. Eng. (N. Y.)* **2005**, *131* (10), 1387-1392.

[57] Tracey, E. M.; Davis, R. H. Protein Fouling of Track-Etched Polycarbonate Microfiltration Membranes. *J. Colloid Interface Sci.* **1994**, *167* (1), 104-116.

[58] Faibish, R. S.; Cohen, Y. Fouling and rejection behavior of ceramic and polymer-modified ceramic membranes for ultrafiltration of oil-in-water emulsions and microemulsions. *Colloids Surf. A* **2001**, *191* (1-2), 27-40.

[59] Speth, T. F.; Summers, R. S.; Gusses, A. M. Nanofiltration Foulants from a Treated Surface Water. *Environ. Sci. Technol.* **1998**, *32* (22), 3612-3617.

[60] Jones, K. L.; O'Melia, C. R. Ultrafiltration of protein and humic substances: effect of solution chemistry on fouling and flux decline. *J. Membr. Sci.* **2001**, *193* (2), 163-173.

[61] Ladewig, B.; Al-Shaeli, M. N. Z. Fundamentals of Membrane Bioreactors - Materials, Systems and Membrane Fouling, 1st ed.; *Springer*, **2017**, 39-85.

[62] Ahmad, A.; Alshammari, M. B. Nanofiltration Membrane for Water Purification, 1st ed.; *Springer* **2023**, 208-212.

[63] Iritani, E. A Review on Modeling of Pore-Blocking Behaviors of Membranes During Pressurized Membrane Filtration. *Dry. Technol.* **2013**, *31* (2), 146-162.

[64] Van de Lisdonk, C. A. C.; Van Paassen, J. A. M.; Schippers, J. C. Monitoring scaling in nanofiltration and reverse osmosis membrane systems. *Desalination* **2000**, *132* (1-3), 101-108.

[65] Sablani, S. S.; Goosen, M. F. A.; Al-Belushi, R.; Wilf, M. Concentration polarization in ultrafiltration and reverse osmosis: a critical review. *Desalination* **2001**, *141* (3), 269-289.

[66] Lee, S.; Kim, J.; Lee, C.-H. Analysis of CaSO4 scale formation mechanism in various nanofiltration modules. *J. Membr. Sci.* **1999**, *163* (1), 63-74.

[67] Hasson, D.; Drak, A.; Semiat, R. Inception of CaSO4 scaling on RO membranes at various water recovery levels. *Desalination* **2001**, *139* (1-3), 73-81.

[68] Meng, F.; Chae, S. R.; Drews, A.; Kraume, M.; Shin, H. S.; Yang, F. Recent advances in membrane bioreactors (MBRs): membrane fouling and membrane material. *Water Res.* **2009**, *43* (6), 1489-1512.

[69] Wang, Z.; Wu, Z.; Yin, X.; Tian, L. Membrane fouling in a submerged membrane bioreactor (MBR) under sub-critical flux operation: Membrane foulant and gel layer characterization. *J. Membr. Sci.* **2008**, *325* (1), 238-244.

[70] Costa, A.; Depinho, M.; Elimelech, M. Mechanisms of colloidal natural organic matter fouling in ultrafiltration. *J. Membr. Sci.* **2006**, *281* (1-2), 716-725.

[71] Cho, J.; Amy, G.; Pellegrino, J.; Yoon, Y. Characterization of clean and natural organic matter (NOM) fouled NF and UF membranes, and foulants characterization. *Desalination* **1998**, *118* (1-3), 101-108.

[72] Warsinger, D. M.; Swaminathan, J.; Guillen-Burrieza, E.; Arafat, H. A.; Lienhard V, J. H. Scaling and fouling in membrane distillation for desalination applications: A review. *Desalination* **2015**, *356*, 294-313.

[73] Feng, H.; Liang, Y. N.; Hu, X. Natural organic matter (NOM), an underexplored resource for environmental conservation and remediation. *Mater. Today Sustain.* **2022**, *19*, 100159.

[74] Al-Amoudi, A. S. Factors affecting natural organic matter (NOM) and scaling fouling in NF membranes: A review. *Desalination* **2010**, *259* (1-3), 1-10.

[75] Janex, M. L.; Baudin, I.; Campos, C.; Laîné, J. M. Understanding membrane fouling: a review of over a decade of research. *Water Supply* **2003**, *3* (5-6), 155-164.

[76] Ishiwatari, R. Molecular weight distribution of humic acids from lake and marine sediments. *Geochem. J.* **1971**, *5* (3), 121-132.

[77] Lipczynska-Kochany, E. Humic substances, their microbial interactions and effects on biological transformations of organic pollutants in water and soil: A review. *Chemosphere* **2018**, *202*, 420-437.

[78] Komlenic, R. Rethinking the causes of membrane biofouling. *Filtr. Sep.* **2010**, *47* (5), 26-28.

[79] Sauer, K.; Camper, A. K.; Ehrlich, G. D.; Costerton, J. W.; Davies, D. G. Pseudomonas aeruginosa displays multiple phenotypes during development as a biofilm. *J. Bacteriol.* **2002**, *184* (4), 1140-1154.

[80] Petrova, O. E.; Sauer, K. A novel signaling network essential for regulating Pseudomonas aeruginosa biofilm development. *PLOS Pathog.* **2009**, *5* (11), 1-16.

[81] Rumbaugh, K. P.; Sauer, K. Biofilm dispersion. *Nat. Rev. Microbiol.* **2020**, *18* (10), 571-586.

[82] Loosdrecht, M. C. M.; Picioreanu, C.; Heijnen, J. J. A more unifying hypothesis for biofilm structures. *FEMS Microbiol. Ecol.* **2006**, *24* (2), 181-183.

[83] Chen, C. L.; Liu, W. T.; Chong, M. L.; Wong, M. T.; Ong, S. L.; Seah, H.; Ng, W. J. Community structure of microbial biofilms associated with membrane-based water purification processes as revealed using a polyphasic approach. *Appl. Microbiol. Biotechnol.* **2004**, *63* (4), 466-473.

[84] Flemming, H. C.; Schaule, G. Biofouling on membranes - A microbiological approach. *Desalination* **1988**, *70* (1-3), 95-119.

[85] Flemming, H.-C. Reverse osmosis membrane biofouling. *Exp. Therm. Fluid Sci.* **1997**, *14* (4), 382-391.

[86] Kappachery, S.; Paul, D.; Yoon, J.; Kweon, J. H. Vanillin, a potential agent to prevent biofouling of reverse osmosis membrane. *Biofouling* **2010**, *26* (6), 667-672.

[87] Drioli, E.; Giorno, L. Encyclopedia of Membranes, 1st ed.; *Springer*, **2016**, 1555-1557.

[88] Hong, S. P.; Bae, T. H.; Tak, T. M.; Hong, S.; Randall, A. Fouling control in activated sludge submerged hollow fiber membrane bioreactors. *Desalination* **2002**, *143* (3), 219-228.

[89] Regula, C.; Carretier, E.; Wyart, Y.; Gesan-Guiziou, G.; Vincent, A.; Boudot, D.; Moulin, P. Chemical cleaning/disinfection and ageing of organic UF membranes: a review. *Water Res.* **2014**, *56*, 325-365.

[90] Maan, A. M. C.; Hofman, A. H.; Vos, W. M.; Kamperman, M. Recent Developments and Practical Feasibility of Polymer-Based Antifouling Coatings. *Adv. Funct. Mater.* **2020**, *30* (32), 2000936.

[91] Razatos, A.; Ong, Y.-L.; Boulay, F.; Elbert, D. L.; Hubbell, J. A.; Sharma, M. M.; Georgiou, G. Force Measurements between Bacteria and Poly(ethylene glycol)-Coated Surfaces. *Langmuir* **2000**, *16* (24), 9155-9158.

[92] Hui, N.; Sun, X.; Niu, S.; Luo, X. PEGylated Polyaniline Nanofibers: Antifouling and Conducting Biomaterial for Electrochemical DNA Sensing. *ACS Appl. Mater. Interfaces* **2017**, *9* (3), 2914-2923.

[93] Lee, J. H.; Kopecek, J.; Andrade, J. D. Protein-resistant surfaces prepared by PEO-containing block copolymer surfactants. *J. Biomed. Mater. Res.* **1989**, *23* (3), 351-368.

[94] Currie, E. P.; Norde, W.; Cohen Stuart, M. A. Tethered polymer chains: surface chemistry and their impact on colloidal and surface properties. *Adv. Colloid Interface Sci.* **2003**, *100-102*, 205-265.

[95] Dalsin, J. L.; Messersmith, P. B. Bioinspired antifouling polymers. *Mater. Today* **2005**, *8* (9), 38-46.

[96] Han, S.; Kim, C.; Kwon, D. Thermal/oxidative degradation and stabilization of polyethylene glycol. *Polymer* **1997**, *38* (2), 317-323.

[97] Kalasin, S.; Letteri, R. A.; Emrick, T.; Santore, M. M. Adsorbed Polyzwitterion Copolymer Layers Designed for Protein Repellency and Interfacial Retention. *Langmuir* **2017**, *33* (47), 13708-13717.

[98] Wang, M.; Yuan, J.; Huang, X.; Cai, X.; Li, L.; Shen, J. Grafting of carboxybetaine brush onto cellulose membranes via surface-initiated ARGET-ATRP for improving blood compatibility. *Colloids Surf. B* **2013**, *103*, 52-58.

[99] Wang, T.; Wang, Y.-Q.; Su, Y.-L.; Jiang, Z.-Y. Antifouling ultrafiltration membrane composed of polyethersulfone and sulfobetaine copolymer. *J. Membr. Sci.* **2006**, *280* (1-2), 343-350.

[100] Venault, A.; Hsu, C.-H.; Ishihara, K.; Chang, Y. Zwitterionic bi-continuous membranes from a phosphobetaine copolymer/poly(vinylidene fluoride) blend via VIPS for biofouling mitigation. *J. Membr. Sci.* **2018**, *550*, 377-388.

[101] Feng, Z.; Feng, X.; Lu, X. Bioinspired N-Oxide-Based Zwitterionic Polymer Brushes for Robust Fouling-Resistant Surfaces. *Environ. Sci. Technol.* **2023**, *57* (18), 7298-7308.

[102] Berking, B. B.; Poulladofonou, G.; Karagrigoriou, D.; Wilson, D. A.; Neumann, K. Zwitterionic Polymeric Sulfur Ylides with Minimal Charge Separation Open a New

Generation of Antifouling and Bactericidal Materials. *Angew. Chem. Int. Ed.* **2023**, *62*, 202308971.

[103] He, M.; Gao, K.; Zhou, L.; Jiao, Z.; Wu, M.; Cao, J.; You, X.; Cai, Z.; Su, Y.; Jiang, Z. Zwitterionic materials for antifouling membrane surface construction. *Acta Biomater.* **2016**, *40*, 142-152.

[104] Leonardi, A. K.; Ober, C. K. Polymer-Based Marine Antifouling and Fouling Release Surfaces: Strategies for Synthesis and Modification. *Annu. Rev. Chem. Biomol. Eng.* **2019**, *10*, 241-264.

[105] Huang, Q.-L.; Xiao, C.-f.; Feng, X.-s.; Hu, X.-Y. Design of super-hydrophobic microporous polytetrafluoroethylene membranes. *New J. Chem.* **2013**, *37* (2), 373-379.

[106] Kujawska, A.; Knozowska, K.; Kujawa, J.; Li, G.; Kujawski, W. Fabrication of PDMS based membranes with improved separation efficiency in hydrophobic pervaporation. *Sep. Purif. Technol.* **2020**, *234*, 116092.

[107] Kuo, C.-Y.; Lin, H.-N.; Tsai, H.-A.; Wang, D.-M.; Lai, J.-Y. Fabrication of a high hydrophobic PVDF membrane via nonsolvent induced phase separation. *Desalination* **2008**, *233* (1-3), 40-47.

[108] Chen, R.; Wan, Y.; Wu, W.; Yang, C.; He, J.-H.; Cheng, J.; Jetter, R.; Ko, F. K.; Chen, Y. A lotus effect-inspired flexible and breathable membrane with hierarchical electrospinning micro/nanofibers and ZnO nanowires. *Mater. Des.* **2019**, *162*, 246-248.

[109] Siedenbiedel, F.; Tiller, J. C. Antimicrobial Polymers in Solution and on Surfaces: Overview and Functional Principles. *Polymers* **2012**, *4* (1), 46-71.

[110] Ping, M.; Zhang, X.; Liu, M.; Wu, Z.; Wang, Z. Surface modification of polyvinylidene fluoride membrane by atom-transfer radical-polymerization of quaternary ammonium compound for mitigating biofouling. *J. Membr. Sci.* **2019**, *570-571*, 286-293.

[111] Zhang, X.; Ma, J.; Tang, C. Y.; Wang, Z.; Ng, H. Y.; Wu, Z. Antibiofouling Polyvinylidene Fluoride Membrane Modified by Quaternary Ammonium Compound: Direct Contact-Killing versus Induced Indirect Contact-Killing. *Environ. Sci. Technol.* **2016**, *50* (10), 5086-5093.

[112] Park, J. A.; Kim, S. B. Antimicrobial filtration with electrospun poly(vinyl alcohol) nanofibers containing benzyl triethylammonium chloride: Immersion, leaching, toxicity, and filtration tests. *Chemosphere* **2017**, *167*, 469-477.

[113] Zhang, X.; Wang, Z.; Chen, M.; Ma, J.; Chen, S.; Wu, Z. Membrane biofouling control using polyvinylidene fluoride membrane blended with quaternary ammonium compound assembled on carbon material. *J. Membr. Sci.* **2017**, *539*, 229-237.

[114] Zhang, X.; Wang, Z.; Tang, C. Y.; Ma, J.; Liu, M.; Ping, M.; Chen, M.; Wu, Z. Modification of microfiltration membranes by alkoxysilane polycondensation induced quaternary ammonium compounds grafting for biofouling mitigation. *J. Membr. Sci.* **2018**, *549*, 165-172.

[115] Ben-Sasson, M.; Zodrow, K. R.; Genggeng, Q.; Kang, Y.; Giannelis, E. P.; Elimelech, M. Surface functionalization of thin-film composite membranes with copper nanoparticles for antimicrobial surface properties. *Environ. Sci. Technol.* **2014**, *48* (1), 384-393.

[116] Huang, L.; Zhao, S.; Wang, Z.; Wu, J.; Wang, J.; Wang, S. In situ immobilization of silver nanoparticles for improving permeability, antifouling and anti-bacterial properties of ultrafiltration membrane. *J. Membr. Sci.* **2016**, *499*, 269-281.

[117] Chen, X.; Zhang, G.; Zhang, Q.; Zhan, X.; Chen, F. Preparation and Performance of Amphiphilic Polyurethane Copolymers with Capsaicin-Mimic and PEG Moieties for Protein Resistance and Antibacteria. *Ind. Eng. Chem. Res.* **2015**, *54* (15), 3813-3820.

[118] Qin, A.; Li, X.; Zhao, X.; Liu, D.; He, C. Preparation and characterization of nano-chitin whisker reinforced PVDF membrane with excellent antifouling property. *J. Membr. Sci.* **2015**, *480*, 1-10.

[119] Tian, M.; Xu, H.; Yao, L.; Wang, R. A biomimetic antimicrobial surface for membrane fouling control in reverse osmosis for seawater desalination. *Desalination* **2021**, *503*, 114954.

[120] Tiller, J. C.; Liao, C. J.; Lewis, K.; Klibanov, A. M. Designing surfaces that kill bacteria on contact. *Proc. Natl. Acad. Sci. U.S.A.* **2001**, *98* (11), 5981-5985.

[121] Bieser, A. M.; Tiller, J. C. Mechanistic considerations on contact-active antimicrobial surfaces with controlled functional group densities. *Macromol. Biosci.* **2011**, *11* (4), 526-534.

[122] Kugler, R.; Bouloussa, O.; Rondelez, F. Evidence of a charge-density threshold for optimum efficiency of biocidal cationic surfaces. *Microbiology (Reading)* **2005**, *151*, 1341-1348.

[123] Salwiczek, M.; Qu, Y.; Gardiner, J.; Strugnell, R. A.; Lithgow, T.; McLean, K. M.; Thissen, H. Emerging rules for effective antimicrobial coatings. *Trends Biotechnol.* **2014**, *32* (2), 82-90.

[124] Purohit, P.; Bhatt, A.; Mittal, R. K.; Abdellattif, M. H.; Farghaly, T. A. Polymer Grafting and its chemical reactions. *Front. Bioeng. Biotechnol.* **2022**, *10*, 1044927.

[125] Zdyrko, B.; Luzinov, I. Polymer brushes by the "grafting to" method. *Macromol. Rapid Commun.* **2011**, *32* (12), 859-869.

[126] Martinez, A. P.; Carrillo, J.-M. Y.; Dobrynin, A. V.; Adamson, D. H. Distribution of Chains in Polymer Brushes Produced by a “Grafting From” Mechanism. *Macromolecules* **2016**, *49* (2), 547-553.

[127] Henze, M.; Mädge, D.; Prucker, O.; Rühe, J. “Grafting Through”: Mechanistic Aspects of Radical Polymerization Reactions with Surface-Attached Monomers. *Macromolecules* **2014**, *47* (9), 2929-2937.

[128] Bhattacharya, A. Grafting: a versatile means to modify polymersTechniques, factors and applications. *Prog. Polym. Sci.* **2004**, *29* (8), 767-814.

[129] Khelifa, F.; Ershov, S.; Habibi, Y.; Snyders, R.; Dubois, P. Free-Radical-Induced Grafting from Plasma Polymer Surfaces. *Chem. Rev.* **2016**, *116* (6), 3975-4005.

[130] Ulbricht, M.; Belfort, G. Surface modification of ultrafiltration membranes by low temperature plasma II. Graft polymerization onto polyacrylonitrile and polysulfone. *J. Membr. Sci.* **1996**, *111* (2), 193-215.

[131] Seman, M. N. A.; Khayet, M.; Hilal, N. Comparison of two different UV-grafted nanofiltration membranes prepared for reduction of humic acid fouling using acrylic acid and N-vinylpyrrolidone. *Desalination* **2012**, *287*, 19-29.

[132] Ulbricht, M.; Matuschewski, H.; Oechel, A.; Hicke, H.-G. Photo-induced graft polymerization surface modifications for the preparation of hydrophilic and low-proten-adsorbing ultrafiltration membranes. *J. Membr. Sci.* **1996**, *115* (1), 31-47.

[133] Zhao, Y.-H.; Wee, K.-H.; Bai, R. Highly hydrophilic and low-protein-fouling polypropylene membrane prepared by surface modification with sulfobetaine-based zwitterionic polymer through a combined surface polymerization method. *J. Membr. Sci.* **2010**, *362* (1-2), 326-333.

[134] Barbey, R.; Lavanant, L.; Paripovic, D.; Schuwer, N.; Sugnaux, C.; Tugulu, S.; Klok, H. A. Polymer brushes via surface-initiated controlled radical polymerization: synthesis, characterization, properties, and applications. *Chem. Rev.* **2009**, *109* (11), 5437-5527.

[135] Yang, Z.; Takagi, R.; Zhang, X.; Yasui, T.; Zhang, L.; Matsuyama, H. Engineering a dual-functional sulfonated polyelectrolyte-silver nanoparticle complex on a polyamide reverse osmosis membrane for robust biofouling mitigation. *J. Membr. Sci.* **2021**, *618*, 118757.

[136] Hadi, M. K.; Wang, X.; Peng, Y.; Sangaraju, S.; Ran, F. Functional Polymeric Membrane Materials: A Perspective from Versatile Methods and Modification to Potential Applications. *Polym. Sci. Technol.* **2024**, *1* (5), 366-412.

[137] Yahya, A. A.; Rashid, K. T.; Ghadhban, M. Y.; Mousa, N. E.; Majdi, H. S.; Salih, I. K.; Alsalhy, Q. F. Removal of 4-Nitrophenol from Aqueous Solution by Using Polyphenylsulfone-Based Blend Membranes: Characterization and Performance. *Membranes (Basel)* **2021**, *11* (3), 171.

[138] Tekinalp, Ö.; Zimmermann, P.; Burheim, O. S.; Deng, L. Designing monovalent selective anion exchange membranes for the simultaneous separation of chloride and fluoride from sulfate in an equimolar ternary mixture. *J. Membr. Sci.* **2023**, *666*, 121148.

[139] Jung, B. Preparation of hydrophilic polyacrylonitrile blend membranes for ultrafiltration. *J. Membr. Sci.* **2004**, *229* (1-2), 129-136.

[140] Zhang, L.; Luo, J.; Menkhaus, T. J.; Varadaraju, H.; Sun, Y.; Fong, H. Antimicrobial nano-fibrous membranes developed from electrospun polyacrylonitrile nanofibers. *J. Membr. Sci.* **2011**, *369* (1-2), 499-505.

[141] Su, Y.-L.; Cheng, W.; Li, C.; Jiang, Z. Preparation of antifouling ultrafiltration membranes with poly(ethylene glycol)-graft-polyacrylonitrile copolymers. *J. Membr. Sci.* **2009**, *329* (1-2), 246-252.

[142] Zhang, G.; Yan, H.; Ji, S.; Liu, Z. Self-assembly of polyelectrolyte multilayer pervaporation membranes by a dynamic layer-by-layer technique on a hydrolyzed polyacrylonitrile ultrafiltration membrane. *J. Membr. Sci.* **2007**, *292* (1-2), 1-8.

[143] Xu, Y.; Lin, J.; Gao, C.; Van der Bruggen, B.; Shen, Q.; Shao, H.; Shen, J. Preparation of High-Flux Nanoporous Solvent Resistant Polyacrylonitrile Membrane with Potential Fractionation of Dyes and Na2SO4. *Ind. Eng. Chem. Res.* **2017**, *56* (41), 11967-11976.

[144] Green, W. A. Industrial photoinitiators. A technical guide, 1st ed.; *CRC Press*, Boca Raton, **2010**, 17-46.

[145] Decker, C.; Zahouily, K.; Decker, D.; Nguyen, T.; Viet, T. Performance analysis of acylphosphine oxides in photoinitiated polymerization. *Polymer* **2001**, *42* (18), 7551-7560.

[146] Zeng, B.; Cai, Z.; Lalevee, J.; Yang, Q.; Lai, H.; Xiao, P.; Liu, J.; Xing, F. Cytotoxic and cytocompatible comparison among seven photoinitiators-triggered polymers in different tissue cells. *Toxicol. In Vitro* **2021**, *72*, 105103.

[147] Benedikt, S.; Wang, J.; Markovic, M.; Moszner, N.; Dietliker, K.; Ovsianikov, A.; Grützmacher, H.; Liska, R. Highly efficient water-soluble visible light photoinitiators. *J. Polym. Sci., Part A: Polym. Chem.* **2016**, *54* (4), 473-479.

[148] Schonemann, E.; Laschewsky, A.; Rosenhahn, A. Exploring the Long-Term Hydrolytic Behavior of Zwitterionic Polymethacrylates and Polymethacrylamides. *Polymers (Basel)* **2018**, *10* (6), 639.

[149] Shao, Q.; Jiang, S. Molecular understanding and design of zwitterionic materials. *Adv. Mater.* **2015**, *27* (1), 15-26.

[150] Ligon, S. C.; Husar, B.; Wutzel, H.; Holman, R.; Liska, R. Strategies to reduce oxygen inhibition in photoinduced polymerization. *Chem. Rev.* **2014**, *114* (1), 557-589.

[151] Ahmad, D.; van den Boogaert, I.; Miller, J.; Presswell, R.; Jouhara, H. Hydrophilic and hydrophobic materials and their applications. *Energy Sources A: Recovery Util. Environ. Eff.* **2018**, *40* (22), 2686-2725.

[152] *NIST X-ray Photoelectron Spectroscopy Database*. https://srdata.nist.gov/xps (accessed 15.04.25).

[153] Tas, S.; Kaynan, O.; Ozden-Yenigun, E.; Nijmeijer, K. Polyacrylonitrile (PAN)/crown ether composite nanofibers for the selective adsorption of cations. *RSC Adv.* **2016**, *6* (5), 3608-3616.

[154] Guo, W.; Ngo, H. H.; Li, J. A mini-review on membrane fouling. *Bioresour. Technol.* **2012**, *122*, 27-34.

[155] Jin, L.; Ong, S. L.; Ng, H. Y. Comparison of fouling characteristics in different pore-sized submerged ceramic membrane bioreactors. *Water Res.* **2010**, *44* (20), 5907-5918.

[156] Nittami, T.; Hitomi, T.; Matsumoto, K.; Nakamura, K.; Ikeda, T.; Setoguchi, Y.; Motoori, M. Comparison of polytetrafluoroethylene flat-sheet membranes with different pore sizes in application to submerged membrane bioreactor. *Membranes (Basel)* **2012**, *2* (2), 228-236.

[157] Quéré, D. Wetting and Roughness. *Annu. Rev. Mater. Res.* **2008**, *38* (1), 71-99.

[158] Imbrogno, A.; Calvo, J. I.; Breida, M.; Schwaiger, R.; Schäfer, A. I. Molecular weight cut off (MWCO) determination in ultra- and nanofiltration: Review of methods and implications on organic matter removal. *Sep. Purif. Technol.* **2025**, *354*, 128612.

[159] Guo, S.; Janczewski, D.; Zhu, X.; Quintana, R.; He, T.; Neoh, K. G. Surface charge control for zwitterionic polymer brushes: Tailoring surface properties to antifouling applications. *J. Colloid Interface Sci.* **2015**, *452*, 43-53.

[160] Laschewsky, A. Structures and Synthesis of Zwitterionic Polymers. *Polymers (Basel)* **2014**, *6* (5), 1544-1601.

[161] Cai, T.; Park, S. Y.; Li, Y. Nutrient recovery from wastewater streams by microalgae: Status and prospects. *Renew. Sustain. Energy Rev.* **2013**, *19*, 360-369.

[162] Ward, M. H.; deKok, T. M.; Levallois, P.; Brender, J.; Gulis, G.; Nolan, B. T.; VanDerslice, J.; International Society for Environmental, E. Workgroup report: Drinking-water nitrate and health--recent findings and research needs. *Environ. Health Perspect.* **2005**, *113* (11), 1607-1614.

[163] Marcus, Y. Thermodynamics of solvation of ions. Part 5.—Gibbs free energy of hydration at 298.15 K. *J. Chem. Soc., Faraday Trans.* **1991**, *87* (18), 2995-2999.

[164] Priya, E.; Kumar, S.; Verma, C.; Sarkar, S.; Maji, P. K. A comprehensive review on technological advances of adsorption for removing nitrate and phosphate from waste water. *J. Water Process Eng.* **2022**, *49*, 103159.

[165] Ferreyra Maillard, A. P. V.; Espeche, J. C.; Maturana, P.; Cutro, A. C.; Hollmann, A. Zeta potential beyond materials science: Applications to bacterial systems and to the development of novel antimicrobials. *Biochim. Biophys. Acta, Biomembr.* **2021**, *1863* (6), 183597.

[166] Murata, H.; Koepsel, R. R.; Matyjaszewski, K.; Russell, A. J. Permanent, non-leaching antibacterial surface - 2: How high density cationic surfaces kill bacterial cells. *Biomaterials* **2007**, *28* (32), 4870-4879.

[167] Sistkova, J.; Fialova, T.; Svoboda, E.; Varmuzova, K.; Uher, M.; Cihalova, K.; Pribyl, J.; Dlouhy, A.; Pavkova Goldbergova, M. Insight into antibacterial effect of titanium nanotubular surfaces with focus on Staphylococcus aureus and Pseudomonas aeruginosa. *Sci. Rep.* **2024**, *14* (1), 17303.

[168] Ouhara, K.; Komatsuzawa, H.; Kawai, T.; Nishi, H.; Fujiwara, T.; Fujiue, Y.; Kuwabara, M.; Sayama, K.; Hashimoto, K.; Sugai, M. Increased resistance to cationic antimicrobial peptide LL-37 in methicillin-resistant strains of Staphylococcus aureus. *J. Antimicrob. Chemother.* **2008**, *61* (6), 1266-1269.

[169] Palecek, S. P.; Zydney, A. L. Hydraulic permeability of protein deposits formed during microfiltration: effect of solution pH and ionic strength. *J. Membr. Sci.* **1994**, *95* (1), 71-81.

[170] Jachimska, B.; Wasilewska, M.; Adamczyk, Z. Characterization of globular protein solutions by dynamic light scattering, electrophoretic mobility, and viscosity measurements. *Langmuir* **2008**, *24* (13), 6866-6872.

[171] Steudle, A.; Pleiss, J. Modelling of lysozyme binding to a cation exchange surface at atomic detail: the role of flexibility. *Biophys. J.* **2011**, *100* (12), 3016-3024.

[172] Taylor, D. J.; Thomas, R. K.; Penfold, J. Polymer/surfactant interactions at the air/water interface. *Adv. Colloid Interface Sci.* **2007**, *132* (2), 69-110.

[173] Parmar, A. S.; Muschol, M. Hydration and hydrodynamic interactions of lysozyme: effects of chaotropic versus kosmotropic ions. *Biophys. J.* **2009**, *97* (2), 590-598.

[174] Mapiour, M.; Abdelrasoul, A. Critical Influences of Plasma pH on Human Protein Properties for Modeling Considerations: Size, Charge, Conformation, Hydrophobicity, and Denaturation. *J. Compos. Sci.* **2023**, *7* (1), 28.

[175] Adamczyk, Z.; Cichocki, B.; Ekiel-Jezewska, M. L.; Slowicka, A.; Wajnryb, E.; Wasilewska, M. Fibrinogen conformations and charge in electrolyte solutions derived from DLS and dynamic viscosity measurements. *J. Colloid Interface Sci.* **2012**, *385* (1), 244-257.

[176] Wu, S.; Shan, Z.; Xie, L.; Su, M.; Zeng, P.; Huang, P.; Zeng, L.; Sheng, X.; Li, Z.; Zeng, G.; et al. Mesopore Controls the Responses of Blood Clot-Immune Complex via Modulating Fibrin Network. *Adv. Sci.* **2022**, *9* (3), 1-16.

[177] Lalani, R.; Liu, L. Synthesis, characterization, and electrospinning of zwitterionic poly(sulfobetaine methacrylate). *Polymer* **2011**, *52* (23), 5344-5354.

[178] Kobus, M.; Friedrich, T.; Zorn, E.; Burmeister, N.; Maison, W. Medicinal Chemistry of Drugs with N-Oxide Functionalities. *J. Med. Chem.* **2024**, *67* (7), 5168-5184.

[179] Hossain, M. T.; Shahid, M. A.; Mahmud, N.; Habib, A.; Rana, M. M.; Khan, S. A.; Hossain, M. D. Research and application of polypropylene: a review. *Discov. Nano.* **2024**, *19* (1), 2.

[180] Chen, M.; Hu, Q.; Wang, X.; Zhang, W. A review on recent trends of the antibacterial nonwovens air filter materials: Classification, fabrication, and application. *Sep. Purif. Technol.* **2024**, *330*, 125404.

[181] Shao, Q.; Jiang, S. Effect of carbon spacer length on zwitterionic carboxybetaines. *J. Phys. Chem. B* **2013**, *117* (5), 1357-1366.

[182] Shin, H.-D.; Suh, J.-H.; Kim, J.-H.; Lee, H.-Y.; Eom, H.-Y.; Kim, U.-Y.; Yang, D.-H.; Han, S.-B.; Youm, J.-R. Determination of Betaine in Fructus Lycii Using Hydrophilic Interaction Liquid Chromatography with Evaporative Light Scattering Detection. *Bull. Korean Chem. Soc.* **2012**, *33* (2), 553-558.

[183] Cao, R.; Liu, X.; Guo, J.; Xu, Y. Comparison of various organic acids for xylo-oligosaccharide productions in terms of pKa values and combined severity. *Biotechnol. Biofuels* **2021**, *14* (1), 69.

[184] Wysocki, M.; Stachowiak, W.; Smolibowski, M.; Olejniczak, A.; Niemczak, M.; Shamshina, J. L. Rethinking the Esterquats: Synthesis, Stability, Ecotoxicity and Applications of Esterquats Incorporating Analogs of Betaine or Choline as the Cation in Their Structure. *Int. J. Mol. Sci.* **2024**, *25* (11), 5761.

[185] Guo, J.; Liu, Z.; Wang, J.; Zhang, R.-Y.; Wang, Y.-C.; Chen, X.-Z.; Yin, X.-G.; Du, J.-J.; Lei, Z.; Xin, L.-M.; et al. Polyfluorophenyl Ester-Terminated Homobifunctional Cross-Linkers for Protein Conjugation. *Synlett* **2017**, *28* (15), 1934-1938.

[186] Ho, B. T.; Roberts, T. K.; Lucas, S. An overview on biodegradation of polystyrene and modified polystyrene: the microbial approach. *Crit. Rev. Biotechnol.* **2018**, *38* (2), 308-320.

[187] Burmeister, N.; Zorn, E.; Preuss, L.; Timm, D.; Scharnagl, N.; Rohnke, M.; Wicha, S. G.; Streit, W. R.; Maison, W. Low-Fouling and Antibacterial Polymer Brushes via Surface-Initiated Polymerization of a Mixed Zwitterionic and Cationic Monomer. *Langmuir* **2023**, *39* (49), 17959-17971.

[188] Temocin, Z.; Yigitoglu, M. Studies on the activity and stability of immobilized horseradish peroxidase on poly(ethylene terephthalate) grafted acrylamide fiber. *Bioprocess Biosyst. Eng.* **2009**, *32* (4), 467-474.

[189] Higaki, Y.; Furusawa, R.; Otsu, T.; Yamada, N. L. Zwitterionic Poly(carboxybetaine) Brush/Albumin Conjugate Films: Structure and Lubricity. *Langmuir* **2022**, *38* (30), 9278-9284.

[190] Zhang, Z.; Rahman, M. M.; Bajer, B.; Abetz, V. Rapid protein fractionation with tunable amphiphilic isoporous block copolymer membranes. *J. Membr. Sci.* **2025**, *727*, 124114.

[191] Dan, M.; Su, Y.; Xiao, X.; Li, S.; Zhang, W. A New Family of Thermo-Responsive Polymers Based on Poly[N-(4-vinylbenzyl)-N,N-dialkylamine]. *Macromolecules* **2013**, *46* (8), 3137-3146.

[192] Van de Wetering, P.; Cherng, J.-Y.; Talsma, H.; Hennink, W. E. Relation between transfection efficiency and cytotoxicity of poly(2-(dimethylamino)ethyl methacrylate)/plasmid complexes. *J. Control. Release* **1997**, *49* (1), 59-69.

[193] *GESTIS-Stoffdatenbank*. https://gestis.dguv.de/ (accessed 05.05.25).

[194] *Sigma-Aldrich*. https://www.sigmaaldrich.com/DE/de/ (accessed 05.05.25).

10 Appendix

10.1 NMR-Spectra

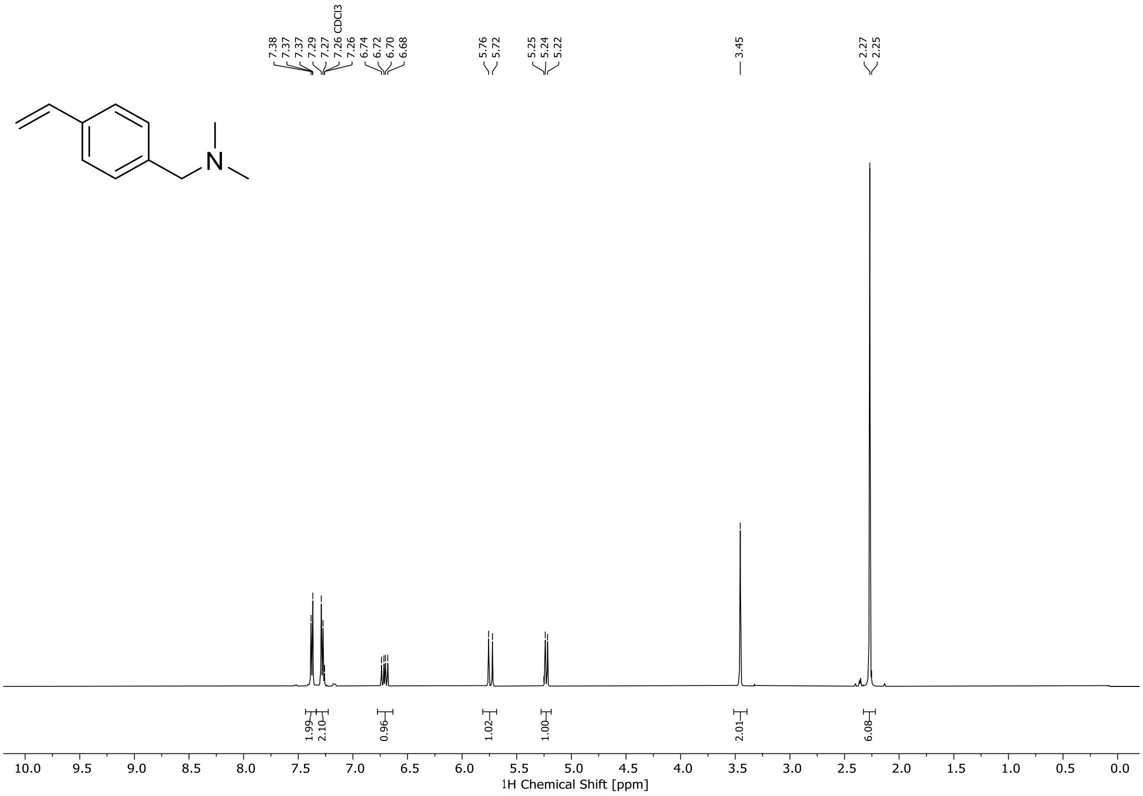

Figure A1: ^{1}H-NMR of *N*,*N*-dimethyl-1-(4-vinylphenyl)methanamine.

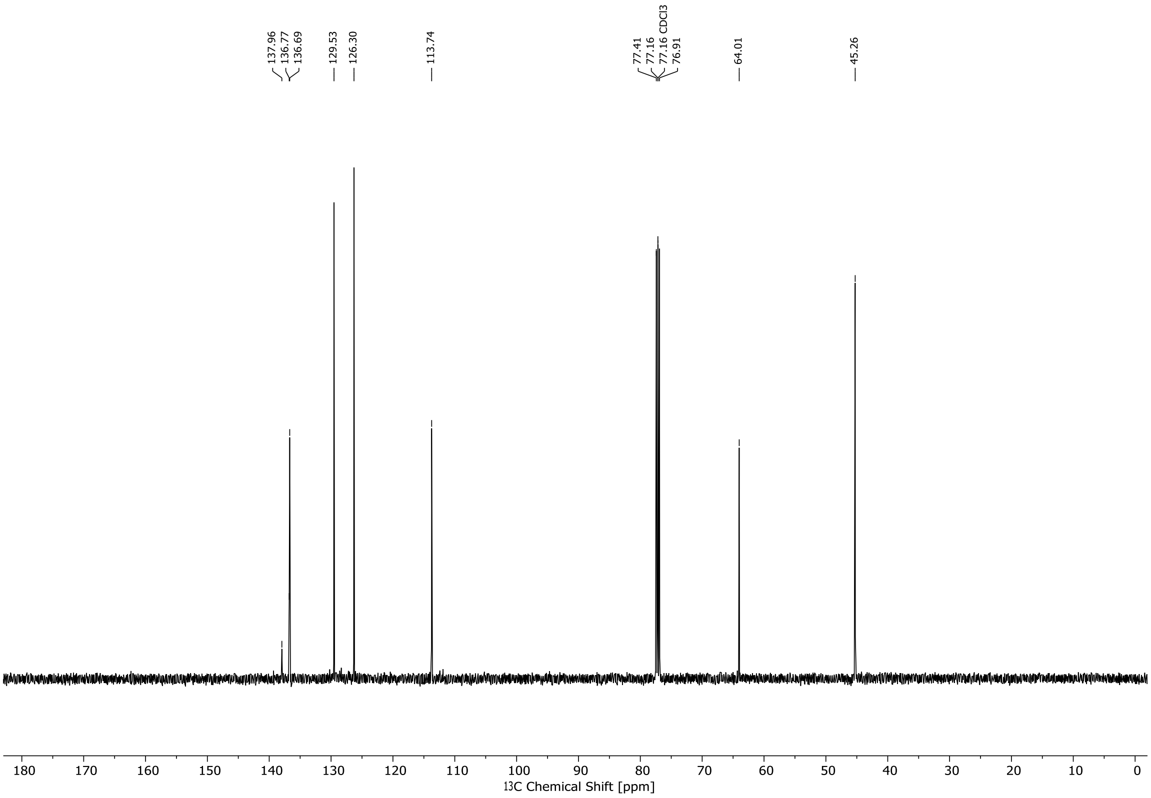

Figure A2: ^{13}C-NMR of *N*,*N*-dimethyl-1-(4-vinylphenyl)methanamine.

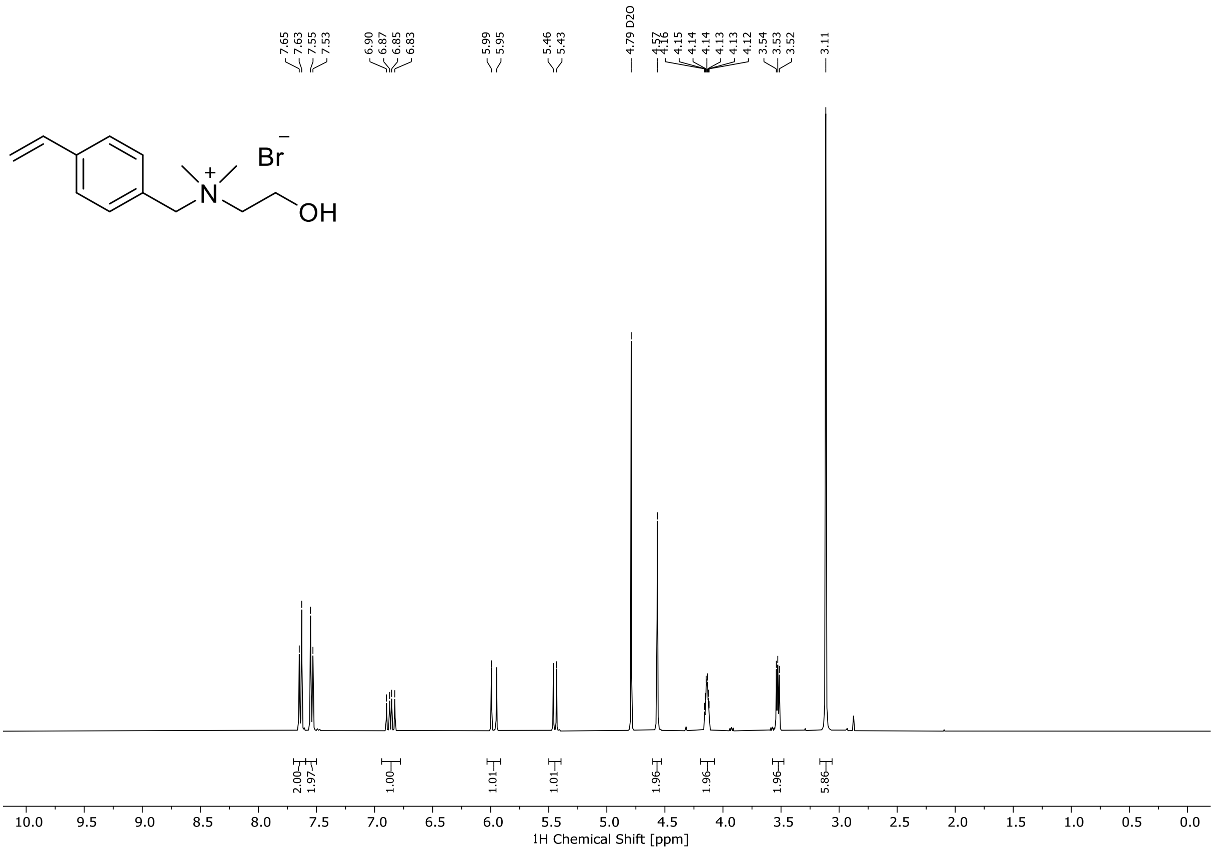

Figure A3: ^{1}H-NMR of 2-Hydroxy-*N*,*N*-dimethyl-*N*-(4-vinylbenzyl)ethan-1-aminium bromide.

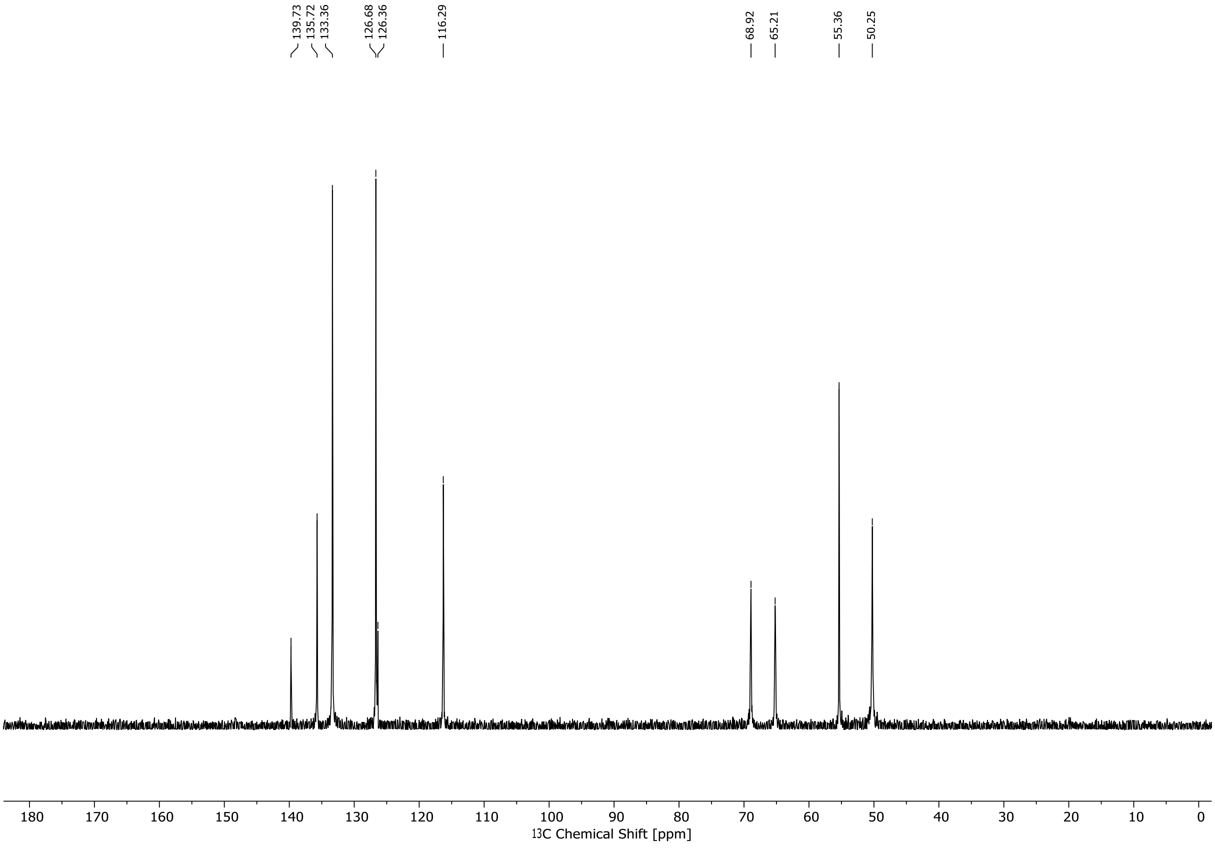

Figure A4: ^{13}C-NMR of 2-Hydroxy-*N*,*N*-dimethyl-*N*-(4-vinylbenzyl)ethan-1-aminium bromide.

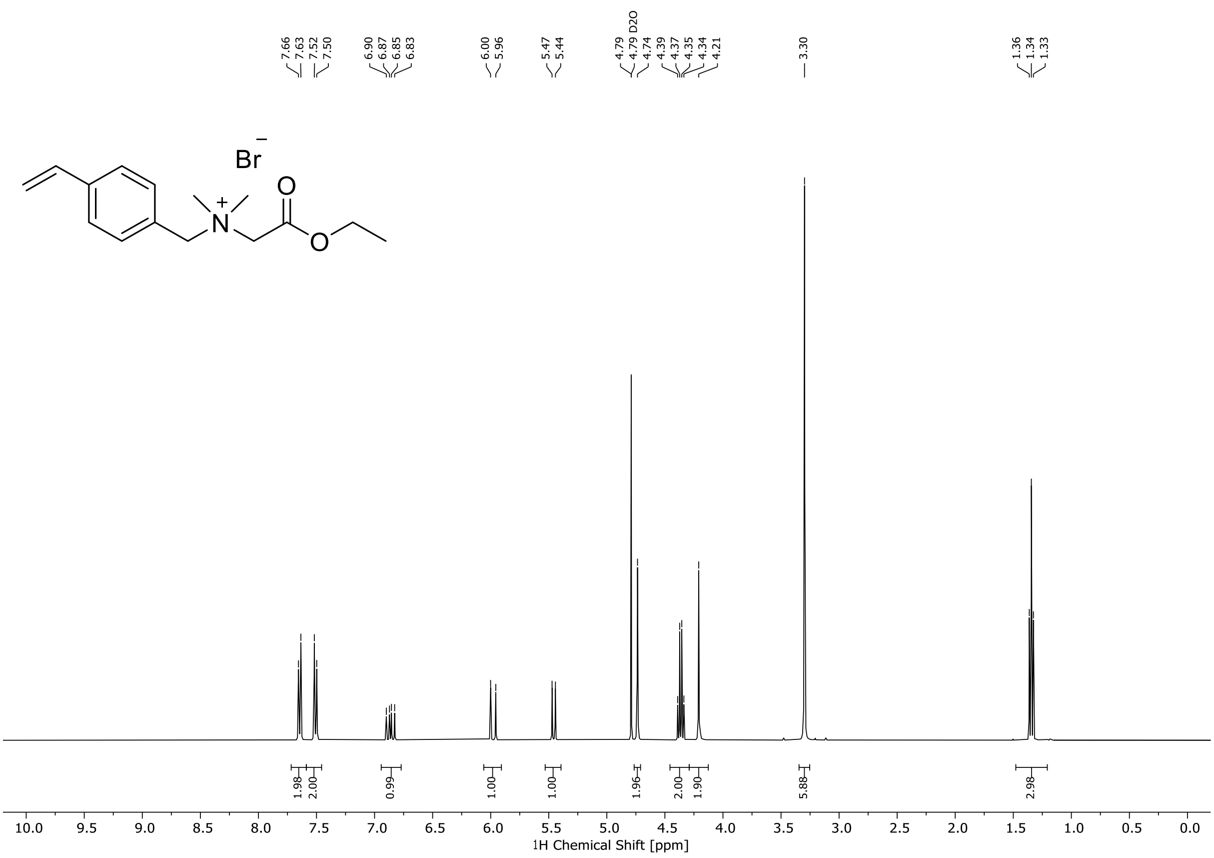

Figure A5: ^{1}H-NMR of 2-Ethoxy-*N*,*N*-dimethyl-2-oxo-*N*-(4-vinylbenzyl)ethan-1-aminium bromide.

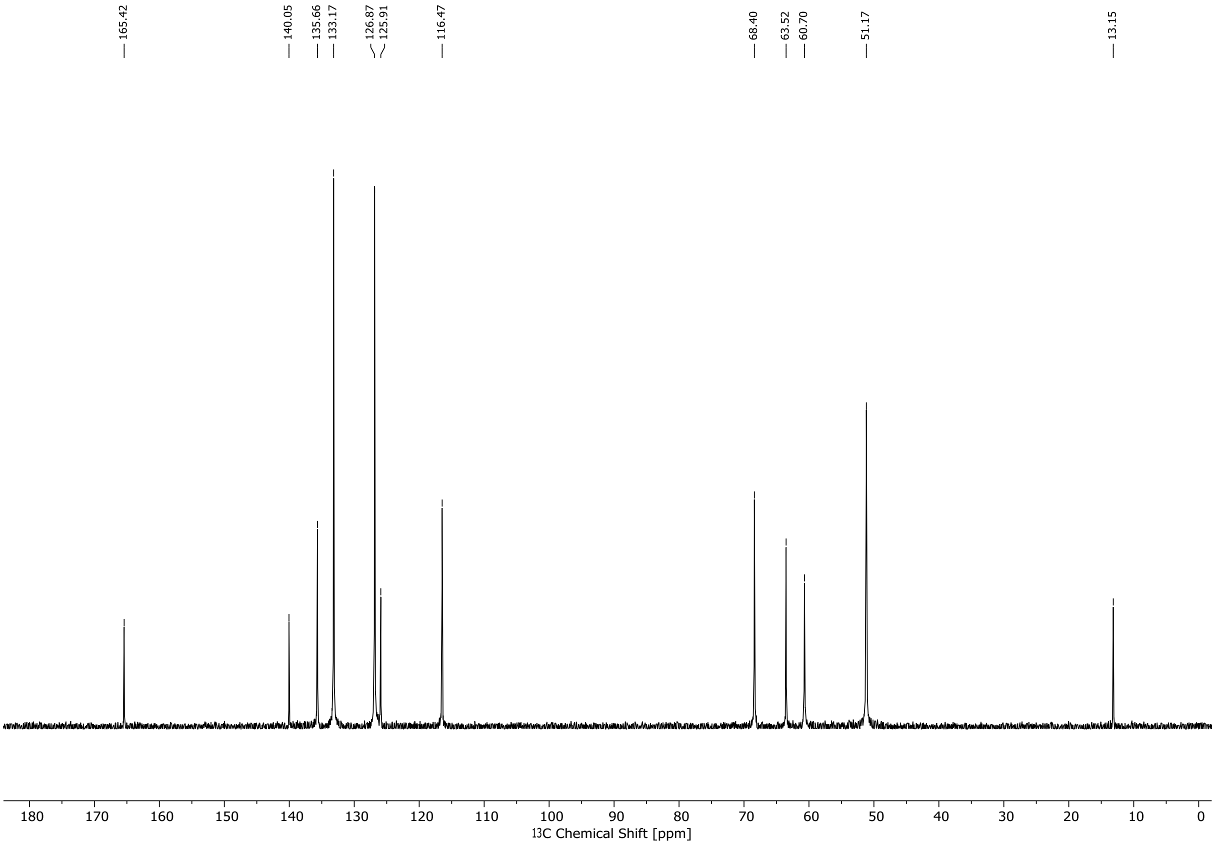

Figure A6: ^{13}C-NMR of 2-Ethoxy-*N*,*N*-dimethyl-2-oxo-*N*-(4-vinylbenzyl)ethan-1-aminium bromide.

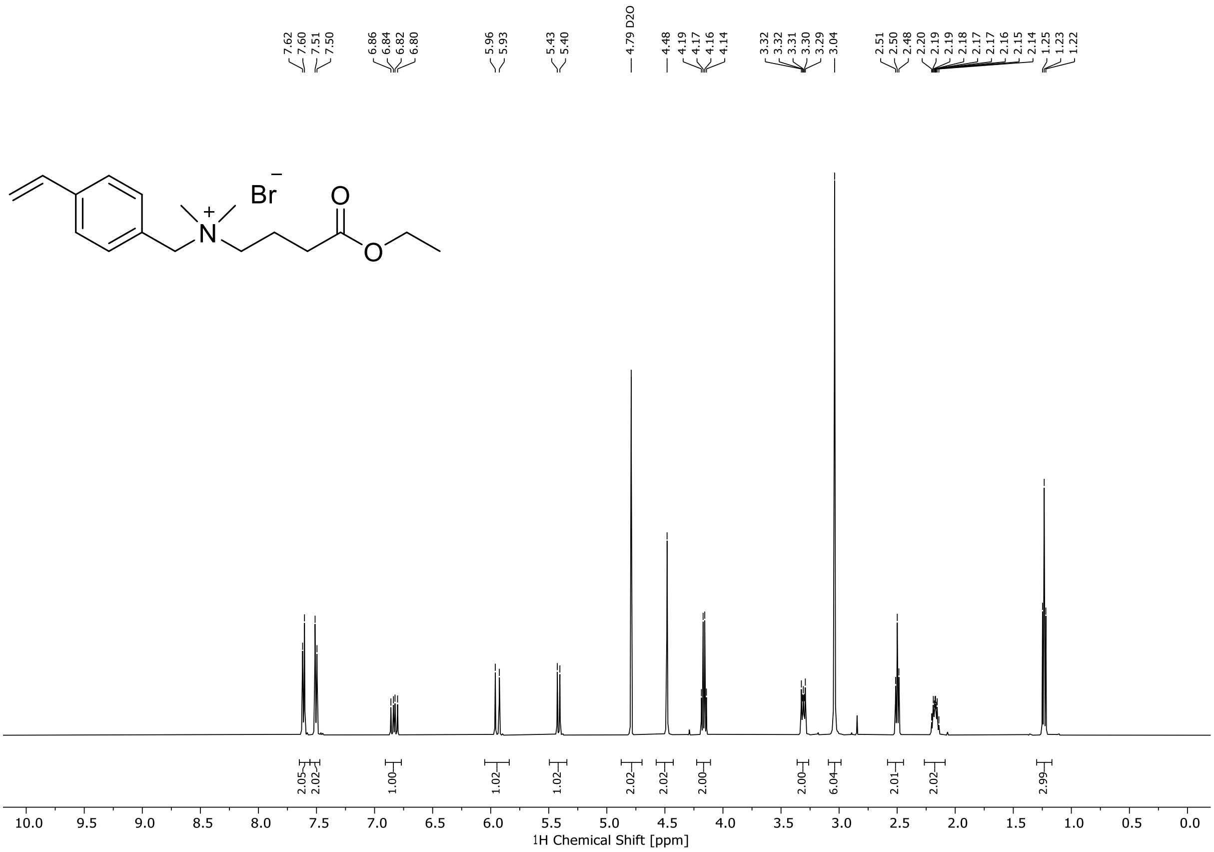

Figure A7: ^{1}H-NMR of 4-Ethoxy-*N*,*N*-dimethyl-4-oxo-*N*-(4-vinylbenzyl)butan-1-aminium bromide.

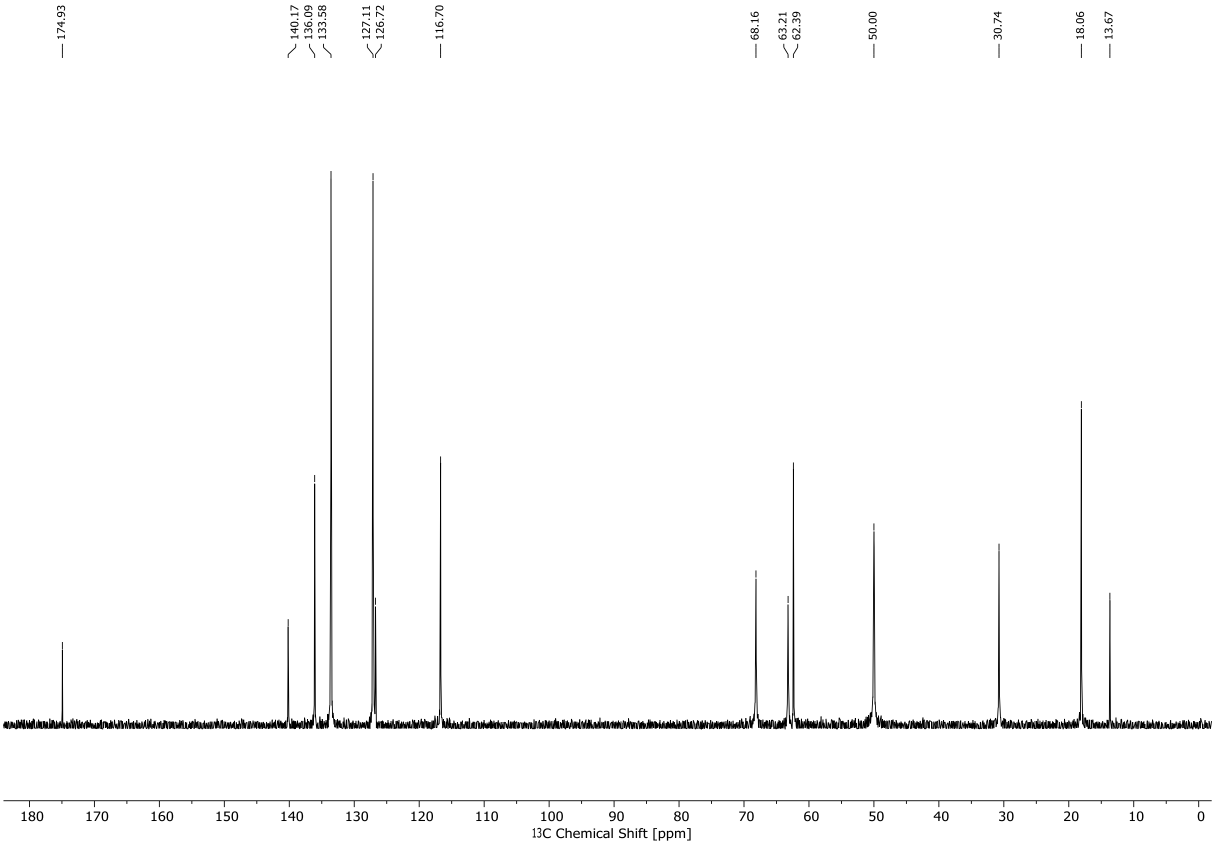

Figure A8: ^{13}C-NMR of 4-Ethoxy-*N*,*N*-dimethyl-4-oxo-*N*-(4-vinylbenzyl)butan-1-aminium bromide.

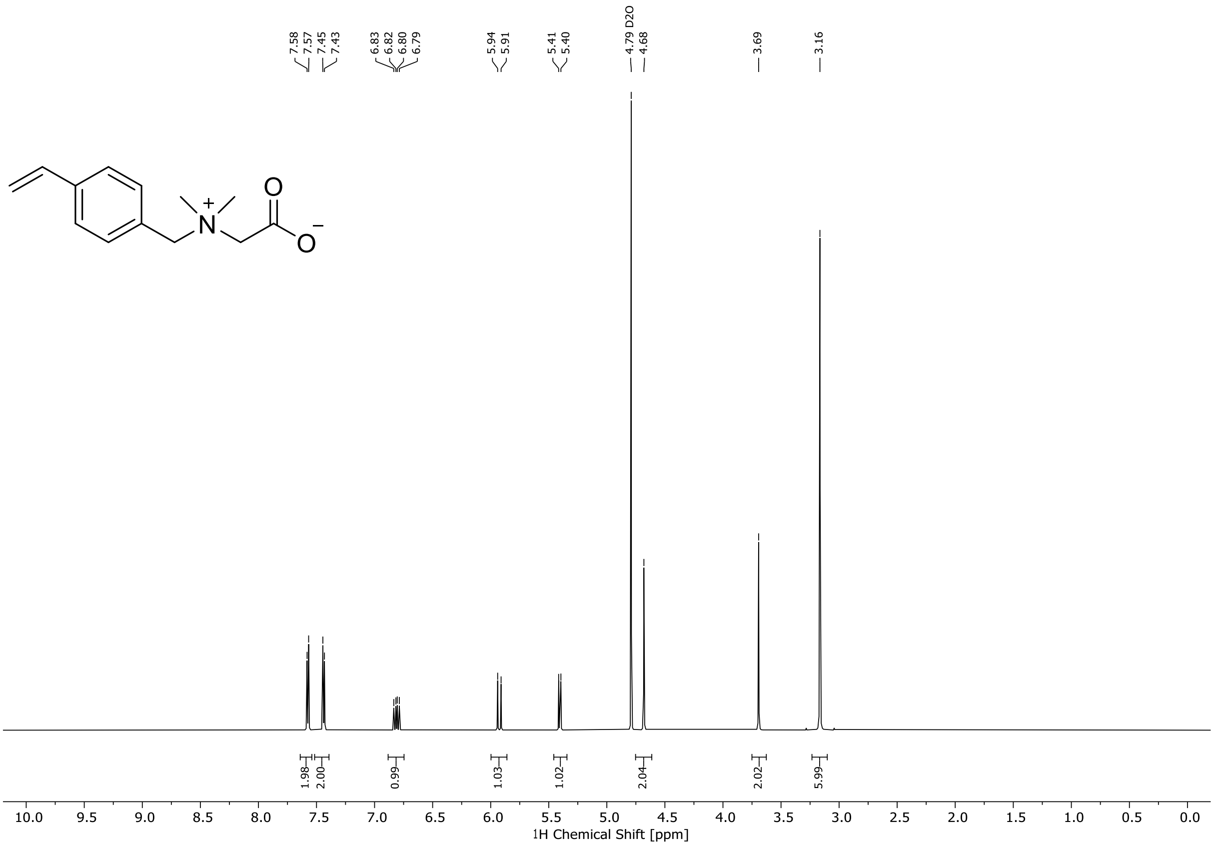

Figure A9: ^{1}H-NMR of 2-(Dimethyl(4-vinylbenzyl)ammonio)acetate.

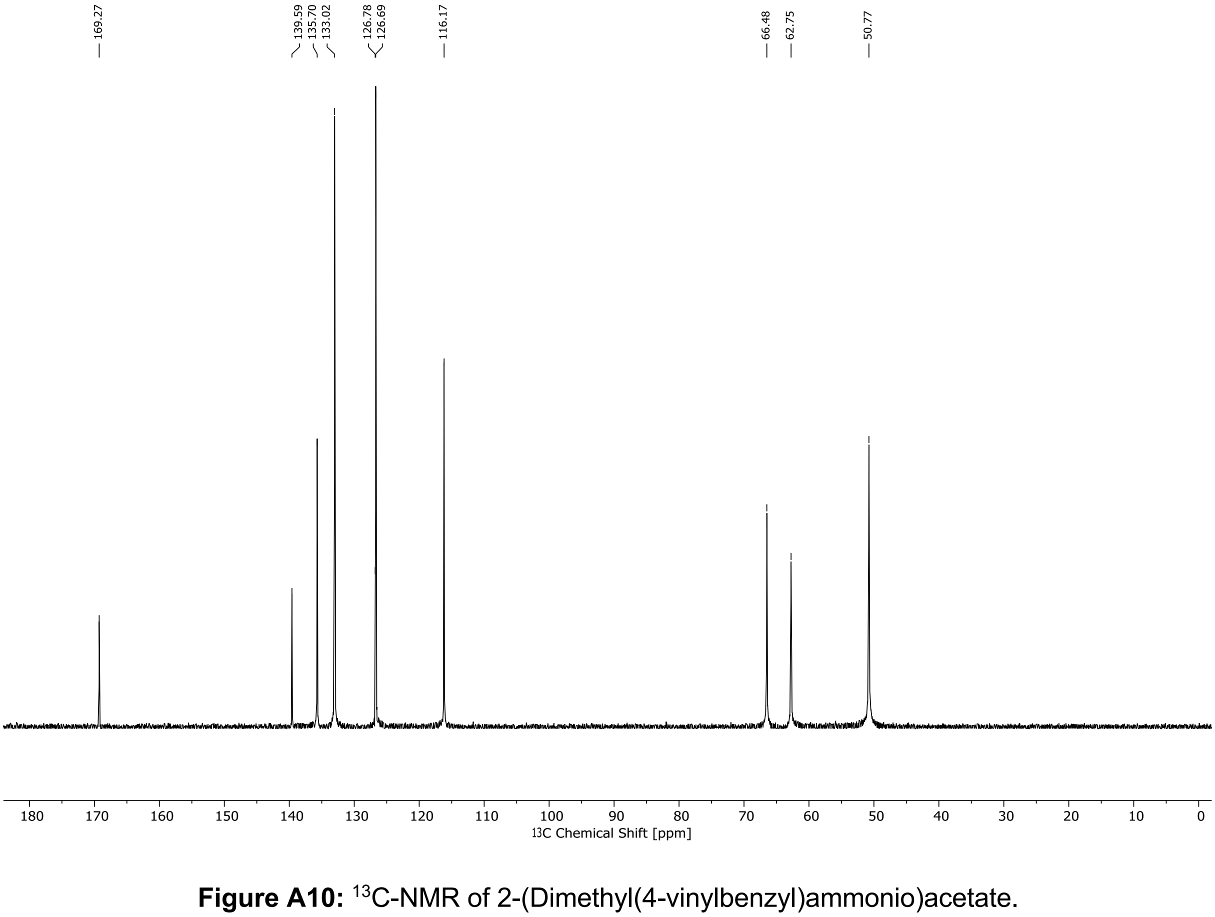

Figure A10: ^{13}C-NMR of 2-(Dimethyl(4-vinylbenzyl)ammonio)acetate.

Figure A11: ^{1}H-NMR of 4-(Dimethyl(4-vinylbenzyl)ammonio)butanoate.

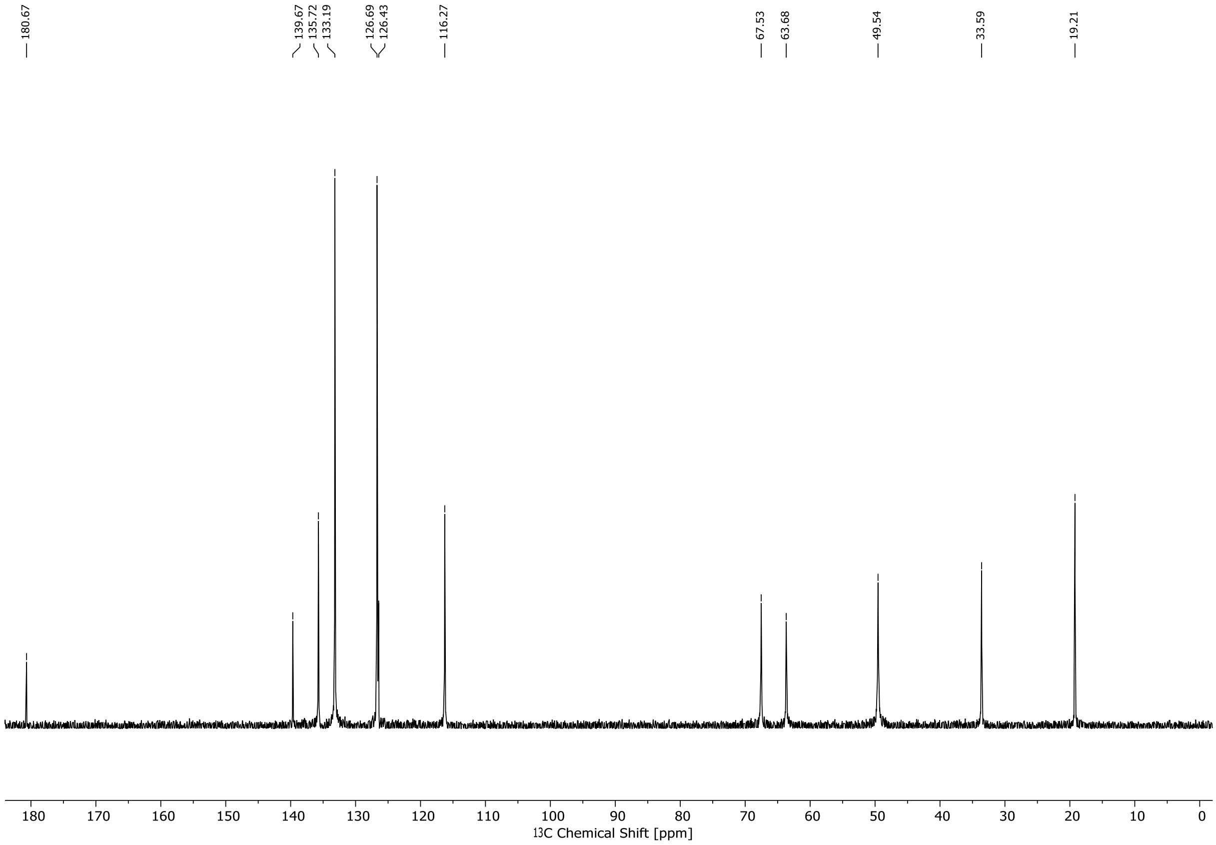

Figure A12: ^{13}C-NMR of 4-(Dimethyl(4-vinylbenzyl)ammonio)butanoate.

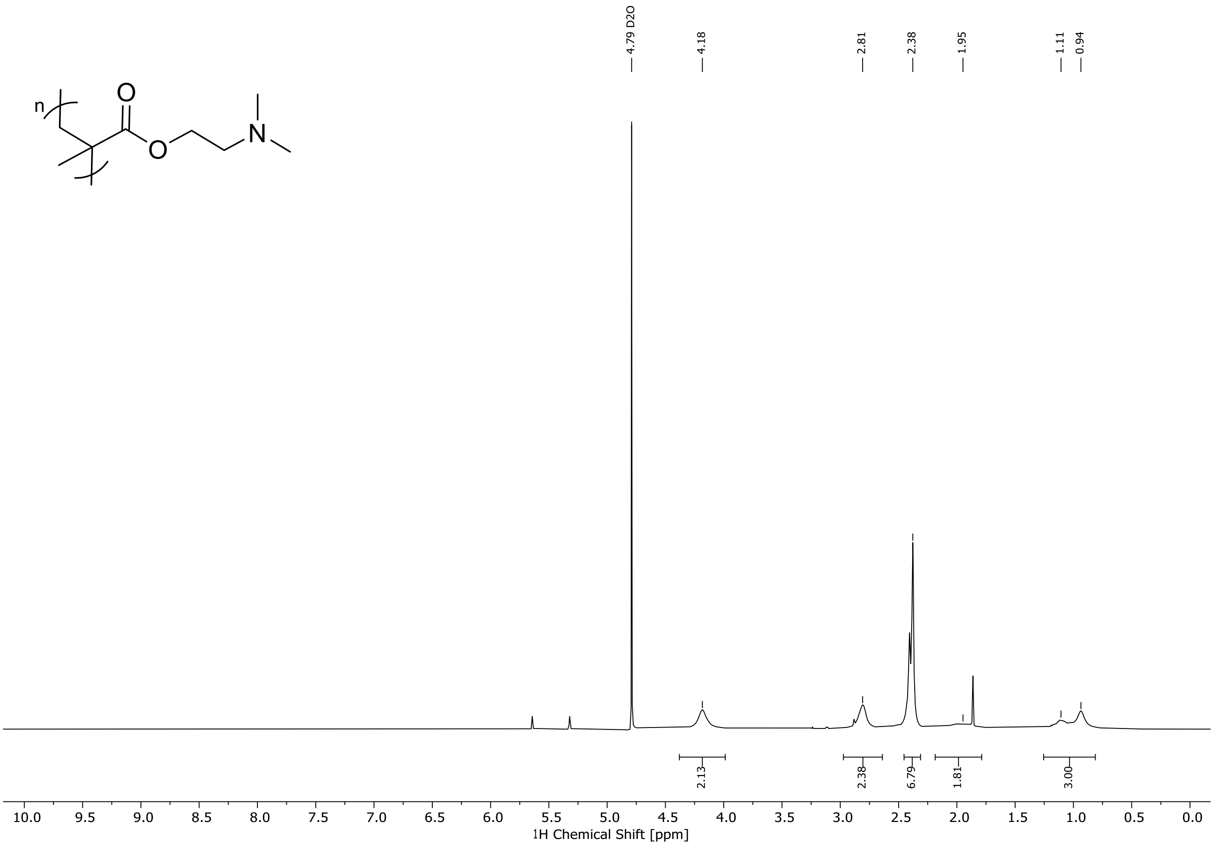

Figure A13: ^{1}H-NMR of Poly(2-(dimethylamino)ethyl methacrylate).

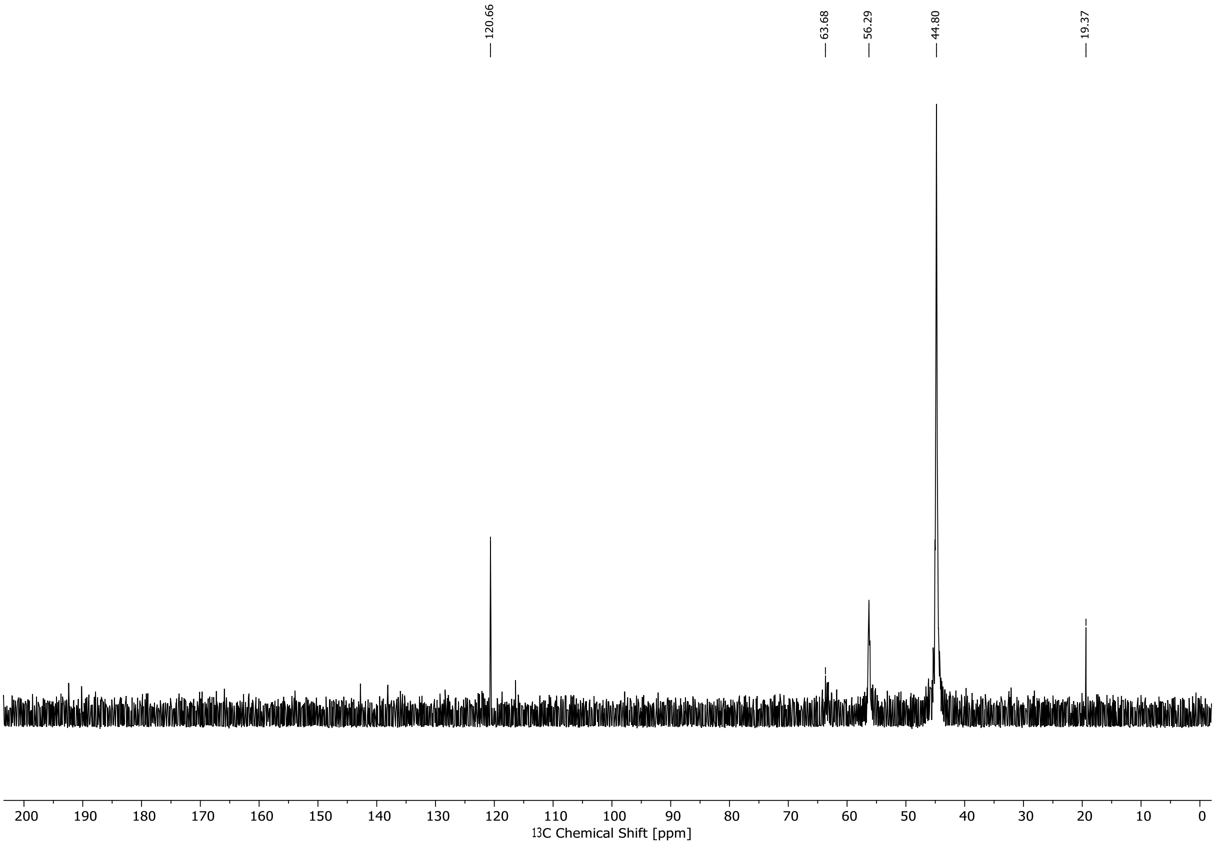

Figure A14: ^{13}C-NMR of Poly(2-(dimethylamino)ethyl methacrylate).

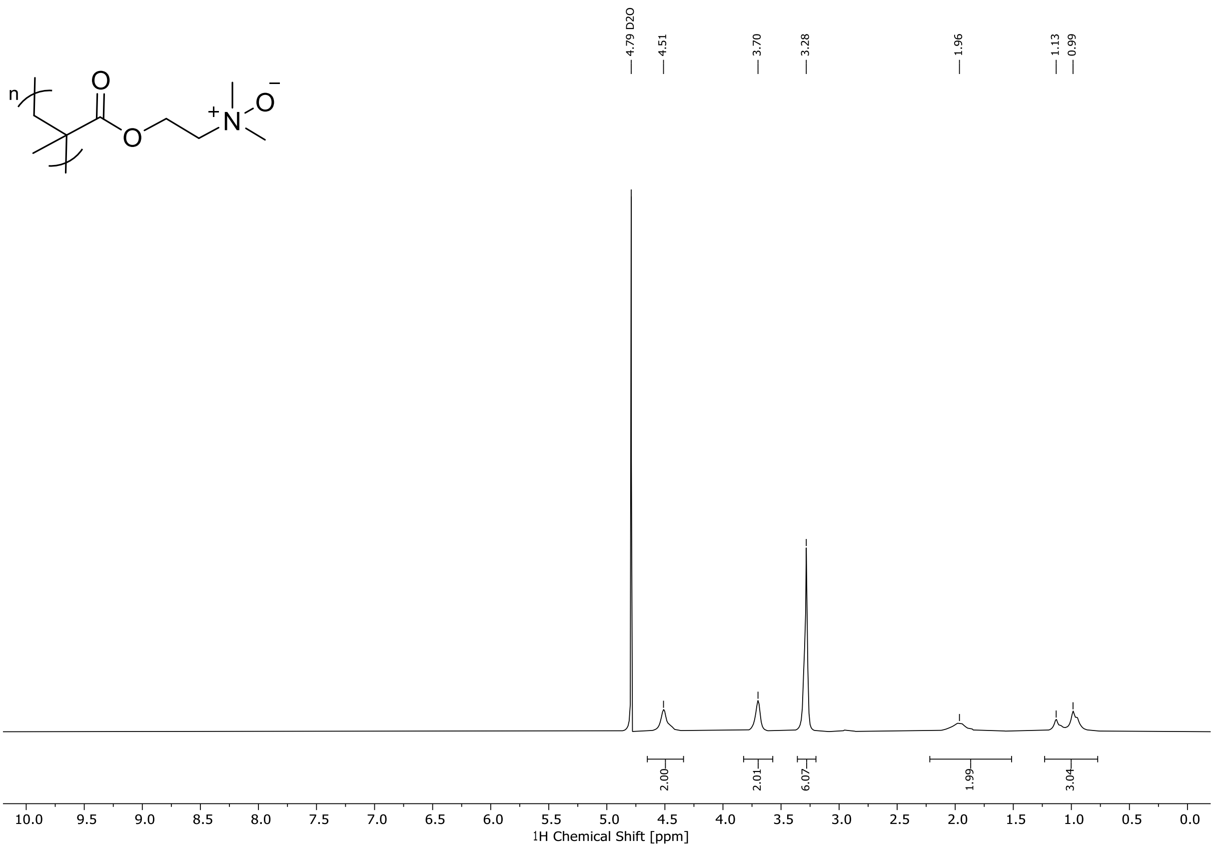

Figure A15: ^{1}H-NMR of Poly(2-(methacryloyloxy)-*N*,*N*-dimethylethan-1-amine oxide).

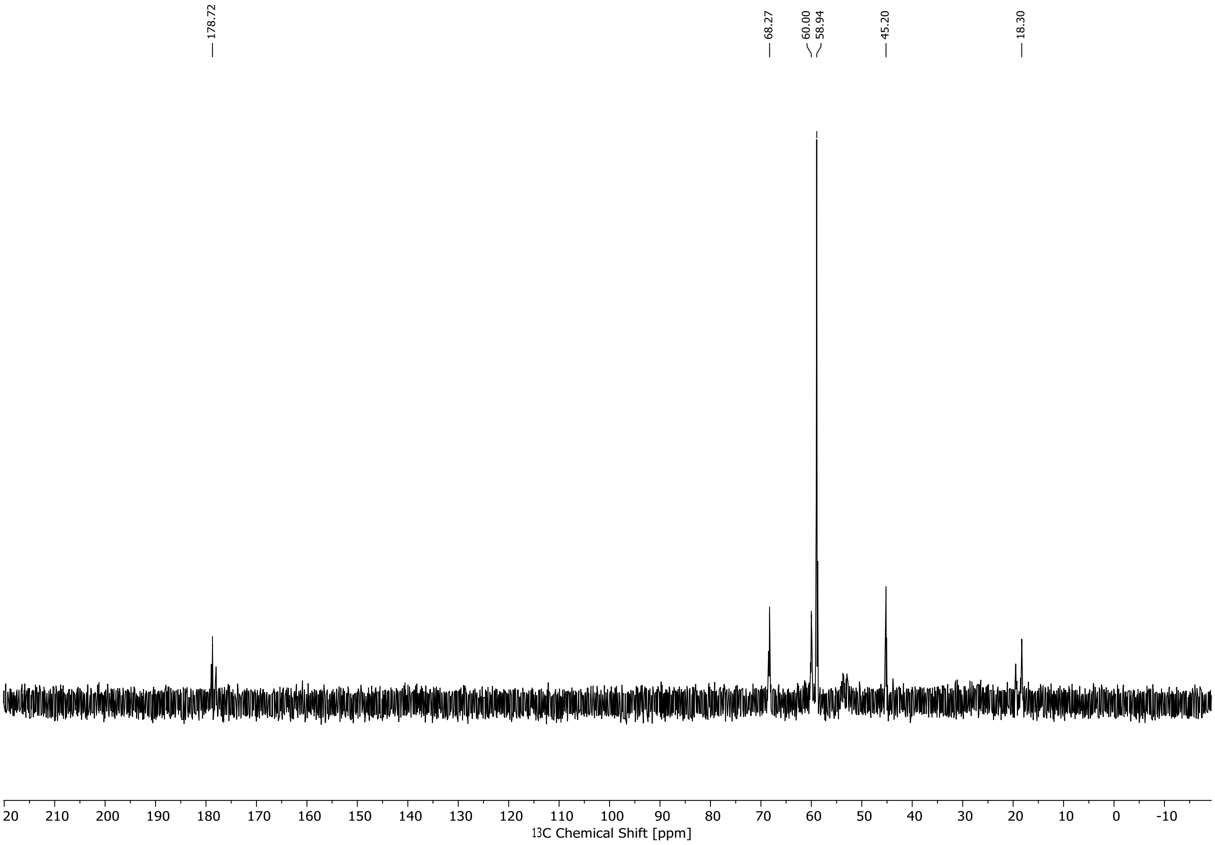

Figure A16: ^{13}C-NMR of Poly(2-(methacryloyloxy)-*N*,*N*-dimethylethan-1-amine oxide).

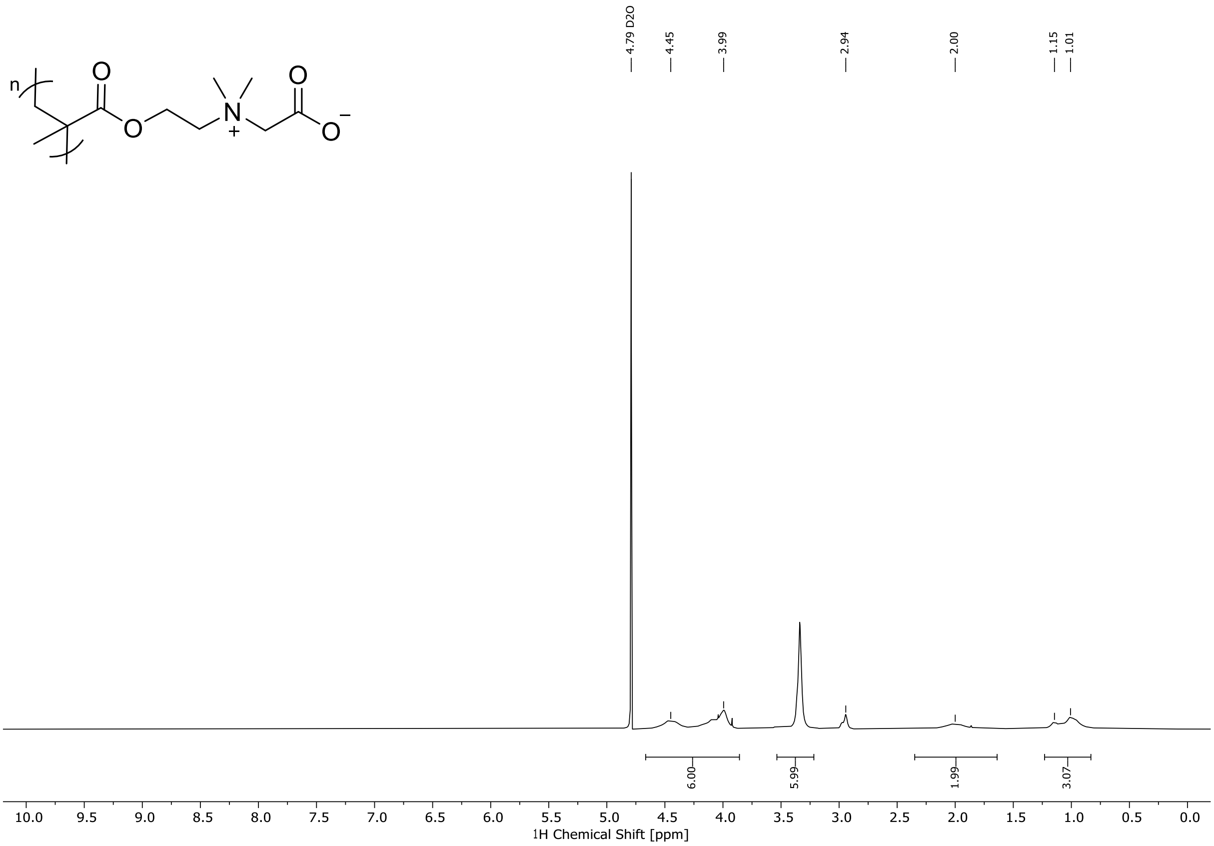

Figure A17: ^{1}H-NMR of Poly(2-((2-(methacryloyloxy)ethyl)dimethylammonio)acetate).

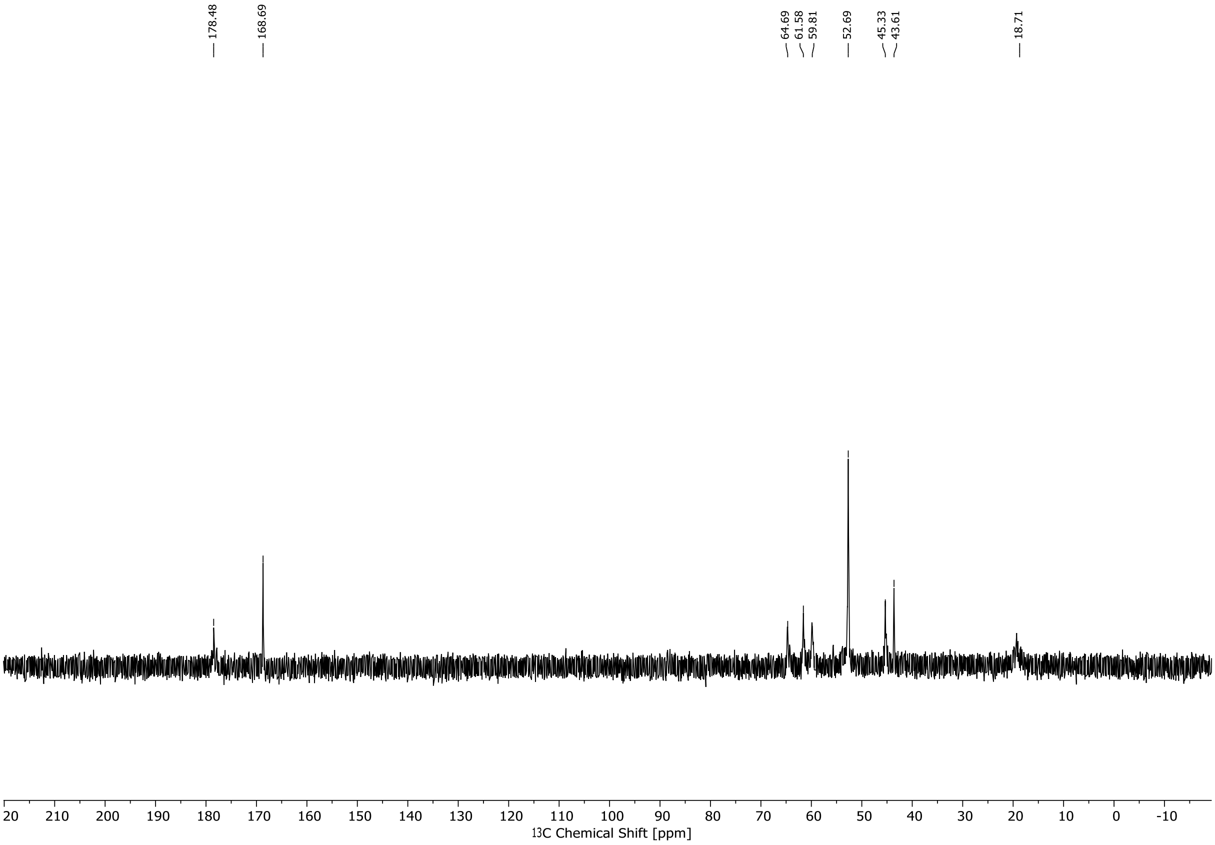

Figure A18: ^{13}C-NMR of Poly(2-((2-(methacryloyloxy)ethyl)dimethylammonio)acetate).

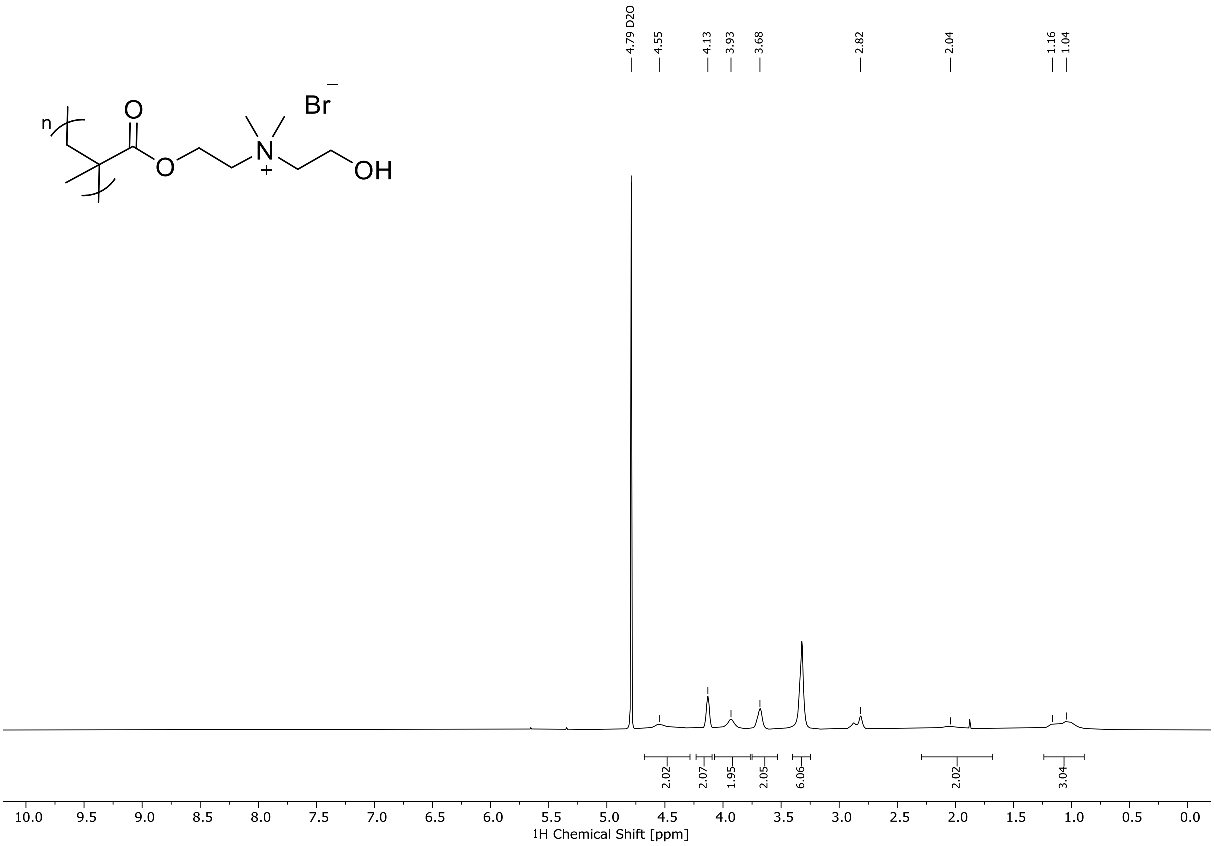

Figure A19: ^{1}H-NMR of Poly(2-hydroxy-N-(2-(methacryloyloxy)ethyl)-*N*,*N*-dimethylethan-1-aminium bromide).

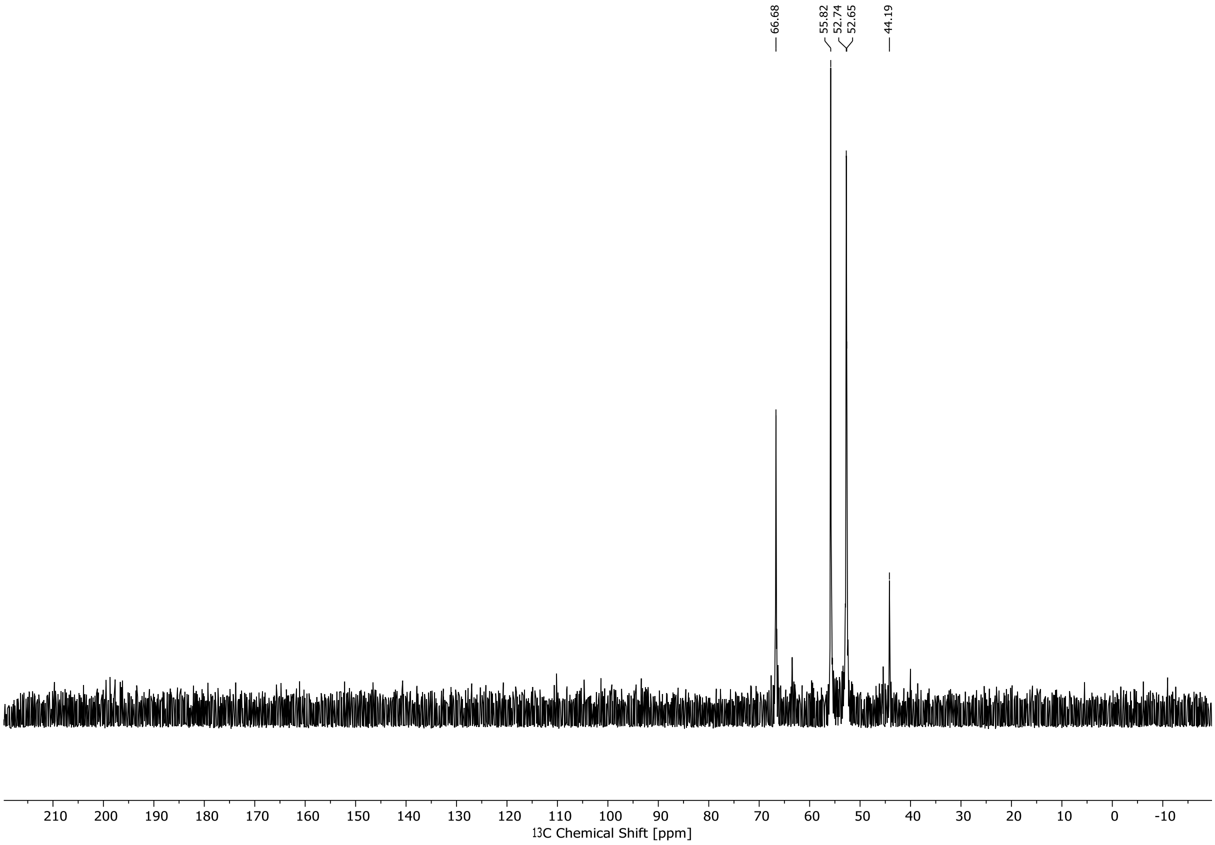

Figure A20: ^{13}C-NMR of Poly(2-hydroxy-*N*-(2-(methacryloyloxy)ethyl)-*N*,*N*-dimethylethan-1-aminium bromide).

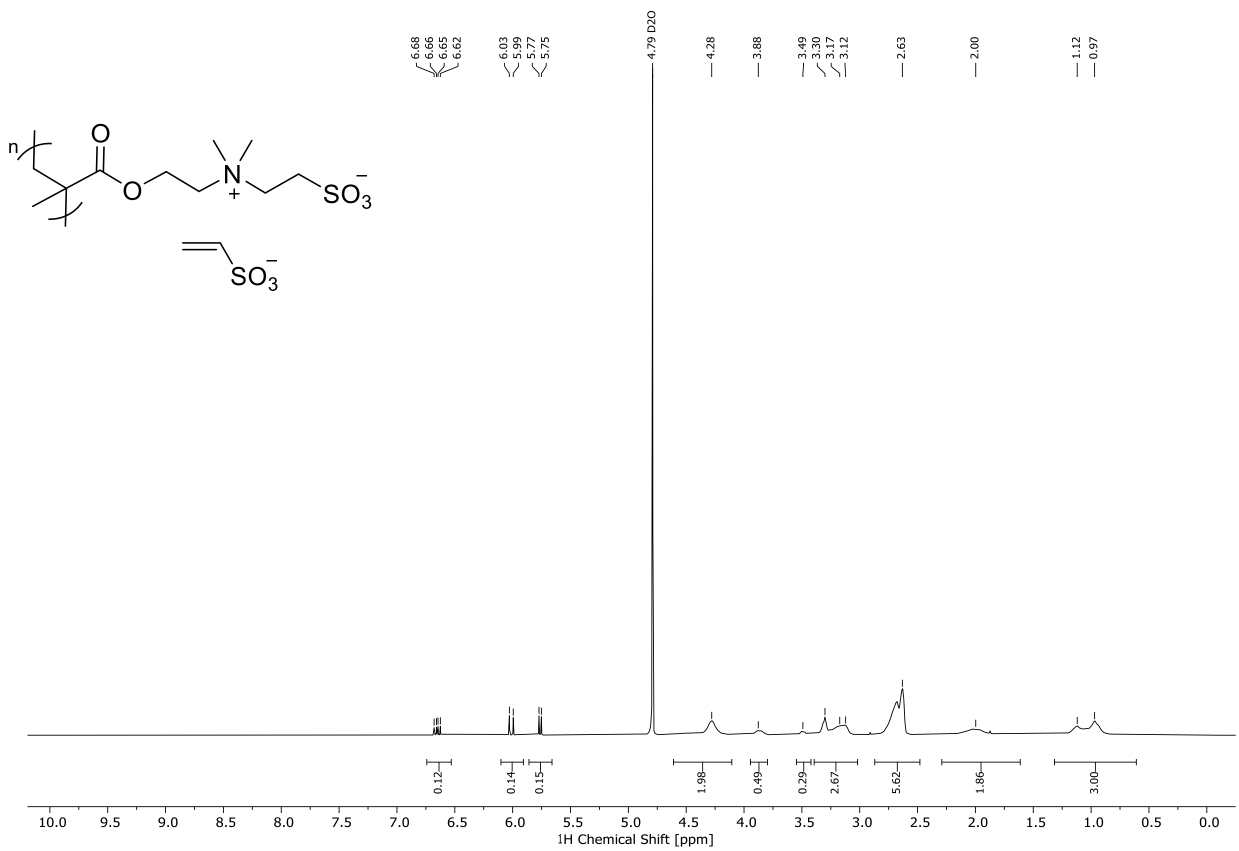

Figure A21: ^{1}H-NMR of Poly(2-((2-(methacryloyloxy)ethyl)dimethylammonio)ethane-1-sulfonate).

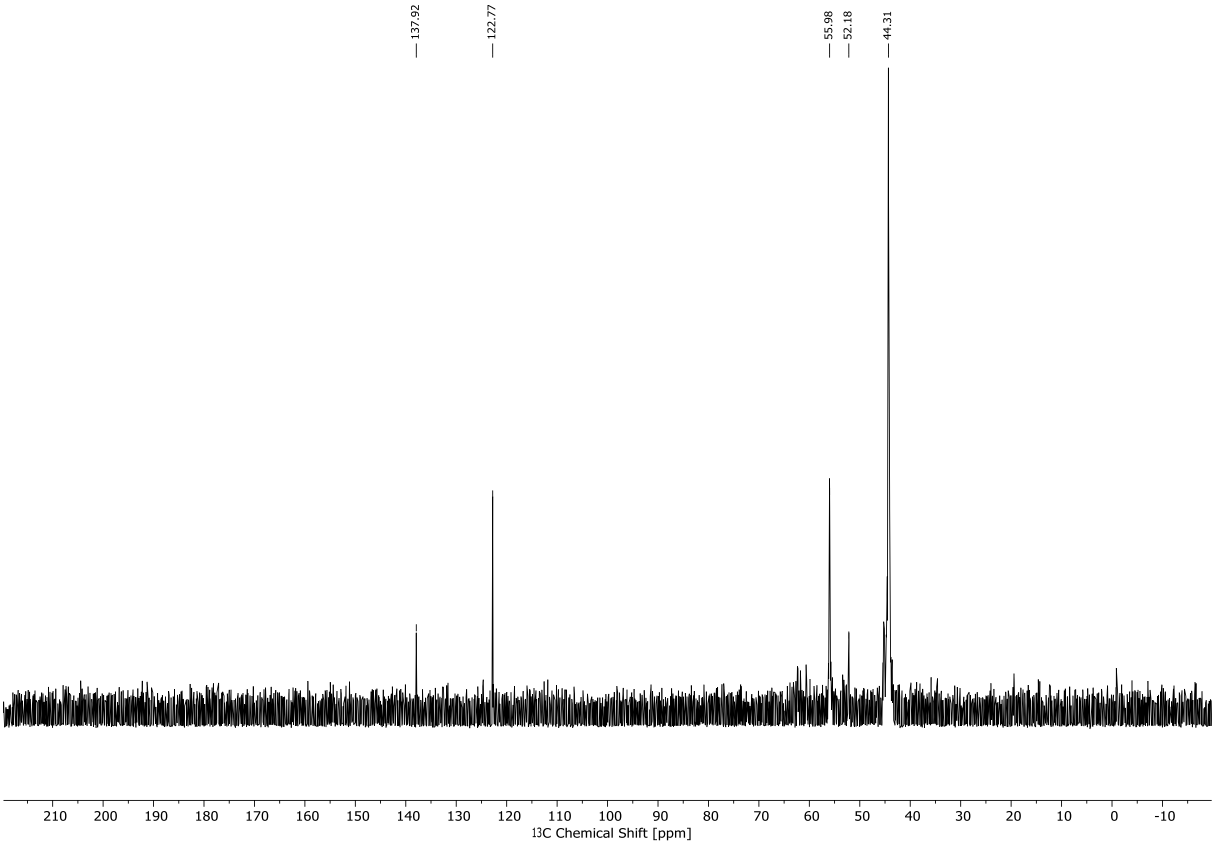

Figure A22: ^{13}C-NMR of Poly(2-((2-(methacryloyloxy)ethyl)dimethylammonio)ethane-1-sulfonate).

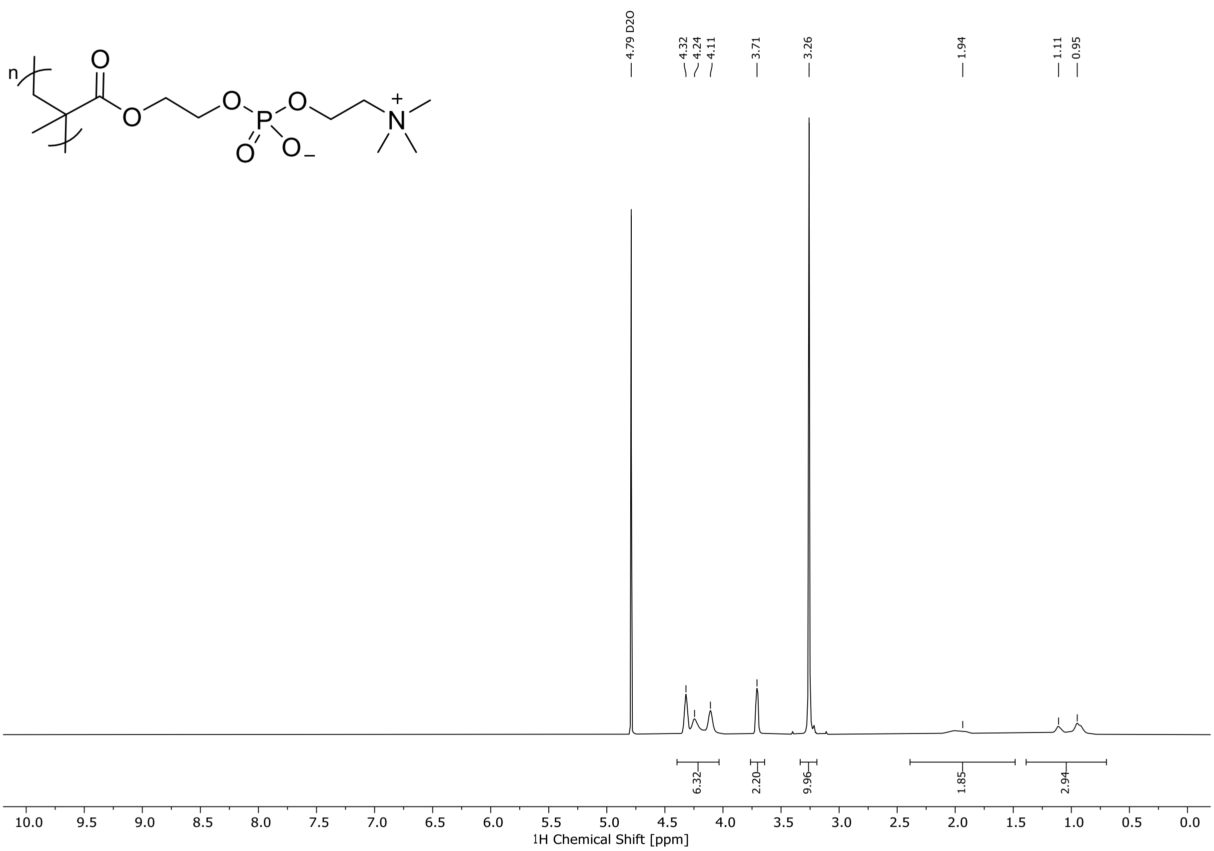

Figure A23: ^{1}H-NMR of Poly(2-(methacryloyloxy)ethyl (2-(trimethylammonio)ethyl) phosphate).

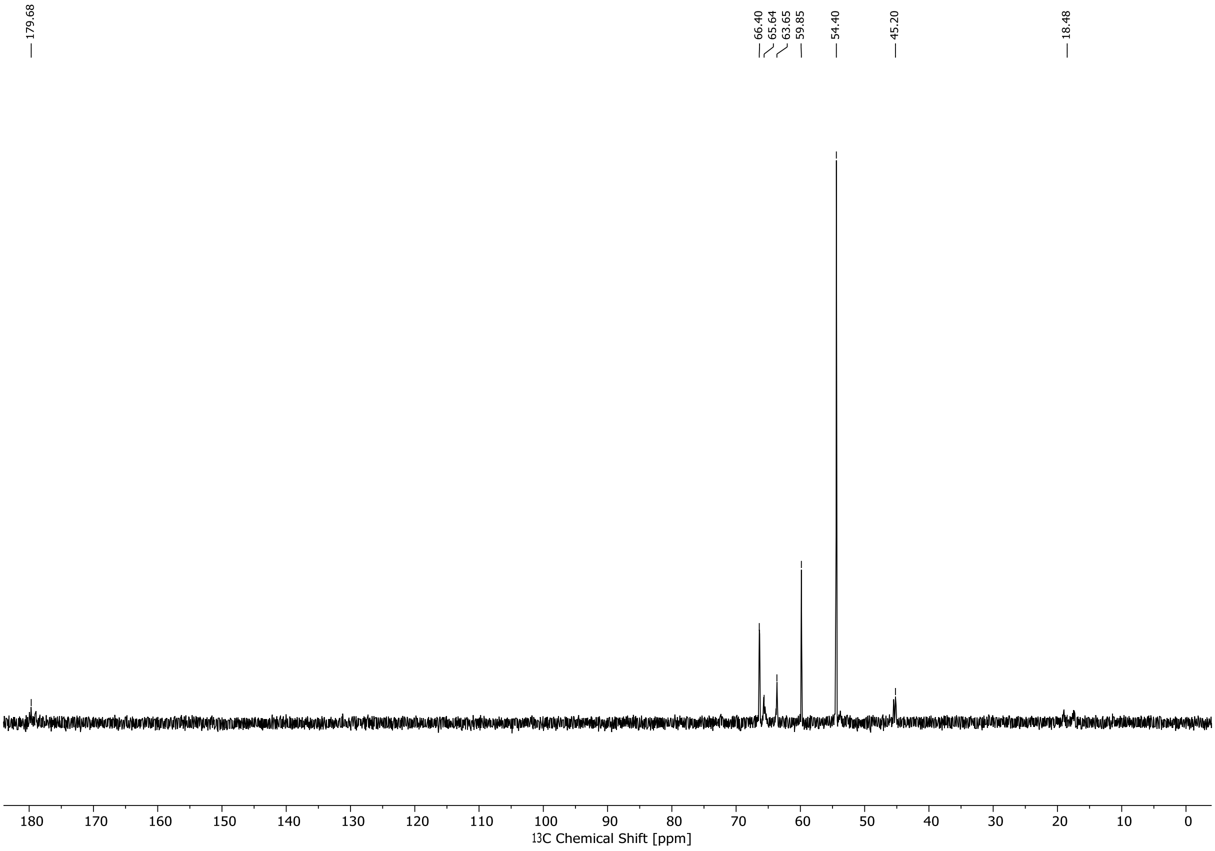

Figure A24: ^{13}C-NMR of Poly(2-(methacryloyloxy)ethyl (2-(trimethylammonio)ethyl) phosphate).

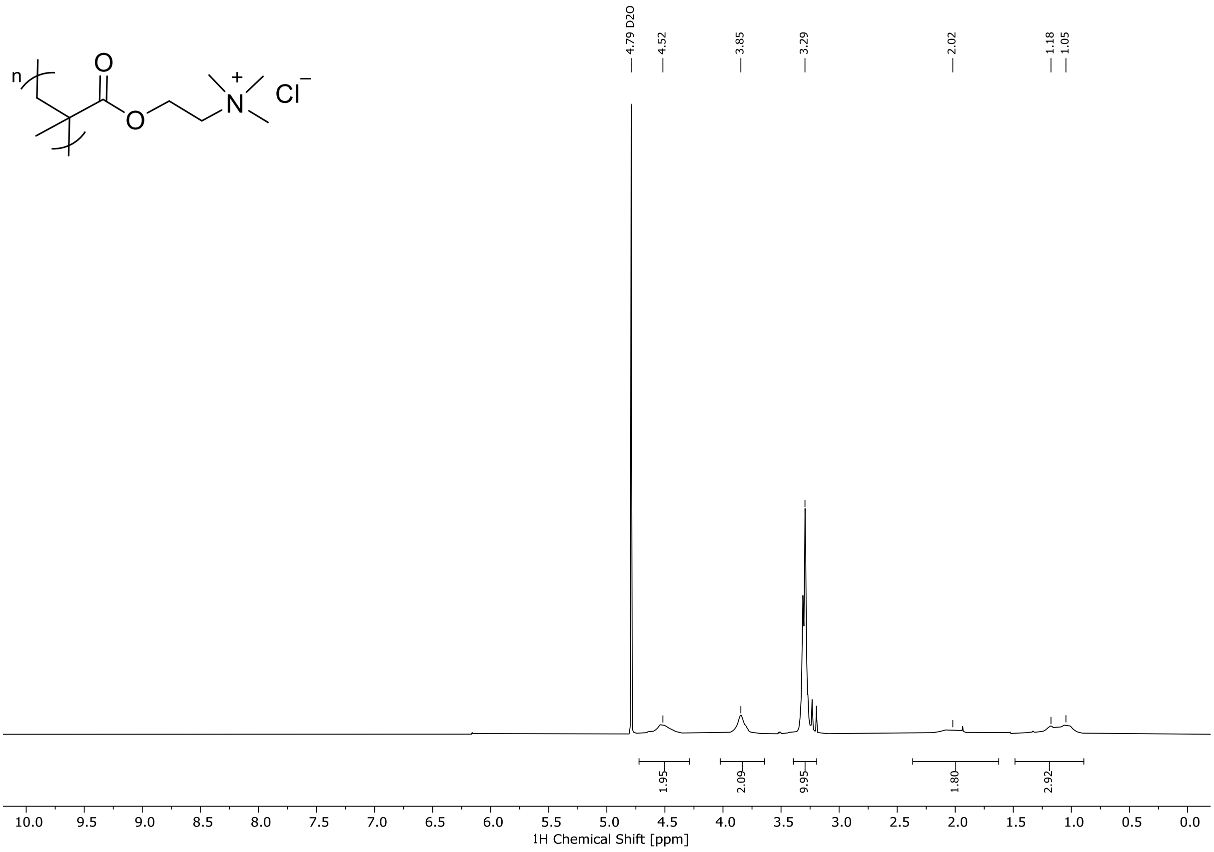

Figure A25: ^{1}H-NMR of Poly(2-(methacryloyloxy)-*N*,*N*,*N*-trimethylethan-1-aminium chloride).

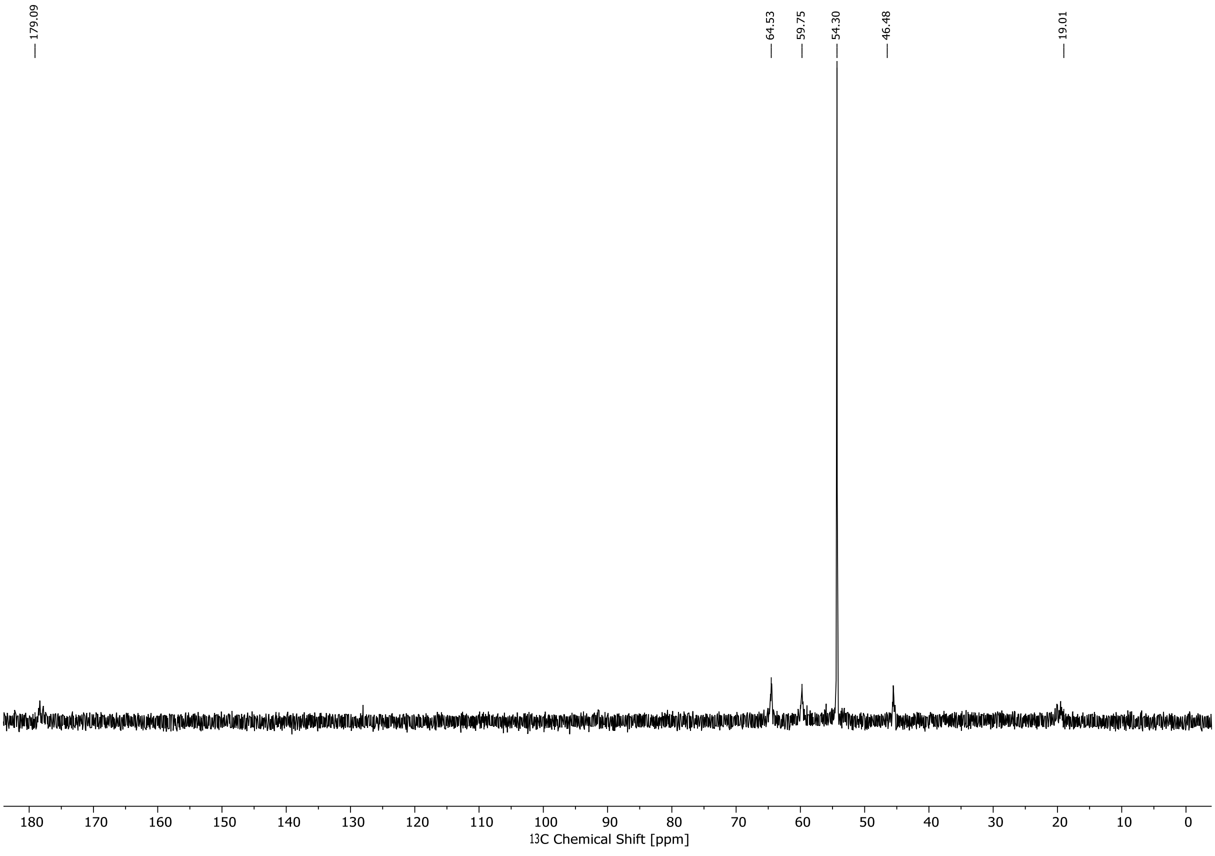

Figure A26: ^{13}C-NMR of Poly(2-(methacryloyloxy)-*N*,*N*,*N*-trimethylethan-1-aminium chloride).

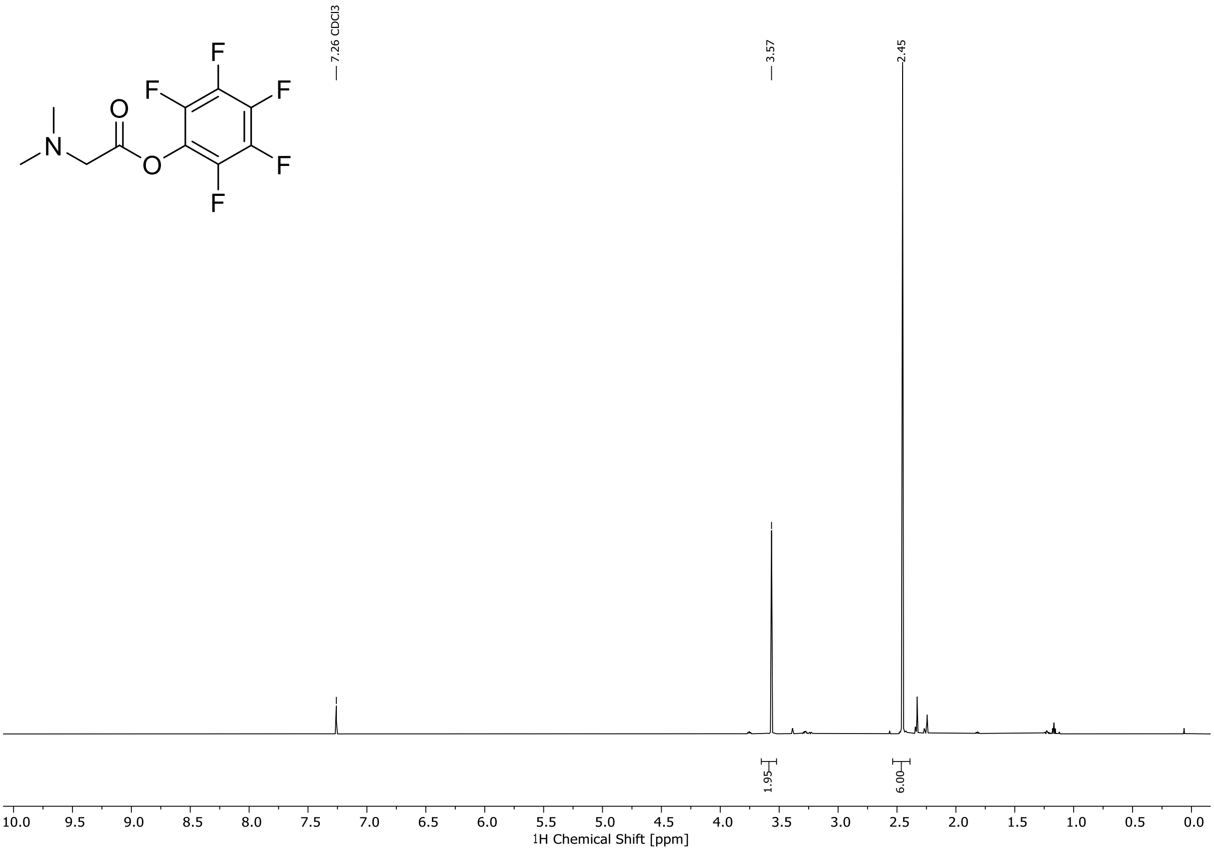

Figure A27: ^{1}H-NMR of Perfluorophenyl dimethylglycinate.

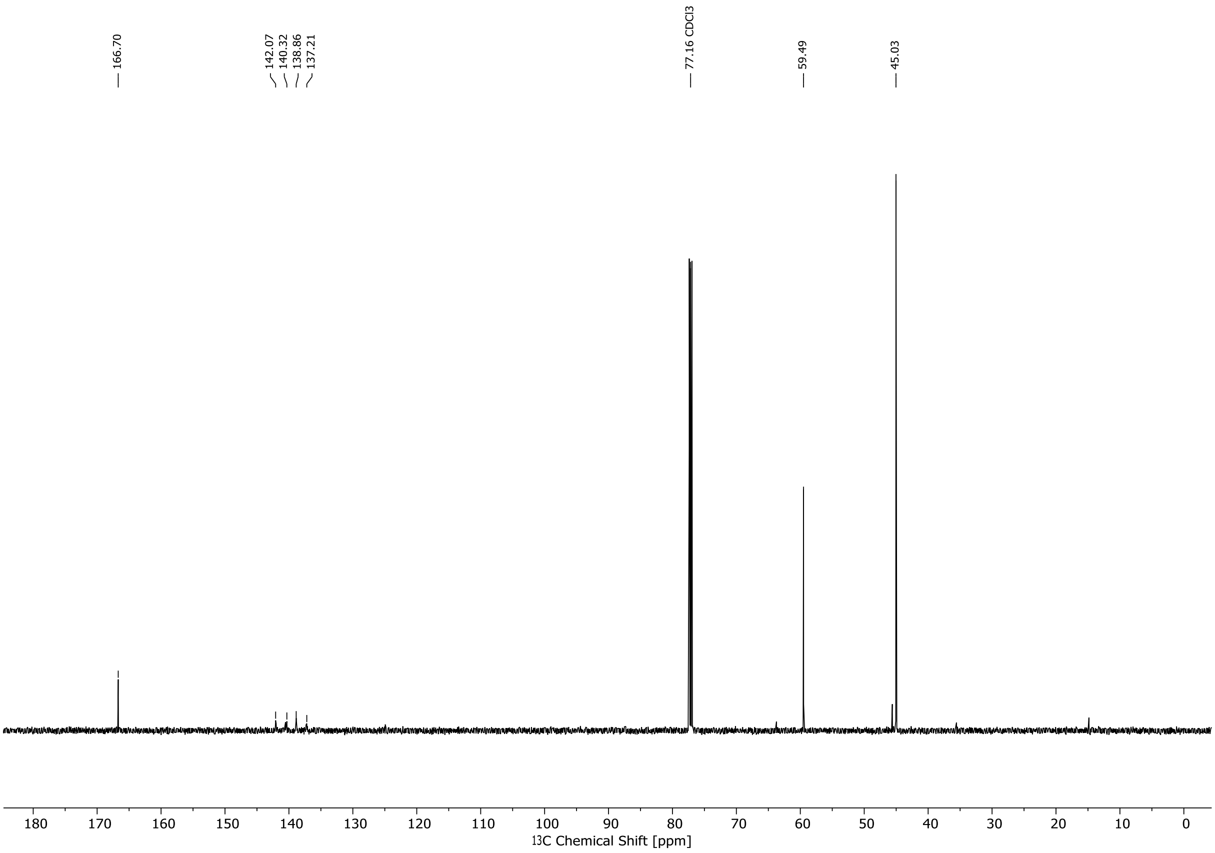

Figure A28: ^{13}C-NMR of Perfluorophenyl dimethylglycinate.

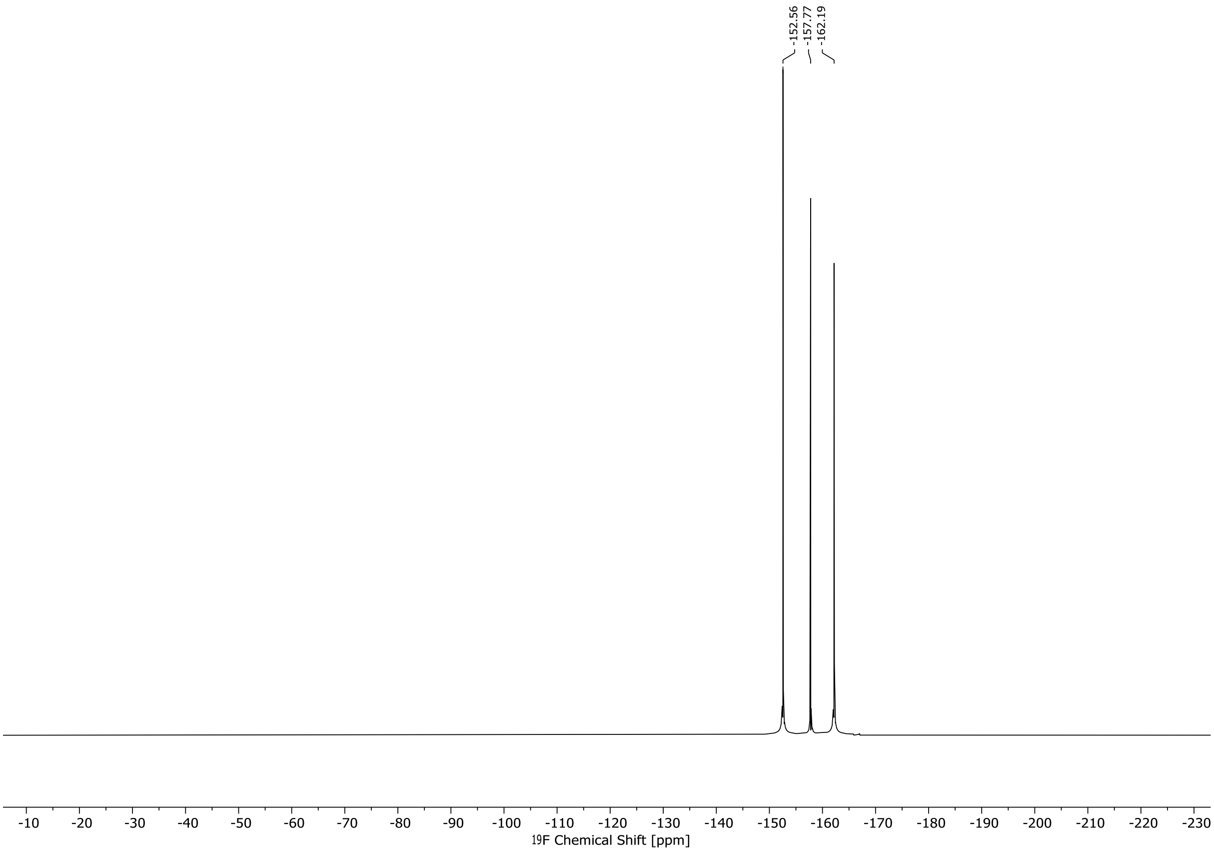

Figure A29: ^{19}F-NMR of Perfluorophenyl dimethylglycinate.

10.2 EDX-Spectra

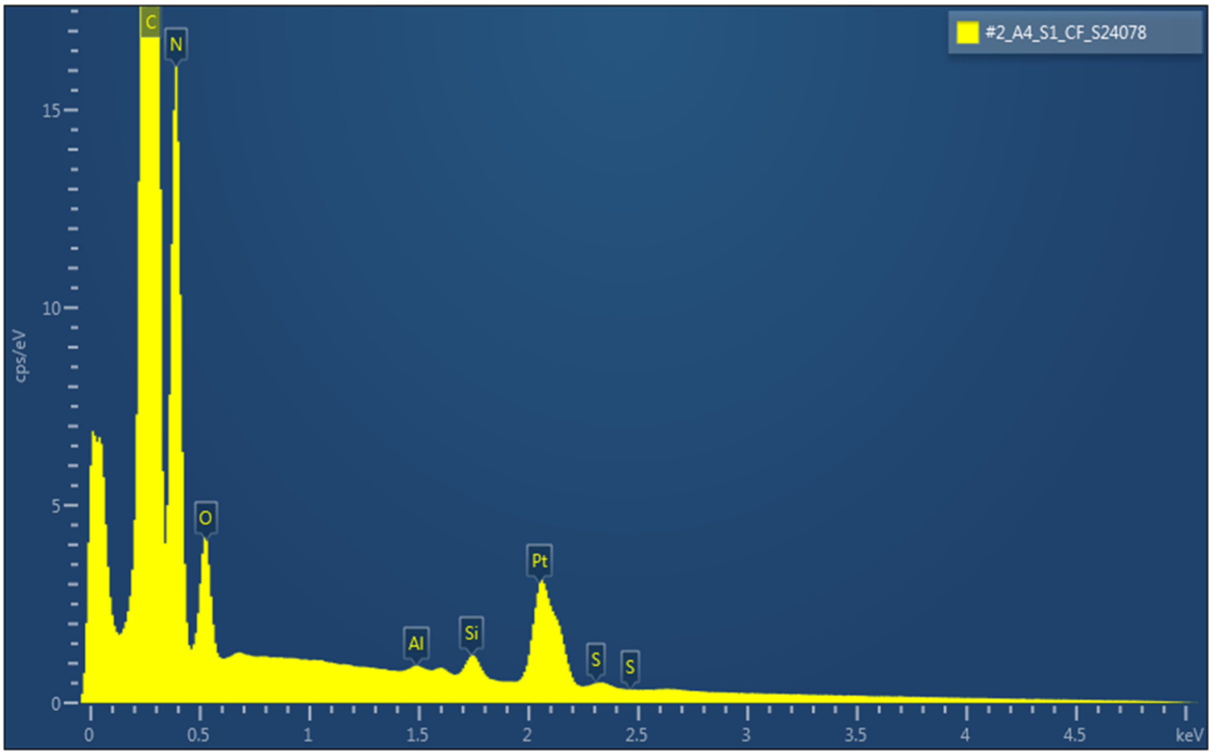

Figure A30: Top-view EDX-spectrum of PAN-*g*-DMAEMA-SB.

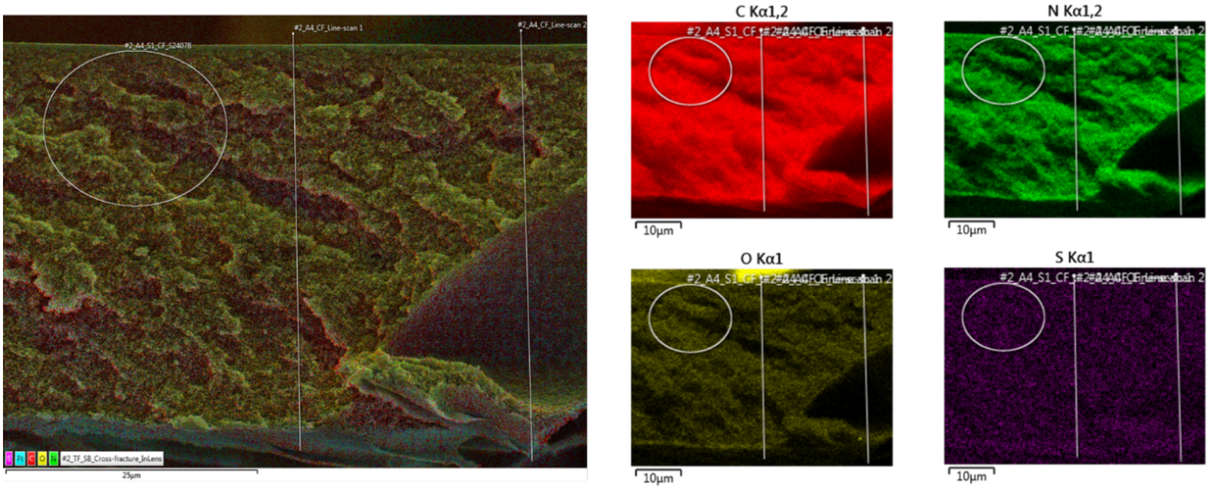

Figure A31: EDX mapping of the cross-section of PAN-*g*-DMAEMA-SB showing the elemental distribution of carbon (red), nitrogen (green), oxygen (yellow), and sulfur (purple), as well as the corresponding overlay image (left).

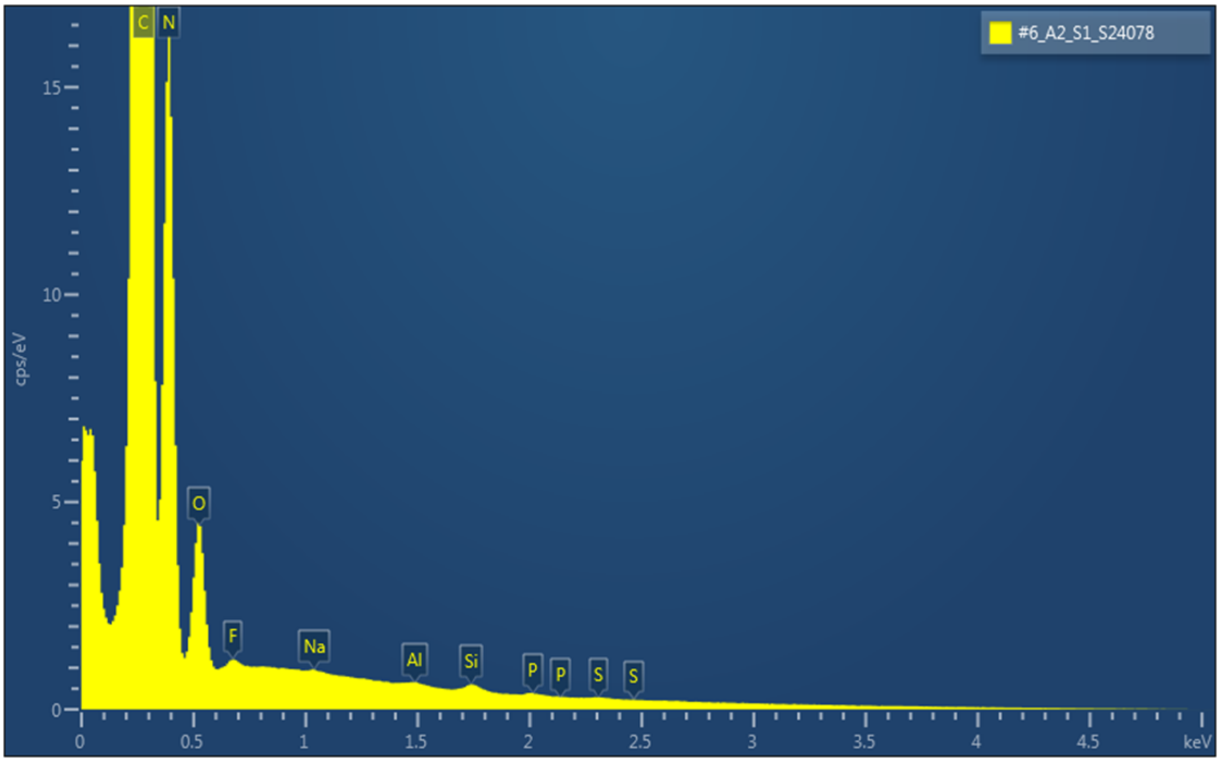

Figure A32: Top-view EDX spectrum of PAN-*g*-MPC.

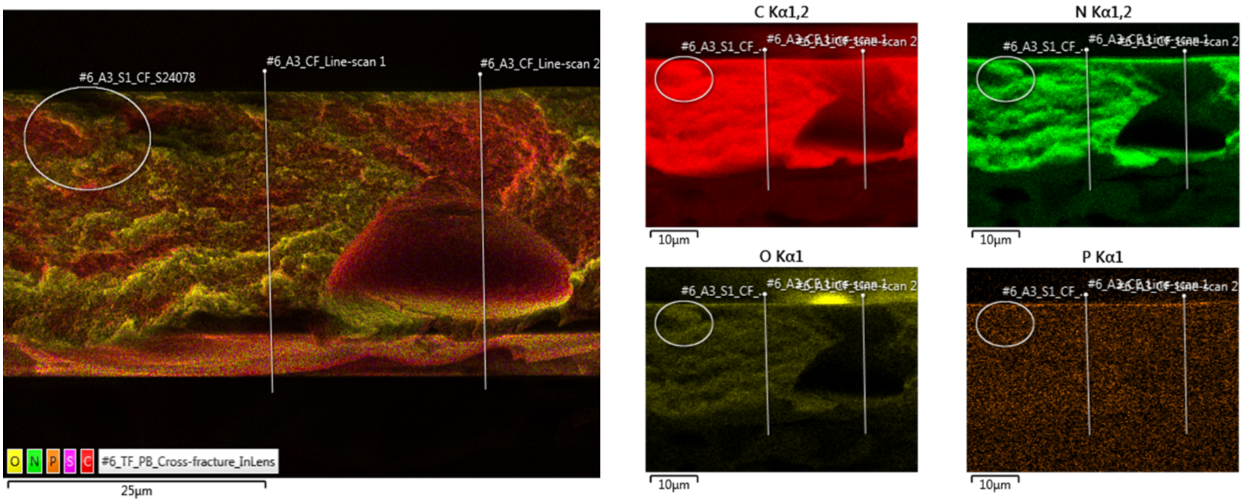

Figure A33: EDX mapping of the cross-section of PAN-*g*-MPC showing the elemental distribution of carbon (red), nitrogen (green), oxygen (yellow), and sulfur (purple), as well as the corresponding overlay image (left).

10.3 XPS-Spectra

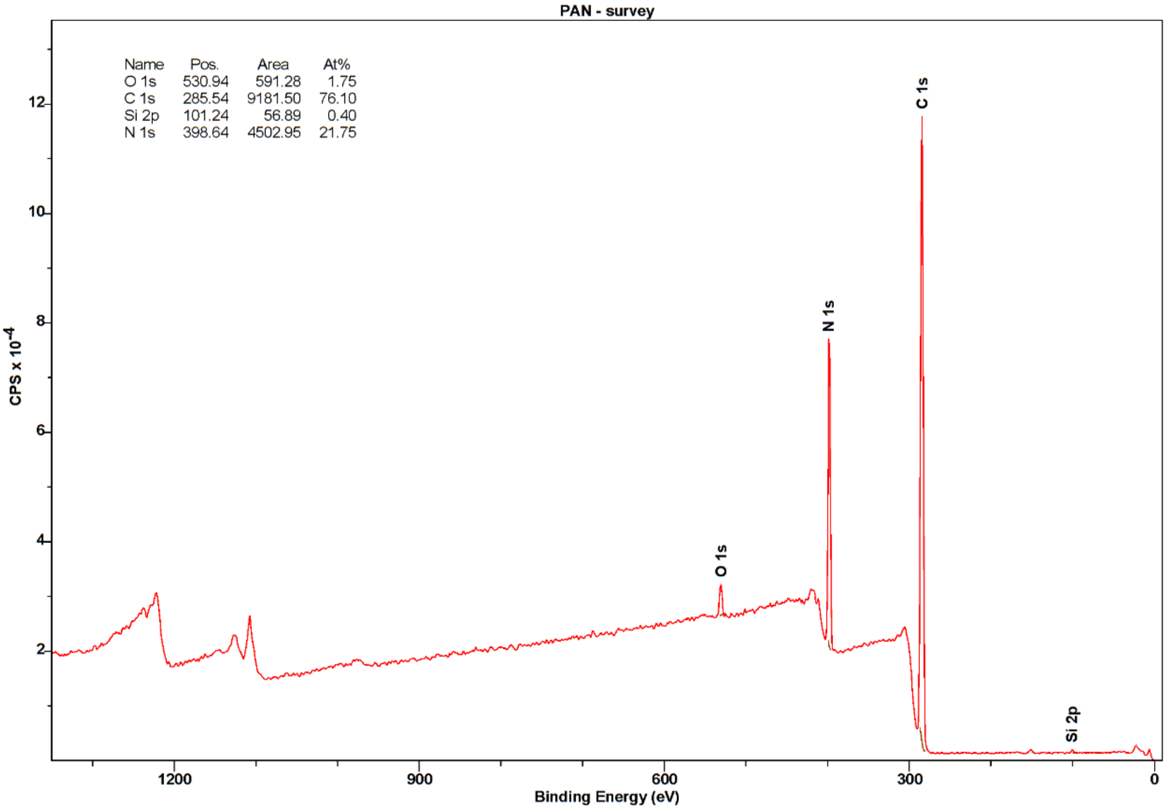

Name	Pos.	Area	At%
O 1s	530.94	591.28	1.75
C 1s	285.54	9181.50	76.10
Si 2p	101.24	56.89	0.40
N 1s	398.64	4502.95	21.75

Figure A34: XPS survey spectrum of pristine PAN.

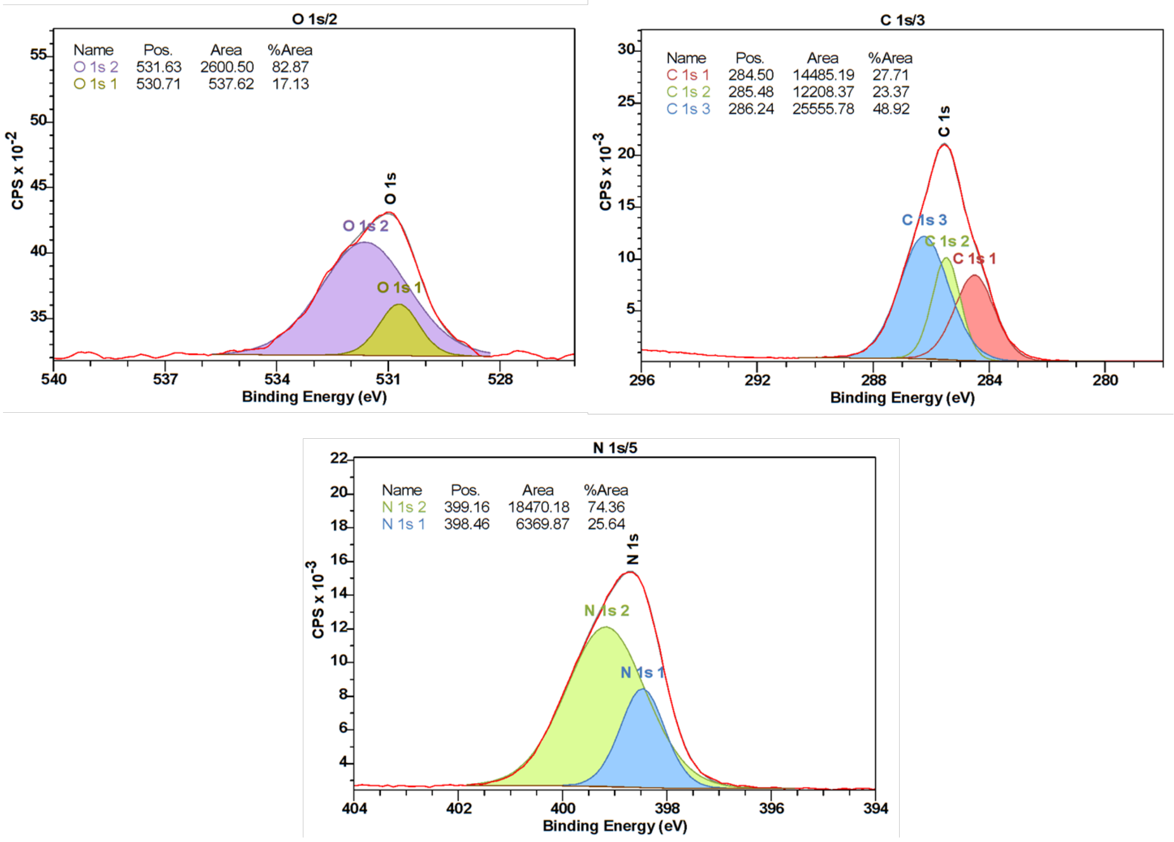

Name	Pos.	Area	%Area
O 1s 2	531.63	2600.50	82.87
O 1s 1	530.71	537.62	17.13

Name	Pos.	Area	%Area
C 1s 1	284.50	14485.19	27.71
C 1s 2	285.48	12208.37	23.37
C 1s 3	286.24	25555.78	48.92

Name	Pos.	Area	%Area
N 1s 2	399.16	18470.18	74.36
N 1s 1	398.46	6369.87	25.64

Figure A35: Deconvoluted XPS spectra of pristine PAN showing the O 1s, N 1s, and C 1s regions.

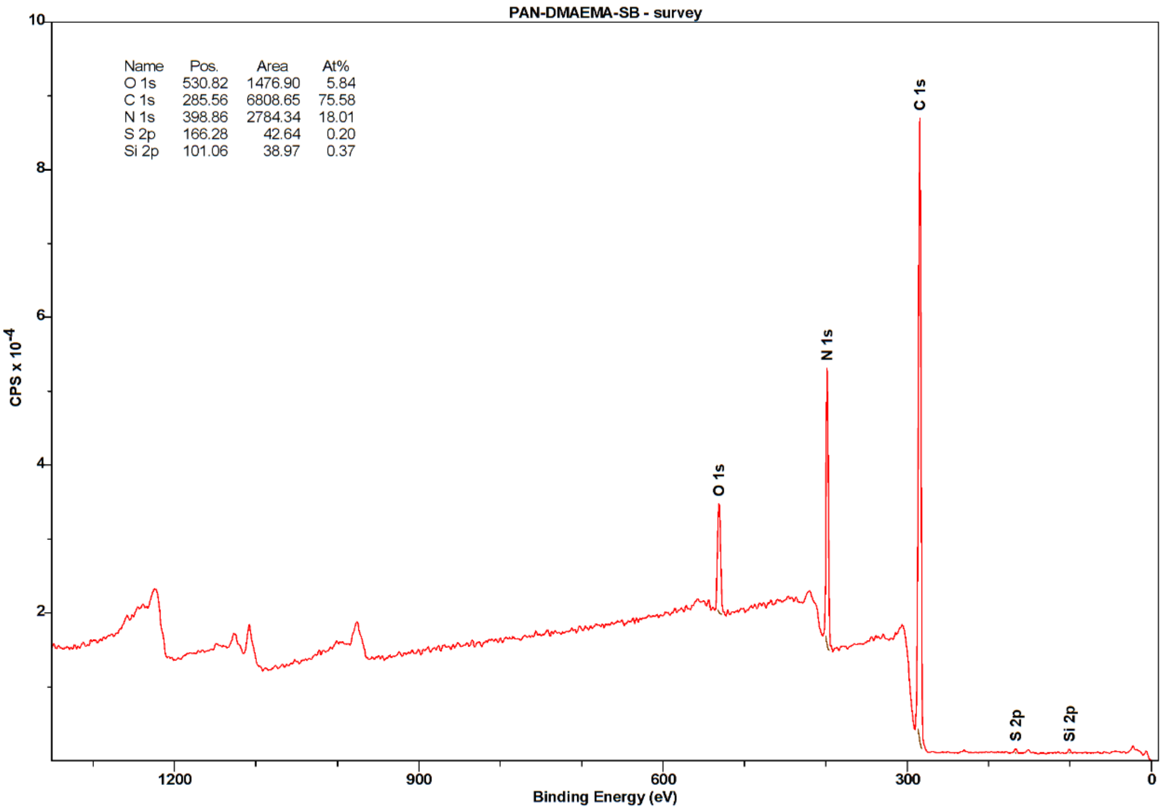

Name	Pos.	Area	At%
O 1s	530.82	1476.90	5.84
C 1s	285.56	6808.65	75.58
N 1s	398.86	2784.34	18.01
S 2p	166.28	42.64	0.20
Si 2p	101.06	38.97	0.37

Figure A36: XPS survey spectrum of PAN-*g*-DMAEMA-SB.

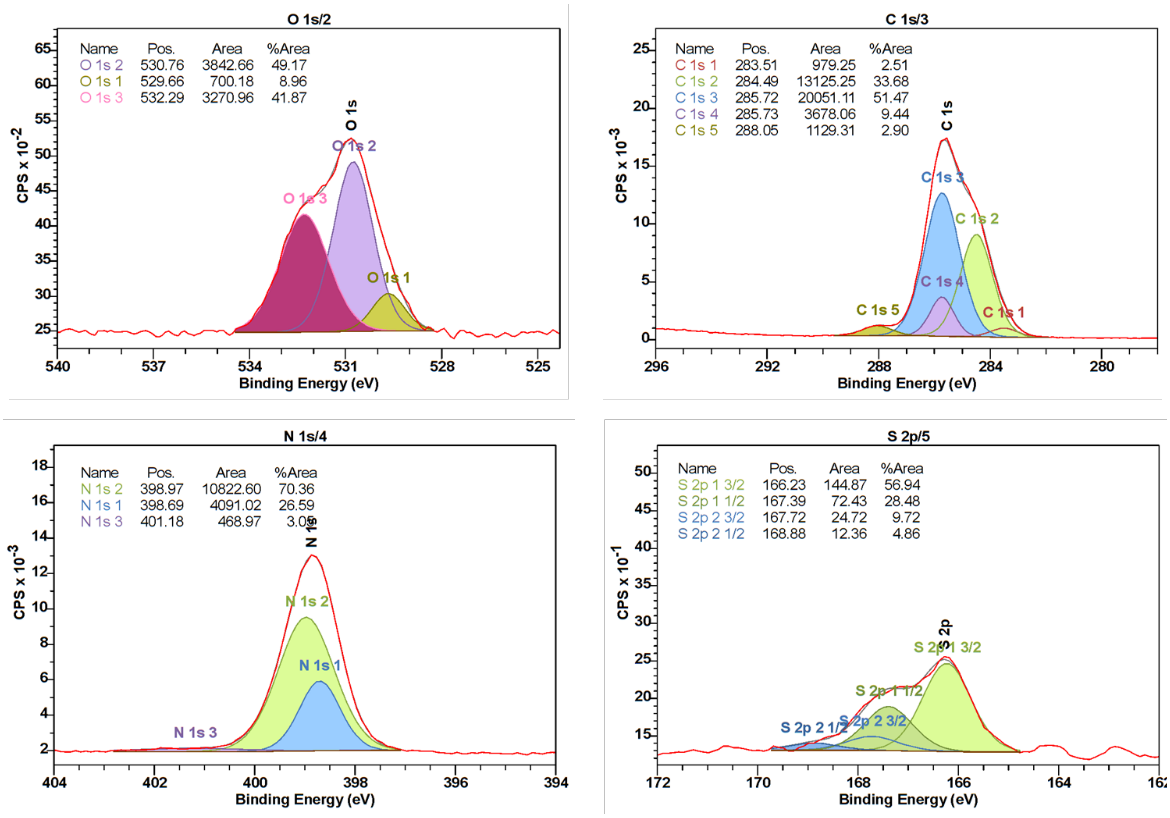

Name	Pos.	Area	%Area
O 1s 2	530.76	3842.66	49.17
O 1s 1	529.66	700.18	8.96
O 1s 3	532.29	3270.96	41.87

Name	Pos.	Area	%Area
C 1s 1	283.51	979.25	2.51
C 1s 2	284.49	13125.25	33.68
C 1s 3	285.72	20051.11	51.47
C 1s 4	285.73	3678.06	9.44
C 1s 5	288.05	1129.31	2.90

Name	Pos.	Area	%Area
N 1s 2	398.97	10822.60	70.36
N 1s 1	398.69	4091.02	26.59
N 1s 3	401.18	468.97	3.05

Name	Pos.	Area	%Area
S 2p 1 3/2	166.23	144.87	56.94
S 2p 1 1/2	167.39	72.43	28.48
S 2p 2 3/2	167.72	24.72	9.72
S 2p 2 1/2	168.88	12.36	4.86

Figure A37: Deconvoluted XPS spectra of pristine PAN-*g*-DMAEMA-SB showing the O 1s, C 1s, C 1s and S 2p regions.

10.4 Calibration for UV-Vis

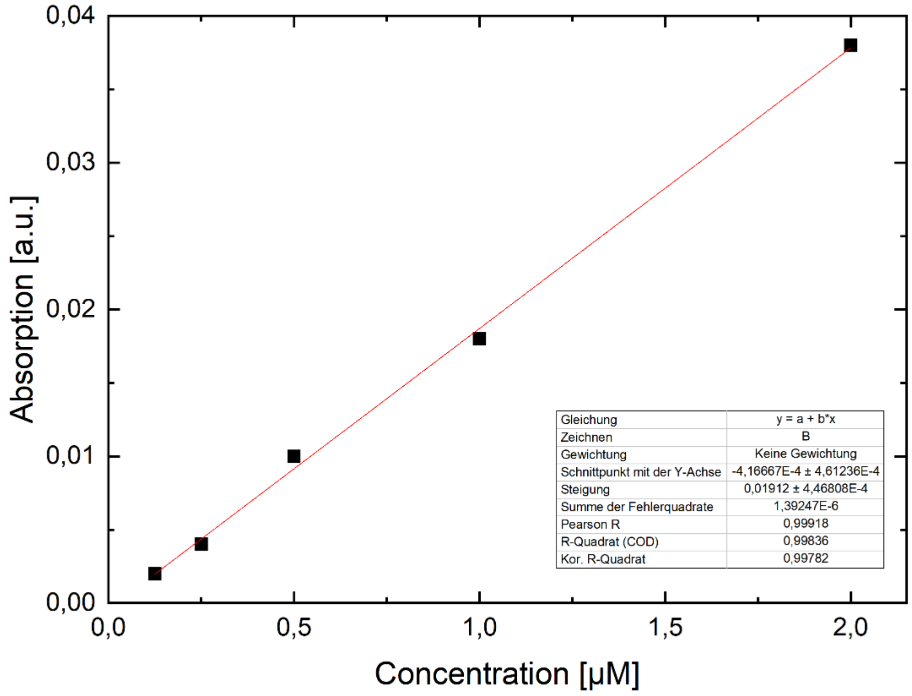

Gleichung	y = a + b*x
Zeichnen	B
Gewichtung	Keine Gewichtung
Schnittpunkt mit der Y-Achse	-4,16667E-4 ± 4,61236E-4
Steigung	0,01912 ± 4,46808E-4
Summe der Fehlerquadrate	1,39247E-6
Pearson R	0,99918
R-Quadrat (COD)	0,99836
Kor. R-Quadrat	0,99782

Figure A38: Calibration of acid orange 7 based on UV-Vis absorbance measurements. The linear relationship between concentration and absorbance was used to determine the adsorption capacity of the modified membranes.

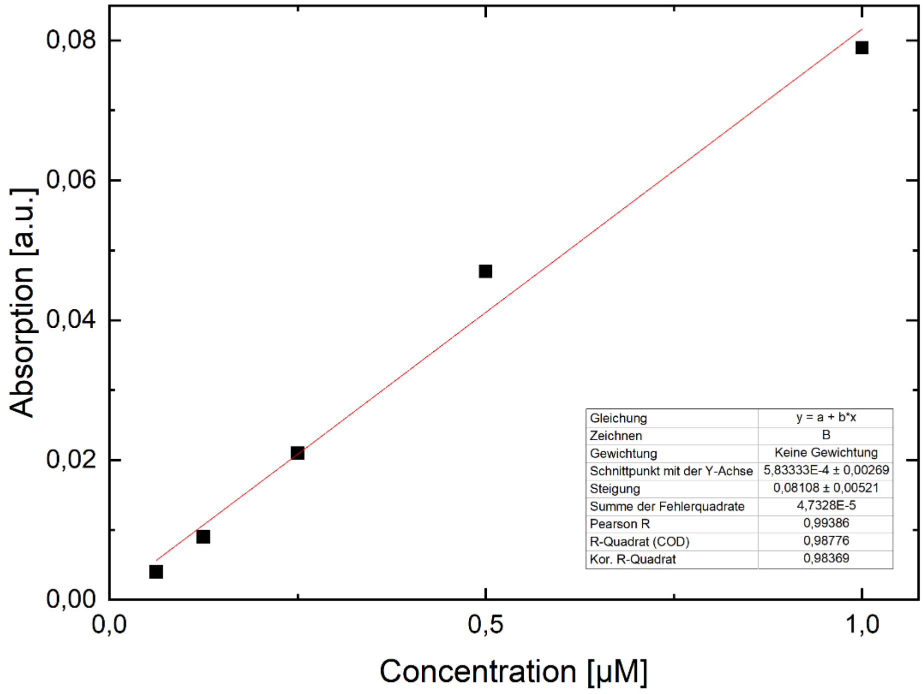

Gleichung	y = a + b*x
Zeichnen	B
Gewichtung	Keine Gewichtung
Schnittpunkt mit der Y-Achse	5,83333E-4 ± 0,00269
Steigung	0,08108 ± 0,00521
Summe der Fehlerquadrate	4,7328E-5
Pearson R	0,99386
R-Quadrat (COD)	0,98776
Kor. R-Quadrat	0,98369

Figure A39: Calibration of methylene blue based on UV-Vis absorbance measurements. The linear relationship between concentration and absorbance was used to determine the adsorption capacity of the modified membranes.

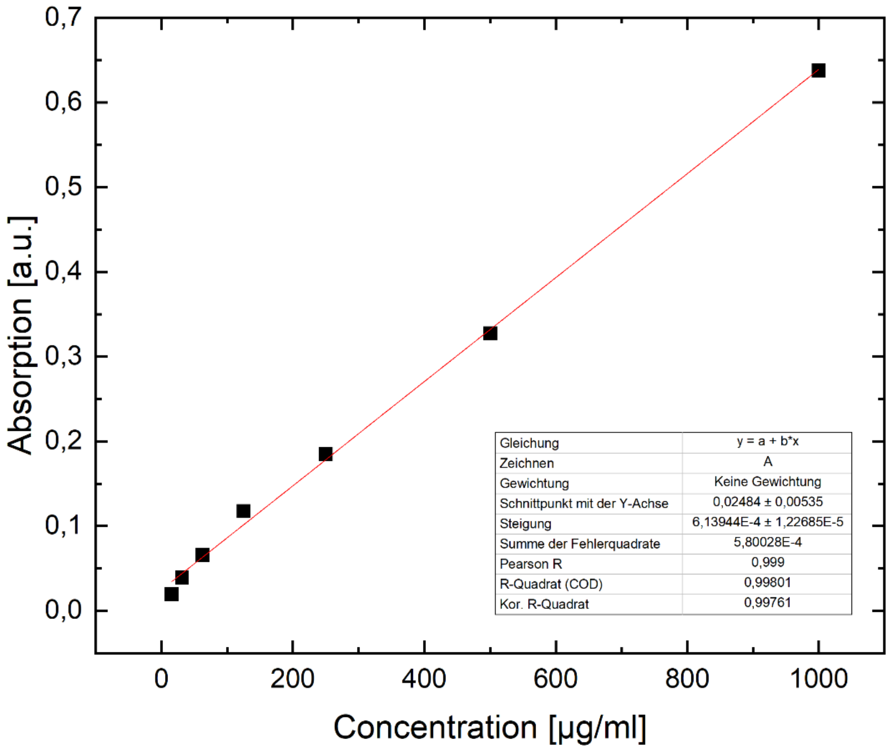

Gleichung	y = a + b*x
Zeichnen	A
Gewichtung	Keine Gewichtung
Schnittpunkt mit der Y-Achse	0,02484 ± 0,00535
Steigung	6,13944E-4 ± 1,22685E-5
Summe der Fehlerquadrate	5,80028E-4
Pearson R	0,999
R-Quadrat (COD)	0,99801
Kor. R-Quadrat	0,99761

Figure A40: Calibration of bovine serum albumin obtained by UV-Vis spectroscopy. The linear fit was used to quantify protein adsorption on membrane surfaces.

10.5 List of hazardous substances

The chemicals used are listed in Table A1, together with the hazard and safety information and the associated hazard pictograms.[193, 194]

Table A1: Hazardous substances with pictograms, H-statements, and P-statements according to GHS.

Substance	Pictograms	H-Statements	P-Statements
Acetone		225, 319, 336 EUH066	210, 233, 240 241, 242 305+351+338
Acetonitrile		225, 319 302+ 312+332	210, 280 301+312 303+ 361+ 353 304+ 340+ 312 305+ 351+ 338
Acid orange 7		372, 412	260, 264, 270 273, 314, 501
Ammonium persulfate		272, 302, 315 317, 319, 334 335	210, 280, 301+312 302+352 304+340+312 305+351+338
BAPO		317, 413	261, 272, 273 302+352 333+313
2-Bromoacetic acid		300, 317, 400 311+331, 314	260, 273, 280 303+361+353 304+340+310 305+351+338
2-Bromoethanol		301, 311, 331 314	280, 261, 310 304+340 305+351+338 303+361+353
Dichloromethane		315, 319, 336 351	201, 302+352 305+351+338 308+313

Dimethylamine solution (33%)		225, 314, 332 334,412	210, 273, 280 303+361+353 304+340+310 305+351+338
Dimethylglycine		302	264, 270 301+312, 280
DMAEMA		302+312 314, 317	261, 270, 280 301+312 303+361+353 305+351+338
DMAPMA		315, 317, 318	280, 302+352 305+351+338 333+313+501
EDC·HCl		302, 311, 315 317, 373,410	260, 301+312 273, 280, 314 302+352+312
Ethanol		225, 319	210, 233, 240 241, 242 305+351+338
Ethyl acetate		225, 319, 336 EUH066	210, 233, 240 241, 242 305+351+338
Ethyl bromoacetate		226 300+310+330	210, 233, 240 280 303+361+353 304+340+310
Ethyl 4-bromobutyrate		315, 319, 335	261, 264, 271 280, 302+352 305+351+338
Hydrogen peroxide (30%)		272, 302, 332 318	220, 261, 280 305+351+338

LAP		302, 315, 319 335	261, 280 301+312 302+352 305+351+338
METAC solution (75 wt.%)		317, 319	280 305+351+338
Methylene blue		302	301+312
MPC		317	261, 272, 280 302+352 333+313 362+364
N-Hydroxysuccinimide		318	305+351+338
Pentafluorophenol		302+312	264, 301+312 280, 362+364 302+352+312 501
Potassium carbonate		315, 319, 335	261, 264, 271 280, 302+352 305+351+338
Pyrogallol		302+312+332 341, 412	273, 301+312 280, 308+313 302+352+312 304+340+312
Sodium 2-bromo-ethanesulfonate		315, 319, 335	280, 261 304+340 305+351+338 337+313
4-Vinylbenzyl chloride (90%)		302, 311, 314 317	261, 272, 280 301+312 303+361+353 305+351+338

11 Acknowledgements

Zuerst danke ich Herrn Prof. Dr. Wolfgang Maison für das mir entgegengebrachte Vertrauen und die Aufnahme in seinen Arbeitskreis sowie für die spannende Themenstellung meiner Arbeit. Ebenso danke ich ihm für seine stets offene Tür bei fachlichen wie auch organisatorischen Fragen, für den gewährten wissenschaftlichen Freiraum und die ausgezeichneten Arbeitsbedingungen während meiner Promotion.

Mein Dank gilt außerdem Herrn Prof. Dr. Ralph Holl für die freundliche Übernahme des Zweitgutachtens.

Herrn Prof. Dr. Volkmar Vill und Frau Prof. Dr. Bianka Siewert danke ich für ihre Teilnahme an der Disputation.

Besonders bedanken möchte ich mich bei der aktuellen und ehemaligen Crew des AK Maison: Leif Kumpmann, Laurens Grosche, Lennart Spickschen, Michelle Kobus, Shirin Mesgarha, Jule Wulf, Erica Moretto, Alek Swierzewski, Donovan Timm, Hauke Eggert, Darius Ludolfs, Dr. Tom Seddig, Dr. Sharah Chandralingam, Dr. Erik Ruf, Dr. Tim Nauendorf, Dr. Eilika Zorn, Dr. Svenja Kerpa, Dr. Nils Burmeister, Dr. Silke Schmidt und Dr. Lasse Outzen.

Ich danke euch für die vielen lustigen AK Abende, Ausflüge, Pizza Fridays und die Kochaktionen sowie für all die fachlichen und vor allem nicht-fachlichen Gespräche, die diese Zeit so besonders gemacht haben.

Mein Dank gilt ebenso dem technischen Personal: Kathleen Pruntsch, Anette Kloodt, Claudia Wackendorff und Melanie Mosler. Ohne euch würden die Praktika nur halb so reibungslos ablaufen.

Meinen Kooperationspartnern am Hereon, Sarah Glass und Volkan Filiz, danke ich für die Möglichkeit, das Wasserlabor zu nutzen, sowie für den regen wissenschaftlichen Austausch.

Ein herzliches Dankeschön geht auch an meine Praktikantinnen und Praktikanten für ihre wertvollen Forschungsergebnisse. Besonders hervorheben möchte ich hier Catharina Pelz und Donovan Timm.

Für das Korrekturlesen dieser Arbeit danke ich Catha, Mimi und Vanni.

Mein besonderer Dank gilt Vanessa. Danke, dass du mich immer unterstützt und motiviert hast, für deinen Zuspruch, gerade in der Endphase dieser Arbeit, und für all die schönen Momente, die wir bereits erleben durften. Ich freue mich auf all das, was noch vor uns liegt. Danke, dass es dich gibt!

Abschließend möchte ich mich von Herzen bei meiner Familie bedanken. Danke, dass ihr mich auf diesem Weg begleitet habt und mir das Studium ermöglicht habt. Ohne euch wäre dies alles nicht möglich gewesen.

12 Declaration on oath

I hereby declare and affirm that this doctoral dissertation is my own work and that I have not used any aids and sources other than those indicated. If electronic resources based on generative artificial intelligence (gAI) were used in the course of writing this dissertation, I confirm that my own work was the main and value-adding contribution and that complete documentation of all resources used is available in accordance with good scientific practice. I am responsible for any erroneous or distorted content, incorrect references, violations of data protection and copyright law or plagiarism that may have been generated by the gAI.

Hamburg, 27.09.2025